Exchange coupling phenomena in Fe-based ferrimagnetic heterostructures

Dissertation

zur Erlangung des akademischen Grades
Dr. rer. nat.

eingereicht an der
Mathematisch-Naturwissenschaftlich-Technischen Fakultät
der Universität Augsburg

von

Johannes Seyd

Augsburg, Dezember 2024

“Waste no more time arguing what a good man should be. Be one.”

- Marcus Aurelius, addressing himself

Erstgutachter:	Prof. Dr. Manfred Albrecht
Zweitgutachter:	Prof. Dr. Felix Büttner
Datum der mündlichen Prüfung:	08. Mai 2025

Contents

CHAPTER 1

Introduction

It is old news that the demand for data storage has increased immensely over the past decades. The increasingly widespread use of the internet, smartphones, social media, cloud storage, and artificial intelligence have made it easier and faster than ever to create, share, and consume digital data. The amount of data generated every day has thus been increasing exponentially over the past years. Statistics show that humanity currently creates around 400 Exabytes (400 million Terabytes) of digital data every day. Accordingly, the internet requires vast databanks for storing everything that we are used to experiencing online. All this data is still mostly stored on hard-drive disks (HDDs) due to their low cost, but in high-performance sectors they are slowly being displaced by solid-state drives (SSDs) with their better performance and better possibility of increasing the bit density.

For commercial HDDs, the formerly steady increase of bit density has slowed down, and bit density has been stagnating around 1.1-1.2 TBit/inch^2 for several years now. Solid-state drives have already achieved densities over 3 TBit/inch^2 [1], but are also still twice as expensive as HDDs, have limited writing cycles, and usually store information for 2-5 years without power supply. It is thus expected that HDDs will remain the workhorse for datacenters in the foreseeable future, especially in the high demand area of cloud service providers.

The issue with bit density in HDDs based on perpendicular magnetic recording (PMR) can be summarized in the *trilemma of magnetic recording*. As the name suggests, this consists of three issues that cannot be perfectly solved together: thermal stability, signal-to-noise ratio (SNR), and writability.

To get higher bit densities, the bit size needs to be decreased. One could of course use fewer magnetic grains per bit, but this would reduce the SNR, which scales with $log_{10}(N)$, N being the number of grains the bit consists of. So, to keep the SNR, the grains need to become smaller. Furthermore, the border between two bits is sharper and bit areas overlap less with smaller grains, similar to a picture becoming sharper with more or smaller pixels. Smaller grains would thus also reduce the bit error rate (BER), which is depicted in Fig. 1.1 a). The BER is simply the ratio of incorrectly read bits to all bits read out within a given time span.

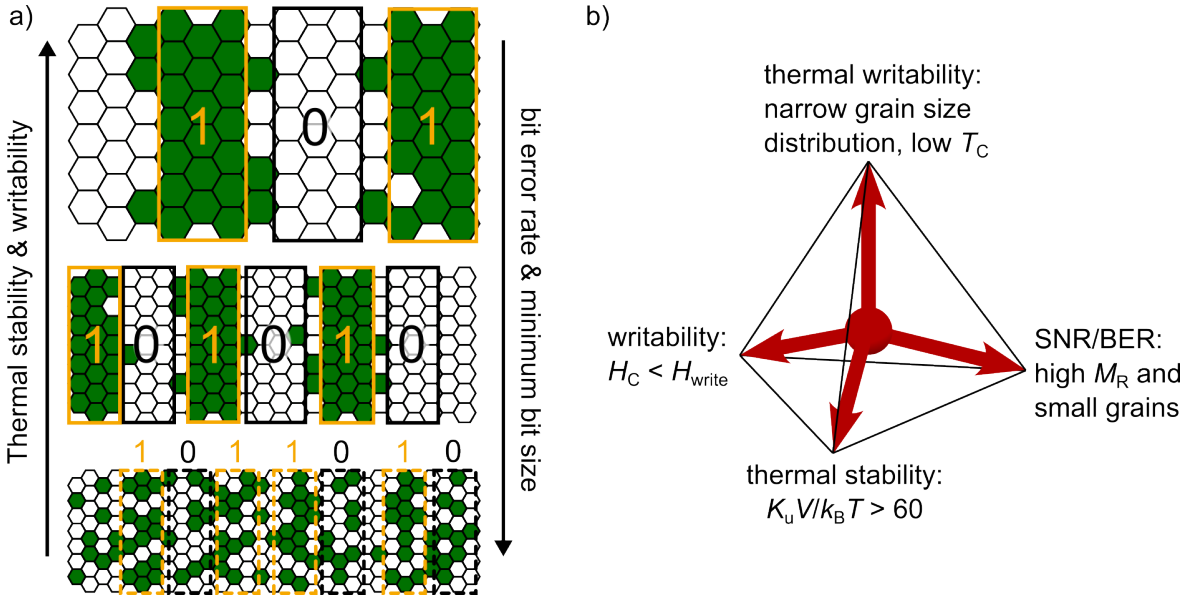

Figure 1.1: a) Depiction of the effect that a reduction of grain size has on bit size and grain stability. Larger grains benefit stability and writability, while smaller grains are needed for smaller bit sizes. If grains become too small, thermal energy can switch the grains, leading to the loss of bit information. b) Schematic of the quadrilemma of heat-assisted magnetic recording (HAMR): the four conditions should all be optimized for an ideal medium, but contradict each other in part.

However, if the grains of regular recording media were reduced in size much further, then the grains themselves would cease being stable ferromagnets and instead behave like a paramagnet with a high saturation magnetization, a so-called superparamagnet. The lower limit of grain size is thus called the superparamagnetic limit, which is a hard limit and cannot be avoided for any material.

Thermal stability requires the magnetic grains to be magnetically stable for at least ten years in order to retain bit information. As a rule of thumb, the equation $\frac{K_u V}{k_B T} \geq 60$ can be taken as the minimum anisotropy energy needed to stabilize a magnetic grain at a temperature T for more than ten years.

There are now two possibilities of increasing the anisotropy energy: increasing the bit volume V or using materials with a higher anisotropy constant K_u [2]. Increasing the grain volume while keeping the bit size fixed is detrimental to the SNR and/or bit size, as already mentioned. But using highly anisotropic materials is also problematic, because writability is limited by the maximum writing field that a writing head can exude. Modern writing heads consist of a CoFe pole head with a writing field of around 2 Tesla, so the grains cannot have a coercivity H_C higher than this if we want to still be able to write them. Materials with a high K_u, however, also have a high coercivity. Accordingly, one has to find a compromise between the three requirements in order to maximize bit density in HDDs.

Naturally, ways of circumventing the trilemma have always been much sought after. Approaches include tilted magnetic recording [3], patterned media [4], shingled media [5], and energy-assisted magnetic recording (EAMR) such as microwave-assisted magnetic recording (MAMR) [6].

One of these approaches (belonging to EAMR) is heat-assisted magnetic recording (HAMR) [7]. This technique utilizes the temperature-dependence of coercivity to make materials with high K_u writable. This is done by locally heating the material with a laser pulse (via a near-field transducer) to a temperature close to the Curie temperature, making it magnetically soft. The field of the writing head is then able to switch the magnetization of the grain before it cools down again. The high K_u means that the grain's magnetization is still stable at room temperature even at reduced size, so the grains and consequently the bits can be made smaller without increasing the bit error rate. However, the process is not without drawbacks: inconsistent heat distribution and thermal fluctuations during the heating process can lead to grains not being switched completely due to insufficient heating or losing the information due to excess heat [8]. Further, non-uniform distribution in T_C, grain sizes, and pitch distances additionally increase noise in HAMR media [9–11]. Consequently, the trilemma is expanded into a quadrilemma, with thermal writability as the fourth condition that needs to be optimized (see Fig. 1.1 b). This additional condition also means that the maximum theoretical density that can be achieved by perfect HAMR media is lower than that of a perfect trilemma medium, around 20 TBit/inch^2 [12, 13].

Seagate has already achieved bit densities of 2 TBit/inch^2 in commercially available HAMR media based on $L1_0$-FePt, with plans of increasing to 3 TBit/inch^2 by 2026. Using bit-patterned media, such as isolated magnetic dots or shingles [14], in combination with HAMR in a hybrid technique called *heated dots magnetic recording* (HDMR) is claimed to reach even up to 10 TBit/inch^2 in the long term. This value was also computed earlier as an ultimately achievable value by Vogler et al. in 2016 [15].

Other factors that get increasingly more important are energy efficiency and speed of reading and writing information. Both of these can be optimized using all-optical switching (AOS), which uses ultrafast femtosecond laser pulses to switch the magnetization of a magnetic bit. This enables switching times in the order of picoseconds, an order of magnitude faster than conventional writing [16]. Field-free AOS even circumvents the usage of magnetic fields for writing, thereby greatly decreasing energy usage.

This type of switching was first observed for GdFeCo in 2007 [17], but it can also be seen in many other systems, including rare-earth transition metal (RE-TM) alloys, ferrimagnet bilayers, rare-earth-free synthetic ferrimagnets, and even ferromagnets [17–22]. However, magnetic fields must sometimes be applied to increase the switching probability.

Another rather new spintronic technology in the field of magnetic memory is magnetoresistive random access memory (MRAM) [23]. It utilizes magnetic tunnel junctions (MTJs), consisting, among others, of two ferromagnetic layers separated by a thin insulating layer. One of these layers is pinned via the exchange bias (EB) effect and acting as a reference for the second (free) layer, enabling the measurement of tunnelling magnetoresistance (TMR) [24]. MRAM technology promises reduced energy consumption and faster read/write speeds by moving away from magnetic field-based writing towards short current pulses, making use of spin-orbit or spin-transfer torque (SOT/STT) to switch magnetic bits [25].

This work focuses on the investigation of the $L1_0$-FePt phase and other $L1_0$ alloys as well as the amorphous ferrimagnet Tb_xFe_{100-x}. $L1_0$-FePt, as already mentioned, is not only one of the most prominent materials in the HAMR field of research, but has also been suggested as a material for spintronic applications [26–28]. Both the amorphous Tb-Fe alloys and the $L1_0$-FePt phase have also been shown to display AOS [18, 22, 29–32], and TbFe can show immensely high exchange bias fields [33, 34], which might improve future TMR applications such as MTJs.

The investigations shown here cover the effect of heat treatment on Tb-covered $L1_0$-FePt layers compared to layers without Tb cover, inducing the $L1_0$ structure in mixed alloys as well as CrPt thin films, and the magnetic interaction between two Tb_xFe_{100-x}-layers of different composition. In the latter, double exchange bias and ultraslow magnetic relaxation effects were observed.

CHAPTER 2

Magnetic interlayer coupling phenomena

In the field of magnetic thin films, a multitude of inter- and intralayer interaction phenomena exist. The following chapters will give a short overview over those ones that are most relevant to the evaluation presented in this work, namely Ruderman-Kittel-Kasuya-Yosida (RKKY) interaction, exchange spring behaviour, and the exchange bias effect.

2.1 RKKY interaction

The most common ferromagnetic materials are based on the well-known elements Fe, Co, and Ni. The long-range magnetic order of these 3d transition metals is caused by the direct exchange interaction, where the delocalized electrons of the 3d orbitals interact between neighbours and cause the parallel alignment of magnetic moments. The same direct exchange is the cause of antiferromagnetic alignment in Mn.

However, most modern magnets also rely heavily on rare-earth (RE) elements like Nd, Sm, or Tb. The magnetic properties of these elements are caused by the electrons of the rather localized 4f orbital, which cannot overlap with the electron orbitals of neighbouring atoms, so the model of direct Heisenberg exchange does not apply here. Instead, the inner 4f electrons polarize the outer 5d or 6s electrons, which can then interact with other atoms over longer distances. This type of interaction has a long range and shows an oscillatory behaviour: depending on the distance, the coupling between two atomic moments can be parallel or antiparallel. This model was first described by M. Ruderman and C. Kittel in 1954 and shortly afterwards expanded by T. Kasuya and K. Yosida in 1956 and 1957, respectively [35–37]. Accordingly, this type of interaction is now known as Ruderman-Kittel-Kasuya-Yosida or RKKY interaction.

The RKKY interaction does not only apply to RE elements, though. It can also describe the interaction between two magnetic layers that are separated by a non-magnetic, metallic layer. The interaction still retains its oscillatory behaviour in this case [38, 39]. This allows the creation of synthetic antiferromagnets, where the magnetizations of two ferromagnetic layers cancel out due to the antiparallel alignment mediated by the spacer layer. Interestingly, the RKKY interaction was fundamental

for the discovery of the giant magnetoresistance (GMR) effect: it was observed in a system of Fe layers separated by Cr layers of different thickness [40–42].

2.2 Exchange spring systems

A good permanent magnet has a high magnetization and is magnetically hard, requiring a high K_u. However, the materials with the highest magnetization are usually not the ones with the highest magnetic anisotropy [43]. This is bad for permanent magnets used e.g. in electric motors or generators. The figure of merit used for such applications is the maximum energy product $(BH)_{max}$. It can be imagined as the energy stored in the magnet and is equivalent to the area of the biggest rectangle that can be fit under the B-H-loop in the second quadrant, as depicted in Fig. 2.1. The theoretical limit for $(BH)_{max}$ is $(BH)_{MAX} = \mu_0 M_S/4$, which would require perfect squareness and a coercivity higher than half the saturation magnetization [44].

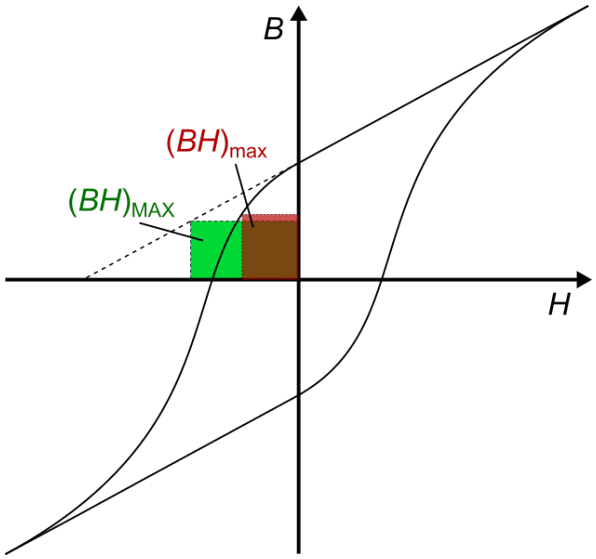

Figure 2.1: Graphical method of determining $(BH)_{max}$ from a B-H-loop. The area of the largest rectangle fitting below the loop in the second quadrant is $(BH)_{max}$, while its maximum value for a perfectly square loop with sufficiently high H_C is $(BH)_{MAX}$.

One way of increasing $(BH)_{max}$ is combining a magnetically hard layer, where H_C exceeds $M_S/2$, and a magnetically soft layer with high magnetization. Depending on the strength of the interlayer coupling, two cases of magnetic behaviour can be differentiated.

In the first case, the magnetic coupling between the two layers is strong, so both layers are switched alongside each other, i.e. the M-H-loop shows a one-step reversal process. This can only happen when the soft layer is not too thick: as a rule of thumb, both layers share the coercivity of the hard layer if the thickness of the soft layer does not exceed the Bloch domain wall width δ of the hard layer, which can be determined by

$$\delta = \pi\sqrt{A/K} \tag{2.1}$$

with the exchange stiffness A and the anisotropy K of the hard layer [45]. Effectively, the strong coupling only allows the soft layer to rotate its magnetization slightly, like in a domain wall, but not to reverse its magnetization completely [46]. This is depicted in Fig. 2.2. For thicker soft layers, the nucleation field H_n for magnetic reversal is quickly reduced, but the two layers remain coupled until the soft layer exceeds a few domain wall widths of the hard layer. Magnetization reversal in this regime happens by inhomogeneous rotation, where the soft layer rotates at lower fields than the hard layer, and the domain wall propagates from the soft layer through the hard layer with increasing field.

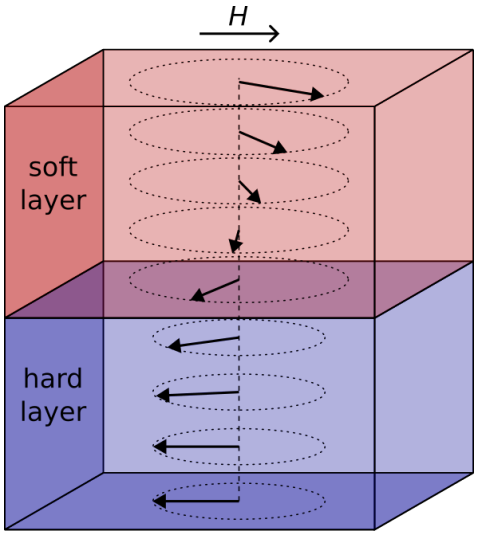

Figure 2.2: A depiction of the exchange spring behaviour of coupled soft and hard ferromagnetic layers with a small magnetic field applied antiparallel to the hard layer magnetization. The magnetization in the soft layer is pinned near the interface and rotates to align with the external field further away from it.

For much thicker soft layers, the coupling between the layers is not strong enough and the M-H-loop shows a two-step reversal process: the hard and soft layers switch independently [47]. However, the magnetic moments of the soft layer are not all reverted at once, but instead show a gradual rotation along the thickness of the layer. This is caused by the magnetic moments at and near the interface, which are still coupled to the hard layer. Effectively, the soft layer contains a domain wall that is compressed towards the interface with increasing field. Once the field is high enough, the domain wall can propagate into the hard layer and the hard layer is switched. However, if the magnetic field is reversed before this point, the domain wall is decompressed again and the magnetic moments of the soft layer revert to their initial state. This reversible rotation of magnetization is similar to the elastic bending of a mechanical spring, hence such a system is called an exchange spring [44].

In specific cases, a hysteretic behaviour of the soft layer can be observed in exchange spring systems. It was long believed that such a behaviour could be caused by a partial switching of a hard layer region near the interface, creating an additional energy barrier for the reversal of the soft layer. However, it was found that it rather depends on the thickness of the soft layer and on the exchange energy between the soft and hard layers

[48–50]. For soft layers above a critical thickness t_c and interfacial exchange coupling constants below a critical value A_{sh}^c, the exchange spring system displays an irreversible switching behaviour of the soft layer. For very low exchange constants, however, the coupling becomes dominated by magnetostatic interactions and the reversal of both layers happens simultaneously.

As already mentioned, the magnetic hardening effect in such exchange spring systems is a valuable tool for increasing the energy product of permanent magnets by using a nanostructured two-phase magnet, utilizing the hard phase to strengthen a soft phase with a high magnetic moment [51]. This technique can be used to create rare-earth-free permanent magnets with high $(BH)_{max}$, as was shown with a $L1_0$-FePt/CoFe bilayer system [52]. Additionally, exchange springs were also proposed as a means of increasing the density of perpendicular magnetic recording media to values near 10 TBit/inch^2 [53–57]. This approach works by increasing the thermal stability of ultrasmall magnetic grains to allow for ultrahigh bit densities.

2.3 Exchange bias effect

Exchange spring magnets usually utilize two coupled ferromagnetic phases. When instead coupling a ferromagnetic layer to an antiferromagnetic layer, a so-called exchange bias (EB) behaviour can often be observed. It can be seen as a horizontal shift of the M-H hysteresis loop of the ferromagnet to either positive or negative fields and also has its origin in the interlayer exchange coupling.

Having discovered the EB effect in Co/CoO particles in 1956 [58], W. Meiklejohn and C. Bean developed a simple model for describing the new phenomenon: a perfectly flat antiferromagnetic layer with uncompensated spins at the interface couples with the ferromagnetic layer, as depicted in Fig. 2.3 b). Due to the alternating direction of the spins in the antiferromagnet in this model, the interfacial spins all have the same alignment. Depending on the sign of the coupling constant, the spins of the ferromagnet will then preferentially align parallel or antiparallel to the uncompensated antiferromagnet spins.

When no external magnetic field is applied, this is the stable magnetic configuration. In order to overcome this pinned state, the Zeeman energy needs to be increased by applying a field in the direction opposite the ferromagnet's magnetization. Once the Zeeman energy is higher than the exchange energy, the ferromagnet will be switched. However, once the field is removed, the ferromagnet can switch back again, depending on the strength of the exchange coupling. Thus, a unidirectional anisotropy is induced in the ferromagnetic layer, shifting the M-H-hysteresis loop horizontally. This is depicted by an exemplary M-H-loop in 2.3 a). The extent of the exchange bias effect is represented by the effective field by which the M-H-loop is shifted: the exchange bias field H_{EB}. This value can be determined by calculating the average of the fields where the field axis is intersected, while the coercivity H_C is their difference divided by two:

$$H_{\mathrm{EB}} = \frac{H_{\mathrm{C2}} + H_{\mathrm{C1}}}{2} \tag{2.2}$$

$$H_{\mathrm{C}} = \frac{H_{\mathrm{C2}} - H_{\mathrm{C1}}}{2} \tag{2.3}$$

The early model by Meiklejohn and Bean with a rigid antiferromagnet gives a simple formula for H_{EB}, using the exchange coupling term J as well as the magnetization M_{F} and the thickness t_{F} of the ferromagnetic layer [59]:

$$H_{\mathrm{EB}} = \frac{J}{M_{\mathrm{F}} t_{\mathrm{F}}} \tag{2.4}$$

This simple model yields highly overestimated values of the exchange bias field, but much more investigation of exchange-biased systems was needed before more sophisticated models could be developed. More than 20 years would pass before two other models were developed, namely the random-field model by Malozemoff and the Mauri-model [60–62]. Both models allowed the existence of magnetic domains within the antiferromagnet (compare Fig. 2.3 c)), but still generally overestimated H_{EB}. Even more refined models were presented another ten years later, focussing more on the role of defects and polycrystallinity in the antiferromagnetic layer [63–65]. With this consideration of magnetic domains and rough interfaces, as depicted in Fig. 2.3 d), simulations finally showed much more realistic values of H_{EB}.

A lot of insight has been gained into the subject over the years, but nevertheless, the precise origin of exchange bias is still not entirely known. The simple phenomenological model as depicted in Fig. 2.3 is still sufficient to understand the general behaviour, though.

As can be seen from the different models, the interface quality can be identified as one of the conditions of highest importance for creating EB. It is often assumed that unpaired antiferromagnetic spins at the interface are essential to create a loop shift, but simulations have shown that a perfectly compensated interface can also lead to EB behaviour [66]. Still, interfacial roughness and spin orientation have been shown to be the most important factor in determining the magnitude of H_{EB} [67–70].

In the as-prepared condition, the antiferromagnetic layer will generally be in an unordered multidomain state. Accordingly, the spins at the surfaces of the domains will have different orientations. The biasing, averaged over all differently oriented domains, will then result in zero shift of the M-H-loop and instead lead only to an increase in coercivity, or in some cases lead to symmetrical biasing in both directions [71].

Thus, in order to maximize the EB effect, the antiferromagnetic domains need to be aligned. This is generally not possible by simply applying an external field due to the missing net magnetization of antiferromagnets. However, this problem can be overcome in different ways. One method includes applying a magnetic field during thin film deposition of the antiferromagnetic layer, but inhomogeneous fields at the sample position can lead to changes in the magnetic behaviour of the sample [72–74]. The most

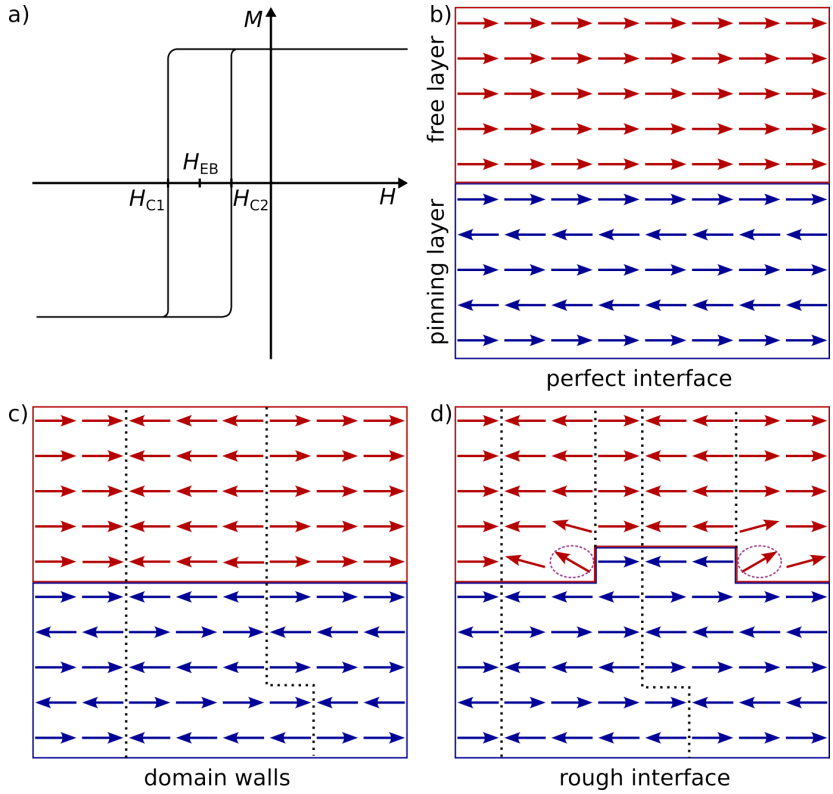

Figure 2.3: a) Exemplary EB loop: the loop is shifted horizontally by H_{EB}. b) Ideal interface for an exchange bias system: the AF layer has a perfectly smooth surface with uncompensated spins. These spins pin the FM layer. c) Magnetic domains in the AF layer leads to pinning of the FM layer in different directions d) A rough AF-FM interface with multiple domains in the AF layer. Arrows in dotted circles represent FM spins that are coupled to two antiparallel AF spins and thus in a frustrated state. H_{EB} is much reduced when compared to b).

common procedure involves first heating the sample above the Néel-temperature T_N of the antiferromagnet, or more precisely its blocking temperature T_B, which is slightly lower [75–78]. The blocking temperature is commonly defined as the temperature at which the exchange bias field becomes zero. It varies with the grain size, with bigger grains showing a higher T_B [79–82]. With the antiferromagnetic thin film consisting of differently sized grains, the overall blocking temperature depends mostly on the biggest grains, which is reflected in a thickness-dependence of T_B [76, 78, 83]. Exchange bias is generally only observed in systems where the Curie temperature T_C of the ferromagnetic layer is higher than T_N of the antiferromagnet, but exceptions are possible [84].

After heating the sample sufficiently, an external magnetic field H_{FC} is applied and the sample cooled down again (field cooling, FC). This induces order in the antiferromagnetic phase in the presence of the ferromagnet via a unidirectional interfacial exchange interaction, imprinting this aligned state into the antiferromagnetic domains when cooling below the blocking temperature. This is schematically shown in Fig. 2.4. The ferromagnet is now exchange-coupled to the aligned interfacial antiferromagnetic spins, leading to an increased $|H_{EB}|$ compared to the unordered as-prepared state. The degree of alignment and thus also $|H_{EB}|$ can usually be increased up to a saturation

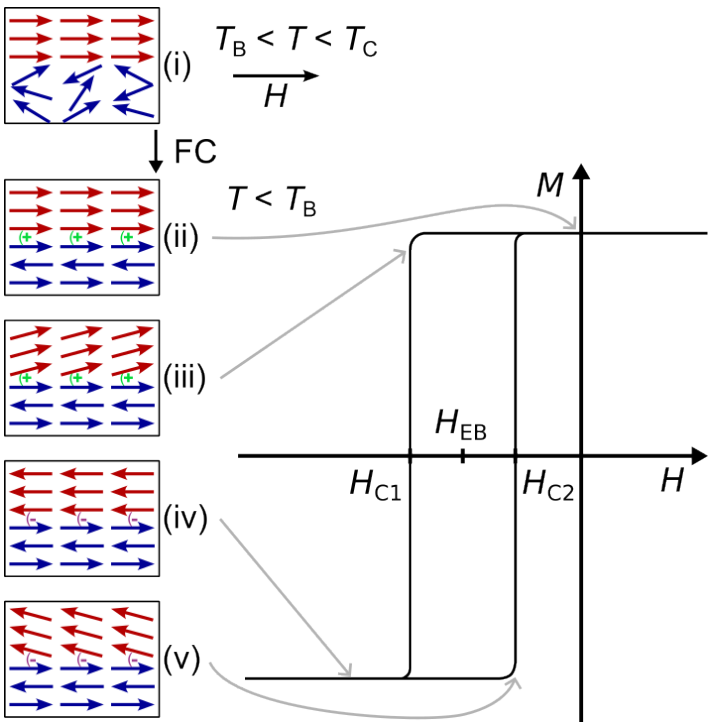

Figure 2.4: The standard exchange bias setting procedure: (i) a magnetic field is applied at $T > T_B$. (ii) After field cooling (FC), the free layer is pinned in the direction of the cooling field. (iii) A strong negative field is needed to start switching the free layer. (iv) The reversed magnetization is an energetically unfavorable state due to the interlayer coupling. (v) The free layer starts switching back earlier than in the other field sweeping direction because of the pinning, leading to a unidirectional anisotropy.

value by using a higher H_{FC}, but exceptions to this rule also exist [85–87]. It should also be noted that the sign of H_{EB} is normally the opposite of H_{FC}, so the M-H-loop is shifted towards negative fields. On very rare occasions, a shift to positive EB fields can be observed after cooling in a positive H_{FC} [83, 85, 87, 88].

If a horizontal loop shift is achieved without applying a magnetic field during deposition or cooling from above T_B, the phenomenon is called spontaneous exchange bias (SEB). This effect was first observed in Ni-Mn-In alloys in 2011 [89]. It is usually ascribed to the formation of a spin-glass state that gets a preferential alignment imprinted on it when a magnetic field is applied to it for the first time. There are even systems where phase transitions at room temperature lead to the formation of the SEB, removing the necessity of heating [90, 91]. An overview of the recent development in the field of spontaneous EB is given in [92]. Other additional methods of setting or re-setting the exchange bias are also investigated, such as applying a current or a voltage [93, 94].

The anisotropy energy KV of an individual antiferromagnetic grain plays an important role for how much it contributes to H_{EB}. The smaller grains can be remagnetized more easily, with the smallest even being superparamagnetic at room temperature [95, 96]. Those remagnetizable grains are not hard enough to resist being switched by the external field, so they also do not contribute to the exchange bias field. Instead, they present an energy barrier for the switching of the ferromagnetic layer in both field sweeping directions, effectively increasing the anisotropy and thus H_C. Grains that are too big can also be undesirable, since the temperature used for setting the EB might be

below the T_B of these bigger grains, leaving them in their as-deposited magnetization state. Consequently, the distribution of the grain sizes of the antiferromagnet is of high importance in EB systems [97, 98].

With increasing temperature, $|H_{EB}|$ decreases because the grains will be heated above their blocking temperature, starting with the smallest grains [78, 96, 99]. The coercivity H_C generally behaves the same, but experiments and calculations have shown that it can show a maximum near the blocking temperature [82, 96, 100, 101]. This behaviour can be explained by the bigger antiferromagnetic grains that can be remagnetized at the elevated temperature near T_B [83]. They lose the property of inducing the *unidirectional* anisotropy leading to EB and instead increase the *uniaxial* anisotropy, which increases coercivity.

It has been shown that the exchange bias field H_{EB} generally decreases with the thickness of the ferromagnet t_{FM}, roughly scaling with $1/t_{FM}$ [99, 102–105]. The same is usually also true for the coercivity H_C.

The dependence of H_{EB} on the thickness t_{AF} of the antiferromagnetic layer is more complicated. While there is sometimes a similar $1/t_{AF}$ dependence observed for large thicknesses [77], H_{EB} most often approaches a saturation value with higher thickness, sometimes reaching a maximum at certain thickness [99, 102, 104–108]. In either case, the exchange bias effect can only be observed if the antiferromagnet exceeds a critical minimum thickness, below which the antiferromagnet usually only increases H_C [109].

Even though so far only bilayers consisting of a ferromagnet and an antiferromagnet have been regarded, EB was also seen in ferro-/ferrimagnetic and ferri-/antiferromagnetic bilayers [110, 111], as well as in ferri-/ferrimagnetic bilayers [112, 113]. However, the M-H loops of samples utilising a ferrimagnet as the pinning layer are often symmetric, displaying a three-step magnetic reversal process. This is caused by the lower hardness of the ferrimagnet when compared to an antiferromagnet: while it is near impossible to switch the magnetic sublattices in the latter, available magnetic fields are usually enough to switch the former. Accordingly, the magnetic field applied while measuring the loop is enough to re-set the EB, leading to the existence of symmetrically shifted satellite hystereses of the pinned layer. A shifted M-H loop in the traditional sense, as is seen for common EB systems, can thus only be obtained as a so-called minor loop, when the maximum applied field is kept low enough as to not switch the pinning layer. Still, the fact that the pinned layer is experiencing an exchange bias by the pinning layer holds true.

In almost all EB systems, it is observed that $|H_{EB}|$ is reduced with multiple subsequent measurement loops. This is known as the training effect [114, 115]. It is most prominent between the first and second loop and diminishes with every further iteration, with H_{EB} approaching a fixed value. It is explained by the antiferromagnetic layer ending up in a multidomain state after the FC procedure. This state is not the thermodynamic ground state, so with every iteration of cycling the pinned layer through the hysteresis loop, a part of the antiferromagnetic domains will relax into the ground state. In order to avoid an overestimation of H_{EB}, the field should thus be cycled multiple times and the resulting loops analyzed regarding the training effect.

In modern technology, EB systems are widely used in spin-valves consisting of two ferromagnetic layers separated by a spacer layer [24]. One of the ferromagnets, called the pinned layer (PL), is coupled to an antiferromagnet and its magnetization kept stable by the EB effect. The other ferromagnet is free to rotate its magnetization and hence called free layer (FL). Depending on the type of spacer layer used, different methods can be used to read out the magnetic state of the FL. If the spacer is a non-magnetic metal, the giant magnetoresistance (GMR) effect can be measured, while the tunnelling magnetoresistance (TMR) effect is seen with an insulating spacer [40, 41, 116]. In both cases, the resistivity of the layer stack is low when the magnetization of both ferromagnet is parallel and high when it is antiparallel. GMR sensors are commonly used in read-heads of HDDs [117], while TMR elements are used in magnetic tunnel junctions (MTJ) in magnetic random access memory (MRAM) [118].

2.4 Superferrimagnetism

One method for creating permanent magnets with a high energy product is coupling a soft ferromagnet with large magnetization to a hard ferromagnet in the frame of an exchange-spring system, as was already described. But what if the ferromagnet that should be magnetically hardened already has a very high H_C? In such a case, one can make use of the concept of superferrimagnetism [119].

In a superferrimagnet, a hard ferromagnet with high M_S is coupled antiferromagnetically to a soft ferromagnet with low M_S. The effect that this has for the magnetic reversal when compared to the uncoupled hard ferromagnet is schematically depicted in Fig. 2.5. In the regular hard ferromagnet, a certain negative field is required to switch the magnetization of a nucleation volume, which is usually an area of reduced anisotropy due to inhomogeneities or defects. The creation of this switched volume creates a domain wall inside the ferromagnetic grain. The energy cost of the formation of this domain wall is balanced by the energy gain of the switched magnetization. Further switching of the grain can then progress by domain wall propagation.

In the superferrimagnetic structure, the remanent state consists of the two magnetization contributions being oppositely aligned. The magnetization of the soft ferromagnet will reduce the net remanent magnetization, so its value should be kept as low as possible. When applying an external field opposite to the magnetization direction of the hard ferromagnet, the creation of a volume of reverse magnetization does not only require the formation of a domain wall within the hard ferromagnetic grain. Additionally, a domain wall must be created between the hard and the soft magnetic layers. This additional cost in energy means that a higher external magnetic field must be applied to nucleate the reverse domain, thereby increasing H_C. The stronger the exchange coupling between the two layers, the higher the increase in coercivity.

The term *superferrimagnet* was chosen to represent such a structure because it has a high coercivity and an antiferromagnetic coupling between its two components (as in a regular *ferrimagnet*), but its magnetization is so high that is comparable to that of a ferromagnet (hence the prefix *super*). Superferrimagnets can be created in many ways, e.g. as a core-shell structure as depicted in Fig. 2.5 [120], a multilayer [119], or

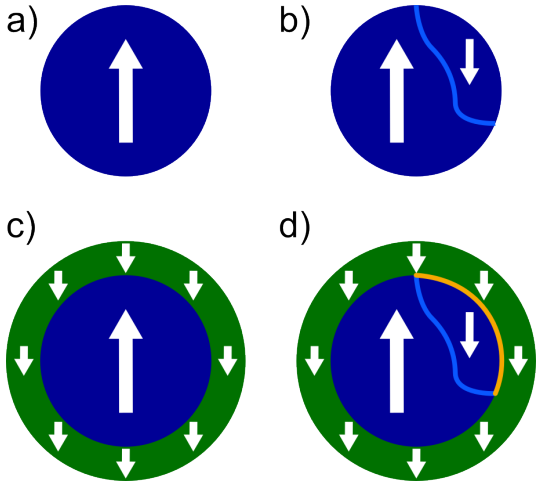

Figure 2.5: Schematic comparison of the nucleation of reversed domains in a,b) a regular hard ferromagnet (dark blue circle) and c,d) a superferrimagnetic structure with an antiferromagnetically coupled soft magnetic shell (green ring), with magnetization depicted as white arrows. a) The ferromagnetic grain is in the remanent state with all magnetic moments aligned in parallel. b) A negative field is applied until a nucleation volume of the grain reverts its magnetization direction, leading to the formation of a domain wall (blue line) within the grain. c) The remanent state in a superferrimagnet with the magnetizations of the two constituents aligned in opposite directions. d) The nucleation of a reverse magnetization volume leads to the additional formation of a domain wall between the hard grain and the antiferromagnetically coupled outer layer (orange line), meaning that the process costs more energy. Consequently, the nucleation in d) requires stronger negative fields than in b).

a granular structure with the soft magnet filling the intergranular volume. The latter is most often used for the magnetic hardening of modern supermagnets like $Nd_2Fe_{14}B$, using a process called grain boundary diffusion (GBD) [121]. For more information about the grain boundary diffusion process, please refer to chapter 6.

CHAPTER 3

Materials

The two main thin film systems investigated in this work are crystalline FePt in the $L1_0$-structure and amorphous TbFe. This chapter will elucidate the very different structures of these two systems as well as go into their respective structural and magnetic properties.

3.1 The $L1_0$ phase of FePt

Thin $L1_0$ FePt films show promising magnetic properties, such as a high uniaxial anisotropy and high saturation magnetization [2]. This makes them suitable not only for HAMR [122], but also spintronic applications [26–28, 123, 124] such as MRAM [125–128] or MTJs [129].

In this work, thin films of $L1_0$ FePt were investigated. These were manufactured by magnetron sputter co-deposition of elemental targets of Fe and Pt on monocrystalline MgO(001) substrates at elevated temperatures, nominally around 800 °C. The substrate and the high temperature are needed in order to achieve good chemical ordering and epitaxial growth along the crystallograpic c-direction. For more information on the sputter deposition technique and heteroepitaxial growth, please refer to chapter 4.1. In the following, the peculiarities of the $L1_0$ structure and the properties of $L1_0$ FePt will be described.

3.1.1 The $L1_0$ crystal structure

The $L1_0$ structure, also known as the CuAu(I)-type structure, consists of alternating layers of two different elements A and B. While each atomic layer is quadratic within its plane, the neighbouring layers are shifted by half a unit cell. The c lattice parameter is unequal to the lattice parameter a within the plane due to different atomic bonds along those directions. This makes the structure have an overall resemblance to a face-centered tetragonal structure, with atomic layers alternating along the crystallographic c axis. c is only slightly smaller than a for almost all $L1_0$ structures, with only very few exceptions like NiFe or TiAl, where c is slightly larger. [130, 131]

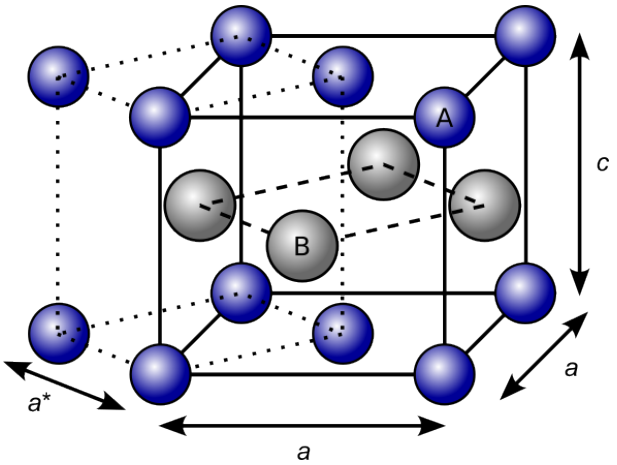

Figure 3.1: A sketch of an $L1_0$ structure consisting of elements A and B. The lattice parameters a and c are unequal. The alternative body-centered tetragonal unit cell is shown with dotted lines. Its basal lattice parameter is smaller than that of the common unit cell: $a^* = a/\sqrt{2}$.

The atomic positions in the unit cell are accordingly:

$$\mathbf{r}_{A,1} = \left(0,0,0\right),\ \mathbf{r}_{A,2} = \left(\frac{1}{2},\frac{1}{2},0\right),\ \mathbf{r}_{B,1} = \left(\frac{1}{2},0,\frac{1}{2}\right),\ \mathbf{r}_{B,2} = \left(0,\frac{1}{2},\frac{1}{2}\right),$$

relative to the a, b, and c lattice directions. If the atoms are not ordered, however, the structure is called the $A1$ structure. This is a face-centered cubic structure with random atoms occupying each lattice site. It is often undesired, e.g. in MPt phases ($M =$ Mn, Fe, Co, Ni), where a high uniaxial anisotropy can only be achieved with the $L1_0$ structure [132].

In the case of the binary alloy FePt, the $L1_0$ structure can form at elevated temperatures above 200 °C [134]. The high ordering temperature is a result of the energy needed for grain growth, which is significantly higher than the grain nucleation energy [135, 136]. If the temperature is too low, atom mobility is not enough for the formation of the ordered $L1_0$-structure, so the atoms are randomly distributed in a face-centered cubic $A1$ lattice.

The degree of $L1_0$ formation can rather easily be checked by X-ray diffractometry, since the fcc lattice does not allow the (001) superlattice reflection, while the $L1_0$ structure does. The ratio of integrated intensities of this reflection peak and the (002) reflection peak in an X-ray diffractogram, $I_{(001)}/I_{(002)}$, can be used to estimate the degree of $L1_0$ formation, also called the *order parameter* S [137]. It can be seen as a measure of the ratio of *correctly* placed atoms in the phase, ranging from 0 for completely random placement to 1 for perfect order. In a binary solid solution of atoms A and B, it is defined as:

$$S = \frac{p-r}{1-r} \tag{3.1}$$

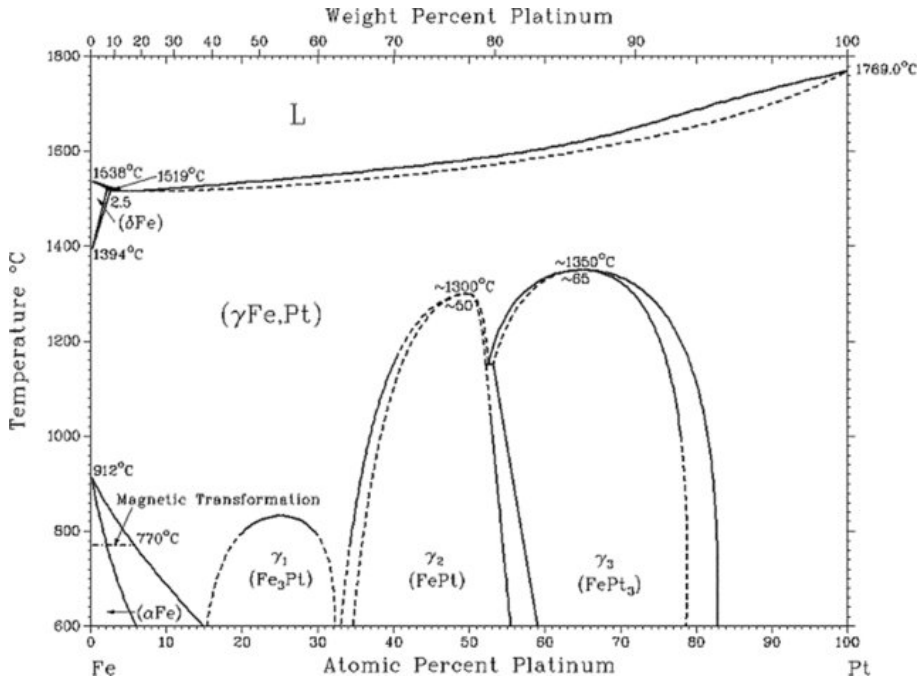

Figure 3.2: The binary equilibrium phase diagram of bulk Fe-Pt alloys [133] The $L1_0$-phase is stable near equiatomic composition below 1300 °C.

where p is the ratio of A (or B) atoms on the correct lattice site and r is the fraction of A (or B) atoms in the solid. It can easily be seen that $S = 1$ if all atoms are on the correct site. If the placement is random, however, $p = r$ and S becomes zero.

In the $L1_0$ phase, imperfectly placed atoms lead to a reduction of the (001) peak intensity, so the measured intensity ratio $I_{(001)}/I_{(002)}$ will always be lower than the ideal one. The ideal intensity ratio can be calculated with regards to the position θ of the peaks in an X-ray diffractogram and the wavelength λ of the radiation used. The precise formula for calculating the order parameter S from a given measurement is as follows [138]:

$$S = \sqrt{\frac{I_{001}|F_{002}|^2 A_{002} L_{002} \exp(-B_{\mathrm{F}} \sin^2 \theta_{002}/\lambda^2)}{I_{002}|F_{001}|^2 A_{001} L_{001} \exp(-B_{\mathrm{S}} \sin^2 \theta_{001}/\lambda^2)}} \tag{3.2}$$

with the absorption factor A, the Lorentz factor F, and the Debye-Waller factor $B_{\mathrm{S/F}}$ of the superstructure or fundamental peak, respectively. All of these correction factors can be quite difficult to determine accurately, but many of these have been tabulated. A thorough look at the different correction factors can be found in [139]. This work shows that a fully ordered, randomly textured polycrystalline $L1_0$ $Fe_{50}Pt_{50}$ film with infinite thickness would show an intensity ratio of 2.14, so this value can be taken as an approximate reference for most thin films of equiatomic composition.

It also has to be remembered that an off-stoichiometric composition reduces the maximum possible value for $I_{(001)}$, since the structure cannot be perfect anymore. This has to be taken into account when calculating the ideal $I_{(001)}/I_{(002)}$ ratio that the measured one is compared to. This further complicates the calculation of the ideal $I_{(001)}/I_{(002)}$

Table 3.1: A comparison of various different alloys exhibiting the $L1_0$ phase. Antiferromagnetic (AF) as well as ferromagnetic (FM) variants exist, as well as such with negative or positive K_u (in-plane or perpendicular magnetic anisotropy, respectively). For most alloys, the lattice parameter a is larger than the c lattice parameter.

$\boldsymbol{L1_0}$ **alloy**	a [Å]	c [Å]	c/a	magnetic order	M_S [emu/cm^3]	K_u [MJ/m^3]
MnPt [143, 144]	4.032	3.687	0.914	AF	0	1.39
CrPt [145]	3.822	3.811	0.997	AF	0	-0.438
MnPd [144, 146]	4.07	3.58	0.880	AF	0	-1.53
FePt [2, 147]	3.85	3.71	0.964	FM	1140	6.6
CoPt [148–150]	3.8	3.7	0.974	FM	820	4.9
FeNi [130, 151, 152]	3.582	3.607	1.007	FM	1170	1.3
MnAl [153, 154]	3.92	3.54	0.903	FM	560	1.7

ratio. A very rough estimation of S^2 is the ratio of integrated intensities divided by two.

3.1.2 Properties of $L1_0$ FePt

Because they usually display a large uniaxial magnetic anisotropy constant, magnetic $L1_0$ alloys are promising candidates for a variety of applications, from ultrahigh density magnetic recording and exchange bias systems to rare-earth free permanent magnets [140–142]. Magnets with ferro- and antiferromagnetic order exist in this structure, with most displaying a strong PMA of a few MJ/m^3. A small overview of different magnetic $L1_0$ alloys is displayed in table 3.1.

The $L1_0$ phase of FePt has a uniaxial magnetic anisotropy constant K_u of up to 7 MJ/m^3 along the c lattice direction, with an anisotropy field of around $H_A = 116$ kOe [2, 155]. This anisotropy is caused by its tetragonal structure and mainly two other factors: the large spin-orbit-coupling of Pt and the hybridization of Pt 5d and Fe 3d orbitals [132, 156]. This value of anisotropy is extremely high, even comparable to those of modern so-called supermagnets, which are all very rare-earth intensive: 5.7 MJ/m^3 ($Nd_2Fe_{14}B$), 3.9 MJ/m^3 (Sm_2Co_{17}), 17.2 MJ/m^3 ($SmCo_5$) [157–159]. Together with its high magnetization, this makes it attractive for a range of applications, the most prominent of which is heat-assisted magnetic recording (HAMR) [160].

The high K_u also means that $L1_0$ FePt possesses a high coercivity [161], which is linearly dependent on the $L1_0$ volume fraction in partially ordered films [162]. As mentioned before, conventional recording media are limited in their coercivity by the maximum writing field exerted by the writing head. However, the coercivity decreases when a material approaches the Curie temperature, and it vanishes completely above. This circumstance is used in HAMR to switch the magnetization of an $L1_0$-FePt grain with a field that is lower than its coercive field at room temperature. By heating a spatially very defined area above or around the Curie temperature with a laser beam,

the coercivity of this area is reduced and the write-head can write the new information on the bit. Upon cooling, this new information is again stored securely, owing to the high uniaxial magnetic anisotropy.

Because this technique allows using thin films of materials with a much higher K_u, the grains can be much smaller, allowing for an increased bit density. $L1_0$-FePt media have been suggested for such a use as early as in the year 2000 [163–166]. HAMR media generally use granular films, since the structural grain borders are natural limits for magnetic domains which make up a magnetic bit, and granular FePt films also show higher H_C than continuous films [167]. There are unique problems to overcome when optimizing granular FePt media, such as distribution of grain sizes, center-to-center pitch distance, magnetic decoupling of grains, achieving a consistent $L1_0$ structure and growth direction of the grains, grains overgrowing other grains if the layer is too thick, and the distribution of T_C [9, 11, 168].

FePt media used for HAMR also have a nanogranular structure, with all grains ideally growing in the c direction for maximum PMA. This is done by using a thin MgO seed layer that strengthens the $L1_0$ structure formation and the (001) growth direction. However, due to the polycrystallinity of the thin MgO layer, off-axis growth is common in such thin films [169]. Together with the distribution of T_C between the grains, this is the main source of noise in HAMR [9, 168]. Separation of the columnar grains is still required, as they would otherwise coalesce during growth. This is done by co-deposition of a matrix phase that is not soluble in the FePt-phase, usually consisting of SiO_2, C, or h-BN [122, 170, 171].

HAMR media can theoretically be grown on a multitude of substrates, but the high deposition temperature needed for a high order parameter limits the amount of substrates usable for FePt media. K_1 strongly depends on the order parameter S [172], so simply reducing the deposition temperature and thus S is no viable option. Hence, many attempts have been made to reduce the ordering temperature of the $L1_0$-phase. These mostly include the addition of low-melting-point elements like Cu or Ag [173–175], but also the deposition of ultrathin [Fe/Pt] multilayers. [176–180]

Ding et al. showed that the chemical ordering can also be influenced by the lattice mismatch to the substrate, and found that an intermediate value of 6-7 % is best for achieving a high order parameter [181]. Further, an increase of the volume fraction of the $L1_0$-phase and thus S can be achieved by post-annealing [182–184]. This can be done either by conventional heating in a furnace, rapid thermal annealing (RTA), or even flash-lamp annealing [185].

Ohtake et al. showed that on MgO substrates, the onset of $L1_0$ formation starts already at a deposition temperature of 200 °C, while order increases for higher temperatures [134]. Calorimetric measurements during post-annealing by Barmak et al. have shown that the formation of the $L1_0$-phase of FePt on Si substrates starts around 350 °C and has its maximum near 400 °C [186]. When using RTA, a temperature of 650 °C is sufficient to induce $L1_0$-ordering, while shorter times at higher T are better for S, as shown by Albrecht et al. [138].

3.2 Amorphous TbFe thin films with perpendicular magnetic anisotropy (PMA)

Ferrimagnetic TbFe binary alloys are known for showing high uniaxial magnetic anisotropy, magnetostriction, and the possibility of all-optical switching (AOS). As such, they have been widely investigated in the 1980s to the 1990s for their use in magneto-optical data storage devices using Curie-point writing [187]. However, such devices were not able to keep up with the rapid development and improvement of HDDs. Still, TbFe alloys and similar tertiary systems such as TbCoFe play a major role in magnetostriction and AOS applications. In the following, an overview of the TbFe system along with its peculiar structural and magnetic properties will be given.

3.2.1 Phase diagram of binary TbFe alloys

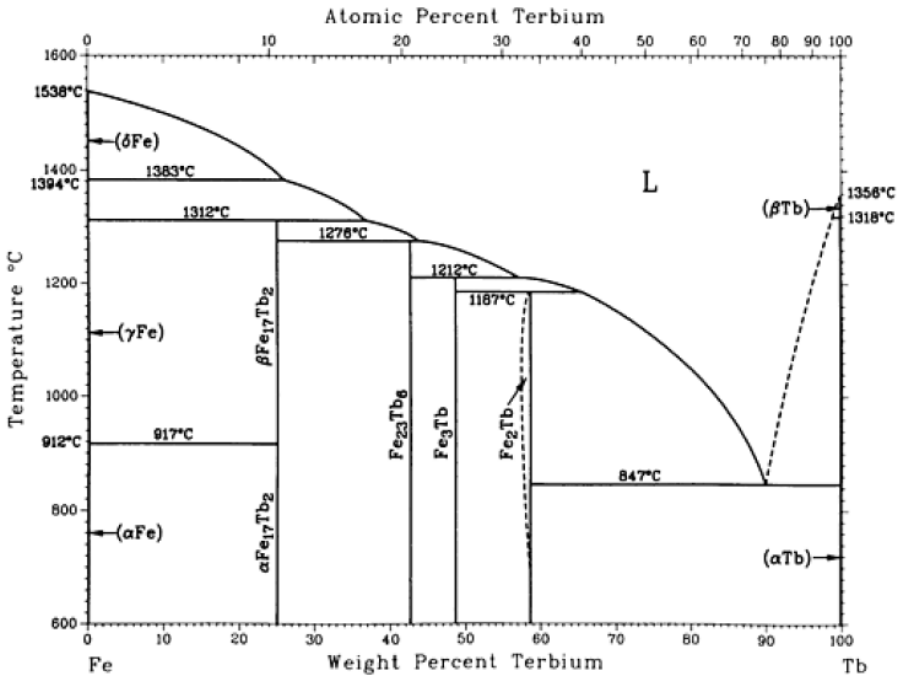

Figure 3.3: The binary equilibrium phase diagram of bulk Tb-Fe alloys [188].

Tb-Fe alloys consist of the 3d transition metal (TM) iron and the 4f rare-earth (RE) element terbium. The phase diagram of the binary TbFe alloy shows four intermediary crystalline phases: Tb_2Fe_{17}, Tb_6Fe_{23}, $TbFe_3$ and $TbFe_2$ [188, 189].

The latter is at the Laves phase composition. Laves phases are intermetallic systems with composition AB_2 which crystallize in hexagonal C14 ($MgZn_2$), hexagonal C36 ($MgNi_2$), or, in the case of $TbFe_2$, the cubic C15 ($MgCu_2$) structure [191]. This phase is especially interesting as it shows the highest saturation magnetostriction constant $\lambda_{\parallel}$ at room temperature of any known material: 2000 ppm at 10 kOe [192], as opposed to only - 9 ppm for pure Fe.

Table 3.2: Structural and magnetic properties of the crystalline TbFe compounds [190].

phase	crystal symmetry	structure type	Curie temperature	T_{comp}
Tb_2Fe_{17}	hexagonal	Th_2Ni_{17}	408 K	-
Tb_6Fe_{23}	cubic	Th_6Mn_{23}	574 K	280 K
$TbFe_3$	rhombohedral	$PuNi_3$	648 - 655 K	595 - 626 K
$TbFe_2$	cubic	$MgCu_2$	696 - 711 K	-

Magnetostriction describes the phenomenon where magnetic materials change their dimensions when being exposed to a magnetic field (which is also the reason that electric transformers hum). It is usually very pronounced in materials with a strong spin-orbit coupling [193], which is the case for Tb. The effect is quantified by the relative length change $\Delta l/l_0 = \lambda$, which can be given parallel ($\lambda_\parallel$) or perpendicular ($\lambda_\perp$) to the field.

This means that the above-mentioned $TbFe_2$ expands its length by 0.2 % along the direction of the applied field. Amorphous films of the same composition still show strong magnetostrictive effects, but the effect is greatly reduced, by a factor of about four [194]. As such, TbFe alloys can be used in magnetostrictive applications, e.g. ultrasonic wave generators or magnetoelastic sensors [195].

The very similar material Terfenol-D ($Tb_{0.3}Dy_{0.7}Fe_2$), developed at the *Naval Ordnance Laboratory* in White Oak, Maryland, is commonly referred to as the most magnetostrictive material. It combines the magnetostrictive properties of $TbFe_2$ and $DyFe_2$ [196]. It reaches a λ_{111} of about 1600 ppm in thin films and up to 2000 ppm in nanocrystalline samples at much lower fields than $TbFe_2$, which makes it much more useful for applications [197, 198]. The name Terfenol-D is derived from the constituents terbium (TER), iron (FE), *Naval Ordnance Laboratory* (NOL) and dysprosium (-D).

Despite the interesting properties of the crystalline phases, the focus of this work will be on amorphous thin films of TbFe deposited at room temperature by magnetron sputtering.

3.2.2 Amorphous magnetism

In the second half of the 20th century, it was found that magnetic behaviour, which up to that point was thought of as requiring long-range order, was also observable in amorphous systems. In 1946, König investigated magnetic iron particles bordering amorphicity by creating supersmall crystallites of only around 1 nm in size [199]. Another paper from 1950 by Brenner et al. only makes a very short reference to the structural analysis, but produced amorphous NiPCo films, albeit non-magnetic ones [200]. This started an era of investigation of various amorphous structures, especially magnets. [201]

In the 60s and 70s, research increased manifold in this area [202–210], looking mainly at alloys of two or more elements, since amorphous elemental films are much less stable than alloys. The term most often used to discern these systems was “metallic glass”,

using glass as a synonym for a noncrystalline solid [207]. Another analogy used was that of a frozen liquid metal. In the meantime, however, physics has encountered the phenomenon of *spin-glasses*, which are ferromagnetic atoms suspended in a non-magnetic crystalline matrix showing a frozen, metastable state of spin orientations. As a consequence, the term *metallic glass* has fallen out of use, and the term *amorphous solid* (or *magnet*) was adopted [203].

Despite the term *amorphous* suggesting no coherent structure, quite some work has been done to understand the structural properties of amorphous magnets [210], like distribution of nearest-neighbour distances and packing density. Since there is no periodic arrangement of atoms in an amorphous solid, the distance distribution to other atoms is the most important structural parameter. Interestingly, the *dense random packing of hard spheres* (DRPHS) model gives a packing density around 63 % [207], so it is in between the packing densities of simple cubic (52.36 %) and body-centered cubic (68.02 %) structures. Also, the nearest-neighbour distances in this model are close to those measured via neutron and x-ray scattering for amorphous alloys [203], so this early model allowed to understand basic structure of amorphous magnets to a certain degree.

But how can collective magnetism exist in a system with no long-range order? In order to align the individual magnetic moments of the atoms without an external field, some form of anisotropy is needed. In a crystal, this is usually the magnetocrystalline anisotropy, which can be very strong. In thin films, shape anisotropy and magnetoelastic anisotropy can also influence amorphous systems, but the anisotropy value found for some amorphous systems is too high to be explained just by these contributions. Also, shape anisotropy in thin films tends to align the magnetization in the film plane, but many films, especially rare-earth transition metal (RE-TM) films, show perpendicular magnetic anisotropy (PMA) [211].

The answer lies in the deposition process of the structure. Especially for thin films, common deposition processes like sputtering can induce a special kind of anisotropy, for example pair order anisotropy. Pair order anisotropy can be shown at the example of GdCo: during sputter deposition, the film is usually resputtered, removing atoms from the already deposited film. The resputtering effect is stronger for more weakly bound atoms, so stronger bonds will remain to a higher degree. This is most relevant for bonds in the out-of-plane direction, as this is the most important bond for a newly deposited atom. The Gd-Co bond is stronger than the Co-Co bond, so it is more likely that a Co atom will remain on top of a Gd atom. This means that most of the vertical bonds of Co will be with Gd, leaving the horizontal bonds for Co. Since the Co-Co bond has a magnetic easy plane perpendicular to the bond direction, the sum of all Co-Co bonds will lead to an easy magnetization direction perpendicular to the film plane [206].

The above-mentioned GdCo alloy shows a collinear antiparallel alignment of the magnetic moments. This is caused by the strong exchange integral J of the elements. However, depending on the strength of exchange and anisotropy, there can be some other interesting variations of the alignment of magnetic moments in amorphous solids.

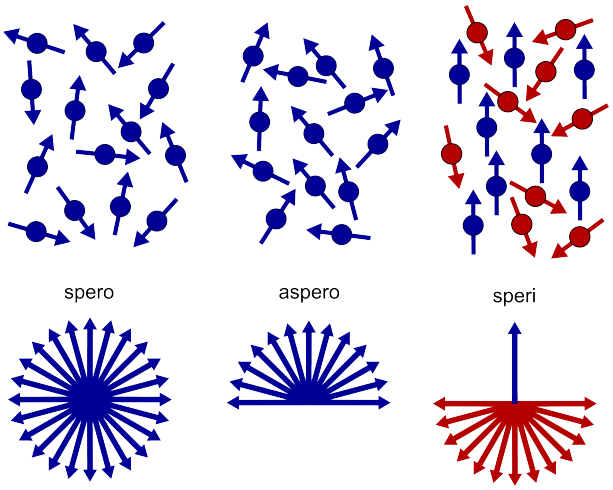

Figure 3.4: Magnetic spin distributions for different types of amorphous magnetic alloys: a) speromagnetism, b) asperomagnetism, c) sperimagnetism.

A simple model for single-site anisotropy in a one-subnetwork system as shown in [204, 212] gives the Hamiltonian

$$\mathcal{H} = -\sum_i D_i S_{iz}^2 - \sum_{i,j} J(\mathbf{r}_{ij}) \boldsymbol{S}_i \cdot \boldsymbol{S}_j \ , \tag{3.3}$$

with the local anisotropy D having different z-directions for each site i, j being nearest neighbours to i, and $\boldsymbol{S}$ being the spin momentum.

There are different cases to differentiate: if the local anisotropy is stronger than the exchange interaction ($|D| \gtrsim |J|$) and J is negative or broadly distributed around zero, the magnetic moments align along the local anisotropy axes, averaging overall to zero net magnetization. This state is called *spero*magnet, after the greek word $\delta\iota\alpha\sigma\pi\epsilon\iota\rho\omega$ (diaspeiro) for "*i scatter*" [205]. If J is positive, the exchange interaction ensures that the magnetic moment will point in the one direction of the local anisotropy axis with a smaller angle to its neighbours. This can be seen as a random ferromagnetic state, with a total magnetization $\neq 0$, called *aspero*magnet.

If the exchange interaction is stronger than the anisotropy ($|D| \ll |J|$), the magnet behaves according to the sign of J. If J is positive, as is the case for the ferromagnetic 3d transition metals with the direct exchange, the result is an amorphous ferromagnet. For RKKY interactions, like in rare-earth elements, J fluctuates around zero, leading again to a speromagnetic configuration.

If there are two magnetic subnetworks, as in the case of RE-TM alloys, the Hamiltonian becomes:

$$\mathcal{H} = -\sum D_a S_{az}^2 - \sum D_b S_{bz}^2 - \sum J_{aa'} \boldsymbol{S}_a \boldsymbol{S}_{a'} - \sum J_{bb'} \boldsymbol{S}_b \boldsymbol{S}_{b'} - \sum J_{ab} \boldsymbol{S}_a \boldsymbol{S}_b \tag{3.4}$$

Here, we are looking only at the z component of the spin momentum $\boldsymbol{S}$, meaning the component that is aligned with the local anisotropy axis. (Note that even though $\boldsymbol{S}$ is

used here, the total angular momentum $\boldsymbol{J}$ should be used for systems where the orbital angular momentum cannot be neglected and $\boldsymbol{S}$ is not a good quantum number.)

The possibilities for alignment of the magnetic moments are now somewhat more numerous. However, they can be summarized with the term *speri*magnet [208]. In the example shown in figure 3.4, one subnetwork has a strong exchange, while the other is dominated by the random local anisotropy. The result is that the first subnetwork is aligned collinearly, while the other has its magnetic moments spread out in a hemisphere. This is the configuration for amorphous RE-TM magnets, except for those with Gd as the RE [204, 210], which will have a collinear alignment. In reality, both RE and TM can have their moments spread out in a fanning cone, with the angle depending on the strength of the exchange interaction and the local anisotropy.

Is there now any advantage of using amorphous magnets instead of crystalline ones? Indeed, one of the biggest advantages that amorphous RE-TM magnets offer is the tunability of the composition. When working with crystalline phases, one is often strongly limited to a certain (sometimes narrow) composition range, and differences between two different phases can be enormous. With amorphous alloys, however, the structural, magnetic, as well as any other properties can be continuously and gradually changed by changing the composition. This will be shown at the examples of coercivity H_C and magnetization M of TbFe alloys in the following chapter.

3.2.3 Magnetism in amorphous TbFe thin films

Fe, as well as the other ferromagnetic 3d transition metal elements Co and Ni, shows a direct exchange interaction of its valence electrons in the 3d orbital with those in other Fe atoms. The electron wave functions overlap, creating a strong exchange interaction. The orbital angular momentum in these elements is usually negligible and is further quenched by the crystal field, so mostly the spin moment $\boldsymbol{S}$ contributes to the magnetic moment. The exchange interaction now leads to the parallel alignment of neighbouring spin moments $\boldsymbol{S}$, which are rather high because of the spin-split 3d orbitals, and thus to the emergence of the characteristic ferromagnetism [193, 213].

Tb has the electron configuration [Xe] $4f^9\ 6s^2$, but in bulk, an electron of the 4f orbital can be transferred to the 5d orbital in the form of a hybridized spd orbital [214]. In either case, the magnetism in Tb and the other 4f rare-earth elements originates in the 4f orbital, which is not completely filled. The 4f orbital is situated rather close to the core, being shielded by the 5s, 5p, 5d, and 6s valence electrons. This prevents any direct exchange with the 4f electrons of any neighbouring atoms as is the case for Fe. Instead, the coupling is mediated by the 5d valence electrons, which are much more delocalized and polarized by the 4f orbital. This type of indirect exchange is also called RKKY interaction (see chapter 2.1), and is a lot weaker than the direct exchange [190]. This can be seen by the greatly reduced Curie temperature of rare-earth elements ($T_\mathrm{C,Gd} = 297\,K,\ T_\mathrm{C,Tb} = 220\,K$) when compared to Fe, Co, or Ni.

The coupling of TM and RE elements happens by hybridization of the 3d electronic states of the TM and the 5d states of the RE. Within the frame of this interatomic exchange coupling, a part of the TM 3d electron density is transferred to the RE 5d

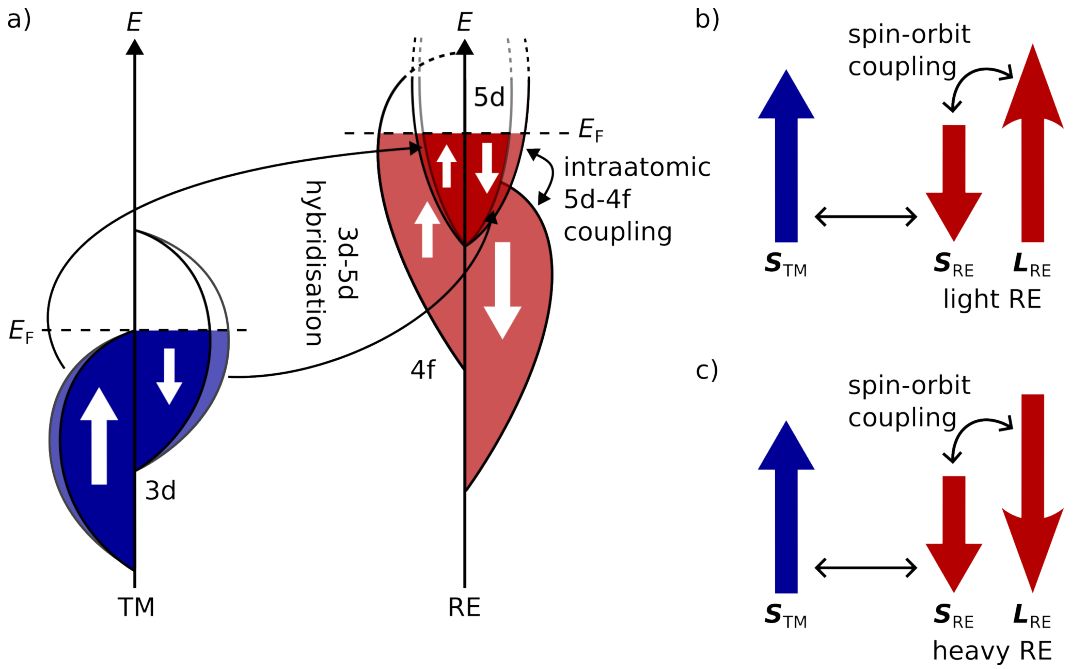

Figure 3.5: a) Representation of the 3d-5d hybridization in RE-TM alloys. The electron density transferred from TM to RE together with the intraatomic 5d-4f coupling leads to an antiparallel alignment of the spin momenta. b) and c) show the resulting alignment of S and L for light and heavy RE elements in the alloy, respectively.

orbital (see Fig. 3.5 a)) [215]. The lower the energy difference between the two orbitals, the stronger the extent of this hybridization. Because the TM 3d orbital is spin-split, the minority part of the TM 3d orbital is situated at higher energy and thus closer to the RE 5d orbital. Accordingly, the 5d orbital becomes spin-polarized in the opposite direction to the TM 3d orbital [190].

The spins of the RE 4f orbital will align parallel to those of the polarized 5d orbital in order to maximize S (Hund's first rule). Depending on the number of electrons in the 4f orbital, the total angular momentum L can then behave in one of two ways: following Hund's third rule, the total angular momentum of RE atoms with their strong spin-orbit coupling can be described by $J_{\text{tot}} = |L - S|$ for light and $J_{\text{tot}} = |L + S|$ for heavy RE elements. Light RE elements are those with a half- or less than half-filled 4f orbital, while heavy RE elements are those where the 4f orbital is more than half-filled. This means that for light RE elements, the orbital angular momentum will be aligned antiparallel to the spin moment due to 5d polarization and thus parallel to the spin moment of the TM, while the opposite is true for heavy RE elements such as Tb (see Figs. 3.5 b) and c), respectively). Accordingly, the alignment of Tb and Fe magnetic moments is always antiparallel.

Because this type of coupling is rather strong, the magnetization and ordering temperature of some RE-TM systems can be very high. This can be seen by two of the most commonly used "supermagnets", $Nd_2Fe_{14}B$ and $SmCo_5$, which have immense energy products and are often doped with heavy RE elements to further increase their coercivity and Curie temperature [216, 217].

Understanding the basic coupling mechanism between Fe and Tb, we can now add our knowledge of amorphous magnets to develop a complete picture of the interactions in amorphous TbFe alloys. For this, one has to look at the competition between the different contributions in the Hamiltonian shown in equation 3.4.

The random single-site anisotropy D has a negligible effect on the Fe subnetwork with its strong exchange interaction J_{FeFe}. However, the Tb subnetwork with its weak RKKY-type interaction is much more affected by the local anisotropy, making the anisotropy term dominate over the exchange term in the Hamiltonian. The Tb-Fe interaction is also strong, so we can simplify the Hamiltonian to:

$$\mathcal{H}_{\mathrm{TbFe}} = -\sum D_{\mathrm{Tb}} \boldsymbol{J}_{\mathrm{Tb_z}}^2 - \sum J_{\mathrm{FeFe'}} \boldsymbol{S}_{\mathrm{Fe}} \boldsymbol{S}_{\mathrm{Fe'}} - \sum J_{\mathrm{TbFe}} \boldsymbol{J}_{\mathrm{Tb}} \boldsymbol{S}_{\mathrm{Fe}} \ , \tag{3.5}$$

with $\boldsymbol{J}_{\mathrm{Tb}}$ denominating the total angular momentum of terbium.

This leads to the Tb moments aligning mostly along the local anisotropy axis, but in the opposite direction of the Fe moments, which all point in the same direction. In other words: the magnetic structure is that of a sperimagnet (compare Fig. 3.4).

In reality, however, the Fe atomic moments are not perfectly aligned with each other. Mößbauer spectroscopy has shown that the angle of the Fe fanning cone in amorphous TbFe alloys is between 21° and 29°, independent of temperature [218], or even up to 35° [219].

The fanning cone angle of Tb cannot be directly measured, but with its weaker exchange coupling it can be safely assumed that the angle is much wider. This assumption is also supported when comparing the atomic magnetic moments of Tb and Fe with the resulting magnetic moment of a TbFe alloy. Assuming atomic moments of 1.73 μ_{B} for Fe [220] and 7.5 to 9.25 μ_{B} for Tb [221, 222] as well as magnetic compensation at a composition of 25 at.% of Tb, the opening angle of the Tb fanning cone can be estimated to be roughly 50 to 60°. Values found in the literature tend to be slightly lower [223, 224]. In very high magnetic fields of multiple Tesla, the fanning cones can actually be compressed as the magnetic moments are tilted away from the local anisotropy axis in order to minimize the Zeeman energy [225]. This can be visible in the M-H-loops as a gradual increase of magnetization, flattening towards higher fields.

With the antiparallel, sperimagnetic alignment of the atomic moments of Tb and Fe explained, there remains the explanation of the perpendicular magnetic anisotropy. Unlike the usually magnetically soft asperomagnets, many sperimagnetic RE-TM alloys tend to show high K_{u} and increased coercivity perpendicular to the film plane. As already mentioned, the cause for this is to be found already during the deposition process. It was shown by multiple groups that there is a tendency for atomic bonds to form along certain directions relative to the film growth directions [226–230]. Bonds between same elements are favoured within the film plane, while bonds between different elements are found preferably along the growth direction. This explanation was confirmed by EXAFS spectroscopy [231], which showed an increased number of same-atom pairs in the film plane. The phenomenon is hence called pair order anisotropy [206, 229].

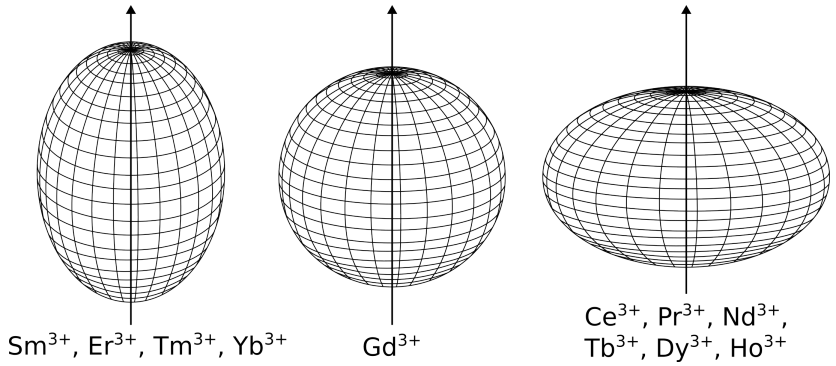

Figure 3.6: Shape of the 4f orbitals of different rare-earth elements (image adapted from [232]). The oblate ellipsoid shape of Tb is essential for the PMA of amorphous TbFe alloys.

The predominant environment of Tb now creates a crystal field that determines the orientation of the 4f orbital [213], which has the shape of an oblate ellipsoid, as depicted in Fig. 3.6 [232]. The orbital angular momentum of the 4f orbital is strongly correlated with the orientation of the orbital due to the spin-orbit coupling: it is pointing along the *c*-direction of the ellipsoid. Together with the anisotropic crystal field around the Tb atom, this leads to the Tb moment being preferentially aligned perpendicular to the film plane. Because the overall anisotropy is caused by the sum of all the individual rare-earth ions, it is also called single-ion anisotropy [190, 204, 233, 234].

Other mechanisms have also been investigated as the cause for PMA in TbFe and other RE-TM films, including strain [235, 236], surface energy minimization [237], anisotropic exchange [238], and dipolar interactions [209]. Furthermore, deposition temperature and sputtering power were shown to influence anisotropy [239–242]. Another work by Prados et al. even explained the PMA in TbFe by the complete inverse orientation of bonds during film growth [243], which was also shown via EXAFS by Hernando et al. [244]. This shows that the precise mechanism is rather hard to understand and that probably many different causes can contribute to this effect. It should also be mentioned that not all amorphous TbFe alloys show an easy magnetization axis perpendicular to the film; for very high or very low Tb contents the influence of the PMA will decrease and the magnetization will tilt towards an in-plane direction due to shape anisotropy [194]. All films investigated in this work, however, show PMA.

Now that the details of the Tb-Fe-interactions in amorphous TbFe alloys have been explained, we can look at their macroscopic behaviour. In general, the TbFe system behaves like a ferrimagnet. Depending on the composition, one magnetic subnetwork usually dominates at a given temperature. This is then also the subnetwork that aligns with an applied external field first. The composition region where the Fe moments dominate at room temperature are between 0 and around 22 at.% Tb content, with the Tb-dominated region starting from about 26 at.% reaching to pure Tb, as depicted in Fig. 3.7 a). The magnetization decreases toward the region from 23 to 25 at.% Tb, where magnetic compensation occurs at room temperature. A precise value is hard to give, since it depends on film thickness [225] as well as many other deposition parameters, and the precise composition is often hard to determine. The coercivity H_C generally behaves inversely to the magnetization. This means that it increases towards

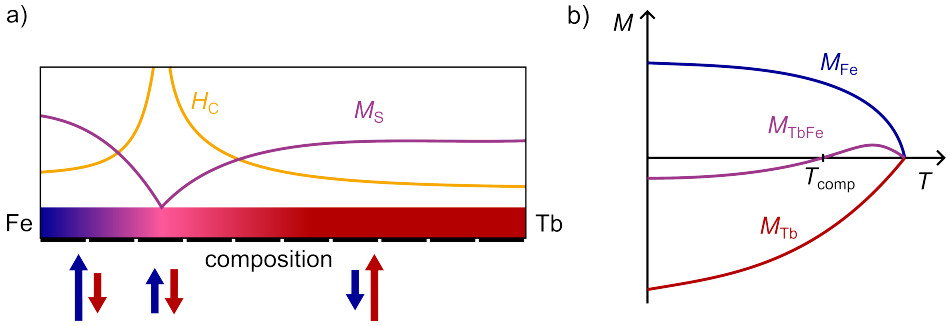

Figure 3.7: a) Room-temperature compensation behaviour of the Tb-Fe system with composition. The blue and red arrows represent the total magnetization of the Fe and Tb subnetworks, respectively. As composition gets closer to compensation, M_S goes to zero and H_C diverges. At room temperature, compensation occurs around 23-25 at.% Tb. For lower Tb concentrations, the Fe magnetization dominates, and vice versa. b) Schematic compensation behaviour of a Tb-Fe alloy with temperature. Since both contributions to the total magnetization M_{TbFe} have different temperature dependencies, the alloy can switch from Tb-dominated at low temperatures to Fe-dominated at higher temperatures.

the compensation composition, where it diverges. At compensation, the system is basically an antiferromagnet, which also means that coercivity is near impossible to determine.

With a change in temperature, the magnetizations of the Tb and Fe subnetworks behave differently. The Fe moment barely changes over temperature, while the moment of the Tb atoms increases strongly towards lower temperatures. This is because the Tb fanning cone is compressed when decreasing the temperature [245], connected to an increase in exchange stiffness [246], thus aligning the Tb moments more collinearly. This has the same effect as an increase in Tb content or contribution in the system. Accordingly, the compensation temperature shifts to lower temperature for TbFe alloys with lower Tb content. Further, this means that the net magnetization of Tb-dominated TbFe alloys varies more strongly with temperature than that of Fe-dominated ones, as can be seen from M-T-measurements (schematically shown in Fig. 3.7 b)).

One of the advantages of amorphous magnetic systems now becomes obvious: the gradual change in H_C and M_S makes it possible to manufacture a TbFe thin film with almost arbitrary values of one of these properties. Another advantage was shown independently by Schubert et al. and Romer et al.: by using amorphous TbFe as the pinning layer in an exchange bias system with Co/Pt multilayers as the pinned layer, they were able to show high values of H_{EB} without the need of optimizing the interface [33, 34]. In conventional crystalline EB systems, using e.g. IrMn as a pinning layer, the strength of the EB depends massively on the quality (e.g. the roughness) of the interface, since uncompensated interface spins are needed for the pinning. This issue does not arise in the amorphous RE-TM magnet [247], as every TM atom will always couple antiparallel to any RE and parallel to other TM atoms, maximizing the EB effect. Further, it was shown that the sign of H_{EB} in EB systems with an RE-TM pinning layer is determined only by the dominant part of the RE-TM magnetization [33, 248].

This property of amorphous ferrimagnetic RE-TM thin films makes them extremely useful in structures exploiting exchange bias. These include magnetic field sensors and spin valve applications based on the giant magnetoresistance (GMR) or tunnelling magnetoresistance (TMR) effect. Also, TbFe might be an interesting soft layer in $L1_0$-FePt-based exchange-coupled composite (ECC) media as proposed by [55] and shown by [56]. The interface exchange interaction could further stabilize the FePt grains while simultaneously reducing the switching field. Especially with a compensation temperature above room temperature, a thermally assisted writing process could show very interesting dynamics when the TbFe layer switches from Tb-dominant to Fe-dominant [249].

CHAPTER 4

Sample deposition and processing

All thin film samples that were investigated in the frame of this work were deposited using by magnetron sputtering. The following chapters will give an insight into the working principle of this deposition technique as well as the two different post-annealing techniques that were used.

4.1 BESTEC magnetron sputtering system

When thinking of thin film manufacture, one usually thinks of very modern, highly sophisticated equipment, such as humanity started using in the 20th century. However, it seems that humanity's interest in creating thin layers of metals has started much earlier.

The first documented intentional manufacture of thin films goes back around 5000 years to the ancient egyptians, who used a chemo-mechanical process for the gilding of artefacts: after producing Au "leafs" of less than 300 nm thickness, they used mercury-based adhesion layers to cover statues and other artefacts with the thin gold film. Another interesting case is the *Moche* culture in northern Peru, who covered copper artefacts, such as masks, with Au via an autocatalytic solution-growth technique, starting around 100 BCE. More examples and details around the interesting history of thin films can be found in [250].

The technique used for thin film deposition in this work is *sputtering*, specifically *magnetron sputtering* [251]. Sputtering in general describes the emission of particles from a solid target surface by bombardment with accelerated ions from a working gas plasma, most often Ar. Although not quite an ancient technique, it was first described in 1852 by Grove [252], much earlier than many other thin film deposition techniques. It was initially disregarded as a means of thin film deposition due to its low deposition rate, low ionization efficiency in the working gas, and high heating effect on the target.

This changed in the 1970s, when the magnetron was invented as a means of increasing the ionization efficiency of sputtering guns. The magnetron makes use of magnetic fields to contain the working gas plasma in a region near the target surface. This is demonstrated in Fig. 4.1. Once a working gas atom is ionized by the applied voltage,

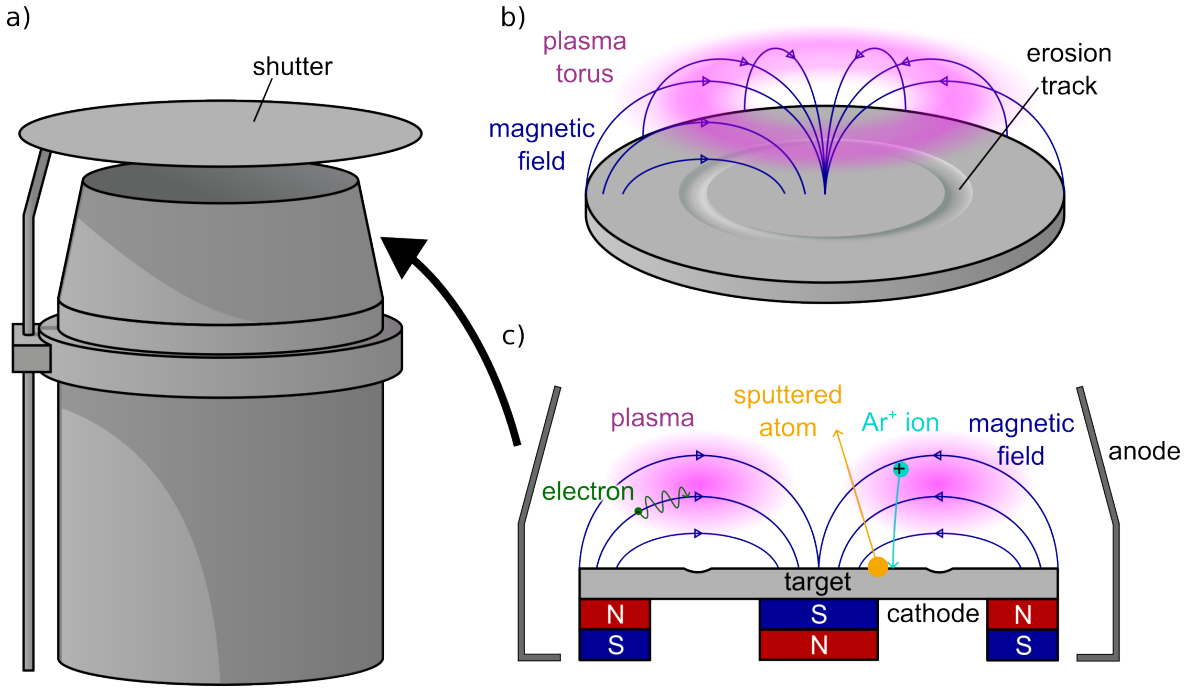

Figure 4.1: a) Sketch of a magnetron from the outside. b) Tilted view of the target with the plasma torus and the erosion ring under the region of highest plasma density. c) Cross section view of the magnetron, depicting the most important elements of the sputtering process.

the now free electron is deflected by the magnetic field onto a cylindrical path around the magnetic field lines [253]. This increases the time that the electron spends in the region above the target, increasing the chance of triggering another ionization event by electron-atom collision. Due to the cylindrical symmetry of the magnetic field, the plasma has the highest ionization efficiency in a torus-like region above the target surface.

The ions created in the plasma are accelerated towards the negatively biased target, colliding with the surface atoms or neutral gas atoms near the target. The collision emits atoms and secondary electrons from the target material. This means that the highest sputtering rate is achieved directly below the region with the thickest part of the plasma torus. This leads to the characteristic erosion ring seen on targets after extended use. Emission can roughly be described by a cosine distribution around the ion impact point, having the highest deposition rate perpendicular to the target. Higher sputter powers elongate the emission lobe (overcosine), while lower powers compress it (undercosine) [254].

When magnets of equal strength are used and all magnetic field lines originate *and* end on the target surface, the magnetron is called "balanced" [255]. When using magnets of unequal strength, some magnetic field lines extend outwards towards the substrate where the film is deposited. This is then called an "unbalanced" magnetron, which can achieve higher ionization densities in the region near the substrate. It also allows more sputtered target ions to reach the substrate and thus increases resputtering effects [256].

Using a magnetron, one can use lower working gas pressure and lower voltages, which reduces the heating of the substrate and helps more sputtered atoms to reach the substrate due to the higher mean free path. This helped sputtering to become one of the most prominent thin film deposition techniques after the 1980s. Many approaches to modify the sputtering process have since been taken, such as reactive sputtering, variable field sputtering, or duplex magnetron sputtering. One such approach that is widely used, namely radio frequency (RF) magnetron sputtering, shall now be explained in more detail.

Conventional sputtering relies on the transport of charges through the target material, as electrons are transferred onto the impinging working gas ions and new electrons need to replace those lost to the plasma. When sputtering an insulating material, this is not possible, and the target is quickly positively charged. This charge ultimately cancels out the applied voltage, leading to the extinction of the plasma, or in some cases is released by plasma arcing, which can severely damage the equipment.

This can be avoided by using an AC voltage with a suitably high frequency, usually in the range of radio frequencies between 5 and 30 MHz [257]. If the frequency is too high, the Ar ions are basically immobile due to their large mass and only the electrons are responsible for the sputtering, making it more similar to an e-beam evaporation method. The International Telecommunication Union (ITU) has specifically designated the frequency band at 13.56 MHz with a bandwidth of 14 kHz to be used by industrial, scientific, and medical (ISM) instruments, which is why this is the frequency generally used in RF generators for sputtering.

When this RF voltage is applied to the magnetron, positive ions and negative electrons are accelerated towards and away from the target surface in an alternating fashion, with electrons moving in the opposite direction of the ions, of course. Since the electrons have a much higher mobility, a lot more electrons than ions can arrive at the target surface during one cycle. This leads to the buildup of a negative charge during the first few voltage cycles, which adds a negative bias to the target. The bias pushes away electrons and pulls additional ions to the target, resulting in a balance of charge carriers over time. Essentially, the ions can be seen as "bouncing" up and down on the target surface. This way, no net current flows through the target material, allowing the use of insulating materials.

When depositing alloys, there are generally two ways of approach. The first is the use of an alloy target of the desired composition. Special attention needs to be given to the different sputtering yields of the elements of the alloy, since multiple factors, most importantly atom size and mass, can affect the amount of sputtered material per time unit at a given sputtering power. This can easily lead to deviations from the target composition when analyzing the composition of the sputter-deposited film.

The second method is co-deposition of elementary targets. This gives the possibility of determining the deposition rates of the individual elements and tuning them accordingly. Additionally, the composition rates can be calibrated to reach any composition value as opposed to being fixed due to a fixed target composition. Even though this does give more control, there is still the effect of resputtering to consider: after the film has been deposited on the substrate and while the deposition is still proceeding,

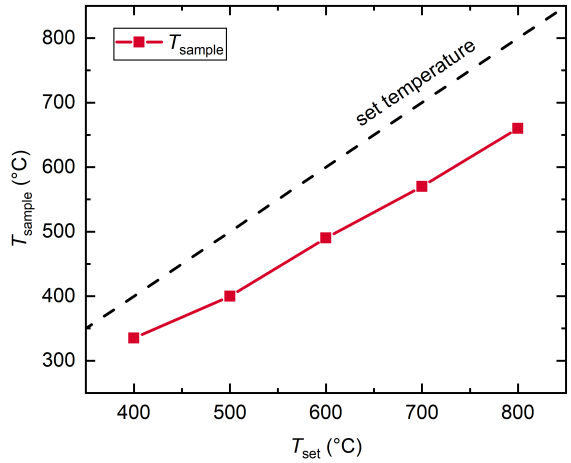

Figure 4.2: A display of the offset between the set temperature T_{set} (additionally depicted by the striped line) and the actual temperature at the sample position T_{sample}. A clear offset between the nominal set temperature and the sample temperature is visible.

impinging atoms can sputter the already deposited film. Similarly to the initial sputtering on the target, the resputtering effect is element-specific, preferentially removing atoms of a certain type, usually those more weakly bound, from the film. This also has an influence on the film composition and structure, and can even lead to some form of growth-induced anisotropy within the film.

All samples investigated in the frame of this work were deposited using a magnetron sputtering chamber from *Bestec GmbH* housing 8 magnetrons with individual shutters. The deposition rates for each element were calibrated using a quartz balance [258]. The base pressure of the chamber was below $8\text{x}10^{-8}$ mbar and Ar gas with a purity of 5N was used as a working gas. Si_3N_4 capping layers were deposited at a reduced pressure of $1.5\text{x}10^{-3}$ mbar using a mixture of 96 % Ar gas and 4 % N_2 gas in order to preserve stoichiometry. Before calibration, the targets were presputtered for several minutes in order to remove any oxide layer that may have formed on the target during storage. Highly oxidizing targets are stored within the chamber in order to reduce oxidization as much as possible.

The chamber is further equipped with a heating stage, allowing to heat the substrate holder to nominal temperatures of up to 1000 °C. A type K thermocouple is used to monitor and adjust the heater temperature. Since the position of the thermocouple is at the heater and not at the substrate position, there is an offset between the nominal set temperature and the actual temperature of the sample. A calibration measurement is depicted in Fig. 4.2, clearly showcasing the difference between the two temperatures. This offset needs to be considered when aiming for a certain deposition temperature, such as for the high-temperature deposition of $L1_0$ FePt on MgO.

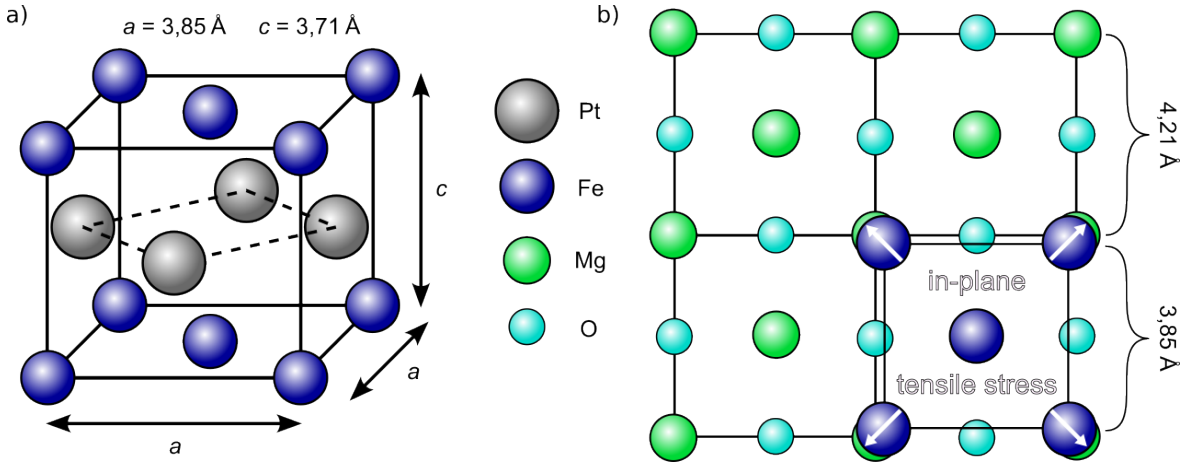

Figure 4.3: a) The unit cell of the $L1_0$ phase of FePt. b) Top view of an $L1_0$ FePt unit cell on top of an MgO substrate. The larger lattice parameter of MgO leads to a tensile strain being exerted on the FePt layer upon deposition.

4.1.1 Heteroepitaxy of $L1_0$ FePt on MgO

Epitaxy is the term used to describe the ordered growth of a crystalline material on a crystalline substrate. During the growth, a distinct crystallographic relationship between the two crystalline materials is established. This relationship is mostly given by lattice parameters and lattice types as well as the interface structure of the substrate.

In homoepitaxy, the deposited layer and the substrate are of the same material, hence the crystallographic orientation is usually continued by the additionally deposited material. In heteroepitaxy, the two materials are different, and thus the interface matching becomes much more important. Depending on the surface structure of the substrate, different crystal faces of the deposited material can fit the interface better.

In this work, $L1_0$ FePt films were epitaxially grown on (001)-oriented MgO substrates at elevated temperatures. The tetragonal FePt phase grows on the cubic substrate by stretching its quadratic base (the a and b lattice directions) to fit the quadratic surface lattice of the MgO. The lattice mismatch is rather high with a value of around 9 %, putting the FePt layer under considerable strain, as shown in Fig. 4.3. However, this strain is considered to facilitate the growth of the tetragonal $L1_0$ phase, since the tensile strain in the a-b-plane causes a compressive strain in c-direction, reinforcing the tetragonality of the system and reducing c/a. The initial strain is then relaxed during further growth by incorporating lattice defects such as dislocations [259]. $L1_0$ FePt can also be grown on $SrTiO_3$ (STO), where the lattice mismatch is much lower, around only 1 %. However, the reduced lattice mismatch actually reduces magnetocrystalline anisotropy in such films, making it a less desirable substrate for most applications [260, 261]. In this case, the lower lattice mismatch is actually more of a hindrance than an advantage, which can also be seen by low order parameters and mixed growth directions in some STO/FePt systems [262].

Depending on the field of application, different film growth modes are wanted for $L1_0$ FePt films: islands or nanograins for HAMR and continuous films without grain boundaries for spintronics. It is thought that dewetting and granular or island-like

growth on substrates with high lattice mismatch and low surface energy are the driving factor for increasing H_C. When combining a sufficient lattice mismatch with a high free surface energy, one can also create continuous $L1_0$ FePt films with a high degree of order and a high PMA, but also rather low H_C [263]. Furthermore, a slightly higher c/a ratio was also shown to increase PMA by first-principles calculation [264]. This serves to show that the subject of substrate choice is not a trivial one for optimizing the magnetic parameters of $L1_0$ FePt films.

Additionally to the lattice mismatch, the deposition temperature and the Ar sputtering pressure also play important roles for controlling the morphology and structure during film growth [265]. The pressure greatly influences the kinetic energy of the sputtered atoms when reaching the substrate. A high pressure means that a lot of momentum is lost before reaching the substrate via collisions with Ar-ions due to the low mean free path, reducing the mobility of the adsorbed atom on the substrate surface. This can in part be balanced out by an increased substrate temperature. If the pressure is too low, the mean free path becomes high, resulting in a low amount of collisions between sputtered atoms and Ar atoms in the sputtering chamber. This means that the sputtered atom arrives at the substrate with a high energy and can thus cause defect formation and distortion in the film when being adsorbed.

Furthermore, the temperature needed for the formation of the $L1_0$ phase is rather high [266]. A lower temperature reduces the diffusion coefficient D of the adsorbed atoms and thus their ability to join already existing nucleation sites as well as to arrange themselves in the structure of the $L1_0$ phase with its alternating layers of Fe and Pt [135, 136]. Instead, the disordered $A1$ structure is formed, where Fe and Pt atoms are randomly placed on the lattice sites of an fcc lattice. A sufficiently high deposition temperature should thus be chosen to enable good $L1_0$ formation. However, the temperature must of course not be higher than the disorder temperature or even the melting point of the FePt alloy, which are around 1300 and 1550 °C, respectively (see Fig. 3.2).

Accordingly, a moderate Ar pressure and a sufficiently high temperature need to be found where the formation of the $L1_0$ phase is optimal. In our case, the pressure is kept at 5 µbar and the nominal temperature at 800 °C. Due to the temperature offset (see Fig. 4.2), the actual sample temperature is around 630-650 °C. At this high processing temperature, adsorbed atoms can diffuse over the substrate surface to join already existing film nucleation sites. Because of the unfavourable surface energy of the substrate-film interface, film growth takes place via island formation and growth. Due to the quadratic symmetry of both sides of the substrate-film interface, the film can only grow in one orientation, minimizing the occurrence of grain boundaries. Hence, different islands all still have the same in-plane coordination. However, antiphase boundaries are still expected to exist in these films, since the initial, lowermost layer of an island can consist either of Fe or Pt atoms. This leads to an inversion of stacking order between two islands with different initial layer element. Effectively, the order parameter switches sign across an antiphase boundary [267]. Antiphase boundaries will then also decrease the intensity of the (001) reflection intensity, as schematically shown in Fig. 4.4, which consequently reduces the measured order parameter. Accordingly,

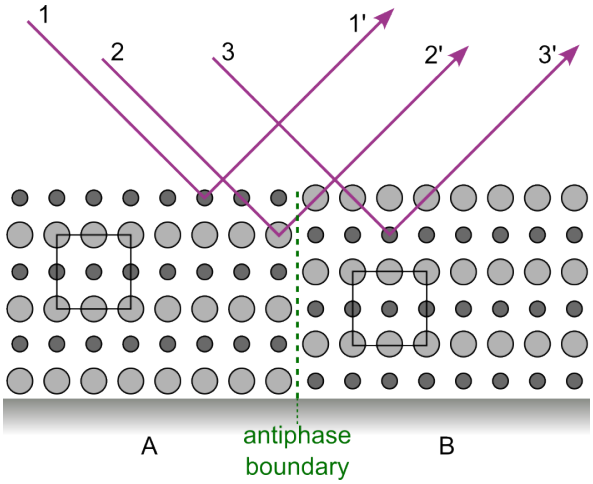

Figure 4.4: Profile view of X-ray scattering near an antiphase boundary (APB) in a film with $L1_0$ structure. Assuming proper alignment to the (001) reflection peak, the path difference Δx between rays 1' and 2' is equal to $\lambda/2$, but the interference is only partially destructive due to the different atomic scattering factors of the neighbouring atomic layers. The stacking orders in areas A and B are shifted by half a unit cell in the perpendicular direction with regards to each other, leading to an inversion of order across the APB. Accordingly, ray 3' has a path difference of $\lambda/2$ *and* the same intensity as ray 1', leading to complete destructive interference. This leads to a decrease of the measured (001) reflection peak intensity.

the order parameter as determined from an XRD measurement is a lower border for the degree of $L1_0$ phase formation, while the actual value might be higher.

4.2 Carbolite tube oven

The post-annealing steps in this work were performed in a commercial tube oven of the type *CTF 17/- -/300* by *Carbolite*. It uses molybdenum disilicide heating elements to heat up a hollow ceramic tube with inner diameter of 75 mm inside of which the sample can be placed.

The setup is equipped with a diaphragm vacuum pump which is used to evacuate the tube, reaching about 30 mbar, before flooding it with the desired atmosphere. The gas inlet is connected to multiple gas lines, so nitrogen, oxygen, and forming gas can be used to flood the chamber. In this case, the forming gas consists of nitrogen gas with 10 % hydrogen gas.

In this work, pumping and flooding with nitrogen gas was performed twice in order to ensure that almost no residual oxygen or water vapour is left in the tube before starting the heating process. Additionally, the tube was evacuated one more time and flooded with forming gas, and the flow was kept constant at 100 sccm during the heating procedure. The hydrogen in the forming gas helps catch remaining oxygen that is released by heating up and prevents the sample from oxidation. This is especially useful when heating RE-containing thin films, which are prone to oxidize even under vacuum conditions.

A built-in *Eurotherm 2408* temperature controller is then used to construct a heating program, which can consist of multiple steps. Here, unless otherwise noted, the standard post-annealing routine consisted of heating up to the desired temperature with a nominal heating rate of 10 °C/min, holding the temperature for the allotted time, and finally cooling to room temperature with the same nominal heating rate.

CHAPTER 5

Experimental techniques

The investigation of the magnetic thin film samples conducted in the frame of this work made use of a variety of structural and magnetic measurement techniques. In the following, a description and short introduction to these techniques and the devices that enable their implementation will be given.

5.1 X-ray diffractometry (XRD)

With X-ray diffractometry (XRD), the low wavelength and rather high penetration depth of radiation from an X-ray source can be used to characterize thin film crystals. The information taken from such measurements can be used to draw conclusions about crystal type, lattice parameters, alloy concentrations, film thickness, strain status and texture of the film sample, to name only a few. The low wavelength is owed to the high energy of the X-ray photons, which are generated by electron transitions. There are two types of X-rays to distinguish: continuous radiation ("Bremsstrahlung") and characteristic radiation [137].

Bremsstrahlung is generated by accelerated electrons. The acceleration of the electrons, e.g. when losing velocity upon hitting a solid surface or moving on a circular path, generates dipole radiation with an energy that depends mostly on the energy lost by the electron in the process. The highest possible energy of the photon is equal to the total kinetic energy of the electron before the photon emission process. Since the energy of the photon can also take any value lower than this, the corresponding energy spectrum is continuous.

Characteristic radiation, on the other hand, is generated by electron transitions within an atom. The energy of the photon is defined by the energy difference of the electron shell before and after the transition. Consequently, the spectrum is not continuous, but consists of sharply defined energies. These energies, usually named according to the shell that the electron dropped onto, vary between elements and are constant for each element. This enables the generation of certain wavelengths by using certain elements in an X-ray cathode. The most commonly used radiation in XRD is Cu-K_α with a value of 8.04 keV, corresponding to a wavelength of 1.5406 Å.

The wavelength in the range of 1 Ångström (Å) is small enough for the photons to experience interference effects when scattered on a periodic crystal lattice, which usually also shows lattice parameters of only a few Ångströms. The mechanism behind this will be explained in the following.

When the incoming X-ray photon hits the sample, it interacts with the electrons in an atom via Thomson scattering. This term describes the elastic scattering of a photon on a charged particle, such as an electron. The electron experiences the electric field of the electromagnetic wave and is accelerated accordingly. This movement of the charged electron in turn emits dipole radiation in the form of a photon with the same energy as the incident photon. This scattered photon can then be detected. Other forms of photon scattering in matter include inelastic Compton scattering, where the photon transfers part of its energy to the electron, and Rayleigh scattering, where the scattering object is a polarizable, usually neutral atom or molecule.

After being scattered, the photon can interact with other scattered photons. The scattered wave vector $\vec{\mathbf{k}}'$ has the same magnitude as the incoming wave vector $\vec{\mathbf{k}}_0$, but is rotated by the angle 2θ. If we now observe two scattered photons from the same source but scattered at neighbouring atom planes with the Miller indices (hkl) in the crystal, their path difference depends on the angle Θ and the spacing d_{hkl} of the planes. d_{hkl} itself depends on the Miller indices (h, k, l) and the lattice parameters (a, b, c):

$$d_{hkl} = \frac{1}{\sqrt{(\frac{h}{a})^2 + (\frac{k}{b})^2 + (\frac{l}{c})^2}} \tag{5.1}$$

In order to observe constructive interference, the total path difference must be an integer multiple of the wavelength λ of the X-rays. Through geometrical considerations, one arrives at the Bragg condition for constructive interference:

$$n\lambda = 2\, d_{hkl}\ \sin\theta \tag{5.2}$$

with n : diffraction order

The maximum in intensity created in this way forms a peak in the measured intensity when plotted over the angle θ. To identify which group of lattice planes is responsible for this peak, it is usually called the "$(h\,k\,l)$ reflection peak".

5.1.1 Structure factor

For many lattices, not all reflections that satisfy the Bragg condition are observed in an XRD measurement. This usually happens because intermediary planes cause destructive interference in the diffracted X-ray beams. The structure factor of a crystal gives information about whether the $(h\,k\,l)$ reflection peak is fully visible, reduced in intensity, or completely extinct. It is the sum of the contributions from all atoms j in a unit cell to the diffraction and can be written as:

$$F_{hkl} = \sum_j f_j \, \exp\left(i * \vec{r}_j * \vec{\mathbf{G}}_{hkl}\right) \tag{5.3}$$

Here, f_j is the atomic scattering factor and $\vec{r}_j$ is the position of the corresponding atom j in the unit cell, while $\vec{\mathbf{G}}_{hkl}$ is the reciprocal lattice vector of the corresponding indices. Inserting the proper values and solving for $F_{hkl} = 0$, one can find the extinction rule for destructive interference for a crystal structure. For example, the extinction rule in an fcc lattice tells us that if the Miller indices are not of the same parity, the corresponding peak is extinguished.

The extinction rule for $L1_0$ structures consisting of elements A and B can be derived as follows:

$$\begin{aligned} F_{hkl} &= f_A \left[e^{\,i\,\vec{r}_1\,\vec{\mathbf{G}}_{hkl}} + e^{\,i\,\vec{r}_2\,\vec{\mathbf{G}}_{hkl}} \right] + f_B \left[e^{\,i\,\vec{r}_3\,\vec{\mathbf{G}}_{hkl}} + e^{\,i\,\vec{r}_4\,\vec{\mathbf{G}}_{hkl}} \right] \\ &= f_A \left[e^{\,0} + e^{\,i\,\pi(h+k)} \right] + f_B \left[e^{\,i\,\pi(h+l)} + e^{\,i\,\pi(k+l)} \right] \end{aligned} \tag{5.4}$$

As can be seen from equation 5.4, the structure factor for $L1_0$ structures only becomes zero when h and k have different parities. This means that reflections that would be suppressed in the face-centered $A1$ phase can be visible in the $L1_0$ phase, such as the (001) reflection, albeit often with reduced intensity.

Since the (001) reflection peak is forbidden in the $A1$ structure, one can determine the order parameter of an $L1_0$ system by comparing the integrated intensities of the (001) and (002) reflection peaks. The result gives information about how many atoms are on the correct lattice sites for a $L1_0$ structure. However, this is often easier said than done, because background signal, overlapping peaks, and other factors can make a proper integration of the reflection peaks difficult. However, qualitative statements about the film can still be made by simply looking at the peak intensities: in a perfect $L1_0$ crystal, the (001) reflection peak has about 2 times the intensity of a (002) reflection peak, as already mentioned in chapter 3.1.1.

The order parameter S is defined by the fraction p of atoms of type A that are on their designated lattice site α and the fraction r of type A atoms in the alloy.

$$S = \frac{p - r}{1 - r} \tag{5.5}$$

In a binary alloy with equal parts A and B ($r = 0.5$), the structure factor is equal to 1 when all atoms of type A are on the proper lattice site α and, accordingly, all type B atoms are on β sites. When there is maximum disorder, type A atoms are evenly distributed among the two lattice sites, so p is 0.5 and thus equal to r, making S zero.

5.1.2 $\theta - 2\theta$ measurements

A standard form of XRD measurement is the $\theta - 2\theta$ measurement, where the angle θ is varied. By also rotating the detector twice as fast as the sample stage, the angle between incoming and scattered X-ray is always kept at 2θ. This setup, also known

as Bragg-Brentano geometry, keeps the measuring geometry symmetrical, so that the Bragg condition can be met.

By varying θ and measuring the diffracted intensity, we can create an X-ray diffractogram. By determining the position of diffraction peaks and knowing the wavelength of the radiation that was used, we can also determine the lattice spacing of the planes responsible for the diffraction peaks. There are many libraries containing information about countless alloys and elements and their respective diffraction peaks, so one can easily use a software like *Match!* to identify the peaks that a given diffractogram contains, especially if the elements contained in the sample are known. Knowing the Miller indices belonging to a peak, the lattice parameters of the film can be obtained by solving equation 5.1 for a, b, or c. This of course means that there are 3 independent peaks necessary to obtain information about all three lattice parameters. Still, one can calculate the c lattice parameter from a single (002) diffraction peak, for example.

Another way of obtaining information about the structure of a film is the full width at half maximum (FWHM). Using Scherrer's equation, one can estimate the crystallite size L (more precisely: the coherent scattering length) of the investigated film along the scattering direction by inserting the FWHM [268, 269]:

$$L = \frac{K\,\lambda}{\beta \cos\theta} \tag{5.6}$$

with K : dimensionless shape factor close to 1
λ : X-ray wavelength
β : FWHM in radians

The bigger the crystallite size, the narrower the peak. This can be very well observed in the case of substrate peaks in diffractograms, which are always very sharp in comparison to the film peaks. This is caused by the much higher thickness of single-crystalline substrates when compared to the thin film.

5.1.3 Rocking curves

When the sample plane is not completely aligned with the plane of the sample holder, the sample has to be tilted in order for the Bragg condition to still apply. This means that the angle between source and stage is increased/reduced by the same amount as the angle between stage and detector is reduced/increased, meaning that the angle between incoming and diffracted X-rays is kept at 2θ. When a maximum in intensity is reached, the sample is properly aligned with the beam. This procedure is displayed in Fig. 5.1. Because the sample is rocked back and forth during the procedure, this type of measurement is called a rocking curve measurement. Since the angle between sample plane and incoming X-ray is usually not equal to θ, it is commonly called ω.

Another use of varying ω shows itself in the measurement of samples with a preferred crystal orientation. While polycrystalline samples show all possible diffraction peaks in their diffractograms, a properly aligned single-crystalline sample will show only one type of reflection peak, plus the corresponding peaks of higher order. In the example

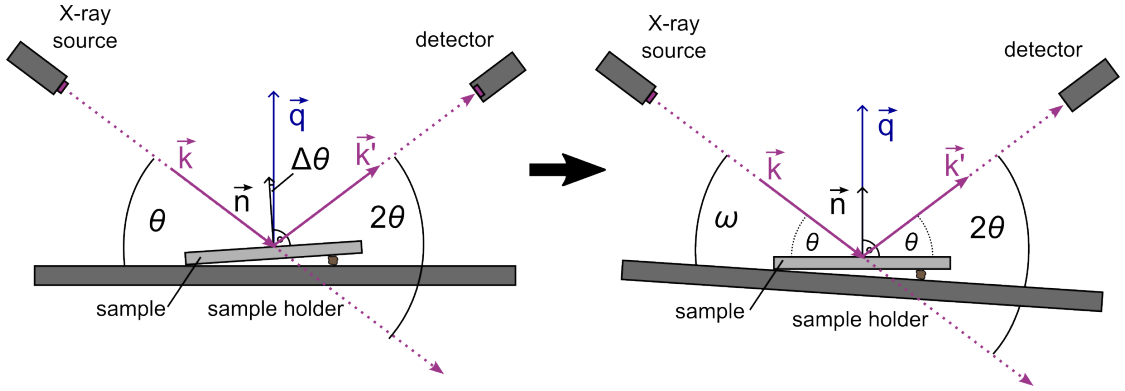

Figure 5.1: Alignment procedure for XRD measurements: the sample holder is tilted so that the sample surface normal $\vec{n}$ is parallel to the scattering vector $\vec{q}$. The angle 2θ between incoming and refracted beam remains the same, and the angle between incoming beam and sample holder is now ω.

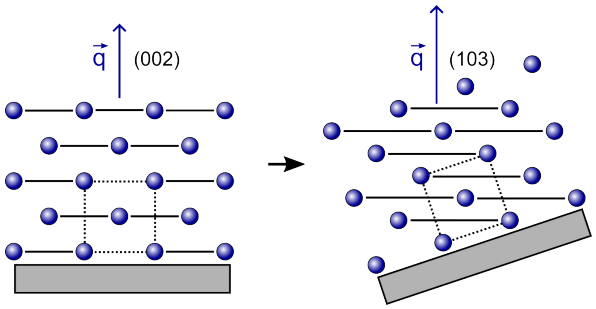

Figure 5.2: Exemplary use of sample tilting for measuring a textured sample: the proper ω or χ allows to measure off-axis reflections, like the (103) reflection peak in this example.

of $L1_0$-FePt grown on single-crystalline MgO(001) substrates, this is the c- or (001)-direction. By tilting the sample, which corresponds to an increase or decrease in ω (or χ for the perpendicular tilting direction), other diffraction peaks can also be observed. This is schematically shown in Fig. 5.2, where the sample has been aligned to the (103) direction. One has to keep in mind that another alignment, namely a rotation of the sample around the scattering vector (φ-scan), is often necessary for a measurement of such off-axis peaks, since the azimuthal orientation of the film crystal is generally unknown.

5.1.4 Reciprocal space mapping

Another equivalent formulation of the Bragg condition in reciprocal space is the Laue condition. It uses the scattering vector $\vec{\mathbf{Q}}$ in reciprocal space, which is defined as the difference between $\vec{\mathbf{k}}_0$ and $\vec{\mathbf{k}}'$ in reciprocal space:

$$\vec{\mathbf{Q}} = \vec{\mathbf{k}}' - \vec{\mathbf{k}}_0 \tag{5.7}$$

The Laue condition says that if a scattering vector is equal to a lattice vector $\vec{\mathbf{G}}_{hkl}$ of the reciprocal lattice, constructive interference can be observed:

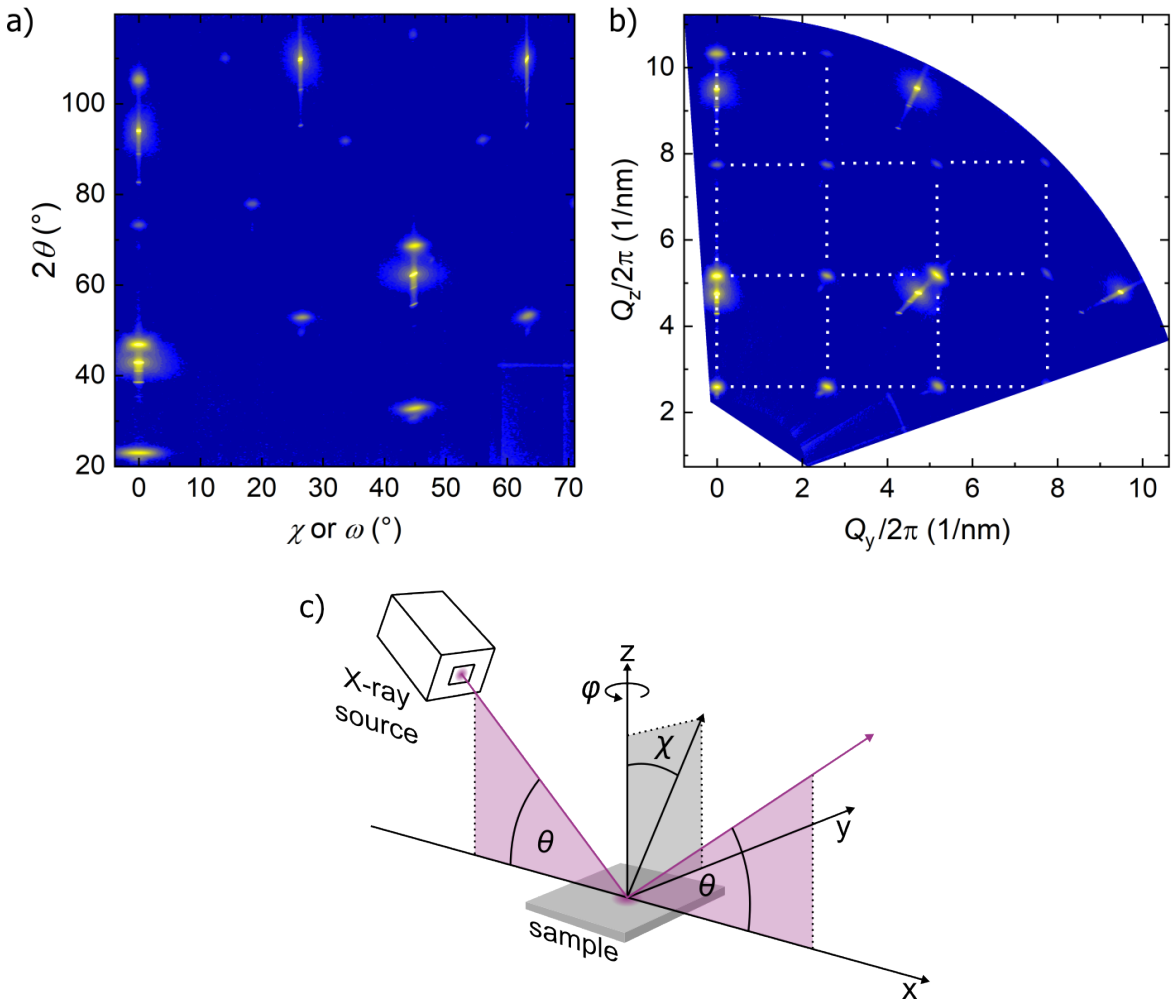

Figure 5.3: An exemplary reciprocal space map is shown in the a) 2θ and ω (or χ) and b) $\mathbf{Q}_z$ and $\mathbf{Q}_y$ representations. The reciprocal lattice (highlighted by dotted lines) is easily discernible in b). The scattering geometry depicted in c) displays the additional degrees of freedom φ and χ often used for measuring reciprocal space maps.

$$\vec{\mathbf{Q}} = \vec{\mathbf{G}_{hkl}} \tag{5.8}$$

A $\theta - 2\theta$ XRD measurement is thus a one-dimensional representation of the reciprocal lattice along the scattering direction when the measured scattered intensity is plotted over $|\vec{\mathbf{Q}}|$ instead of 2θ. If a two-dimensional representation is wanted, some way of rotating either the scattering vector $\vec{\mathbf{Q}}$ or the (reciprocal) lattice is needed.

This can be done by combining the $\theta - 2\theta$ measurements with a variation in ω (or χ, alternatively): for every variation of ω, one whole $\theta - 2\theta$ diffractogram is recorded. The increase (or decrease) of ω effectively tilts the scattering vector into the film plane. This way, one can create a map of the scattered X-ray intensity over 2θ and ω, as shown in Fig. 5.3 a). Such a diagram is called a reciprocal space map (RSM).

It is also possible to plot the intensity over the two components of the scattering vector. This requires the transformation from θ and ω to $\mathbf{Q}_y$ and $\mathbf{Q}_z$ as described

in equations (5.9) and (5.10) [270]. This makes the evaluation of the reflection peaks easier and more intuitive. An example of the resulting map is shown in Fig. 5.3 b). Not only is the map now a direct, undistorted two-dimensional representation of the reciprocal lattice, but the coordinates of the peak positions, $\mathbf{Q}_\mathrm{y}$ and $\mathbf{Q}_\mathrm{z}$, can be directly converted to the distance of the lattice planes d_{hkl} as shown by equation (5.11).

$$|\mathbf{Q}_\mathrm{y}| = [\cos(2\theta - \omega) - \cos(\omega)]\,\frac{2\pi}{\lambda} \tag{5.9}$$

$$|\mathbf{Q}_\mathrm{z}| = [\sin(2\theta - \omega) + \sin(\omega)]\,\frac{2\pi}{\lambda} \tag{5.10}$$

$$|\vec{\mathbf{Q}}| = \sqrt{|\mathbf{Q}_\mathrm{y}|^2 + |\mathbf{Q}_\mathrm{z}|^2} = \frac{2\pi}{d_{hkl}} \tag{5.11}$$

The same can be done by varying χ instead of ω by tilting the sample normal out of the scattering plane. The principle stays the same, only the scattering vector is tilted into another direction. Since ω cannot exceed 2θ, a χ-variation is often preferable, especially when one wants to cover a big part of the reciprocal space. The formulae in this situation (assuming $\omega = \theta$) change to:

$$|\mathbf{Q}_\mathrm{y}| = [\cos(\theta - \chi) - \cos(\theta + \chi)]\,\frac{2\pi}{\lambda} \tag{5.12}$$

$$|\mathbf{Q}_\mathrm{z}| = [\sin(\theta - \chi) + \sin(\theta + \chi)]\,\frac{2\pi}{\lambda} \tag{5.13}$$

As mentioned in the previous chapter, a proper φ- and χ-alignment of the sample has to be done before an RSM measurement to make sure that the crystal lattice is properly aligned with the tilting direction of the scattering vector. For the sake of clarity, these additional rotational angles are depicted in Fig. 5.3 c).

5.2 Superconducting quantum interference device - vibrating sample magnetometry (SQUID-VSM)

In the frame of this work, a commercially available MPMS (magnetic property measurement system) superconducting quantum interference device - vibrating sample magnetometer (SQUID-VSM) by the company *Quantum Design* was used for the investigation of static magnetic properties. A SQUID-VSM is a device that can measure the magnetic moment of a sample with very high precision [271]. This precision can reach mere fractions of the flux quantum Φ_0, which is the quantization of magnetic flux in a superconducting loop and defined as $\Phi_0 = h/2e \approx 2.068$ x 10^{-15} Vs [272].

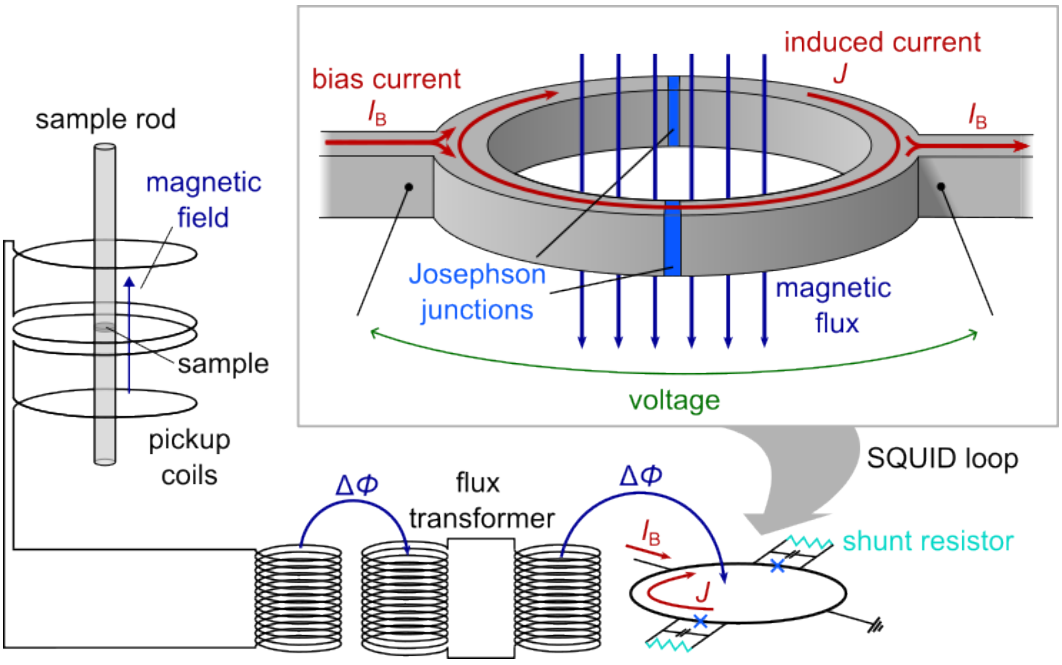

Figure 5.4: Working principle of a SQUID-VSM: the SQUID loop on the right is coupled to the pickup coils on the left via a flux transformer. The moving sample creates a variation in flux that is transformed into a voltage signal in the SQUID loop, which is used to measure the sample's magnetization.

5.2.1 Working principle of the SQUID-VSM

The central element of a SQUID-VSM is the SQUID, which consists of a superconducting loop with two small insulating barriers, called Josephson junctions [273]. A simple representation of such a loop is shown in Fig. 5.4. With no flux in the loop, the maximum critical current of the loop is equal to the sum of the critical current I_0 of the two junctions: $I_{c,max} = 2I_0$. At this current, the superconductor transitions from superconducting to regular behaviour. During measurement, a biasing current I_B just above $I_{c,max}$ is usually applied.

If a magnetic flux is now applied to the loop, a current J is induced in the loop to counteract the flux, according to the Meissner effect. This circular current is added to the biasing current on one of the Josephson junctions, while it is subtracted on the other one. The maximum critical current is hereby reduced. Further increase in flux continues this reduction until the applied flux reaches $\Phi_0/2$. At this point, it is energetically favourable to increase the flux inside the loop by Φ_0 and reverse the direction of J. The maximum critical current at this point is unaffected, but a further increase in flux now reduces J, which increases $I_{c,max}$. This continues until the flux reaches Φ_0 and $J = 0$, which is identical to the state in the beginning, except for the increased flux. $I_{c,max}$ is thus periodic in the flux, with a periodicity of Φ_0.

As mentioned before, the biasing current I_B applied to the loop is usually chosen such that the current at both junctions is slightly above their critical current I_0. Given the I-V-characteristics of a Josephson junction, depicted in Fig. 5.5, one can see how the change in flux leads to a change in voltage across the loop: with no flux applied, the

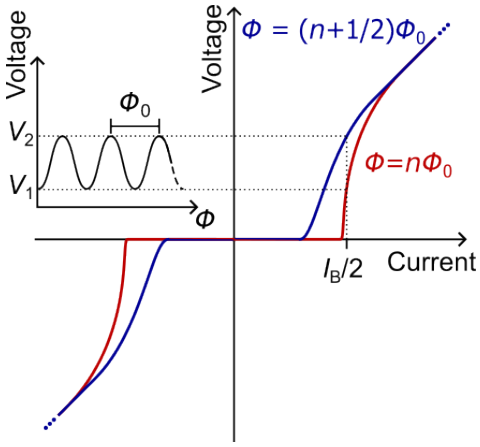

Figure 5.5: The I-V-charactesistics of the Josephson juntions in a SQUID loop: the voltage drop over the Josephson junction is periodic in the magnetic flux Φ. At a current close to the critical current, the voltage can change drastically for very small changes in flux Φ, allowing for a high precision of measurement.

current is at its maximum value and the voltage corresponding to $I_B/2$ is low. When the flux is increased, the current drops until it reaches the minimum at $\Phi_0/2$. The voltage corresponding to $I_B/2$ is now high. Hence, the voltage drop across the loop is also periodic, only now it is minimal when the flux is a multiple of Φ_0. Thanks to this procedure, the SQUID is essentially a flux-to-voltage transducer, turning the difficult-to-measure quantity *flux* into the easily measurable quantity *voltage*. By using a feedback mechanism, the SQUID can be kept at the region between maximum and minimum, ensuring a maximum change in voltage for small changes in flux. By then sensing the feedback current, the sensitivity of this measuring technique can be kept extremely low, reaching 10^{-17} Wb/m^2.

The SQUID has to be magnetically shielded from outside magnetic influence as well as continually cooled in order to stay in the superconducting state. This means that the SQUID has to be separate from the sample chamber, where strong fields and varying temperatures can be applied. Of course, the measured signal from the sample still needs to be transported to the SQUID somehow. This is achieved via a series of coils.

The most important of these are the pickup coils around the sample chamber near the sample position. These measure the magnetic flux lines that are not closed within them, i.e. those that penetrate the area enclosed in the loops. They are symmetrical with counter-wound outer loops, which makes the coils act as a second-order gradiometer, which measures an approximation of the second spatial derivative of the magnetic field. Such a gradiometer suppresses the magnetic signal of distant sources as $1/R^{3+M}$, with M being the order of the gradiometer and R being the distance of the source of the signal [274]. The sample signal, due to being created within the gradiometer, is basically not attenuated at all, while exterior disturbance is effectively suppressed.

By vibrating the sample up and down with a known frequency during the measurement process, the magnetic signal of the sample being measured by the pickup coils changes, while the applied field stays constant. This change of flux density in the pickup coils is transferred via two coupling coils to the SQUID, where it is translated

into a voltage signal. The translation from voltage to magnetic moment is done by the system automatically, and the process is regularly calibrated by measuring a Pd calibration sample of known size.

The magnetic field is generated by a solenoid consisting of the type-II semiconductor niobium-titanium (NbTi), which is He-cooled. The solenoid is located around the sample position and can generate magnetic fields of up to 70 kOe along the axis of rotation of the solenoid. Since the direction of the magnetic field is fixed, different sample holders can be used to apply a field either along the surface normal of the thin film plane (out-of-plane) or along the sample plane (in-plane). For out-of-plane (oop) measurements, the sample piece is clamped into a plastic straw, while it is glued to a flattened quartz glass rod for in-plane (ip) measurements.

5.2.2 Sources of error and measurement corrections

While the precision of the SQUID-VSM is extremely high, there are multiple factors that influence the measurement. In the following, a short overview of possible sources of errors will be given.

Sample geometry and vibration amplitude
In order to give reliable values for the magnetic moment, the SQUID-VSM system is regularly calibrated with a reference sample. It consists of a pure Pd cylinder with length 3.8 mm and diameter 2.8 mm. This paramagnetic sample with known magnetic susceptibility is measured and the system calibrated to fit the reference value.

This only works because the shape and size of the reference sample are known. When any of these change, e.g. when measuring a thin film sample, the shape of the stray field also changes. Since this is what the pickup coils measure, there is a systematic difference in measured magnetic moment when measuring thin film samples. Further, the vibration amplitude also influences the measured signal, since it effectively moves the stray field in relation to the coils.

Luckily, a correction of this is possible. Correction factors derived from numerical simulations are given by the manufacturer *Quantum Design* for quadratic thin film samples of given edge length and a certain vibration amplitude. For an edge length between 3 and 4 mm and a vibration amplitude of 5-7 mm, the correction factor for oop-measurements lies between 1.09 and 1.15. The factor is larger for larger samples and smaller vibration amplitudes. For ip-measurements, the factor lies between 1.0 and 1.03. This means that the same sample measured in both directions will always show a higher magnetization in the oop direction, with the moment measured in the ip-direction being more precise.

The measurements shown in this work have been corrected assuming an average sample size of 11 mm^2, i.e. a side length of about 3.3 mm, and a vibration amplitude of either 5 or 7 mm, as corresponding to the measurement.

Sample position
Since the vibration of the sample should be symmetrical around the center of the pickup

coils, the sample position has to be known in order to receive useful measurements. This is achieved by scanning the sample height and recording the resulting magnetic signal. The signal is at maximum when the sample is at the center of the pickup coils, so the maximum position is set as the sample position.

If the magnetic moment of the sample is very low, it is advisable to use a guiding field to increase its signal for the centering process. Even then, additional sources of magnetic moment like glue, debris left from sample cutting, or asymmetries of the sample holder can influence the measured sample position. However, these influences are usually very weak, giving only a 2 % reduction in measured moment for an offset of 0.5 mm with 2 mm vibration amplitude (as stated by *Quantum Design* in an application note). Higher vibration amplitudes further reduce this. Accordingly, no correction concerning the sample position has been applied in the frame of this work.

Measured background

When evaluating the measurements, one has to keep in mind that the measured signal is not only caused by the film, but also by the substrate and the sample holder. Luckily, those extra contributions are normally either diamagnetic or paramagnetic, so their contribution in an M-H loop is simply a linear background. This background can be subtracted by fitting a part of the curve that is known to be flat, usually the high-field-region, where the film is saturated. This technique mostly works well, but a user is faced with difficulties when the film is not saturated even at the highest applicable magnetic fields. Such measurements should be evaluated with caution, since the real magnetization values are near impossible to know.

In this work, difficulties arose when evaluating ip-measurements of $L1_0$ FePt samples and some low-temperature measurements of TbFe samples. The anisotropy field of $L1_0$ FePt is higher than the available field, so the samples can never be saturated in the in-plane direction. For these samples, the regular background subtraction was applied, so the slope at the highest field is zero. Accordingly, these measurements can only be interpreted regarding their shape, not their magnetization values. For some of the TbFe samples, a similar effect could be observed, caused by the high PMA. For these samples, another region known to show a slope near zero was used to subtract the background. Further information will be given in the chapters addressing those samples.

Sample volume

The measured magnetic moment is normalized to the volume of the magnetic film. The volume is determined by measuring the sample surface via an optical microscope and multiplying it by the film thickness. The film thickness can be determined by EDX (see chapter 5.4), but this requires knowledge of the density of the layer. This can be difficult to estimate, since it is usually not known what percentage of the film is crystalline or amorphous, or what the respective densities of these constituents are. Some samples can not even be properly analyzed by EDX due to overlapping signals from two or more elements, which is the case for Tb and Fe in this work. Hence, the nominal thickness has been used to calculate the thin film volume. A maximum error of $\pm$ 15 % is thus assumed for the film thickness.

The determination of the film area is also a source of errors, since the sample edges are often jagged due to being broken when the sample is cut to size. Also, scratches on the surface can effectively remove a small part of the film. As a result, an error of $\pm$ 5 % is assumed for the sample area.

In total, this leads to a maximum error of about 20 % for the sample volume and consequently the magnetization. The volume error for samples whose thickness can actually be measured is considered to be only about 10 %, though.

Magnetic artefacts

There are two more phenomena of the SQUID-VSM that should be mentioned. Firstly, the superconducting magnet can trap currents inside itself even when there is no outside current applied. This usually happens when the magnet has been set to very high fields and is afterwards set to zero field. As a result, there is a small opposite field of about 20 to 50 Oe, even though the system is set to zero. In our case, this effect is mostly negligible, because most samples have coercivities much higher than that. However, very soft samples can show seemingly unexpected behaviour when this effect is disregarded.

Secondly, a so-called "soft phase" is often visible in the measurements, even when there is no soft magnetic phase contained in the sample. The reasons for this are not known for certain, but edge regions of the film are a likely cause [275]. The main idea behind this is that there is material deposited at the edges and the side of the substrates during sample preparation. The missing epitaxial growth then leads to the formation of amorphous, magnetically soft film regions at the edges. This can be circumvented by using a mask during deposition or by cutting away the edges.

However, a soft phase was observed in nearly all measurements conducted in the frame of this work, also those without substrate edges. It could be identified by its extremely low variation with temperature and its changing magnitude between different measurement runs. This goes contrary to the previous explanation, which suggests the soft phase to be identical for different measurements of the same sample piece. This leads to the conclusion that soft phases can additionally be caused by magnetic debris and dirt on the sample holder. This cannot be avoided even with the greatest care, since the straws used for oop measurements tend to gather static charge and thus attract small particles like dust.

Another way of getting rid of the soft phase contribution is to use regionally confined measurement techniques like Magneto-Optical Kerr Effect (MOKE) magnetometry. However, the available MOKE magnetometer relies on conventional coil magnets that can only reach up to 1.5 Tesla. Furthermore, the setup has no way of cooling the sample, so only room-temperature measurements are possible. Both of these are conditions that make MOKE magnetometry unfit for the investigations of the samples at hand.

In this work, the soft phases, when identified, were fitted with an *arctan* function and subtracted from the *M*-*H* loop.

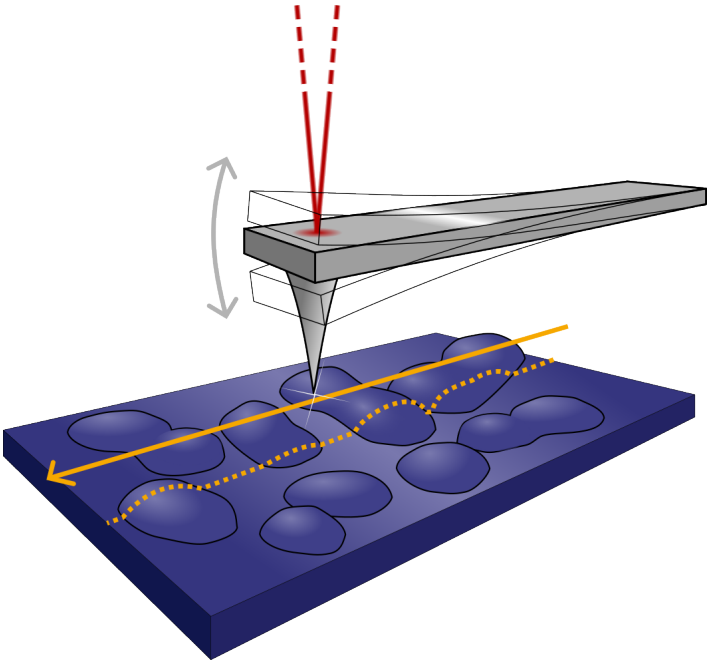

Figure 5.6: Working principle of an AFM: the vibrating cantilever scans its tip over the sample surface, tracing the height profile along the line. A two-dimensional area can be measured by measuring multiple neighbouring lines.

5.3 Atomic force microscopy (AFM)

Atomic force microscopy is a well-established technique for investigating the topography of sample surfaces [276, 277]. It uses a sharp tip with a tip diameter of around 10 to 20 nm, situated on the end of a cantilever, to probe the surface of the sample and determine the height profile along a line. Scanning one line next to the other, as depicted in Fig. 5.6, one can create height maps of the surface. The resolution is mostly determined by the tip radius, but can be greatly worsened if dirt gathers on the tip. Dirt particles can furthermore act as a kind of "second tip", leading to the creation of measurement artefacts. Frequent changing of the tip is thus necessary.

The readout of the cantilever deflection is done with a laser, which is reflected from the back of the cantilever onto a detector screen. The alignment of the laser has to be adjusted carefully every time the system is used. To do so, the laser spot is first aligned to hit the cantilever. This can be done via two adjustment knobs for controlling x and y coordinates of the laser spot. A camera with magnifier helps track the position of the spot near the cantilever, and a value of the total photocurrent on the detector screen helps optimizing the laser position. Next, the reflected laser spot is adjusted to hit the center of the detector. This is done via an adjustable mirror, which can be manipulated with two further adjustment knobs. Once the reflected laser hits the center of the detector, the system is ready to measure.

There are multiple modes of operation in AFM, one of the most common being the tapping mode. In this mode, the cantilever is driven by a piezoelectric motor to oscillate with a constant amplitude at a fixed frequency near or at its resonant frequency. When

in close proximity to the sample surface, the cantilever tip will experience various forces like dipole-dipole-interactions, van der Waals forces, or electrostatic forces, which alter the oscillating amplitude and/or resonance frequency. In tapping mode, the feedback regulates the amplitude to a constant value at each point along the measured line, so in effect the cantilever is always moved to the same vertical distance from the surface, tracing the profile along the way.

Other than tapping mode, there are also the contact and non-contact modes. The non-contact mode is similar to the tapping mode, only the cantilever is driven at its resonance frequency. This is ensured by a feedback loop, which couples the cantilever position back to the actuator with a phase shift of 90°. The change in resonance frequency due to the forces between tip and sample is then taken as an indicator for the tip-sample distance. The contact mode includes the constant force mode, where the tip is pushed down until a certain flexure of the cantilever is reached, and the constant height mode, where the variation of the flexure is a measurement of the sample-cantilever-distance. Both of these are most suitable for very flat, mechanically hard surfaces, since lateral forces of rough surfaces can easily damage the tip.

5.4 Energy-dispersive X-ray spectroscopy (EDX)

Energy-dispersive X-ray spectroscopy, EDX or EDS in short, is a non-destructive measurement technique that analyzes the characteristic X-ray spectrum of a sample. This can be used for discerning the elemental composition or the film thickness of a thin film sample.

The excitation of inner-shell electrons is the basis of this technique. In many table-top EDX devices, this is done via X-ray bombardment. In electron microscopes, the electrons of the electron beam can be used to achieve the same, with the added benefit of receiving spatial information, since the recorded spectrum contains only the information of the sample area that the electron beam was focused on.

Once an electron has been removed from one of the inner shells, an electron from a higher shell can fill the newly formed hole, emitting X-rays in the process (see Fig. 5.7 b)). The energy of these X-rays is characteristic for each element and depends on the precise energy levels of the energy state of the electron before and after the transition [137].

The transitions and the corresponding radiation are usually classified using the Siegbahn notation [278], as shown in Fig. 5.7 c). Transitions from higher shells to the K-shell are denoted with a K, transitions to the L-shell with an L, et cetera. This is followed by an index of a lowercase Greek letter and a number, both given in descending order of peak intensity, e.g. $K_{\alpha 1}$. While this nomenclature is still extremely common due to its brevity, it has some drawbacks: the denomination is based on phenomenology, i.e. the measured intensity of the peaks, and not e.g. the energy or the electron subshells involved. This should not be seen as an error of M. Siegbahn or his colleagues, though, since the details of electronic structure were simply not yet known back then.

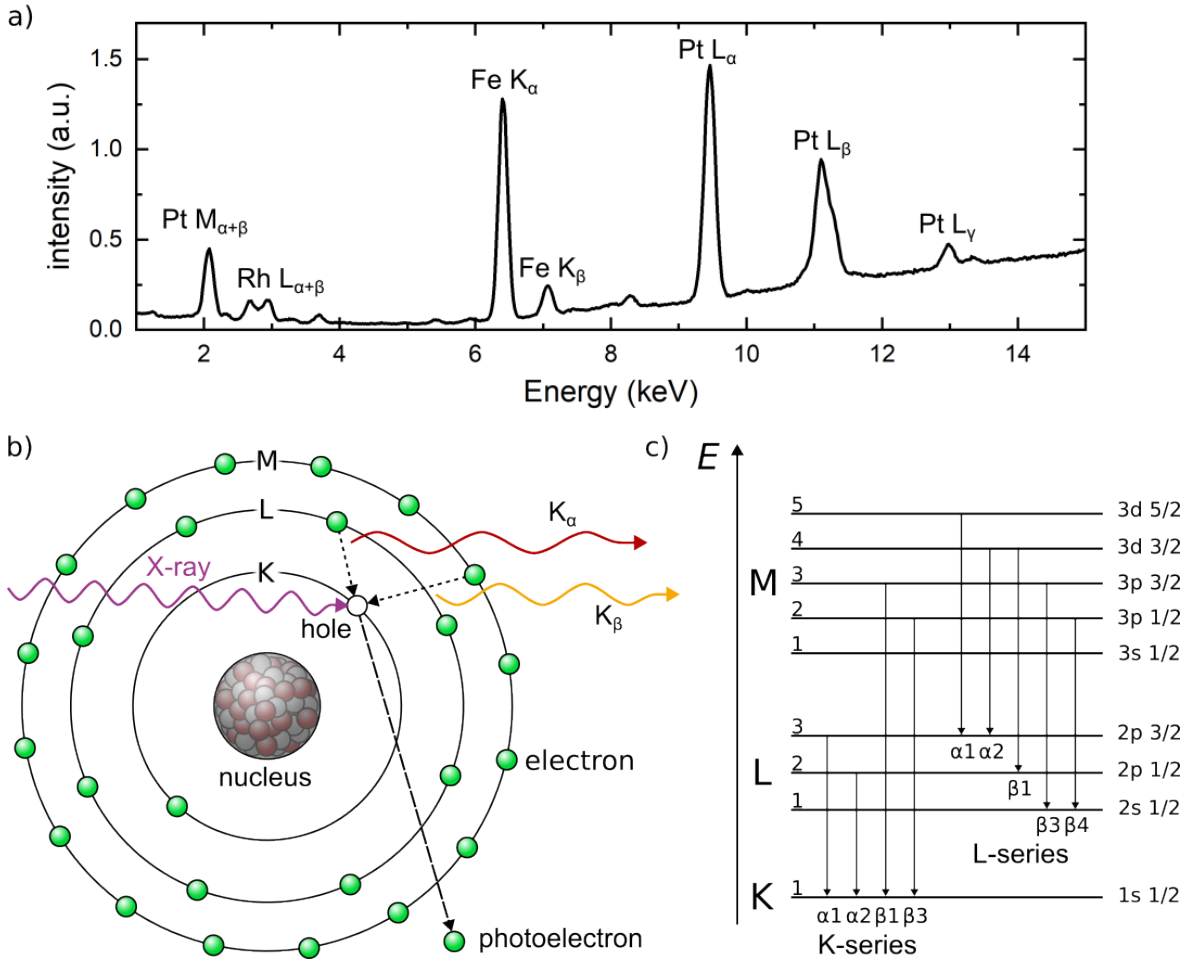

Figure 5.7: a) Exemplary EDX measurement of an FePt sample. The positions of the peaks can be positively assigned to distinct transitions in the elements. b) Origin of the characteristic X-rays used in EDX: an incoming X-ray knocks an electron out of an inner shell, which is subsequently replaced by another electron dropping down from an energetically higher shell. c) Electron transitions and the Siegbahn notation of the resulting X-radiation in EDX.

In 1991, the *International Union of Pure and Applied Chemistry* (IUPAC) has introduced its own notation of X-ray denomination [279]. It consists of the names of the shell of the hole (bottom shell) and the shell of the electron filling the hole (top shell), so the $K_{\alpha 1}$ transition becomes K-L_3. However, this more logical notation has not yet replaced the Siegbahn notation, possibly because of the longer names it provides. Accordingly, the more common and familiar Siegbahn notation will be used throughout this work.

Because the energy of the X-rays can be attributed to individual elements, evaluation of the X-ray spectrum immediately can confirm the presence of certain elements. Further, with a proper fitting software, the integrated peak intensities can be transformed into a quantitative value for the areal density of a given element, allowing to calculate compositions and also thicknesses of individual layers. However, the quality of this information is dependent on the quality of background and peak fitting, which often can not be controlled. As a result, the accuracy of composition is 1 at.% at best. Special care needs to be taken when characteristic X-ray energies overlap, since the deconvolution of the peaks is essential for a reliable fitting result.

In this work, an *EDX-720-P* by *Shimadzu* with a Rh-tube was used to determine the composition for selected samples. The evaluation was done by the software *PCEDX* distributed with the instrument. An exemplary measurement of an FePt film can be seen in Fig. 5.7 a).

5.5 Electron microscopy

Similar to optical microscopy using visible light, electron microscopy can be used to look at the surface morphology of a sample in strong magnification. However, the lateral resolution of optical microscopy is limited to about 200 nm, mostly due to the lower limit of wavelength of visible photons. Electrons, on the other hand, can easily have much smaller wavelengths, depending on their kinetic energy. This enables much better resolutions, as can be seen by Abbe's diffraction limit [280, 281]:

$$d = \frac{\lambda}{2n \sin \alpha} \tag{5.14}$$

with d : resolution, or minimal distance between two points that can be resolved
λ : photon/electron wavelength
n : refractive index of the medium through which the observation takes place
α : angular aperture of the objective

As an example, electrons with a kinetic energy of 30 keV have a wavelength of only about 7 picometers, with higher acceleration voltages resulting in even shorter wavelengths. Additionally, many element-specific types of measurement can be accessed through observing electron transitions within the sample atoms via the corresponding X-radiation.

However, one cannot use regular lenses for electron microscopy, since these would simply block the electron beam. Instead, electromagnetic lenses and apertures have

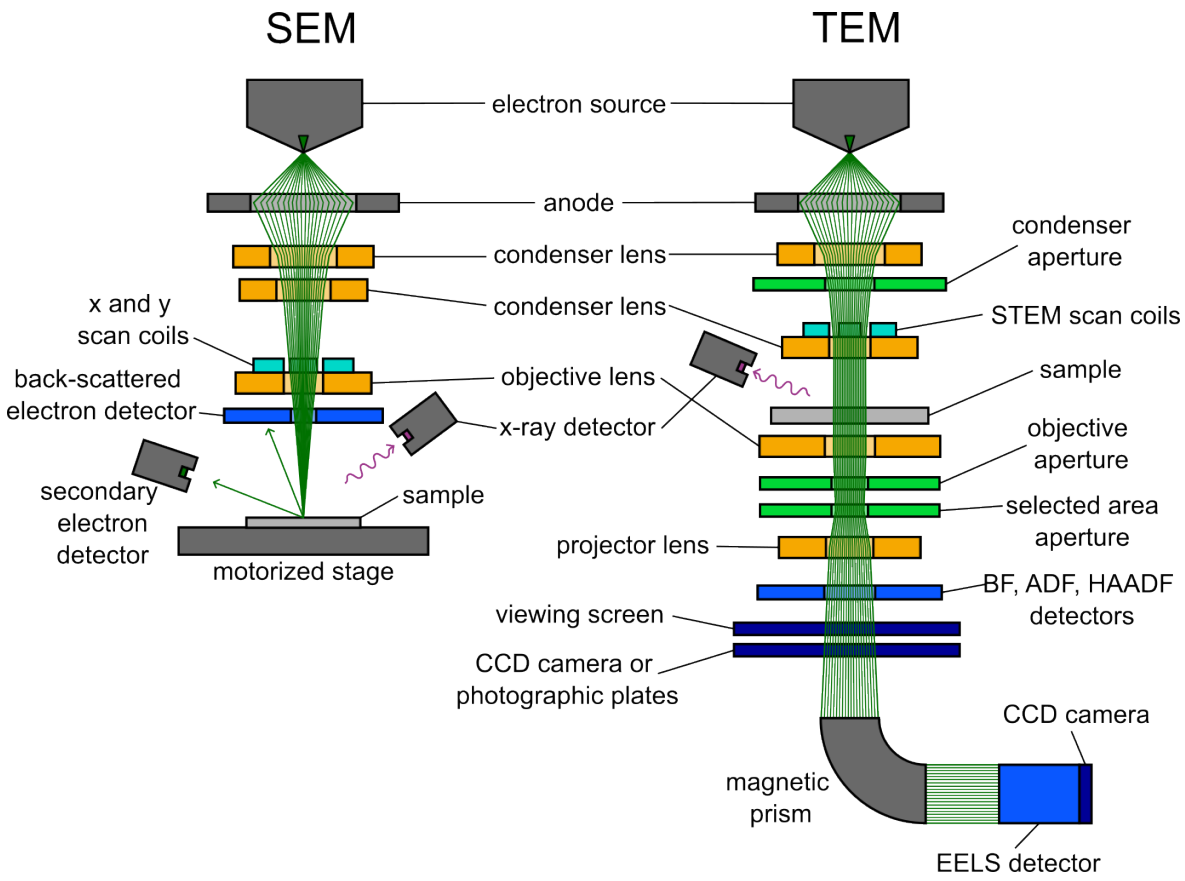

Figure 5.8: Schematic build-up of the two main types of electron microscopes. Left: the scanning electron microscope (SEM). Right: the transmission electron microscope (TEM). Both types share common features that are essential for electron microscopy, such as the electron source and focussing lenses.

to be utilized. These are more difficult to produce and adjust, which, along with the need for other electronics like electron gun and detector, makes the technique a quite expensive one. Further, aberrations and lower numeric apertures have a much higher influence on the resolution, so the actually attainable resolution is about one and a half orders of magnitude higher than the wavelength used. Still, electron microscopy opens up a plethora of investigation techniques that otherwise are inaccessible. Among those, scanning and transmission electron microscopy are the most versatile.

5.5.1 Scanning electron microscopy (SEM)

Scanning electron microscopy is a versatile imaging technique for investigating sample surfaces. The general setup can be seen in Fig. 5.8. The electron beam is scanned point by point over the whole investigated sample area and different types of electrons or X-rays are gathered, which carry information about the measured point. The most common measuring techniques include:

Backscattered electrons (BSE): When the high-energy electrons hit the atomic nuclei in the sample, they can be elastically scattered back at high angles between

90° and 180°. The amount of backscattered electrons depends very much on the mass of the nucleus, since heavier and larger atoms not only have a higher scattering cross section, but also cause the electron to maintain more kinetic energy. Accordingly, BSE can be used as an element-specific measuring technique as long as the topological contrast can be neglected, i.e. for flat surfaces. Due to the high energy of the electrons, they can escape from a big volume within the sample when compared to the spot size of the electron beam, which reduces the resolution.

Secondary Electrons (SE): Secondary electrons are emitted by inelastic scattering events of primary electrons from the electron beam in the sample. The primary electron transfers energy to an electron in the higher atomic shells in the sample, either directly or via the Auger-Meitner-effect. This electron can overcome the work function and leave the atom if the transferred energy is high enough. Secondary electrons have rather low energies (< 50 eV) and thus can only escape from a small volume near the surface, making this technique the most precise, with a resolution of 1-10 nm. Because of the dependence of SE emission on tilt angle, enhanced emission at edges, and the shadow contrast, SE images can be understood quite intuitively, similar to regular photographs.

Energy-dispersive X-ray spectroscopy (EDX): When an electron gets knocked out of an inner shell by a primary electron, characteristic X-radiation is emitted when a higher-shell electron drops to the now empty place. This radiation can be detected in an SEM to get insight about the quantitative composition of the sample. However, this method has the lowest resolution of around 1 µm, since X-rays can escape from comparatively large volumes.

5.5.2 Transmission electron microscopy (TEM)

Instead of measuring the electrons reflected from a sample, one can also measure electrons transmitted through it, which is done in transmission electron microscopy **??**. The technique requires a sample thickness no higher than 200 nm, since thicker samples would attenuate the intensity of the electron beam too much. Also, the electron energies are higher than in SEM, since the penetration depth of faster electrons is much higher, increasing the transmission rate. The acceleration voltage in modern TEM microscopes can reach up to 300 kV.

The setup is also quite complex, using multiple different lenses and apertures at different points in the beam path. Different detection systems, also situated at specific locations, offer a wide range of investigation methods, such as:

Bright field (BF): This standard method of imaging uses an object aperture to filter out elastically or inelastically scattered electrons, so only unscattered electrons are measured. Thus, areas with higher scattering rates reduce the amount of transmitted electrons and show a darker contrast next to a bright background. Increased scattering can be observed for areas with larger thickness, higher density, higher atomic mass, as well as at dislocations or grain boundaries.

Dark field (DF): Similar to the BF mode, but it uses the aperture to select only electrons scattered at a certain angle. Consequently, areas with a high scattering at this angle are bright in this mode.

High angle annular dark field (HAADF): Like DF, but the detector is set to very high angles. The contrast thus strongly depends on the atomic number of the scattering elements.

Scanning transmission electron microscopy (STEM): The electron beam is focused on the sample and scanned line after line. The focussing increases the resolution, so STEM is a more precise investigation technique than regular TEM imaging. However, the precision comes at a price: the long scanning process means that a whole image can take multiple minutes to create. This requires the sample to not drift, which can happen easily e.g. with insulating substrates where charge accumulates over time. Accordingly, drift correction must be good, otherwise a skewed image will be the result.

Energy-dispersive X-ray spectroscopy (EDX): Since the high-energy electron beam easily excites the atoms it passes through, characteristic X-radiation is emitted from the area under the beam. By subtracting the background signal of Bremsstrahlung and analysing the characteristic peaks, a qualitative composition can be obtained. In combination with STEM, a map of elemental composition with a much higher resolution than in SEM can be created. Problems with this technique mainly concern the overlap of signals from different elements due to similar characteristic X-ray energies, e.g. Fe-$K_{\alpha 1}$ with 6.4 keV and Tb-$L_{\alpha 1}$ with 6.27 keV. In such cases, the EDX spectrum can not be reliably fitted and no information on composition can be obtained.

High-resolution TEM (HR-TEM): Using the diffraction patterns of high-resolution images, precise atomic positions can be reconstructed in this method. This requires ultrathin samples of less than 15 nm thickness.

Electron energy loss spectroscopy (EELS): When being scattered on atomic nuclei, electrons often lose energy in an inelastic scattering process. The amount of energy lost is proportional to the atomic mass of the scattering atom. In EELS measurements, the transmitted electrons are sent through a magnetic prism after passing through the sample. Here, the electrons are deflected according to their energy. By analysing the energy loss distribution of the transmitted electron beam, a relative elemental composition can be obtained. Similar to EDX, this method is often used in combination with STEM for high spatial resolution. Contrary to EDX, there is no overlap of signals from different elements, since only the atomic mass determines the amount of energy lost. This makes EELS suitable for detecting even very small amounts of dopants. However, the measurement window of investigated energies is limited, so very light and very heavy elements cannot be detected in the same measurement run.

Electron diffraction: Since electrons also behave like waves, they can also be used to observe diffraction phenomena. Similar to XRD, the resulting diffraction image from elastically scattered electrons gives insight into the structural characteristics

of the sample. As an alternative, a Fourier transform of a regular TEM image can also be used to obtain similar information.

CHAPTER 6

Grain boundary diffusion of Tb and Gd in $L1_0$ FePt

Grain boundary diffusion (GBD) is a technique that is used to increase magnetic hardness in permanent magnets with the intention of reducing the amount of (heavy) rare-earth ((H)RE) elements used. Commonly used super-magnets like $Nd_2Fe_{14}B$ or $SmCo_5$ are doped with rare-earth elements like Nd, Tb, Dy, or Pr in order to increase the maximum energy product ($(BH)_{\max}$) or their coercivity H_C at elevated temperatures [282–285]. Since there is a lot of heat generated in electric motors and generators, which is one of the main areas of use for these magnetic alloys, the improvement of elevated-temperature performance greatly increases the efficiency of these devices.

However, the world market situation of rare-earth elements is a precarious one. China controls the largest reserves of rare-earth elements and is the biggest producer and supplier of rare-earth ores and technologies like permanent magnets. This can quickly give rise to international conflict of interests, such as the *rare earths trade dispute* between 2010 and 2015, where China's reduction of rare-earth exports resulted in a lawsuit filed with the World Trade Organization by many other countries [286]. The production is also often coupled to bad working conditions and the accumulation of large amounts of waste, containing high amounts of poisonous heavy metals and the radioactive elements Th and U.

Over the last decade, the production in some "western" countries was increased manifold to counter this market imbalance, the biggest producers being the USA and Australia. For most other countries, even those possessing a larger deposit of rare-earth ores, the production is still not economically viable. Thus, the situation is motivating researchers to find more resource-conserving methods of creating and enhancing super-magnets, GBD being one of them [121].

GBD is an approach that highlights the importance of grain boundaries in a polycrystalline sample for its magnetic behaviour. Grains that are effectively magnetically isolated from each other cannot easily influence neighbouring grains [45]. This inhibits domain wall propagation, which is the most dominant manner of magnetic reversal in most magnetic samples. Additionally, nucleation points of magnetic reversal, which are most commonly found in very small grains or at corners of bigger grains, can be effectively antiparallelly exchange-coupled to the grain boundary material as in a superferrimagnetic structure (compare chapter 2.4, which further helps increase magnetic

hardness. Actually, it was found that the grain boundary phase not only helps with decoupling the grains, but also drives a diffusion-depth-dependent formation of core-shell particles [287–289]. The shell consists of a highly doped version of the host material, which has nearly the same effect as doping the whole magnet. This shows that GBD circumvents the necessity of doping the bulk of the sample by instead using the costly HRE elements mostly in the grain boundaries, thereby greatly reducing the amount of HRE needed.

The RE elements most frequently used for GBD are Tb and Dy, since they show the highest effect of increasing the anisotropy [121, 216]. Here, the lower RE content is also beneficial since both Tb and Dy reduce the magnetization of the host magnet, so a lower content means higher $(BH)_{\max}$. Even though Tb is the better element in this regard, Dy is still used more often due to being half as expensive [288, 290]. Of course, it would still be preferrable to not use any rare-earth elements at all, or at least rely only on those that are abundant. Research in this direction is done mostly with Al, Cu, La, and Ce as additives [291–294]. However, the improvements in $(BH)_{\max}$ and H_{C} have usually been quite low when compared to GBD with HREs and also most often accompanied with a loss in M_{S} [291]. Often, a compromise is sought for by combining abundant materials with rare-earths [295–297].

For starting a GBD process, a layer of the HRE element is firstly deposited on top of the magnetic layer. The amount is comparatively very small: on bulk samples of some millimetres thickness, the Tb layer is only a few µm thick [298]. The sample is then heated to the desired temperature, possibly under inert atmosphere or vacuum to prevent oxidation. The thermal energy allows the HRE to diffuse into the sample, where it chooses the path of least resistance, which is along the grain boundaries. There it can react with the surface of the grains and with the grain boundary phase itself, ideally creating a magnetically hard shell in the grain and intergranular area outside of it. The degree of change and HRE incorporation is dependent on its concentration at a given depth. The diffusion of the HRE atoms can be described by Fick's laws of diffusion [299]. However, the diffusion coefficient D depends strongly on the temperature and the environment of the diffusion, so results can often only be modelled in retrospect and rarely simulated beforehand.

It has been shown that magnetic reversal of $L1_0$ FePt nanodots first starts at the edges [300]. The same can be assumed to hold true for unpatterned $L1_0$ FePt grains, since the surface of small FePt grains is usually disordered and soft, and can also be strongly influenced by a matrix material [301]. Consequently, if the surface of the grain could be magnetically hardened, the whole grain would exhibit a higher resistance against a reversal of magnetization, i.e. a higher H_{C}. This could be achieved by using Tb , since TbFe alloys can show immense coercivity and PMA values, depending on the composition [34, 240, 242]. If such an alloy formed at the surface of a FePt grain, the grain would be exchange-coupled to the TbFe alloy on all sides. This coupling would be strongest at the grain surface, which was previously the point most likely for a reversed magnetic domain to nucleate. This effective shell could prevent domain walls from entering the grain. Instead, the reversal mechanism within the grain could be

more like a coherent rotation of magnetization as described by the Stoner-Wohlfarth-model.

Assuming that the intermixing of Tb and Fe is only marginal, the intergranular region would mostly consist of Tb or a Tb-dominated TbFe alloy. In this case, the intergranular material would still be coupled antiferromagnetically to the FePt grains, thus creating a superferrimagnet. This term denominates a magnet that consists of two antiparallelly coupled elements, just like any other regular ferrimagnet, and also has a high H_C, but has the high magnetization of a ferromagnet. Such a magnet could replace NdFeB and SmCo as the dominant permanent magnets, provided it has a high enough PMA, magnetization, and Curie temperature [159]. $L1_0$ FePt, however, will never be used in bulk due to the high cost of Pt, and instead be limited to thin film usage.

One can compare the GBD technique with that used for producing HAMR media: both ideally achieve a decoupling of grains by inserting another compound into the intergranular space. However, while co-deposition works for the separating matrix in HAMR media, such as C or *h*-BN, this is not possible for rare-earths. The HAMR media matrix compound is not soluble in the FePt alloy and is thus expelled from the grains, but the RE elements, if sputtered alongside Fe and Pt, would be incorporated into the FePt mixture and disrupt the formation of the $L1_0$ structure due to their big size [302]. Thus, in order to keep the RE element between the grains, the GBD technique could be advantageous.

The FePt films deposited in the frame of this work are not polycrystalline, but rather consist of partially conjoined islands with the same lattice orientation. Hence, there are no real grain boundaries for RE elements to diffuse into. However, the film thickness is low enough that the FePt islands are still mostly disconnected, leaving space in between them. These pits or trenches between neighbouring islands can easily be filled by a subsequently deposited layer, and also antiphase boundaries or dislocation lines could be weak spots for the RE to diffuse into.

6.1 Sample preparation

The $L1_0$ FePt thin film samples investigated here were deposited on polished MgO(001) substrates using DC magnetron sputter co-deposition of elemental Fe and Pt targets at an Ar pressure of 5 µbar and at a nominal deposition temperature of 800 °C, which roughly corresponds to a substrate temperature of 610 - 650 °C. A slightly increased Fe content of ca. 51 at.% was chosen to counterbalance the higher resputtering effect of Fe. After the deposition of the FePt layer, the samples were allowed to cool down to room temperature before depositing the rare-earth layer, also at 5 µbar Ar pressure. Some samples were left without the rare-earth layer in order to serve as a reference. Lastly, a Si_3N_4 capping layer of 5 nm thickness was deposited on all samples using RF sputtering at 1.5 µbar pressure, in an atmosphere of 96 % Ar and 4 % N_2.

The layer stack is thus: MgO(sub.)/FePt(t_{FePt})/RE(t_{RE})/Si_3N_4(5 nm). The set of samples deposited is summarized in table 6.1, comprising one series with added Tb

and one with added Gd. These will be called the Tb-series and Gd-series for short from here on.

Table 6.1: Overview of the investigated FePt-samples. Listed are the nominal thicknesses of the $Fe_{51}Pt_{49}$ (t_{FePt}) and rare-earth layers (t_{RE}).

sample name	t_{FePt}	t_{RE}	short name
B210419	20 nm	10 nm (Tb)	20nm+Tb
B210420	20 nm	-	20nm
B210421	30 nm	-	30nm
B210428	30 nm	10 nm (Tb)	30nm+Tb
B220608_1	20 nm	10 nm (Gd)	20nm+Gd
B220608_2	20 nm	-	20nm noGd

For the post-annealing step, the samples were transferred into a *Carbolite* tube oven as described in chapter 4.2. The gas used for post-annealing was forming gas with 10 % H_2 content.

6.2 Annealing temperature series with Tb

For the first series of measurements, we took one sample piece of each sample of the Tb series and consequently annealed them ex-situ at increasing temperatures. After each post-annealing step, the magnetic properties of the sample pieces were measured in the SQUID-VSM and the structural changes observed by XRD.

All sample pieces were put into the ceramic sample holder of the tube oven together. This ensured that all sample pieces experienced the exact same heat treatment and that the only differences between them are inherent from the start.

First, the magnetic and structural properties of the as-prepared samples of the Tb-series shall be investigated. Please note that in the following, when multiple measurements of the four sample pieces of this series are compared, the arrangement will always be kept the same: top left shows the 20nm sample, top right the 30nm sample, bottom left the 20nm+Tb sample, bottom right the 30nm+Tb sample.

The X-ray diffractograms of the Tb-series can be seen in Fig. 6.1. The measurements are dominated by the diffraction peaks belonging to the MgO substrate (highlighted by blue lines), which can be easily identified by their low full width at half maximum (FWHM). Since no monochromator was available for these measurements, there are multiple MgO-related peaks visible in the diffractograms, caused by additional Cu-K_β and W-L_α radiation present in the experiment. These are situated at slightly lower angles due to the shorter wavelength of the X-rays and have a lower intensity.

All samples display strong $L1_0$ ordering, as can be seen from the existence and intensity of the (001) and (002) diffraction peaks. These peaks are sharp and intense enough that the peaks caused by the Cu-K_β radiation are visible on the left of the respective peaks. In the case of the (002)-peaks, however, these additional peaks are overshadowed by the shoulder of the MgO (002) peak, making them harder to observe.

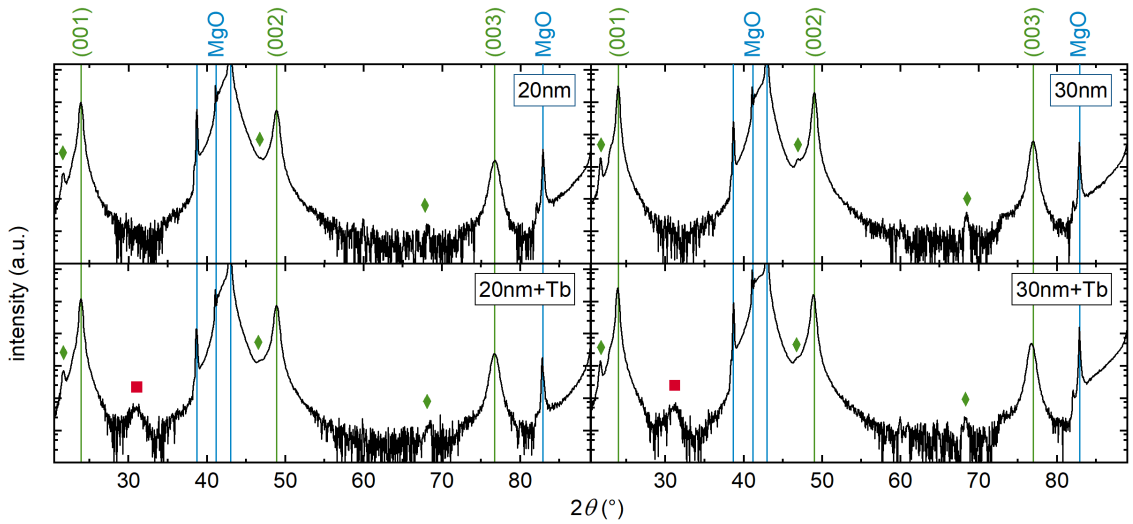

Figure 6.1: The $\theta-2\theta$ X-ray diffractograms of the four samples of the Tb series of FePt-samples. The top row shows the two samples without Tb, the bottom one the Tb-containing samples. The blue lines highlight the position of peaks originating from the MgO substrate, while the green lines highlight the expected (00l) peaks of $L1_0$ FePt. Small peaks from the $L1_0$ FePt layer caused by additional Cu-K$_\beta$ radiation are highlighted by green diamonds. All samples show a good $L1_0$ structure. The samples containing the Tb-layer additionally show a peak at 31°, highlighted by the red squares, belonging to the (002) diffraction peak of Tb.

While the Tb layer is assumed to be either polycrystalline or mostly amorphous, there seems to be a very slight alignment of the crystallites in the (001) direction, as is evidenced by the presence of the Tb (002) peak of hexagonal Tb at 31° (red squares in Fig. 6.1).

Figure 6.2 shows the M-H hysteresis loops of the four sample pieces investigated in this series in the as-prepared state. As can be seen, the samples are not identical in their magnetic properties. The 20nm+Tb sample shows a much increased H_C and a broader switching field distribution, while for the 30nm sample, the saturation magnetization is notably increased.

The former fact can be quite easily explained: since all samples were deposited in their own separate deposition runs, small differences in deposition conditions can lead to a variation in microstructure, most importantly a difference in granularity. The fact that the thinner FePt layers have a higher H_C can thus be explained by the island-like growth mode of FePt on MgO substrates at elevated temperatures. The islands start growing from individual nucleation centers and grow with further deposition. Once they become large enough, they start touching neighbouring islands and merge with them. This happens mostly between 10 and 20 nm film thickness, still leaving some separation between coalesced grains at a thickness of 20 nm. At a thickness of 30 nm, virtually all of the islands have grown together and the film can be considered mostly continuous.

As the separation of grains impedes domain wall motion during magnetic reversal, the thinner layers show a higher resistance to domain wall propagation and consequently a

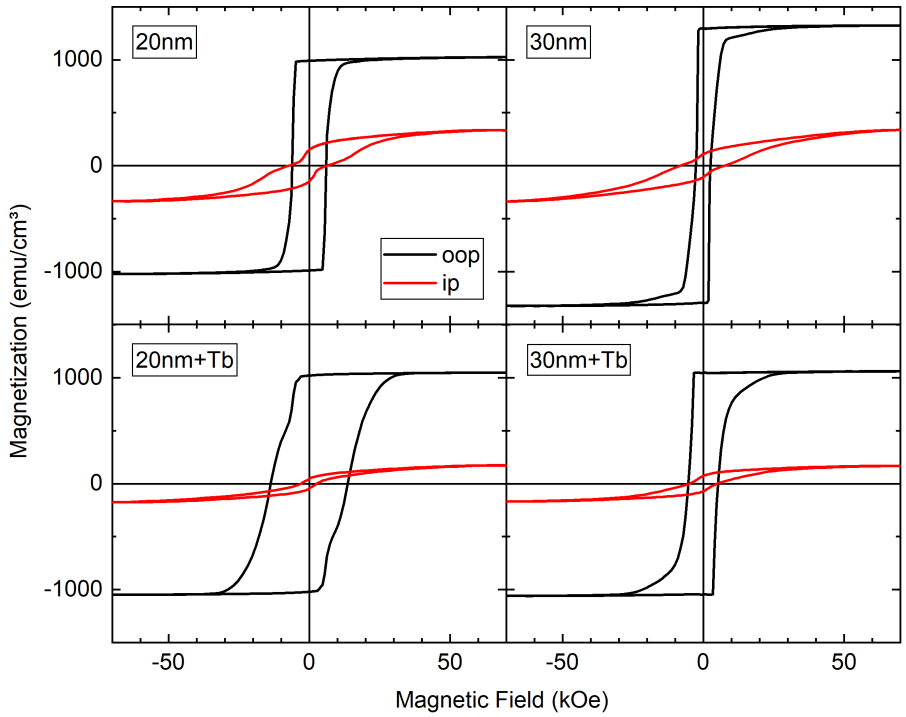

Figure 6.2: Comparison of the as-prepared out-of-plane (oop) and in-plane (ip) hysteresis loops of the Tb series, with the Tb-containing samples shown in the lower row. The high magnetization of the 30nm sample is puzzling and likely a measurement error, as discussed below. The in-plane loops are not saturated at the maximum field of 70 kOe, so their true slope can not be determined.

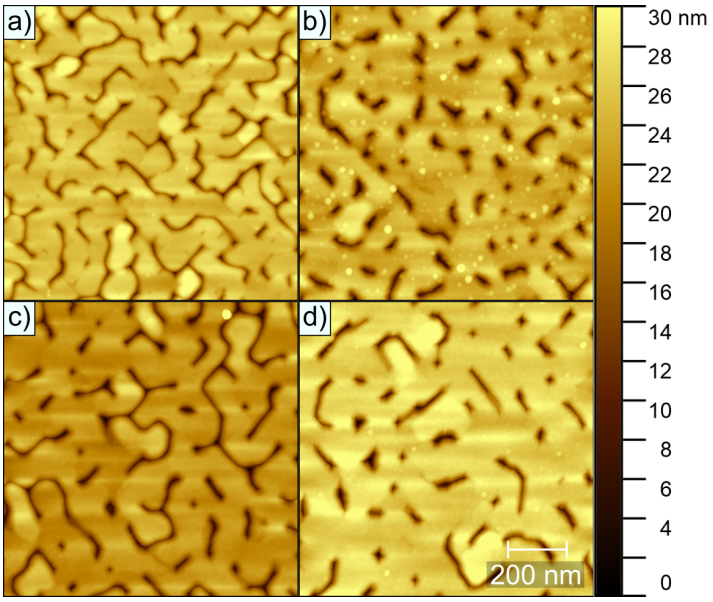

Figure 6.3: The AFM measurements showing the surface topology of the a) 20nm, b) 30nm, c) 20nm+Tb, and d) 30nm+Tb samples. The scale bar is valid for all four images.

higher H_C. On the other hand, the continuous nature of the FePt films with a thickness of 30 nm enables the easy propagation of domain walls throughout the whole film.

This explanation of the difference in H_C can be backed up by atomic force microscopy images as shown in Fig. 6.3. The difference in morphology between the 20 nm thick films on the left and the 30 nm thick films on the right is obvious: the trenches between the grains are all but disappeared for the thicker films, but still clearly visible and present for the thinner ones.

It also seems like the samples with an added Tb layer show an increased coercivity compared to the films of the same thickness without the Tb layer. However, it seems improbable that a Tb layer deposited at room temperature would lead to such an increase of grain separation, since Tb itself is not a hard magnet at room temperature and no noteworthy intermixing of Tb into the FePt alloy is expected. Instead, a difference in microstructure is more likely to be the reason for the observed differences.

A feature that can not easily be explained is the increased magnetization of the 30nm sample. While the other three samples show an M_S of around 1050 emu/cm^3, this one is increased by almost 30 % to around 1320 emu/cm^3. It was controlled multiple times that the correct sample volume was used for the calculation of magnetization. As a consequence, the increased magnetization is assumed to be a result of a measurement error in the SQUID-VSM.

In general, the magnetization of the thin films is lower than the value of bulk $L1_0$ FePt given in the literature, 1140 emu/cm^3 [2]. This is likely caused by an overestimation of the film volume, since the surface region of the FePt grains is likely not contributing fully to the magnetization due to being amorphous [301]. The reduced magnetization is the same for all samples, so an offset in deposition rates compared to the nominal ones could explain this offset, since the same rates were used for all samples.

The in-plane measurements (red lines in Fig. 6.2) generally look very similar because they cannot be saturated due to the strong PMA of the $L1_0$ FePt system. As a result, the slope and thus the magnetization at maximum fields cannot be determined, instead displaying a seemingly low value due to background subtraction. Interestingly, the samples without Tb show bigger loop openings for the ip measurements, suggesting that some grains are harder to switch in the in-plane direction. If the system had perfect PMA, one would assume these loops to have no opening at all, due to the in-plane direction being the hard axis. The existence of these openings tell us that not all grains are perfectly aligned with the (001) direction pointing out of the sample plane.

This seems to be the case to a bigger extent in the samples without the Tb layer, which on the one hand would explain the lower coercivity in the oop direction, but on the other hand suggest a reduced oop remanent magnetization. However, the reduction is usually negligible if the tilt angle is small enough. A tilt of 10 °, for example, would result in an ip remanence of 17 % of the total M_R, while the oop remanence would only be decreased by about 1.5 %. The tilting of anisotropy axes among the FePt grains is thus sufficient to describe the opening of the ip hysteresis loops.

Now that the samples have been analyzed before the post-annealing procedure, the results of it can be discussed. As already outlined at the beginning of this chapter, the treatment of the samples in the annealing temperature series consisted of heating the samples to the desired temperature in an atmosphere of forming gas for the duration of 1 hour, then measuring the magnetic and structural properties. This was repeated with the same sample pieces for increasing temperatures up to 850 °C . Accordingly, all sample pieces have experienced multiple heating treatments at the end of the series of measurements.

Figure 6.4 shows the evolution of the X-ray diffractograms of the Tb-series upon consequent annealing at increasing temperatures. As can be seen, there is next to no change observable for the two samples without Tb-layer.

Since no monochromator was available for these measurements, there are other wavelengths present in the X-ray beam during measurement next to the desired Cu-K_α, most prominently Cu-K_β and W-L_α. These lead to the additional peaks to the left of larger peaks, such as the leftmost highlighted peak of MgO or the small peaks visible to the left of the (003)-peak of $L1_0$ FePt. The small sharp peak observable at 27 °, visible for all heat-treated samples, can be assumed to result from the substrate due to its sharp profile. Later measurements performed with monochromator do not show the peak, so it is most likely caused by impurities in the X-ray tube.

The Tb-containing samples additionally show peaks at 29 ° up until the last annealing step, highlighted by red squares in Fig. 6.4. This is again caused by the Tb layer, this time being the (100) peak. The first post-annealing step at 400 °C was seemingly sufficient to enable a reconfiguration of the partially crystalline Tb layer. This slight Tb alignment stays stable up until the last heating run at 850 °C, where three peaks at 20.4 °, 30.8 ° and 52.6 ° appear (orange diamonds in Fig. 6.4). These can be attributed to Tb_2O_3, suggesting that oxidation of the Tb layer was taking place during the heating process.

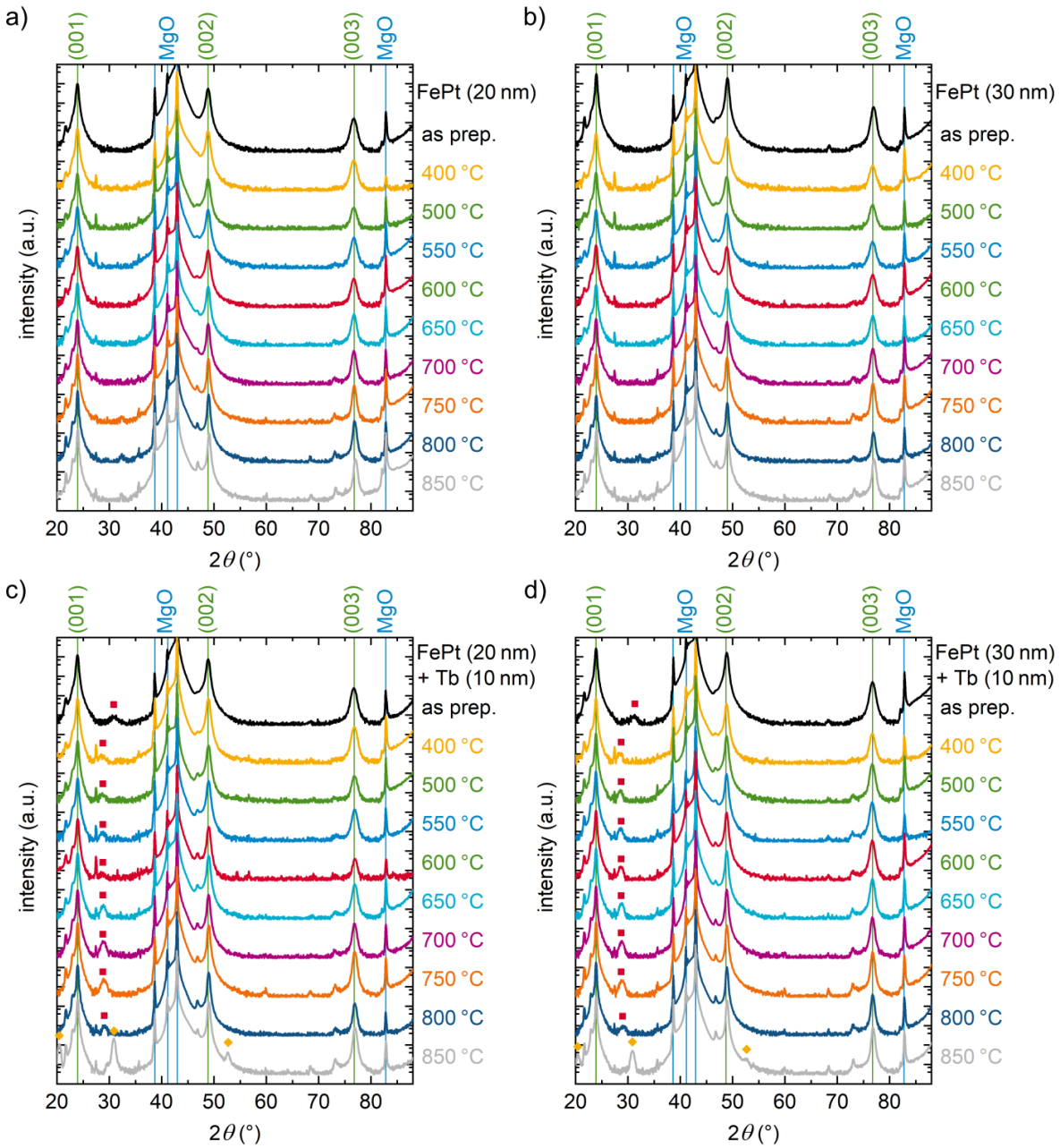

Figure 6.4: X-ray diffractograms of the a) 20nm, b) 30nm, c) 20nm+Tb, and d) 30nm+Tb samples. Blue lines highlight the positions of reflection peaks originating from the MgO substrate, green lines highlight the position of (00l) reflection peaks of the $L1_0$ FePt phase. Reflection peaks caused by Tb (red squares) and Tb_2O_3 (orange diamonds) are also highlighted.

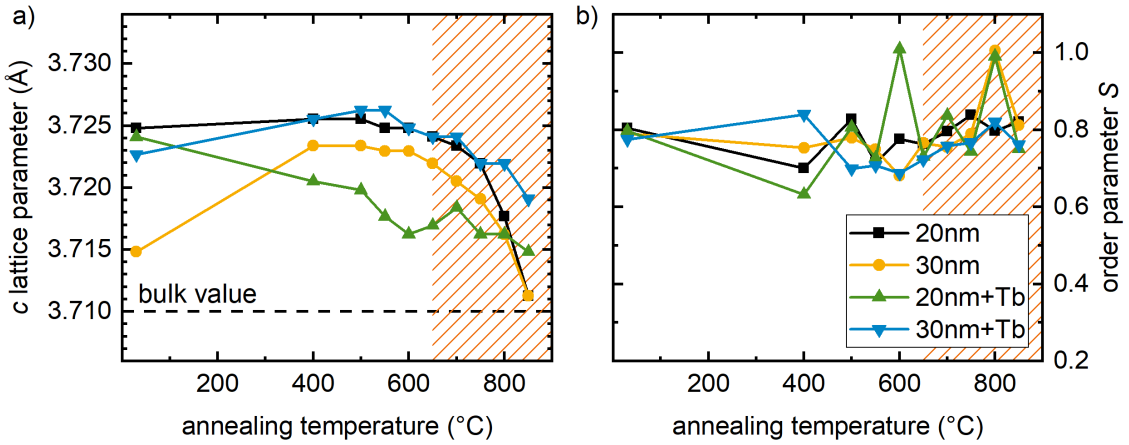

Figure 6.5: The evolution of a) the c lattice parameter and b) the order parameter S of the different FePt sample pieces after post-annealing at increasingly higher temperatures. The shaded area highlights the temperature range above the deposition temperature. The legend is valid for both diagrams.

The position of the (00l) reflection peaks of the $L1_0$ FePt layer can now be used to calculate the c lattice parameter and consequently observe its change with each post-annealing step. Further, the (001) and (002) reflection peaks can be integrated and their integrated intensity ratios compared to an ideal value to receive the order parameter S. The results are shown in Fig. 6.5 a) and b), respectively. For all samples, the c lattice parameter is larger than the bulk value. This is somewhat surprising, since the tensile in-plane stress would suggest a increase in the basal lattice parameter a, which could be compensated by a *decrease* in c.

This only happens with further heating, as the unit cell is generally contracting along the c lattice direction with further annealing. The only exceptions are the beginning phases of both 30 nm thick layers, which first show an increase of c. The approach towards the bulk value of c is expected, as stress and deformations caused by the lattice mismatch can be relieved by introducing more thermal energy to the crystal lattice for prolonged time. The reduction of c in the samples without Tb is generally stronger for higher annealing temperatures, while this effect is somewhat reduced in the samples with Tb. The effect of higher temperatures on the samples without Tb seems stronger, as the decrease of c above 700 °C is notably stronger than below for these samples.

The order parameter S varies slightly with temperature, but generally stays near a value of 0.8. The error bar here is hard to estimate, as the uncertainty of the fit and integration is given with only about 5 %. However, there is no reason to assume that the order parameter should drop remarkably by the cause of post-annealing, as is the case for most samples at the first step at 400 °C. Further, there are three points with an order parameter above 1, which is of course not possible. This leads to the conclusion that the uncertainty of the graph in Fig. 6.5 is at least 10 %. With this assumption, the order parameter can be seen as very slightly increasing with annealing temperature. This behaviour can easily be explained by the increased energy available to the system

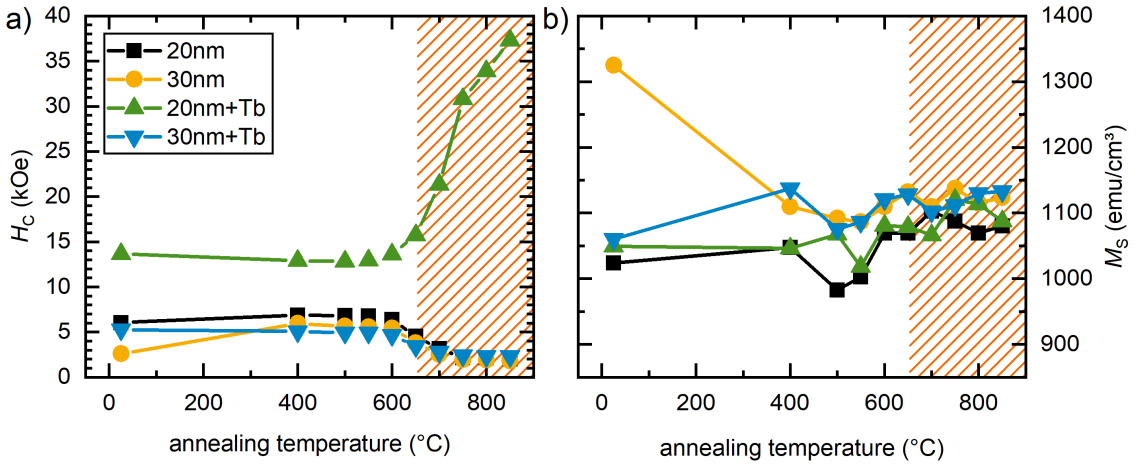

Figure 6.6: a) The change of coercivity of the FePt samples over the course of the post-annealing treatment. A clear increase is seen for the 20 nm thick FePt film with added Tb film. b) The change of magnetization of the same samples. The shaded area highlights the temperature range above the deposition temperature. As mentioned in the text, the high starting value for the 30 nm thick FePt film is likely a measuring error.

for the energy-intensive process of atomic diffusion that is needed for an increase of the order parameter.

Since all samples show the same qualitative behaviour in their structural change, it can be concluded that the addition of the Tb layer has no exceptional influence on the structure of the $L1_0$ FePt layers. Even if some Tb was incorporated in the surface regions of the $L1_0$ FePt grains, no extraordinary change of the lattice parameters is observed as a result of this.

Since a display of all the M-H hysteresis loops measured in this series would take up too much space, only the relevant values of H_C and M_S and the loops taken after the final post-annealing step will be displayed.

The change of H_C with annealing temperature is displayed in Fig. 6.6 a). The trend for the samples without Tb layer is very similar: the coercivity increases slightly after the first post-annealing step at 400 °C, after which it starts dropping again. This drop becomes more pronounced at annealing temperatures above 600 °C, ending at a coercivity values of only 2.0 kOe and 1.8 kOe for the 20 nm and 30 nm thick FePt films, respectively.

The same behaviour is also observable for the 30 nm thick FePt film with added Tb layer. Here, the ultimate H_C is 2.3 kOe, so only about 25 % higher than its counterpart without the Tb layer. In this case, the Tb seems to not have had any substantial magnetic hardening effect on the FePt layer.

In the case of the 20 nm thick FePt layer with Tb (blue graph in Fig. 6.6 a)), the opposite behaviour can be observed. The initial annealing step marginally reduced the coercivity, but starting at 600 °C, it starts increasing notably. The biggest step is observed for an annealing temperature of 750 °C, where H_C increases by 45 % from 21.3 to 30.8 kOe.

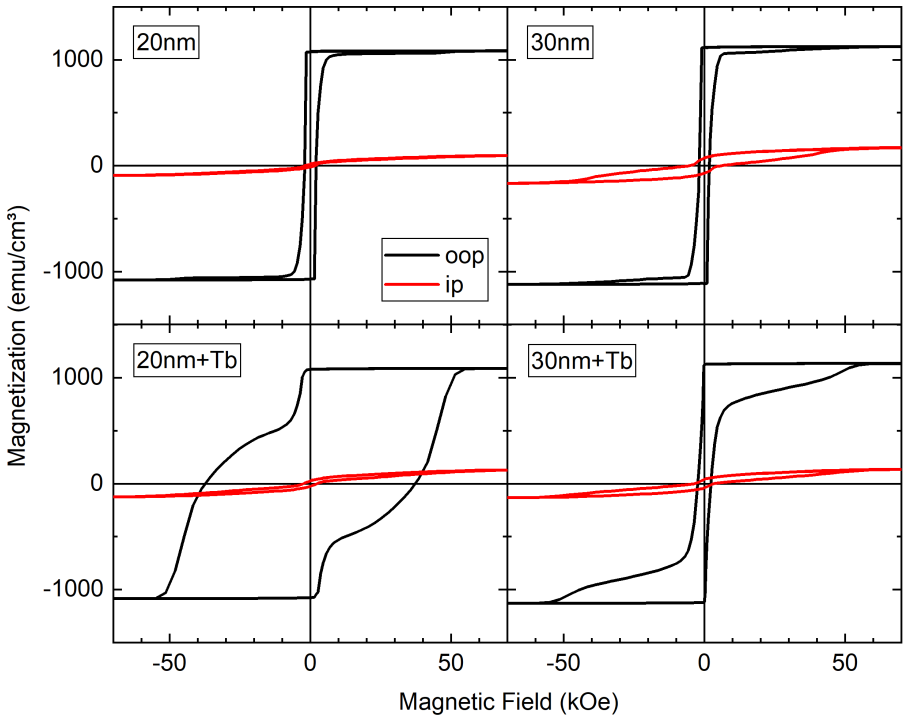

Figure 6.7: *M-H* hysteresis loops for the Tb-series after the last post-annealing step at 850 °C. Both samples without Tb show a narrow loop, while both Tb-containing samples show an extended switching behaviour. The coercivity of the 20nm+Tb sample is strongly increased.

Since this temperature lies above the deposition temperature, it is possible that the FePt layer actually does integrate some of the Tb into its surface regions. The fact that we observed no indication of this in the X-ray diffractograms, however, weakens this hypothesis considerably. Nevertheless, it is possible that the presence of Tb in the intergranular regions of the FePt layer helps to further separate them from each other when the temperature is sufficient.

The M_S values (Fig. 6.6 b)) stay nearly constant for all samples, with only a slight increase with further post-annealing. The only exception is the increased magnetization measured for the 30nm sample in the as-prepared state, which was already argued to likely be a measurement error. The slight increase in M_S could be a result of slightly increased ordering in the $L1_0$ FePt layers.

It is noteworthy that the magnetization of the 20nm+Tb sample has not decreased. This is another indicator that no substantial amount Tb has been incorporated into the $L1_0$ FePt layer, since the antiparallel coupling between Fe and Tb would have resulted in a reduction of M_S. Tb can thus be assumed to be confined to the intergranular regions throughout this whole series of measurements.

A look at the *M-H* hysteresis loops of this series gives more insight into the behaviour of these samples. As can be seen in Fig. 6.7, the hysteresis loops of the samples without Tb (top row) are virtually unchanged when compared to the as-deposited measurements in Fig. 6.2. The only difference is the reduced oop coercivity and reduced opening of

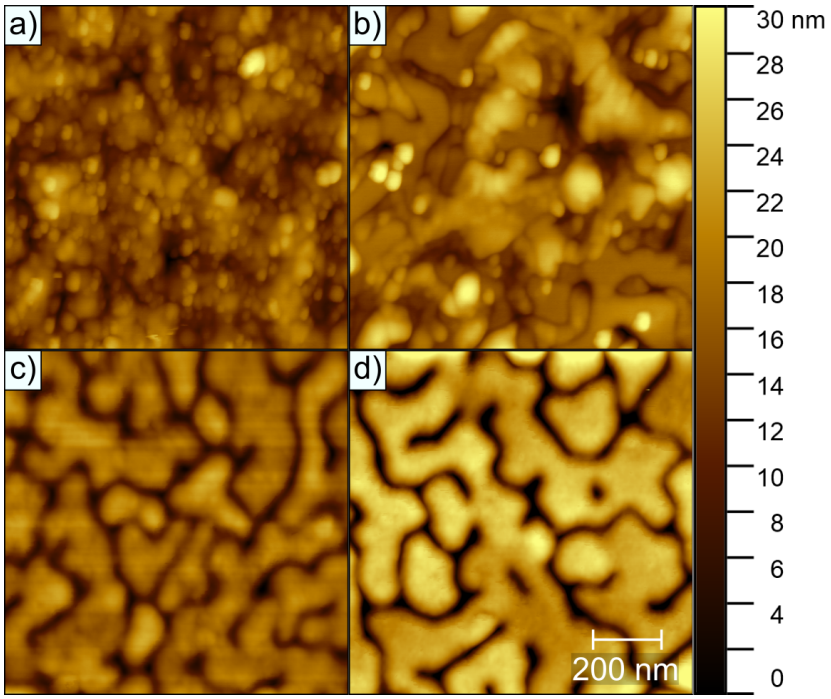

Figure 6.8: The AFM measurements showing the surface topology of the a) 20nm, b) 30nm, c) 20nm+Tb, and d) 30nm+Tb samples after the last post-annealing step at 850 °C. Both samples with Tb show deep trenches between the FePt islands and small, isolated islands in the case of the 20nm+Tb sample, while no individual islands are discernible for the samples without Tb.

the in-plane loops. The latter could be a result of a better ordering of the films in the (001) lattice direction due to relaxation of epitaxial stress during annealing. However, the increased ordering is not helpful for increasing H_C in this case.

Looking at the oop hysteresis loops of the samples with Tb, a deviation from the hard switching behaviour seen in the as-prepared samples can be observed. For the 30nm+Tb sample, most of the film switches before the field reaches 10 kOe. The rest of the film shows a very broad switching field distribution and requires higher fields to be switched, leading to the "arms" extending to 50 kOe. This suggests that there is a sizeable part of the film that has a high resistance to magnetic reversal. A very similar behaviour is observable for the 20nm+Tb sample. In this film, however, the increased-coercivity part of the layer comprises the largest percentage, resulting in the large H_C.

Again, the behaviour of coercivity can be explained by the microstructure. Depicted in Fig. 6.8 are the AFM images of the samples after the last post-annealing step. The two samples without Tb (Figs. 6.8 a) and b)) are not easy to interpret, but they do show a rough grown-together film without any noticeable separation between the grains. On the other hand, the two samples with Tb (Figs. 6.8 c) and d)) clearly display the trenches separating the grains, with some grains being completely cut off.

As already explained, isolated grains are harder to switch magnetically since domain walls can hardly propagate into them. Figure 6.8 c), showing the 20nm+Tb sample,

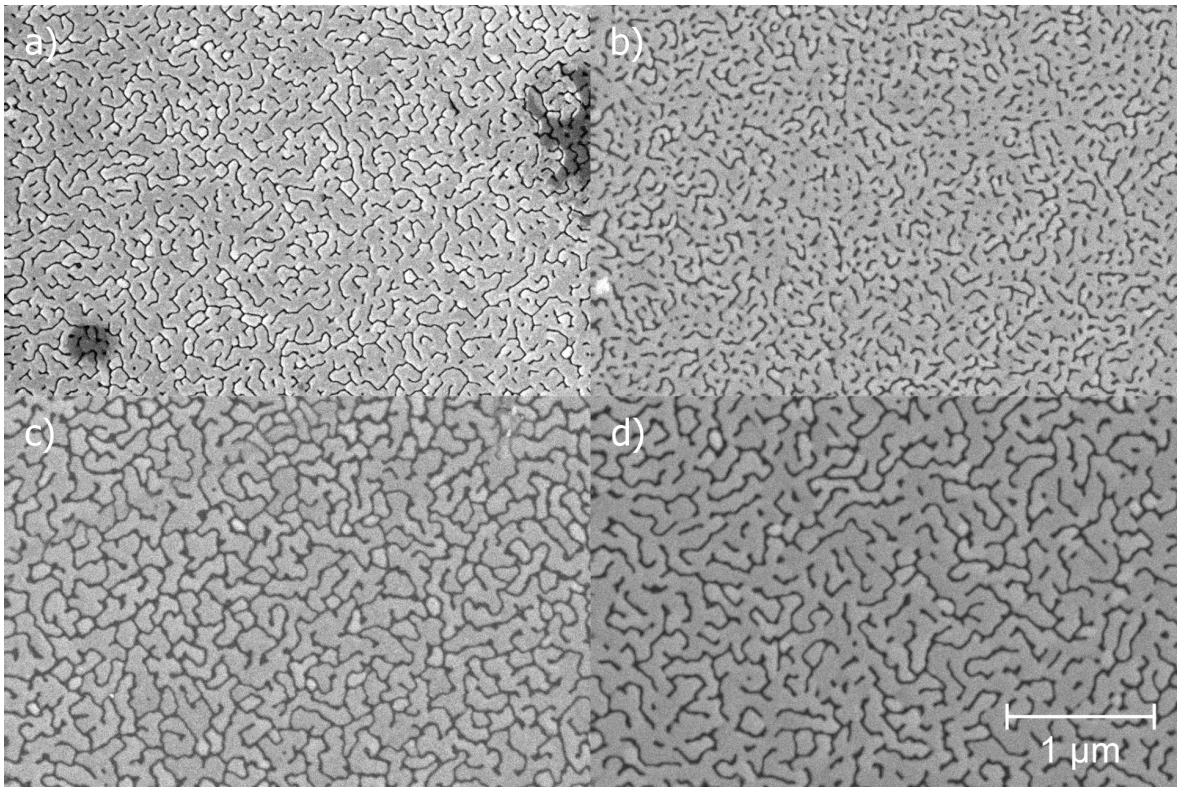

Figure 6.9: SEM micrographs of the a) 20nm, b) 30nm, c) 20nm+Tb, and d) 30nm+Tb samples after the post-annealing step at 700 °C. While trenches are visible for all samples, only c) shows isolated islands. Nearly all islands have coalesced in a), b), and d), but the trenches in the Tb-containing sample (d) are slightly wider and more connected.

shows more isolated grains than the 30nm+Tb sample in Fig. 6.8 d), which fits the conclusions drawn from the *M-H* loops.

A larger picture of the microstructure can be in Fig. 6.9, where SEM measurements of the four samples are displayed. The images of the two samples without Tb shown in Figs. 6.9 a) and b) are much clearer here, confirming that the islands have nearly completely grown together. The two samples with Tb (Figs. 6.9 c) and d)) not only show a much better separation of grains, but interestingly also slightly larger grains than their counterparts without Tb.

In conclusion, it seems that the Tb helped separate the $L1_0$ FePt islands during the heat treatment steps. Still, a good separation of grains in the as-prepared state is needed in order to ensure that H_C is increased, as otherwise only a small percentage of the film will be hardened, as was the case for the 30nm+Tb sample.

6.3 Annealing duration series with Tb

After seeing the influence that different annealing temperatures can have on the samples of the Tb series, the influence of annealing duration was investigated. Two temperatures were chosen based on the change that was observable in the annealing temperature

series, namely 650 °C and 700 °C. These are the temperatures at which the increase in coercivity for the 20nm+Tb sample started.

Since high processing temperatures can damage samples, it is sometimes advisable to instead rely on longer heat treatments instead of higher temperatures. The influence of annealing duration on the structural and magnetic properties of the samples of the Tb series should thus be investigated.

Similarly to the annealing temperature series, one sample piece each of the four different samples was first measured in the as-prepared state and subsequently post-annealed at the given temperature for the duration of one hour. After structural and magnetic measurements in the XRD and the SQUID-VSM, the same sample pieces were again transferred to the tube oven and annealed for another hour. The same procedure is repeated two more times, but the additional annealing durations increased to 2 and 4 hours, respectively. Thus, the measurements display the change after a total of 1, 2, 4, and 8 hours of heat treatment.

This is of course not identical to a single post-annealing process of the same duration, as the samples experience the heating and cooling procedure multiple times instead of just once. However, using multiple sample pieces introduces the chance of different microstructures affecting the observed changes in properties. This gives rise to an uncertainty as to whether the post-annealing procedure or a difference in the initial microstructure of the sample is responsible for a certain behaviour. Accordingly, we chose to minimize the number of variables and chose multiple annealing steps of the same sample pieces.

6.3.1 650 °C series

Before looking at the effect of post-annealing, the samples should again be characterized in their as-deposited state. The corresponding M-H hysteresis loops are depicted in Fig. 6.10.

The overall image resembles that of the previous measurements of the Tb-series in the as-prepared state shown in the chapter on the annealing temperature series. The coercivities of the 20 nm films (left column) show larger coercivities than the 30 nm films (right column), and the samples with added Tb film (bottom row) show slightly increased coercivites than their RE-free counterparts.

The 20nm+Tb sample displays an extended switching field distribution, with about a third of the film switching at fields above 10 kOe. Based on previous measurements, we can assume that isolated FePt grains are the cause of this behaviour. For the other samples, nearly all of the film switches at the same field, thus showing a sharply defined switching step at H_C.

The M_S values for the as-prepared samples range from 1060 to 1150 emu/cm^3 and are thus close to the bulk value. The differences are within the error range resulting from the determination of the film volume.

With the samples described in their as-prepared states, the effects of the post-annealing on their magnetic and structural properties can be investigated. Figure 6.11 shows a

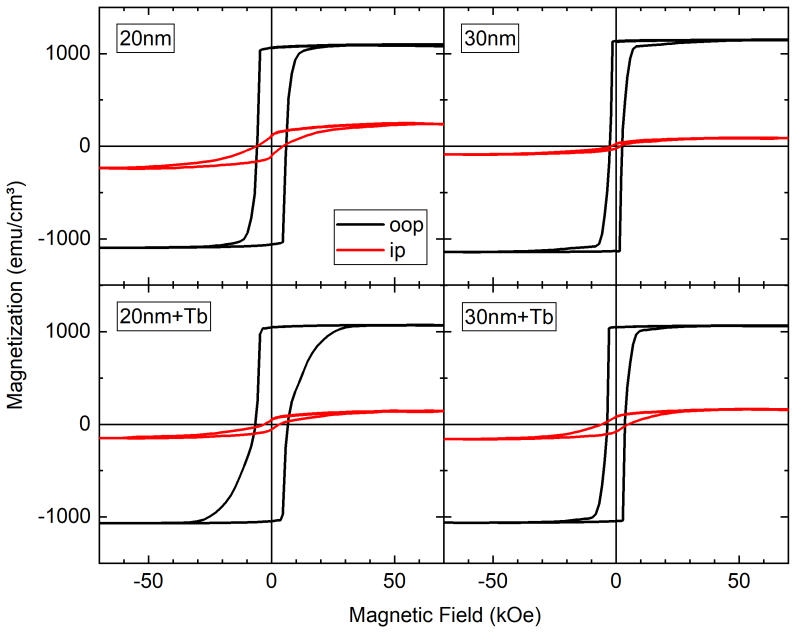

Figure 6.10: As-prepared hysteresis loops of the FePt-based samples of different thickness with and without Terbium. Before the post-annealing treatment at 650 °C, the thinner FePt films show a higher coercivity than the thicker ones, while the Tb-containing samples have a wider switching field distribution.

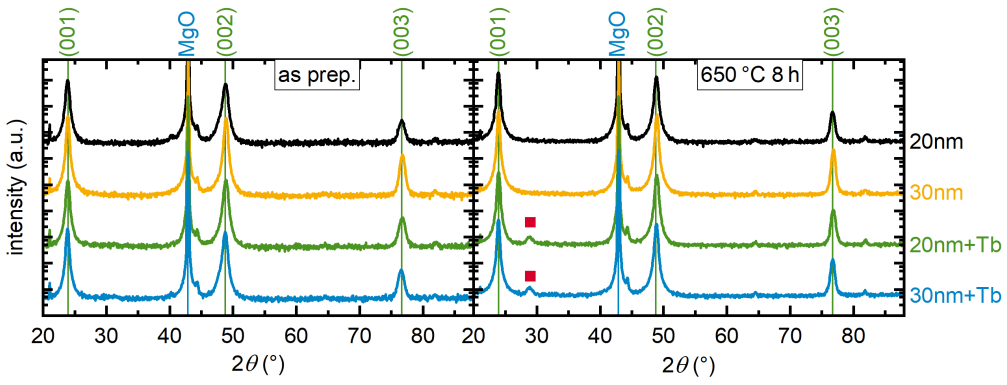

Figure 6.11: Comparison of the θ-2θ-diffractograms of the as-prepared FePt-based samples and the same samples after a total of 8 hours of post-annealing at 650 °C. The only observable change is the appearance of a small Tb reflection peak (red squares) for the samples containing Tb.

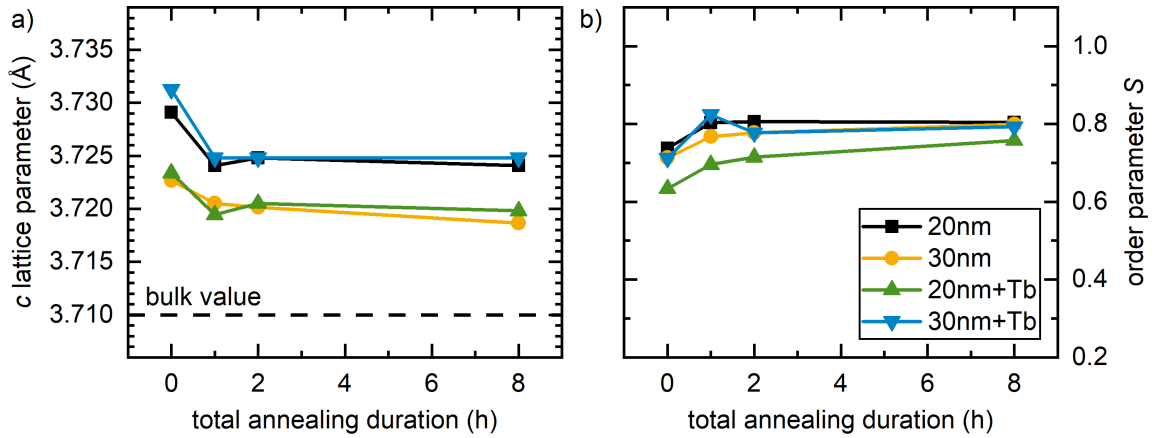

Figure 6.12: Evolution of a) the c lattice parameter and b) the order parameter S for the FePt-based samples for increasing annealing durations at 650 °C. Both values show the strongest change for the first annealing step of 1 hour and barely any change after that. The legend is valid for both diagrams.

comparison of the X-ray θ-2θ diffractograms of the samples in their as-prepared state and after a total of 8 hours of post-annealing at 650 °C.

Similar to the previous series, the as-prepared samples only display the reflection peaks of the MgO substrate and the $L1_0$ FePt film together with the small signal from the steel sample holder. Again, the heat treatment did not incur any major structural changes, so the samples mostly display the same reflection peaks after the heating procedure as before. The only difference is the appearance of a small Tb (100) reflection peak for the Tb-containig samples, visible at 28.9° (red squares in fig. 6.11).

The change of the c lattice parameter and the order parameter with annealing duration at 650 °C is shown in Fig. 6.12 a) and b), respectively. All samples seem to behave quite similarly in this series. The lattice is extended in the c direction, similar to the previous series, but relaxes slightly towards the bulk value of c with the first post-annealing step. After this, no significant change of c is observable, indicating that these values are near the stable state for these samples.

A similar behaviour can be seen for the order parameter: starting at a value between 0.6 and 0.75, S increases towards a value of around 0.8. The increase is most noticeable for the first post-annealing step, after which it increases only very slightly. Both of these behaviours suggest that longer heat treatment would most likely not change the structural properties much further.

The change of the magnetic properties with annealing duration is depicted in Fig. 6.13. The overall coercivity is decreasing for all samples, with the exception of the 20nm sample at the first post-annealing step. This stands in contrast to the temperature series, were a strong increase of H_C was observable for the 20nm+Tb sample at the annealing temperature of 650 °C. Here, the heat treatment seemingly allows the FePt grains to further grow together and form a more continuous film. This makes it easier for domain walls to propagate through the FePt film and thus reduces its coercivity.

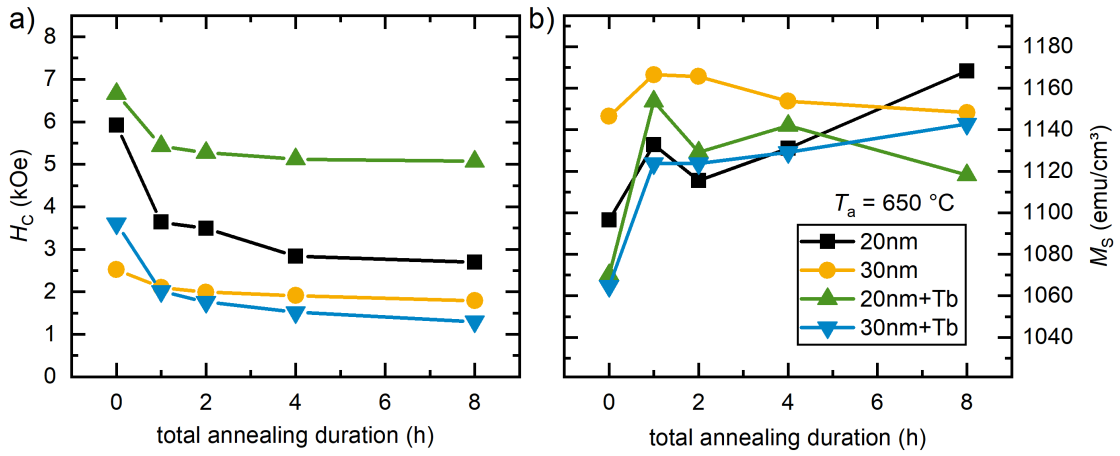

Figure 6.13: Change of the magnetic parameters a) H_C and b) M_S of the FePt-based samples with and without Tb with increased total annealing duration at 650 °C. H_C decreases for all samples, while M_S increases slightly. The legend is valid for both diagrams.

The saturation magnetization, on the other hand, is generally increasing with longer annealing duration. All samples except the 20nm sample show a starting M_S below the bulk value and subsequently increase towards it upon start of the post-annealing procedure. Similar to the change of c and S, the change is strongest at the first post-annealing step, so it is likely linked to the structure of the $L1_0$ FePt film.

The M-H hysteresis loops of the samples after a total post-annealing duration of 8 h at 650 °C are shown in Fig. 6.14. The in-plane hysteresis loops still show the behaviour of a hard axis loop, with only slightly increased loop openings compared to the as-prepared state. The oop loops show that the observed decrease in H_C is valid for the whole film in the case of the samples without Tb and the 30nm+Tb sample, but not for the 20nm+Tb sample (shown on the bottom left). For this sample, there is about a third of the FePt film that actually shows an *increased* switching field and also a wider switching field distribution after the post-annealing process. The gradual broadening of the hysteresis loop in the region beyond 10 kOe with increased annealing duration can be seen by comparing the corresponding M-H hysteresis loops.

This fits exactly to the observation made about the as-prepared behaviour of the sample. Accordingly, we can assume that the part of the film consisting of isolated grains experienced a change in microstructure that improved the isolation of those grains from the remaining film and thus increased their resistance to magnetic reversal. Because this fraction of the film is so small, it does not get reflected in the depiction of H_C alone.

Again, the additional Tb layer seems to have facilitated the magnetic hardening process in the 20nm+Tb sample, albeit less than shown before. Next, the effect of prolonged post-annealing at 700 °C will be investigated.

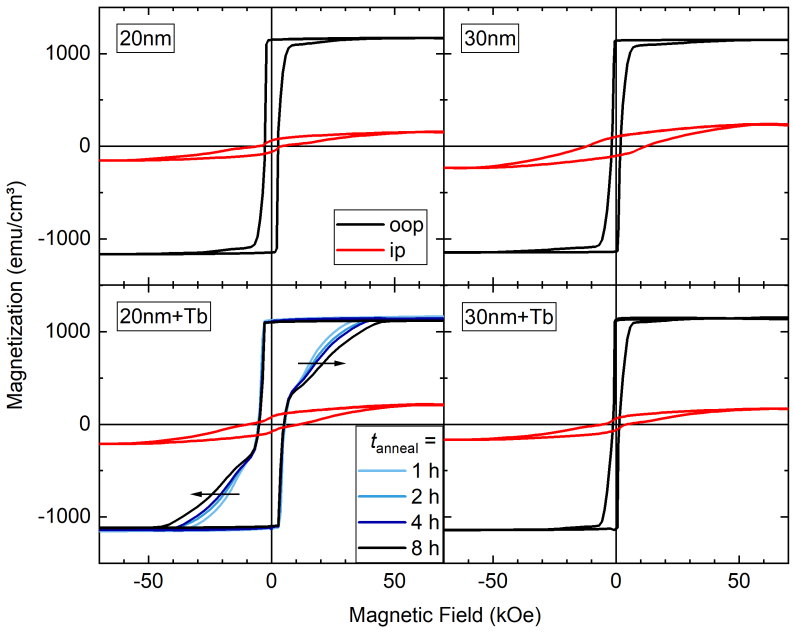

Figure 6.14: The *M-H* hysteresis loops of the different FePt-based samples after a total annealing duration of 8 hours at 650 °C. Even though the coercivities of all samples is decreased, the switching field distribution of the 20nm+Tb sample is actually *in*creased. The development of this can be seen by the oop hysteresis loops taken after different annealing durations, additionally displayed in increasingly darker shades of blue.

6.3.2 700 °C series

Identical to the annealing duration series at 650 °C, the samples of the 700 °C series shall first be investigated in their as-prepared states. This post-annealing temperature is higher than the estimated deposition temperature of $T_{dep} \approx 630 - 650$ °C, so structural changes *within* the FePt grains can be expected.

The *M-H* hysteresis loops of this sample series are shown in Fig. 6.15. Compared to the previous series, there are some differences observable. Firstly, the oop coercivity of the 20nm sample is the highest of all four samples, whereas the 20nm+Tb samples showed the highest value before. This is not unexpected, since the microstructure of sample pieces can vary even on the same substrate due to slightly different conditions during deposition. This sample piece likely contains more isolated $L1_0$ FePt grains than the sample pieces investigated in the previous series. Conversely, the 20nm+Tb sample shows a lower coercivity than before, suggesting that the opposite is the case for this sample piece. Other than this, the two samples with a 30 nm thick FePt film behave similarly to the previous samples, with the Tb-containing sample showing a slightly large H_C than the one without.

Secondly, the in-plane hysteresis loops for the 20nm and 30nm+Tb samples show an increased opening when compared to the commonly observed ip-loops. This indicates that there are parts of the FePt film whose anisotropy axis is tilted away from the film normal. The same was already observed for as-prepared *M-H* hysteresis loops of the annealing temperature series with Tb, and the same reasoning is applicable here.

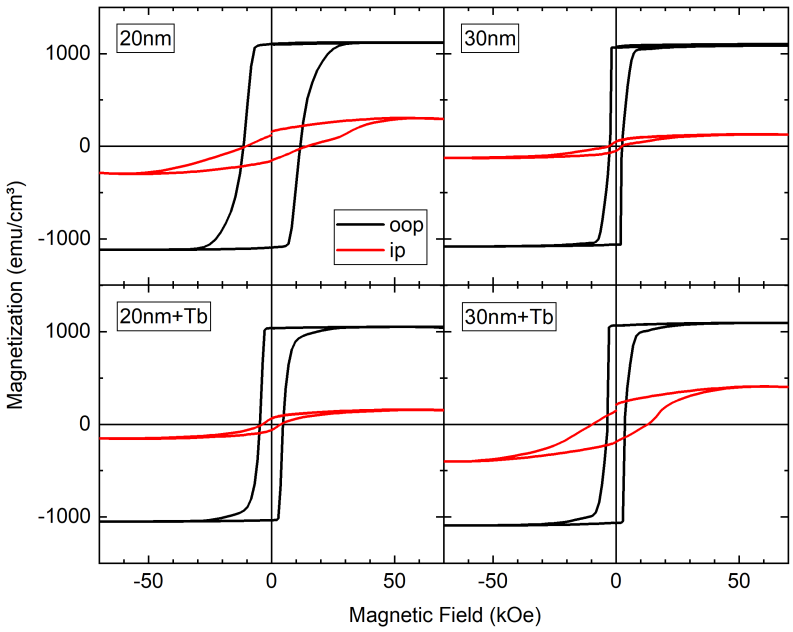

Figure 6.15: As-prepared hysteresis loops of the FePt-based samples of different thickness with and without Terbium. Before the post-annealing treatment at 700 °C, the thinner FePt films show a higher coercivity than the thicker ones, but the 20 nm thick FePt film in particular shows a very large coercivity. The asymmetry of the in-plane loops is very likely caused by measurement errors.

With a tilting angle of 8°, for example, 14 % of the remanent magnetization would be measured in the ip direction, while still 99 % can still be measured in the oop direction, thus only reducing the measured oop magnetization at saturation by 1 %. With the ip remanence being around 14 % of the oop remanence, an average tilting of 8° is assumed for the 20nm and 30nm+Tb samples.

After measuring the magnetic properties of the as-prepared samples, their structural properties were investigated by XRD. After this was completed, the post-annealing procedure was started and measurements done in between the heat treatments.

A comparison of the X-ray diffractograms of the samples in their as-prepared state and after a total of 8 h of post-annealing at 700 °C is shown in Fig. 6.16. The biggest difference between the two sets of measurements is the fact that they were made in two different diffractometers. The measurements of the annealed samples was done in a setup with a monochromator, whereas it was missing in the device used for the earlier measurements for the as-prepared samples. As a result, the θ-2θ measurements of the as-prepared samples include the additional peaks caused by Cu-K_β and W-L_α radiation to the left of the main reflection peaks.

The diffractograms of the as-prepared samples all show the peaks associated with the MgO substrate and the $L1_0$ FePt film. The only additional signal that is visible is a very low Tb (002) reflection peak at 30.9° for the two samples containing the Tb layer. These samples thus show the same structure as the ones shown in the preceding chapters.

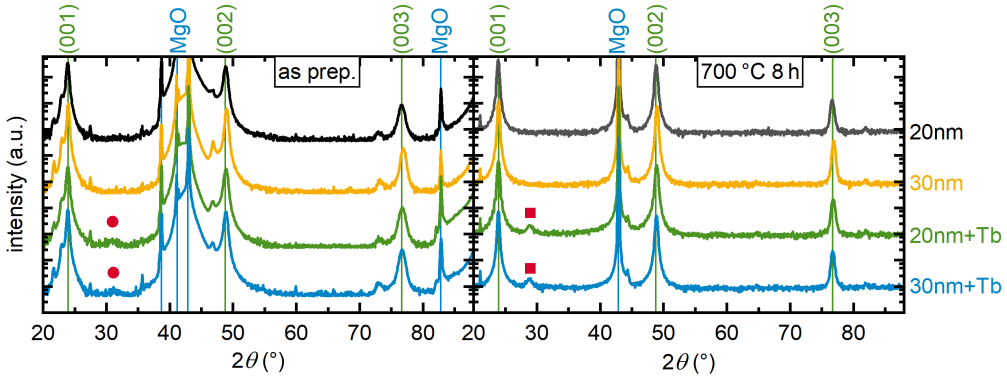

Figure 6.16: Comparison of the θ-2θ-diffractograms of the as-prepared FePt-based samples and the same samples after a total of 8 hours of post-annealing at 700 °C. The only observable change is a shift away from the small (002) Tb reflection peaks (red circles) towards small (100) Tb reflection peaks (red squares) for the samples containing Tb. Note that the as-prepared measurements were performed without monochromator, leading to the appearance of secondary peaks to the left of main reflection peaks such as those highlighted.

After experiencing the post-annealing treatments at 700 °C, the samples do not show the presence of any new phases. Similar to the series annealed at 650 °C, the only signals other than those of MgO and $L1_0$ is the Tb (100) reflection peak at 29°. The Tb film has thus not alloyed with the FePt film, but only slightly restructured itself from a slight (002) to a slight (100) orientation normal to the film plane, while the rest of the film did not significantly change its structure.

The change of the c lattice parameter of the FePt film with annealing duration at 700 °C is depicted in Fig. 6.17 a). Contrary to the previous results for the Tb series, the c lattice parameter barely changes at all for each respective sample piece in the 700 °C series of measurements. Even though a decrease of c towards the bulk value would be expected, the samples are seemingly already in a state where c is stable. The difference to the bulk value is low, however, with the values at hand surpassing it by less than 0.5 %.

The order parameter, on the other hand, does show some change. Its development with increasing annealing duration is depicted in Fig. 6.17 b). The values for the as-prepared samples start between 0.64 and 0.77, the highest being that of the 30nm sample, and increase after heat treatment. The final values are around or above 0.8, the highest again being the 30nm sample with 0.87. As expected, the longer heat treatment allows the FePt film to improve the chemical order, the maximum S being reached after a total of 4 h of post-annealing treatment. Further annealing will most likely not alter the order parameter, as can be seen from the values after a total of 8 h of annealing.

Seeing that the structure of the samples has not changed much in the course of the post-annealing process, the change of the magnetic properties shall be investigated next. The change of H_C and M_S is shown in Fig. 6.18 a) and b), respectively.

The coercivity for most of the samples decreases for longer annealing durations. In these cases, the coalescence of the grains proceeds during the heat treament to form

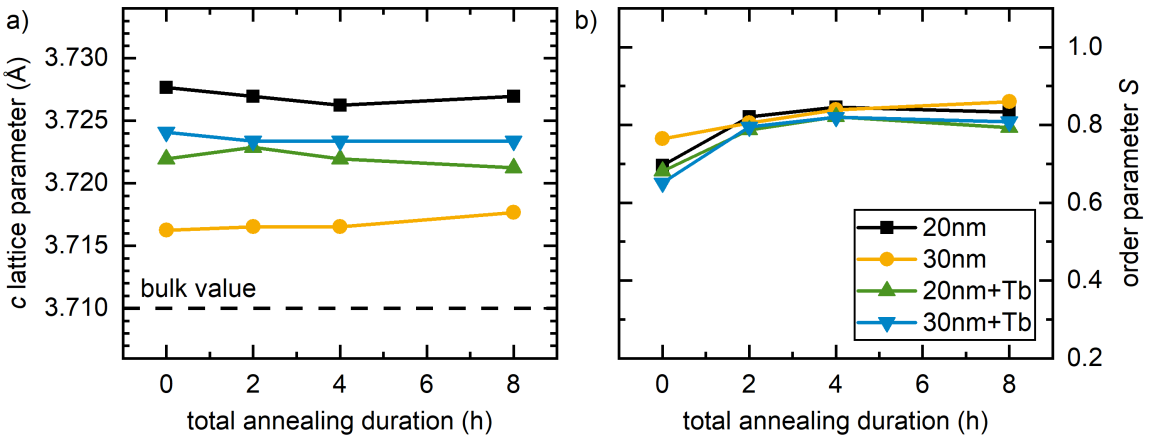

Figure 6.17: Evolution of the structural parameters of the FePt-based samples with total annealing duration at 700 °C. a) the c lattice parameter is slightly different for the four samples, but stays constant throughout the treatment. b) The order parameter S increases for all samples, with the largest increase seen after the first 1-hour-long post-annealing step. The legend is valid for both diagrams.

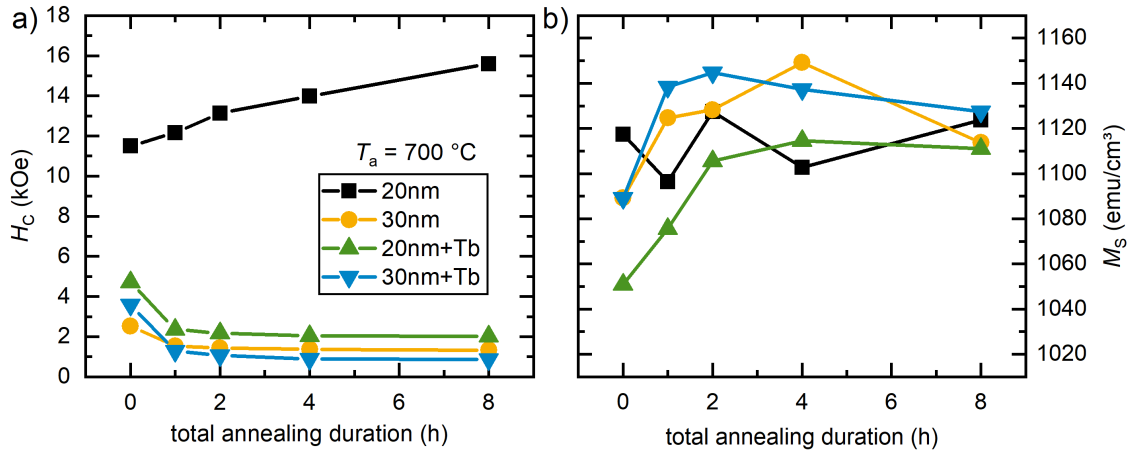

Figure 6.18: Change of a) coercivity H_C and b) M_S with total annealing duration at 700 °C. The high initial coercivity of the 20 nm thick FePt film increases further throughout the treatment, while all other samples show a clear decrease of H_C. M_S for all samples roughly approaches the value of bulk $L1_0$ FePt of about 1140 emu/cm^3. The legend is valid for both diagrams.

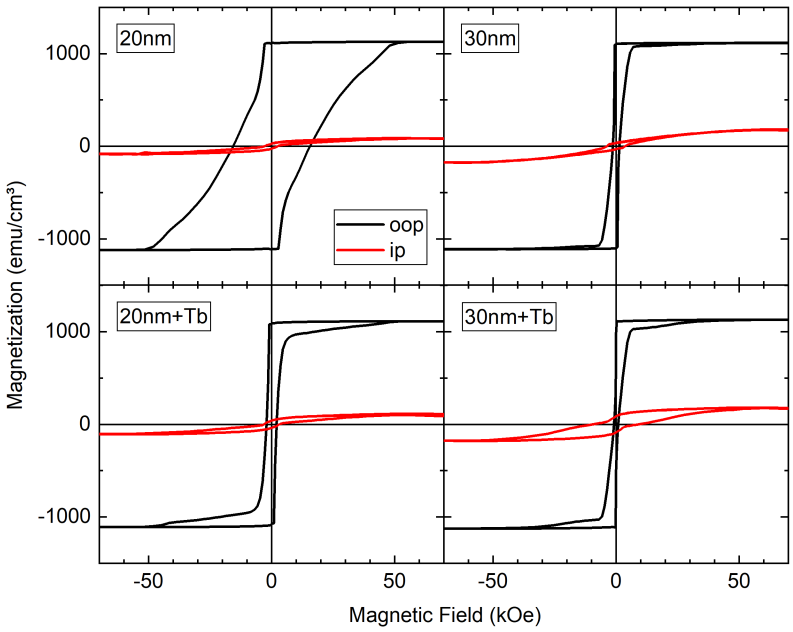

Figure 6.19: *M-H* hysteresis loops of the FePt-based samples after a total annealing duration of 8 hours at 700 °C. The increased coercivity seen for the 20 nm thick FePt film is caused by an overall increase in switching field distribution, resulting in the sheared shape of the loop. All other samples show a sharp switching field distribution with a decreased H_C.

a more continuous film through which domain walls can propagate more easily, thus reducing the coercivity. Among these samples, the 20nm+Tb sample shows a slightly higher H_C, likely due to the FePt being thinner and thus containing better isolated grains.

The opposite is the case for the 20nm sample. Here, the coercivity increases from a starting value of 11.5 kOe to 15.6 kOe after a total of 8 h of post-annealing at 700 °C. This is somewhat unexpected, as the only samples that showed a noticeable increase in H_C so far were those containing the additional Tb layer. This sample now achieves the same without relying on the rare-earth element to fill the trenches between FePt grains and potentially hardening their surface regions. The heat treatment allowed the grains to separate more by themselves, potentially with the Si_3N_4 capping layer filling the trenches, subsequently providing more resistance for the propagation of domain walls.

Taking a look at the *M-H* hysteresis loops of the samples after the heat treatment (Fig. 6.19), more information can be gathered on the effect of the post-annealing. Of the three samples that show reduced oop coercivity, the two samples with added Tb layer show a small part of the FePt film that switches at higher fields, as can be seen by the extended "arms" of the loop. In these samples, there are thus some grains isolated from the generally coherent film that got more isolated during the post-annealing.

The same happened for the 20nm sample, but the isolated grains make up a much larger percentage of the FePt film. As a consequence, a large part of the switching now happens at higher fields, thus increasing the switching field distribution and the

average coercivity of the sample. Similar to previous samples that showed an increased H_C, the switching does not happen all at the same field, but is distributed over a wide range of fields. This can be seen as a representation of the grain size and grain isolation distribution, since both factors affect the coercivity of a given FePt grain.

The ip loops have lost most of their opening, with only the 30nm+Tb sample still showing an opening. The increase of ordering has thus rectified the tilting of anisotropy axes away from the film normal that was present in the as-prepared samples.

The Tb sample series processed with a post-annealing temperature T_a of 700 °C has thus shown a deviation from the trend seen for the previous measurement series, where a noteworthy increase of coercivity was only observable in samples containing an additional Tb layer.

6.4 Annealing temperature series with Gd

The same heat treatment procedure of increasing the annealing temperature that was applied to the Tb series was also applied to a similar series with an added Gd layer. Here, the samples were limited to 20 nm thickness for the $L1_0$ FePt layer, as this film thickness shows a better grain separation and thus more potential for a magnetic hardening effect in the course of the post-annealing procedure. Hence, the Gd series consists only of two samples: one sample with a 10 nm thick Gd film and one without Gd. These will be named *20nm+Gd* and *20nm noGd*, so the reference sample without the Gd layer will not be confused with the nominally identical sample from the Tb-series.

The *M-H* loops in the as-prepared state, displayed in the top row of Fig. 6.20, are very similar to each other. Both show a saturation magnetization around 1100 emu/cm^3 and a low oop coercivity of roughly 2.3 kOe (20nm noGd) and 1.3 kOe (20nm+Gd). The in-plane loops are closer to being saturated than those of the Tb series, as can be seen from the change in slope at higher fields. This suggests that the anisotropy field H_A in these samples is not as high.

The hysteresis loops of the samples after the last post-annealing treatment are displayed in the bottom row of Fig. 6.20. Comparing these to their as-prepared counterparts, there is hardly any change observable. The oop coercivity has been reduced, and in the case of the sample with Gd, the ip loop shows a lower slope and curvature, hinting at an increased PMA.

A more detailed view of the change of H_C and M_S can be seen in figs. 6.21 a) and b), respectively. The coercivity of the sample without Gd starts decreasing at an annealing temperature of 650 °C, which is close to the deposition temperature. In the same temperature range, the sample with Gd shows a small local maximum after an inital decrease of H_C. This could be an indicator that the elevated temperature allowed the FePt grains to reshape and thus increase the grain separation by Gd filling the trenches between the grains. Above 700 °C, the coercivity of both samples drops below 1 kOe, meaning that the presence of Gd does not make a difference at these high temperatures.

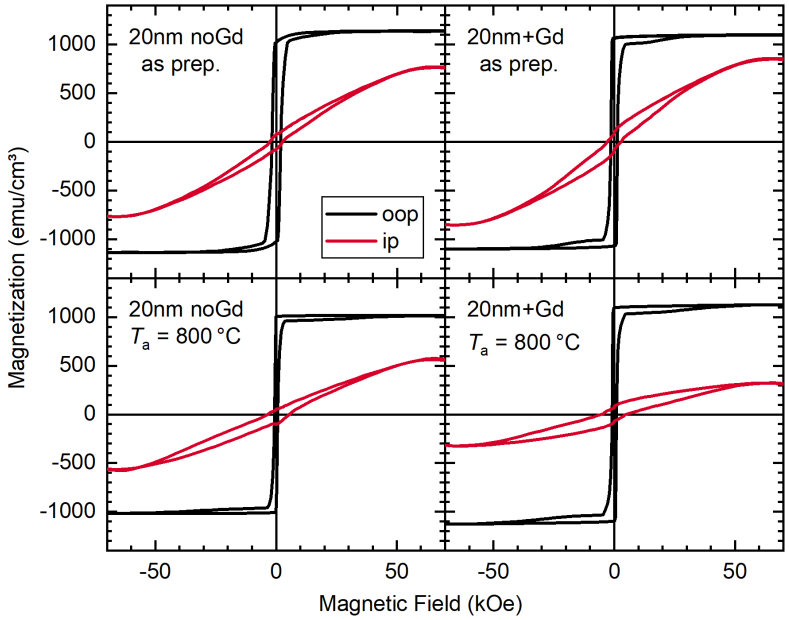

Figure 6.20: Comparison of the *M-H* hysteresis loops of the Gd-series of FePt samples in the as-prepared state and after the post-annealing treatment. No major difference in magnetic behaviour can be seen between the measurements except a slight reduction of the in-plane magnetization.

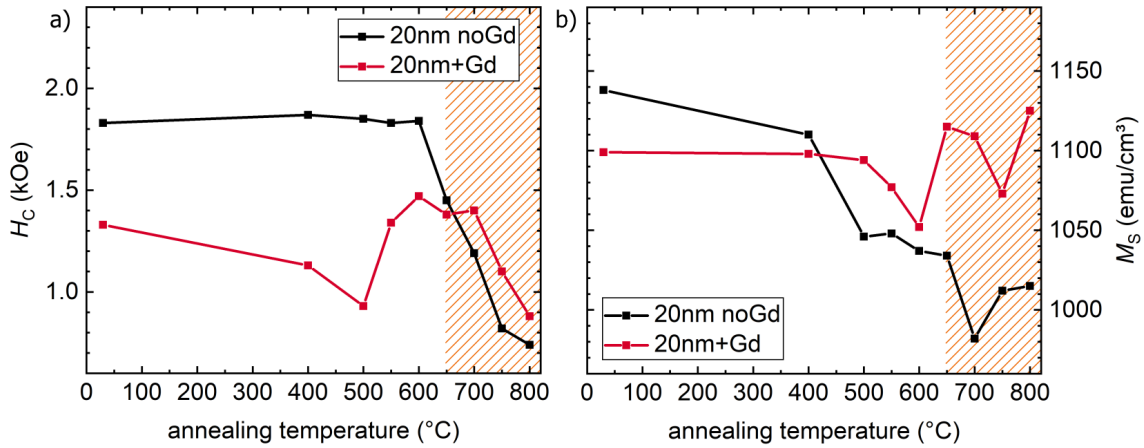

Figure 6.21: The change of a) oop coercivity H_C and b) oop saturation magnetization M_S of the Gd-series of FePt samples with annealing temperature. Both values decrease stronger for the sample without Gd, while the Gd-containing sample also shows a small increase of H_C between 600 and 700 °C annealing temperature. The area shaded in red highlights the temperature range above the deposition temperature of the FePt layer.

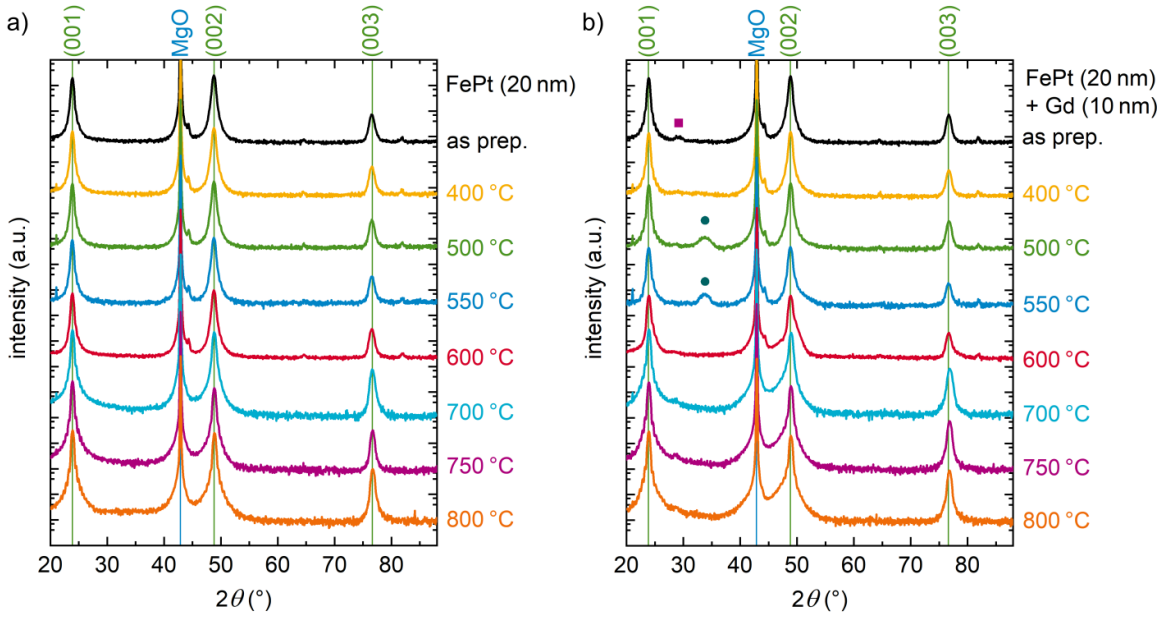

Figure 6.22: Change of the X-ray diffractograms of a) the 20nm noGd and b) 20nm+Gd samples over the course of the post-annealing treatment. The blue line highlights the (002) reflection peak of the MgO substrate, the green lines highlight the (00l) reflection peaks of $L1_0$ FePt. There is next to no structural change observable between the measurements. The purple square denotes the (100) reflection peak of Gd, and the dark green circle is likely the (220) reflection peak of $GdFe_2$.

Interestingly, the magnetization of the sample without Gd decreased throughout the post-annealing treatment, while that of the sample with Gd stayed almost constant. Since Gd and Fe couple antiferromagnetically, the opposite was expected. This leads to the conclusion that Gd is not incorporated into the $L1_0$ FePt film in relevant quantities, as was the case for Tb in the previous series. The reduction in M_S for the sample without Gd can only be partially explained by the loss of Fe moment by the formation of iron oxide. The real reason is not known.

The structural changes have been measured by XRD and the measurements depicted in Fig. 6.22. As a monochromator was used for these measurements, no additional peaks appear on the left side of the main reflection peaks. The diffractograms of the as-prepared samples look similar to those of the Tb-series. The only peaks visible here belong to the substrate and the $L1_0$ FePt film together with a weak Gd (100) reflection at 29° for the sample with Gd. Additionally, the small peaks visible at 44.3° and 82°, fitting to the Fe (110) and (211) reflection peaks, respectively, are caused by the steel sample holder used for the first few measurements. The peak disappears after transitioning to a 3D-printed plastic sample holder for the last three measurements of each sample.

For the sample without Gd, no additional peaks appear throughout the whole heat treatment. For the three highest annealing temperatures, the intensity of the (00l) reflection peaks of $L1_0$ FePt increases, suggesting a better ordering of the FePt grains in this sample.

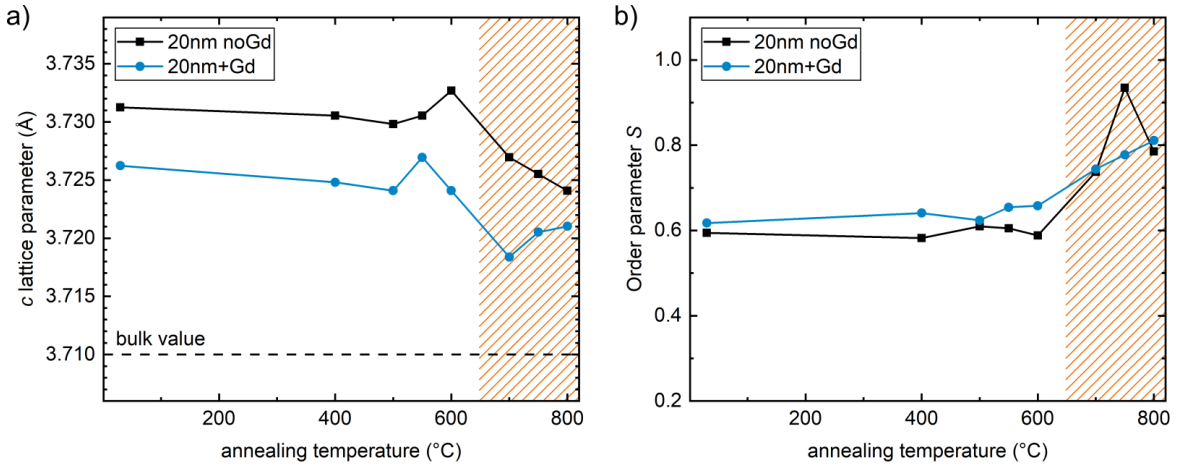

Figure 6.23: Change of a) the c lattice parameter and b) the order parameter S of the FePt samples with and without Gd film. Both samples behave very similarly, with order increasing and lattice parameters approaching the bulk value for higher annealing temperatures. The area shaded in red highlights the temperature range above the deposition temperature of the FePt layer.

The sample with Gd shows a little change for intermediate annealing temperatures: after heat treatment at 400 °C, the small Gd (100) peak disappears and gets replaced by a peak at 33.6° after annealing at 500 °C. This peak disappears again at 600 °C and cannot be identified beyond doubt. The *Match!* matching software gives a good fit to the Si_3N_4 (101), Pt_2Gd (220), and Pt_6Si_5 (311) reflections. However, the crystallization temperature of Si_3N_4 is above 1400 °C [303], and the Si_3N_4 capping layer is not in direct contact with the FePt layer. Pt_2Gd is also not easy to synthesize, usually needing temperatures above 700 °C to form [304]. Accordingly, all three possibilities can be ruled out.

Another, albeit less well-fitting, possibility is cubic $GdFe_2$, which shows its (220) reflection peak at around 34.2°. As the samples have been prepared with a slight surplus of Fe, the formation of small $GdFe_2$ particles is considered more likely. The deviation of the peak position could be explained by strain or an off-stoichiometric composition. Additionally, the small shoulder on the right side of the (002) reflection peak of $L1_0$ FePt for the 600 °C curve could also fit to the (400) reflection of $GdFe_2$, but neither the change in orientation nor the disappearance of the peaks can be explained. Still, the slight reduction in M_S between annealing temperatures of 500 and 600 °C would be explained by the formation of the ferrimagnetic $GdFe_2$ compound.

Finally, the (00l) peak intensities increase for annealing temperatures above 700 °C, similar to the sample without Gd. Also, Laue oscillations appear at these temperatures, indicating that the $L1_0$ FePt display a high degree of ordering after the heat treatment.

It can thus be concluded that almost none of the changes of the magnetic properties seen in Fig. 6.21 are caused by the appearance of new phases. Instead, they are again mostly caused by changes in the microstructure of the $L1_0$ FePt film.

To observe changes in the $L1_0$ FePt structure, the c lattice parameter has been extracted from the (002) reflection peaks of the diffractograms and the order parameter

S determined from the integrated (001) and (002) peak intensities. Their change with increasing annealing temperatures is depicted in Fig. 6.23 a) and b), respectively. Similar to the samples of the Tb series, both samples of the Gd-series show a larger c than the bulk value in the as-prepared state. Again, further annealing finally leads to a relaxation of the tensile stress and reduced lattice parameter. However, both samples display a small local maximum at intermediate temperatures. These maxima do not seem to correlate to any specific change in the magnetic properties, though.

The order parameter, starting off at a rather low value near 0.6, starts to increase once the post-annealing temperature passes 600 °C. This is not surprising, as the effective deposition temperature at the substrate is estimated to be around 650 °C and either higher temperatures or longer annealing durations are usually needed to increase order in such an alloy. However, there does not seem to be a direct connection between S and the magnetic parameters depicted in Fig. 6.21.

In summation, the Gd layer did not induce any substantial difference in the change of structural and magnetic properties of the FePt sample investigated here. However, since both samples had a low H_C to begin with, it cannot be ruled out that Gd could indeed help increase the coercivity of a sample with another microstructure, i.e. a sample with better separated FePt grains.

6.5 Discussion and summary

The post-annealing treatment of $L1_0$ FePt thin films grown on MgO gave some insight into the behaviour of the films when heated ex-situ in forming gas atmosphere.

We were able to observe a decrease of coercivity for most samples, while only a few samples showed an increase of coercivity after the post-annealing process. The first of these was the sample containing a 20 nm thick FePt film with an added 10 nm film of Tb on top. This sample showed a strongly increased H_C when annealed at increasingly higher temperatures, with the strongest increase observed for annealing temperatures between 650 and 750 °C, which is just above the effective deposition temperature.

The second was an identical sample post-annealed for longer duration at 650 °C, which did show some broadening of the hysteresis loop, but still, the largest part of the film actually had its coercivity decreased by about a quarter.

The third was a sample consisting only of the 20 nm thick FePt layer and, of course, the capping layer, which was post-annealed at 700 °C for longer durations. Contrary to the previously mentioned samples, this one did not contain an added Tb layer, which was previously assumed to facilitate the separation of grains and possibly harden the grain surfaces by ways of the antiferromagnetic interaction between Tb and Fe. Of the Gd-series of samples, no sample showed any increase of coercivity using the same treatment of increasing annealing temperature as the first series of samples with Tb.

Interestingly, it seems that only those samples that already show a high H_C value in the as-prepared state can have their coercivity increased by the post-annealing treatment. The threshold in this case seems to be around 10 kOe, as both samples with an actual increase in H_C show an as-prepared oop coercivity value above 10 kOe. A lower value

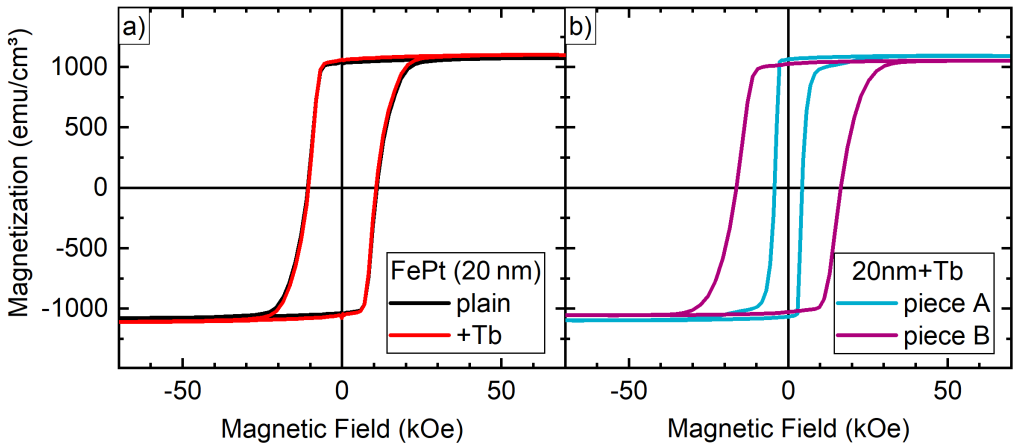

Figure 6.24: a) Comparison of the same sample piece containing a 20 nm thick $L1_0$ FePt film before and after the additional deposition of a 10 nm thick Tb film on top. The identical shape of the two measurements proves that the Tb does not alter the magnetic properties if the film purely by interfacial coupling effects in the as-prepared state. b) Two oop M-H hysteresis loops of nominally identical FePt sample pieces cut from the same substrate. The difference in coercivity shows the large variability of magnetic properties seen even in $L1_0$ FePt samples that are assumed to be identical.

seems to indicate that most of the film is already grown together, so any further heat treatment will only help this interconnected network of grains grow.

On the other hand, any part of the film that switches at fields above 10 kOe in the as-prepared state seems to consist of grains that are isolated enough from the rest of the film that further heat treatment will not make it coalesce with other grains, but on the contrary further improve its isolation. This will in turn increase the field necessary to switch this grain.

If the percentage of isolated grains in the film is small, this will lead to the loops displaying the extended arms seen for some of the post-annealed samples (e.g. bottom right in Fig. 6.7 or bottom left in Fig. 6.19). If the percentage is large, these arms are larger vertically, since they account for a larger part of the magnetization, and thus broaden the entire M-H loop.

The question is then what influences the oop coercivity in the as-prepared state. To test if the interfacial interaction between Tb and Fe has any influence on the coercivity, a 20 nm thick FePt film has been deposited in the same way as for the previously shown sample series, only without a Si_3N_4 capping layer. This sample was measured in the SQUID-VSM and subsequently returned to the BESTEC sputtering system to deposit a Tb layer of 10 nm thickness on top of the FePt layer. The M-H hysteresis loop of the new sample was then measured and the two measurements compared (see Fig. 6.24 a)).

As can be seen, the Tb layer has no noteworthy effect on the magnetic properties of this FePt film. It can thus be concluded that the interfacial antiferromagnetic interaction between Fe and Tb is not sufficient to effect any change by itself, at least in the as-prepared state.

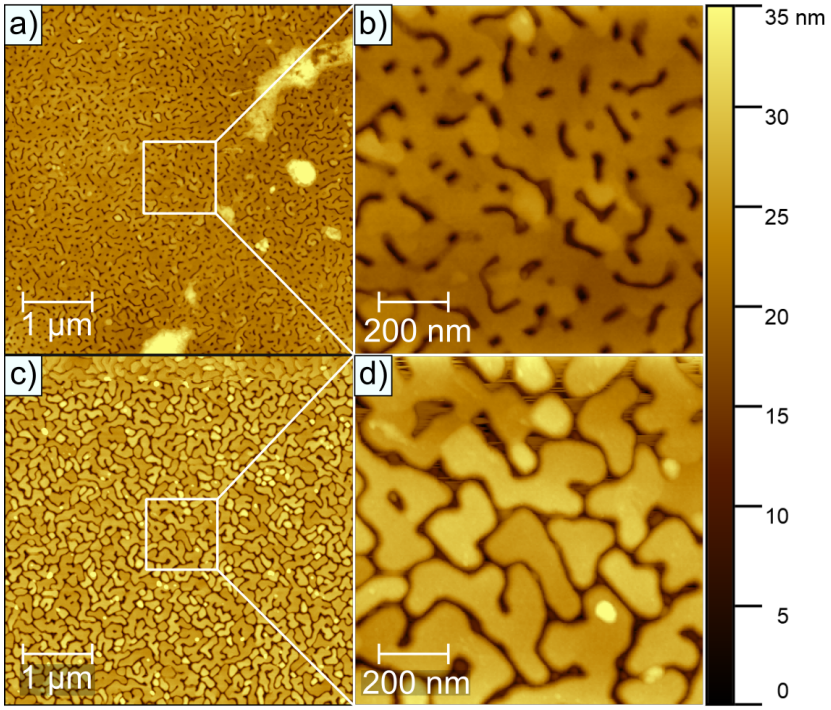

Figure 6.25: Comparison of the microstructure of the two nominally identical FePt-based samples. Even though both samples were deposited in the same deposition run, they show largely different degrees of separation and coalescence of the FePt islands. The sample shown in a) and b) shows a significantly lower H_C than that shown in c) and d), indicating that this difference is caused by the structural difference observed here.

Next, multiple sample pieces from the same substrate piece of the 20nm+Tb sample have been measured to see the variance of coercivities that can occur even on the same substrate. Surprisingly, the observed oop coercivities varied by a substantial amount. Shown in Fig. 6.24 b) are the two sample pieces displaying the highest and lowest value of H_C of the 20nm+Tb sample. As can be seen, the coercivity of these sample pieces varies between 4.3 (piece A) and 16.4 kOe (piece B), so nearly by a factor of 4.

To confirm whether the microstructure really varies that much on the same substrate piece, both samples were investigated with atomic force microscopy. Their measurements at two different resolutions are displayed in Figs. 6.25. Indeed, the difference of microstructure between the two samples is substantial. Sample piece A, shown in Fig. 6.25 a) and b), displays a continuous network of interconnected grains and almost no individual grains. On the other hand, sample piece B, shown in Figs. 6.25 c) and d), shows a clearly coherent network of trenches separating the grains. The film topology thus explains the difference in magnetic reversal behaviour and confirms the interpretations made in previous chapters.

This difference in microstructure is surprising, since the substrate pieces are rather small, measuring only 10 x 10 mm^2, and one would assume the deposition conditions to be rather uniform across these dimensions. Since the substrate is clamped to the substrate holder in two places, the proximity of a certain place on the substrate to the holding clamps could influence the precise flow of heat. As such, small differ-

ences in local temperature could influence the local microstructural growth during the deposition.

In any case, the difference in microstructure can be confirmed to be the most important part in defining the as-prepared H_C of a sample piece and thus the possibility to increase it by post-annealing treatment.

In summary, we can conclude that the presence of Tb is definitely not a necessary prerequisite for the increase of coercivity upon post-annealing. In order to be able to say if Tb is still beneficial for this purpose, one would need to compare two FePt thin films with identical microstructure, one of which has an added Tb film on top. This can be very hard to achieve, as was shown by the disparity of magnetic properties for sample pieces cut from the same substrate piece.

Nothing certain can be said about the influence of Gd on the properties of the $L1_0$ FePt film since the initial coercivity values of this series were too low. Again, identical microstructures with well separated FePt grains for the samples with and without Gd layer would be needed to see the real influence of the RE layer.

CHAPTER 7

Exchange coupling effects in amorphous TbFe-based bilayers

As already mentioned, amorphous TbFe thin films with their tunable composition and consequently tunable magnetic properties are useful in a wide variety of applications. Arguably the most useful one is the field of exchange coupling and exchange bias. The amorphous structure leads to the emergence of giant exchange bias fields [34, 248], and the tunability can be used for the tuning of the magnetic reversal behaviour of synthetic antiferromagnets [305].

Some more interesting behaviour can be observed when coupling two TbFe thin films to each other. Previous results by Birgit Hebler et al. showed a double exchange bias (DEB) phenomenon at low temperatures for the combination of $Tb_{19}Fe_{81}$ and $Tb_{36}Fe_{64}$ [306]. In her work, she showed that the formation of an interlayer region between the two Tb_xFe_{100-x} layers, working as the pinning layer, is the reason for the exchange bias. This interlayer is assumed to form by intermixing of the two nominal layers during deposition. The composition of the interlayer is very close to magnetic compensation, which leads to an almost vanishing magnetization and an immense H_C. As such, it takes the role of the pinning layer for both TbFe layers, biasing them in opposite directions because the sign of the exchange coupling to the dominant magnetic element in each layer has a different sign.

An exemplary low-temperature M-H loop of a sample showing DEB is shown in Fig. 7.1b). In this case, the partial loop of the Tb-dominated layer is shifted to positive fields, while the partial loop of the Fe-dominated layer is shifted to negative fields. When the magnetizations of the two layers point in the same direction, an interfacial domain wall is formed, because the magnetic moments of Fe (or Tb, respectively) point in opposite directions in the two different TbFe layers. Since the cooling field used for the FC procedure of this measurement had a positive sign, the pinning layer at the interface between the two TbFe layers must be Fe-dominant, because the Fe moments tend to stay in the positive direction. Knowing the direction of the cooling field thus allows to determine the dominant element in the pinning layer when evaluating such DEB loops.

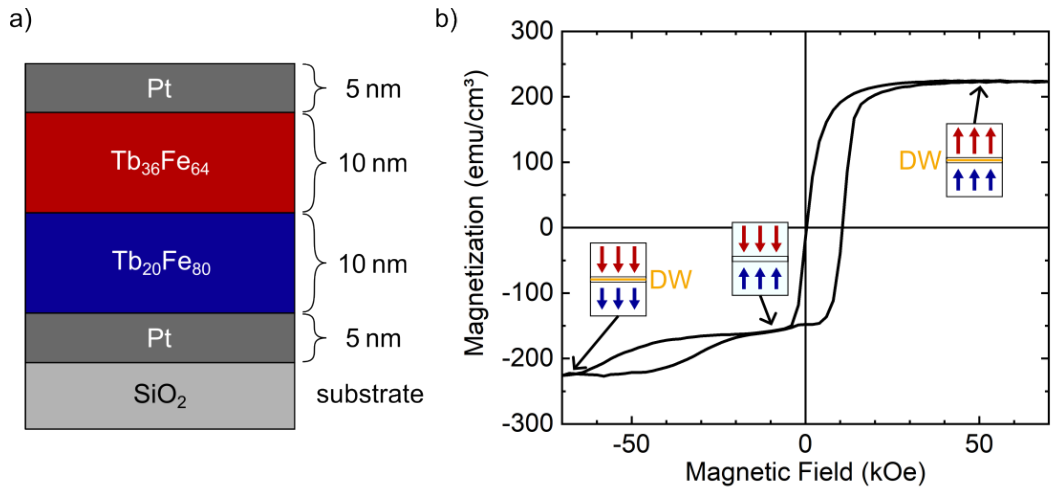

Figure 7.1: a) The standard layer stack of the TbFe-based bilayers, using exemplary compositions. The Fe-dominant layer is at the bottom in this case, but the order of the layers was varied. b) An exemplary low-temperature double exchange bias loop. The insets show the magnetization of the Tb-dominated layer (red) and the Fe-dominated layer (blue) as well as the presence of an interlayer domain wall (yellow) at saturation. The two TbFe layers can be differentiated by their magnetizations and are biased in opposite directions.

In order to expand on the work of Hebler et al. and deepen the understanding of the DEB behaviour, we prepared multiple samples to investigate the change of the magnetic behaviour with different compositions of either of the two TbFe layers as well as the influence of an intentionally deposited interlayer on the DEB.

7.1 Sample preparation

The TbFe samples analyzed in the frame of this work were deposited using magnetron sputter deposition, as outlined in chapter 4.1. The thin films were deposited on thermally oxidized Si (100) substrates with a SiO_2 thickness of 100 nm. A Pt seed layer and a Pt capping layer of 5 nm each protect from oxidation, both from the ambient atmosphere and the substrate. The sputtering pressure of Ar was kept at 1.5 µbar for all layers. The change of composition was achieved by varying the deposition rate of Fe while keeping the Tb deposition rate constant.

The standard sample layout consists of two Tb_xFe_{100-x} layers with different compositions: one layer is Fe-dominant ($0 \leq x \leq 23$), the other Tb-dominant ($25 \leq x \leq 100$), as exemplarily depicted in Fig. 7.1a). Deviations from the nominal composition arise from deviating sputtering rates, which can also slightly change over the duration of the sputtering process. Accordingly, the magnetically compensated state at room temperature can only be assumed to appear for a range of compositions (instead of a fixed one), namely between 23 and 24 at.% Tb content.

In order to investigate the DEB phenomenon further, we prepared samples with different combinations of layers, starting with $Tb_{19}Fe_{81}$ and $Tb_{36}Fe_{64}$. Varying the composition of the layers not only changes the properties of the layers themselves, but presumably also of the interlayer. Additionally, we prepared samples containing an

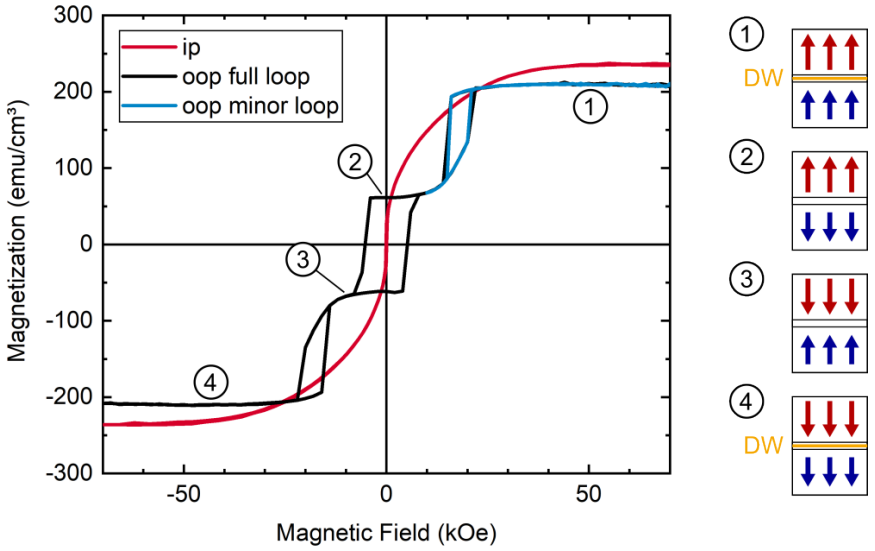

Figure 7.2: Room temperature hysteresis loops of a $Tb_{20}Fe_{80}/Tb_{36}Fe_{64}$ bilayer sample in ip and oop directions. The difference between the two measurement directions shows the strong PMA of the amorphous film, while the minor loop shows the strong exchange coupling between the two layers, leading to the satellite hysteresis of the Fe-dominated layer. On the right side, the magnetic configuration of the two layers (Fe-dominated: blue, Tb-dominated: red) at different points of the oop loop is depicted. At saturation, a domain wall is created at the interface.

intentional interlayer, allowing us to control the interlayer properties without changing the other two layers.

During investigation of these samples, we chanced upon another interesting property: the overcrossing of ascending and descending hysteresis loop branches at low temperatures. This seems to be connected to an inherent inertia of the magnetic reversal process, leading to a slow change in magnetization at certain parts of the hysteresis loop. This behaviour was termed "ultraslow magnetic relaxation" and has similarities to the behaviour of a spin glass below the critical temperature and magnetic viscosity behaviour.

7.2 Double Exchange Bias

Hebler et al. showed a DEB behaviour of TbFe-based bilayers at temperatures between 80 K and 160 K [306]. This was achieved by cooling the samples down from room temperature to 80 K and applying a magnetic field of 7 T during the cooling process. This DEB is not to be confused with that of a layer being pinned in two different directions, as can be seen in some exchange-biased systems [72, 307, 308].

In this work, we proceeded in the same manner, only cooling down further to 10 K before measuring M-H hysteresis loops at increasing temperatures. The measurements were performed at 13 different temperatures between 10 and 300 K, which gave a good range of temperatures to observe the change of magnetic behaviour of all samples.

At first, the room temperature magnetization of a $Tb_{20}Fe_{80}/Tb_{36}Fe_{64}$ bilayer shall be investigated to get a general idea of the magnetic behaviour of such a system. Figure 7.2 shows the oop and ip hysteresis loops of such a system. It can clearly be seen that the ip direction is the hard axis and that there is a three-step reversal process observable in the oop direction.

These three steps show the switching events in the sample: the outer switching events represent the switching of the Fe-dominated layer ($Tb_{20}Fe_{80}$), which is shifted to high fields due to the interlayer exchange coupling with the Tb-dominated layer. This satellite hysteresis is identical in the minor loop, confirming that the Fe-dominated layer is indeed exchange-biased to show its switching at these positive fields. The gradual change of magnetization between 10 and 20 kOe indicates that not all of the Fe-dominated layer switches to a parallel alignment at once, but that there is a domain wall slowly being pushed through the layer with increasing field until the Zeeman energy is higher than the interlayer exchange coupling energy between the two layers, leading to a sudden switch to parallel alignment at 22 kOe. The domain wall then ends up between the two layers.

The central opening represents the simultaneous switching of both layers, as the antiferromagnetic coupling between the two layers is strong enough that an antiparallel alignment is energetically more favourable than a parallel alignment which would minimize the Zeeman energy. This also indicates a strong coupling between the two layers, as a less strongly coupled bilayer structure would most likely show only two switching events, one for each of the two layers. As will be shown later, this is also the case for some of the samples investigated here.

Knowing the general behaviour of the samples at room temperature, especially the switching behaviour, its changes at lower temperatures can be understood more easily.

7.2.1 Investigation of TbFe/TbFe bilayer structures

For the first investigation of the DEB behaviour, three different samples were deposited to test the reproducibility of the results of Hebler et al. All of them were deposited using a fixed Tb deposition rate and a variable Fe deposition rate in order to create two TbFe layers of different compositions. For the first of these samples, the Fe sputtering power was changed by 4 W/s between the two layers, identical to how Hebler did it in her work. During this power change, the magnetron shutters were closed, so the sample nominally only contains the two TbFe-layers of different composition. This sample is referred to as "*fast change*", since this rate of change of the power is higher than the 1 W/s usually used. The second sample was deposited using this slow change of power, also with the shutters closed during the power adaptation. This sample is referred to as "*slow change*". The third sample was also deposited using the slower rate of power change, but the target shutters were left open while the deposition powers were changed, ensuring that an interlayer with a composition gradient was deposited. This gradient interlayer can be estimated to be around 2 nm thick. This sample is referred to as "*with gradient*".

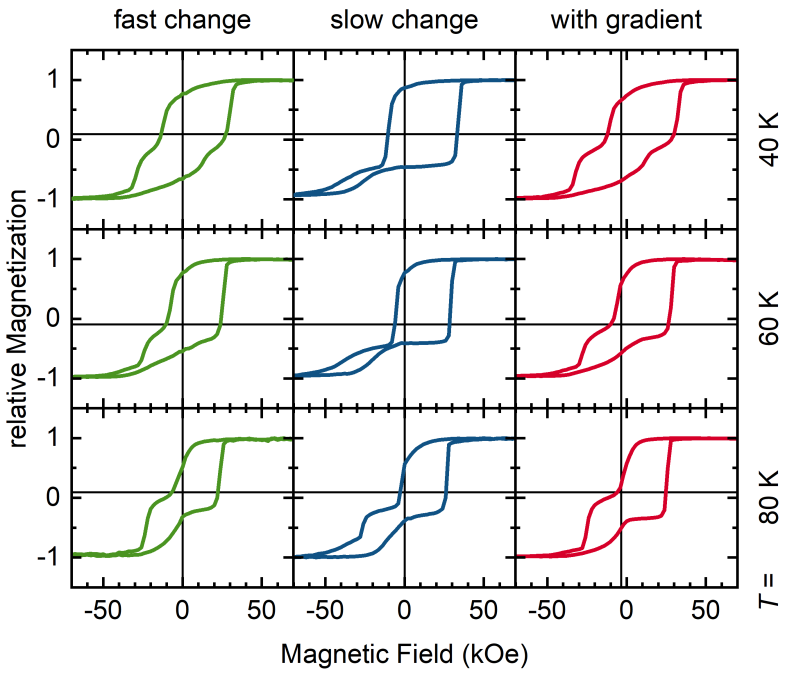

Figure 7.3: Low-temperature hysteresis loops of the different $Tb_{19}Fe_{81}/Tb_{36}Fe_{64}$ bilayers after FC in +70 kOe. The sample deposited with a slow change of Fe sputtering power between the two layers shows the best separation of the two oppositely biased loops and the most stable unidirectional anisotropy.

The FC *M-H* hysteresis loops of these three samples between 40 and 80 K are shown in Fig. 7.3. The first important observation is that any EB can only be observed at temperatures below 80 K, a much lower value than expected based on previous results. Above this temperature, the hysteresis loops become symmetrical. Also, a very pronounced DEB behaviour can only be seen for the *slow change* sample. For the other two, the subloop of the Tb-dominated layer (higher magnetization) is already split between positive and negative biasing, thereby overlapping with the signal of the Fe-dominated layer with the lower magnetization.

The bidirectional biasing indicates that the pinning layer is not yet reversible at this temperature, but also that it is not uniformly magnetized. One reason for this could be a non-uniform composition in the interlayer, making part of it Fe-dominated and another Tb-dominated. Such a local variation of the composition is not unheard of and actually rather normal in amorphous alloys [309–311]. Another possible reason would include opposing directions of magnetization being "frozen" in the pinning layer, which is highly unlikely if all of the interlayer is dominated by the same element. The first explanation is thus preferred.

Interestingly, the *fast change* and *with gradient* samples show almost identical loops from 40 to 80 K. This again confirms that an intermixing of the layers at the interface creates a region of gradient composition, leading to the emergence of DEB behaviour. The reason for the similarity between the two samples might be that the actual Fe deposition rate has not yet reached its final value when the second layer starts being deposited due to the quick change of sputtering power. Since higher powers lead to a

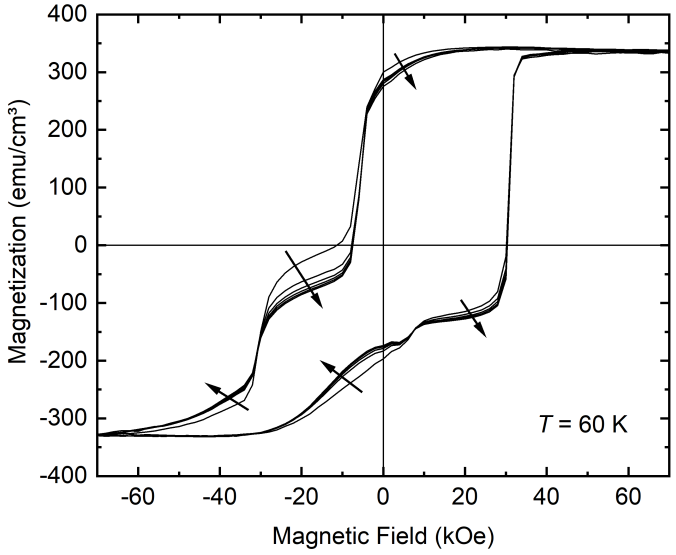

Figure 7.4: An example of the training effect in a $Tb_{19}Fe_{81}/Tb_{36}Fe_{64}$ bilayer. Measuring multiple consequent hysteresis loops after field-cooling shows the gradual change of the loop shape, as indicated by the arrows. With increasing cycle number, the difference to the previous loop becomes ever smaller.

higher heat dissipation in the target and thus influence the sputtering yield, a quick change of power could well influence the rate over at least a few seconds, until thermal equilibrium in the target is reached again. This would lead to an effective change of composition of the interlayer region.

In general, it can be seen that the *slow change* sample shows a much more stable DEB behaviour. The Tb- and Fe-dominated subloops are completely biased in opposite directions and clearly distinguishable. Accordingly, the regular slow change of sputtering power was chosen as the default for all further samples.

After observing the presence of DEB behaviour, the stability of the biasing was tested by cycling the whole field range multiple times. Such a "training" of the hysteresis loop is necessary to rule out the influence of reversible parts of the pinning layer on the observed H_{EB} [115, 312]. For this, the *slow change* sample was field-cooled to 60 K and the magnetic field swept from maximum to minimum five times. The resulting *M-H* hysteresis loops can be seen in Fig. 7.4. The change with successive field sweep cycles is indicated by the arrows.

As expected, the change is most noticeable between the first and second field cycle. The change in the fields at which certain switching events occur, however, hardly change at all after the second field cycle. Accordingly, it was deemed sufficient to cycle the field once before every measurement. This was done for all following measurements.

Notably, the overall behaviour of the measurement shown in Fig. 7.4 differs from that of the same sample shown in Fig. 7.3. The sample displayed two well separated subloops in the latter, while a part of the Tb-dominated subloop is not completely pinned in the former. This behaviour of increased bidirectional pinning over time was also observed for repeated measurements of the *fast change* and *with gradient* samples.

It is thus assumed that a sort of ageing effect might be responsible for the observed changes, since the diffusion of atoms or even some oxidation could subtly influence the composition and thus the behaviour of the interlayer region of these samples. Slight changes between original and repeated measurements were also observed for some of the other samples investigated in this work, but they were usually minor, even when months had passed between the two measurements. Still, this shows that the TbFe-based samples discussed here are not perfectly stable in regards to their magnetic properties.

Varying the composition of the Fe-dominated bottom TbFe layer

The next sample series that was investigated was prepared such that it had different compositions of the Fe-dominated layer. The overall layer stack can thus be described by $Si/SiO_2(sub.)/Pt(5\,nm)/Tb_xFe_{100-x}(10\,nm)/Tb_{36}Fe_{64}(10\,nm)/Pt(5\,nm)$, with x being the Tb-content that was varied for the Fe-dominated bottom TbFe layer. All of these samples were then measured in the same way as described at the beginning of this chapter.

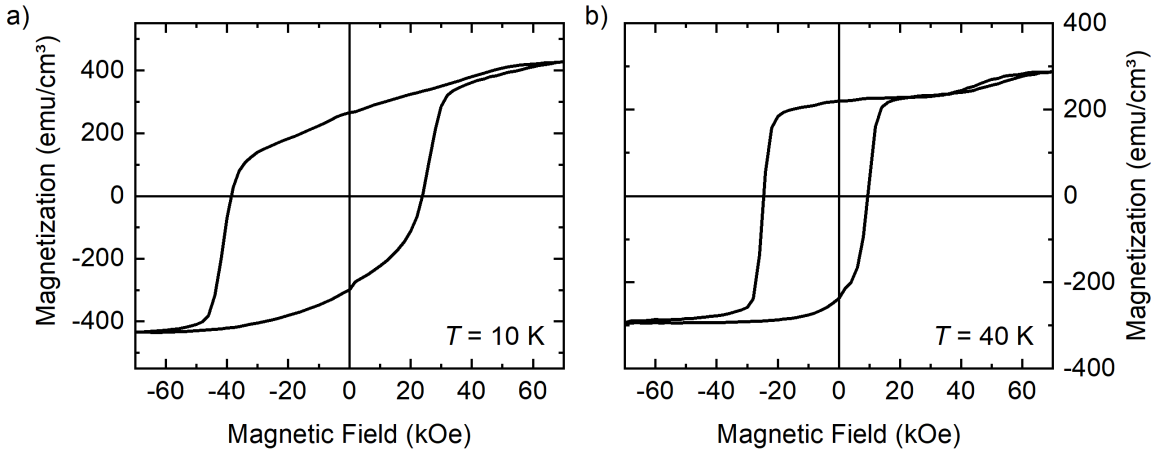

Figure 7.5: Comparison of the exchange-biased loops of a $Tb_{20}Fe_{80}/Tb_{36}Fe_{64}$ bilayer at a) 10 K and b) 40 K. While the switching of both layers is observable in b), only a single loop is observable in a), indicating that the Fe-dominated layer is not switchable with the available field at this temperature.

Before the EB behaviour of these samples will be investigated, one of the issues of this investigation shall be highlighted. Shown in Fig. 7.5 are the two M-H loops of the sample with $x = 20$ at a) $T = 10\,K$ and b) $T = 40\,K$. While the latter shows two easily distinguishable subloops shifted to opposite sides, the former seems to consist mostly of only one large opening. A second small opening at high positive fields cannot be clearly seen at such low temperatures. The reason for this is most likely that the Fe-dominated layer giving this highly shifted, low-magnetization signal is magnetically too hard to be switched by the available fields at very low temperatures below 40 K. Accordingly, only a very slight opening of the loop at high positive fields can be seen in Fig. 7.5 a), because most of the Fe-dominated layer has a $H_C + H_{EB}$ that exceeds the

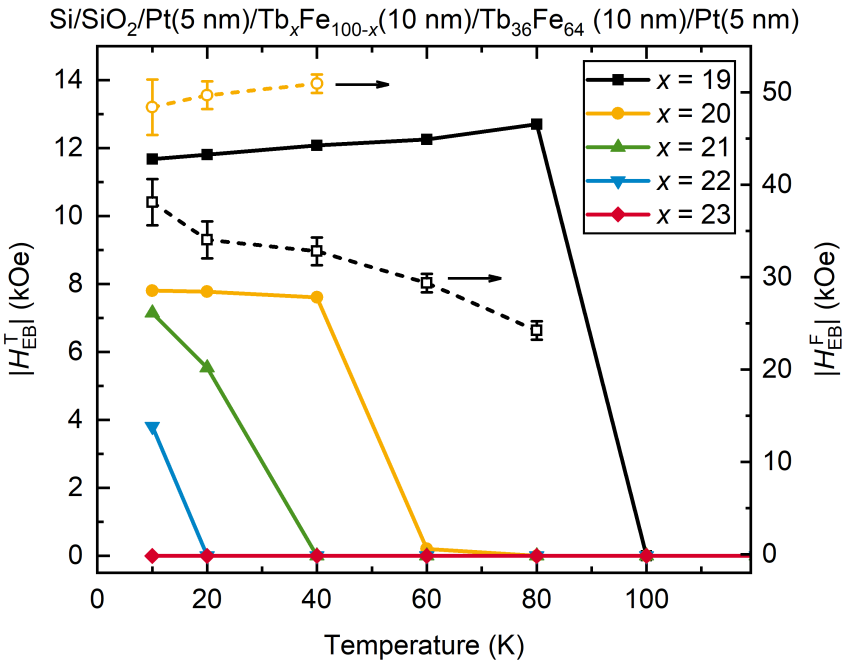

Figure 7.6: The change of the absolute value of the exchange bias field of the Tb-dominated layer (H_{EB}^{T}, solid symbols, left axis) and the Fe-dominated layer (H_{EB}^{F}, open symbols, right axis) of field-cooled $\mathrm{Tb}_x\mathrm{Fe}_{100-x}/\mathrm{Tb}_{36}\mathrm{Fe}_{64}$ bilayers with temperature and different composition x of the bottom layer.

available 70 kOe. The rest of this layer can be considered fixed and part of the pinning layer. Accordingly, the H_{EB} of the Fe-dominated layer can not always be determined at very low temperatures.

Further, the subloop of the Tb-dominated layer in Fig. 7.5 is shifted to negative fields. This is the opposite of what was observed in Fig. 7.3, suggesting that the interlayer for this second series of samples must be Tb-dominated. Since the Tb-content of the bottom layer was increased in this sample series, this can easily be attributed to the likewise increased Tb content in the interlayer, which was close to the compensation composition to begin with. This can also be regarded as a confirmation that the interlayer for the first three samples (those shown in Fig. 7.3) was indeed extremely close to the compensation composition and likely also in part Tb-dominated.

Knowing this about the behaviour of these samples, the values of the EB fields as determined from the M-H hysteresis loops can be investigated. The values for $|H_{\mathrm{EB}}|$ for the samples with varying Tb content x in the bottom TbFe layer are depicted in Fig. 7.6. The values for $x = 19$ are taken from the *slow change* sample discussed above, which had the same sample layout, only a different sign of H_{EB}. Accordingly, the values shown here are the absolute values to facilitate comparison.

The solid symbols in Fig. 7.6 show the shift H_{EB}^{T} of the Tb-dominated layer (left axis), while the open symbols show that of the Fe-dominated layer, H_{EB}^{F} (right axis). As can be clearly seen, the temperature at which the DEB behaviour can be observed

is strongly reduced with increased Tb content x in the Fe-dominated layer. The value of H_{EB}^{T} varies only slightly with temperature, but decreases with increasing x.

On the other hand, H_{EB}^{F} changes more strongly with temperature and is increased by an increase in x, seemingly behaving complementary to H_{EB}^{T}. For the samples with $x \geq 21$, no value for H_{EB}^{F} could be determined since only the loop of the Tb-dominated layer could be observed in the measurements, most likely due to the insufficient magnitude of the available magnetic field. However, the Fe-dominated layers did not increase the pinning of the Tb-dominated layer, as both the magnitude of H_{EB}^{T} and the maximum temperature at which EB can be observed are reduced even when the Fe-dominated layer can not be switched.

These results show that the interlayer properties are strongly influenced by the composition of the bottom Fe-dominated layer. The change in sign of the exchange bias fields shows that the interlayer switched from Fe- to Tb-dominated by increasing the Tb composition from 19 to 20 at.%.

TbFe/TbFe bilayers with added TbFe interlayer

Seeing how the bottom layer can influence the interlayer and thus the magnetic behaviour, we prepared another set of samples containing an intentional interlayer of fixed composition. In order to ensure maximum comparability, the total thickness of the TbFe layers was kept the same, so the total TbFe film was made up as follows: $\mathrm{Tb_{19}Fe_{81}}(9\,\mathrm{nm})/\mathrm{Tb}_x\mathrm{Fe}_{100-x}(2\,\mathrm{nm})/\mathrm{Tb_{36}Fe_{64}}(9\,\mathrm{nm})$. As always, the film was sandwiched between two Pt layers of 5 nm thickness each. Starting with $x = 25$, a composition at which the magnetic moments of Fe and Tb should compensate each other, the Tb content was increased up to $x = 30$ within this sample series.

For this sample series, x denotes the Tb content of the 2 nm thick $\mathrm{Tb}_x\mathrm{Fe}_{100-x}$ interlayer. The hysteresis loops of the samples at 80 K and 100 K are shown in Fig. 7.7. These are the temperatures at which the transition from exchange-biased to symmetrical M-H loops can be seen. Interestingly, the shifting direction of the subloop of the Tb-dominated layer indicates that the interlayer is mostly Fe-dominated for all values of x. This is surprising, as the interlayer compositions are all on the Tb-dominated side of the compensation composition. If the deposited interlayer was acting as the pinning layer, the Tb-dominant layer should be pinned in the direction of the cooling field, meaning that its subloop would be shifted to negative fields. One has to keep in mind, though, that thinner TbFe films show compensation at higher Tb contents than thicker ones. However, this is likely counterbalanced by the presence of the other two TbFe layers, effectively increasing the total thickness, so it is hard to say what the precise magnetic state of the interlayers is.

We can thus conclude that even though an intentional interlayer was deposited, the pinning itself was likely created by another Fe-dominated interlayer that must have formed between the $\mathrm{Tb_{19}Fe_{81}}$ layer and the intentionally deposited interlayer. This also explains why the pinning for $25 < x < 27$ is partially reversible, while it becomes much more stable and unidirectional for higher x: the higher Tb-content in the deposited interlayer helps forming an interlayer near compensation composition. A nearly

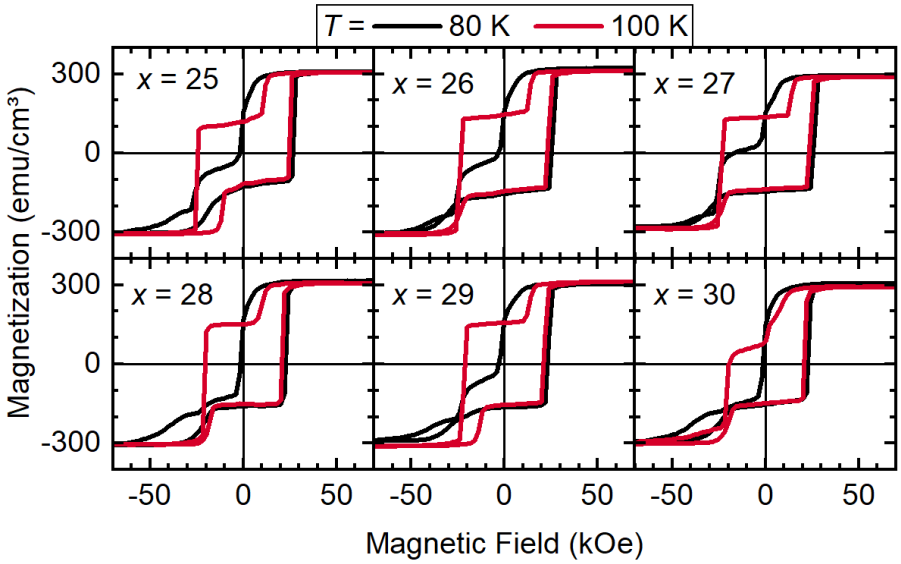

Figure 7.7: Comparison of the field-cooled hysteresis loops of various $Tb_{19}Fe_{81}(9\,nm)/Tb_xFe_{100-x}(2\,nm)/Tb_{36}Fe_{64}(9\,nm)$ trilayers at 80 K and 100 K. This is the temperature range at which these films show the transition from exchange-biased to symmetric loops. The samples with a higher Tb content in the interlayer (bottom row) show a more stable biasing at 80 K.

compensated pinning region with slightly higher Tb content would show magnetic compensation and thus a high H_C at slightly higher temperatures, making DEB visible for higher temperatures as well. This pinning region is too low in Tb-content for $x < 27$ to be uniformly high in coercivity, thus the biasing effect is only partial and we do not observe a whole loop shift as for $x = 28$ or 30.

Further, $x = 25$ was apparently too far away from compensation to serve as a pinning layer on its own. Since the temperatures at which we observed DEB were also much lower than those seen by Hebler et al., we decided to investigate the general magnetic behaviour of single layers of TbFe at different temperatures and different compositions.

7.2.2 Revision of the magnetic behaviour of TbFe thin films

Five different samples with Tb contents ranging form 19 to 23 at.% were deposited using the same procedures as described in chapter 7.1. The thickness of these single layers was kept at 10 nm, the same as that of the individual TbFe layers in the bilayer structures.

The hysteresis loops of a $Tb_{19}Fe_{81}$ layer in the two measurements directions and at low temperatures are depicted in Fig. 7.8. Again, the ip direction can be determined as the hard axis, with the oop direction showing a sharp switching behaviour. This narrow switching field distribution is retained for lower temperatures as well. The coercivity strongly increases with lower temperatures, while the magnetization only decreases slightly, as is expected for such an Fe-dominated TbFe film. Accordingly, the identification of the subloops shown in the previous chapter can be confirmed, as the

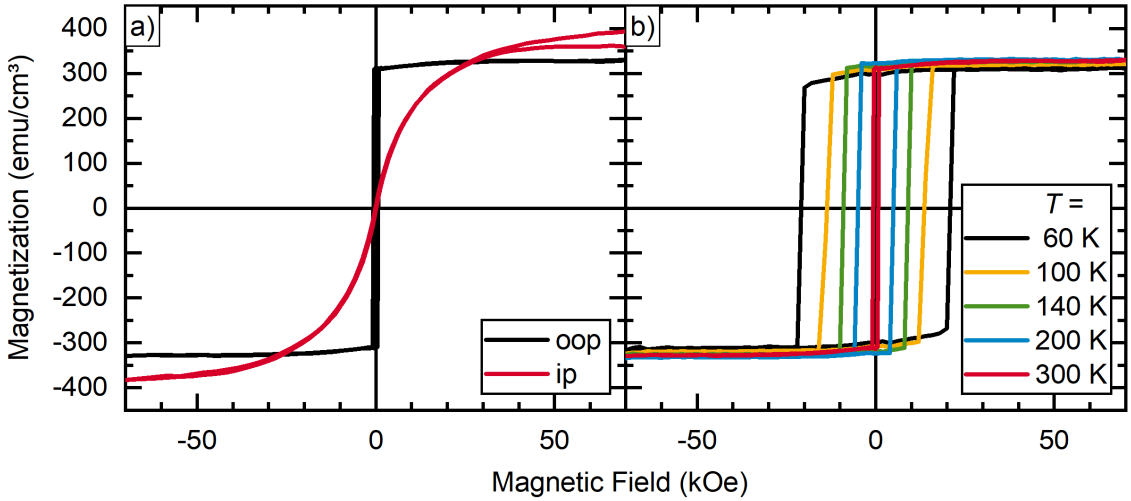

Figure 7.8: Hysteresis loops of a $Tb_{19}Fe_{81}$ single layer of 10 nm thickness a) in ip and oop directions at room temperature and b) in oop direction at various temperatures.

change of their respective magnetizations was the deciding factor for differentiating the signals from the two TbFe layers.

Comparing the different compositions of the Fe-dominated TbFe films, we can observe how the TbFe films get closer towards a compensated state with higher Tb content. The change of M_S and H_C of these samples with temperature is shown in Fig. 7.9. As is expected, the saturation magnetization decreases with lower temperatures and higher Tb content, while the opposite is true for the coercivity. Comparing the measurements shown here with those in ref. [225], we should expect a compensation to occur for a composition of $Tb_{25}Fe_{75}$, which the trends of M_S and H_C seem to confirm. However, the results shown in Fig. 7.7 suggested that the 2 nm thick $Tb_{25}Fe_{75}$ interlayer was not at magnetic compensation. Since the compensation temperature depends both on Tb content and thickness of the film, deviations can be expected not only between the samples investigated here and those in literature, but also between nominally identical bilayer samples investigated in this work.

This can be seen exemplarily by the oop M-H hysteresis loops of nominally rather similar samples at room-temperature. Figure 7.10 shows a comparison of samples consisting of nominally very similar TbFe layers, but displaying clearly different magnetic behaviour at room temperature.

The samples exhibit either a two-step or a three-step magnetic reversal. Which one of these is the case depends on the strength of the coupling between the two layers, but also on the K_u of the individual layers and their respective magnetizations. In general, there are three main energy terms determining the magnetic behaviour: the Zeeman energy, the interlayer exchange coupling energy between the two layers, the dipolar energy, and the uniaxial magnetic anisotropy of the respective layer. Depending on the strength of the different contributions, exchange-coupled systems can display two-step or three-step reversals [313, 314].

In all cases seen here, the Fe-dominated layer is the first one to reverse its magnetization when coming from saturation due to its lower K_u. In the case of Fig. 7.10 a), the

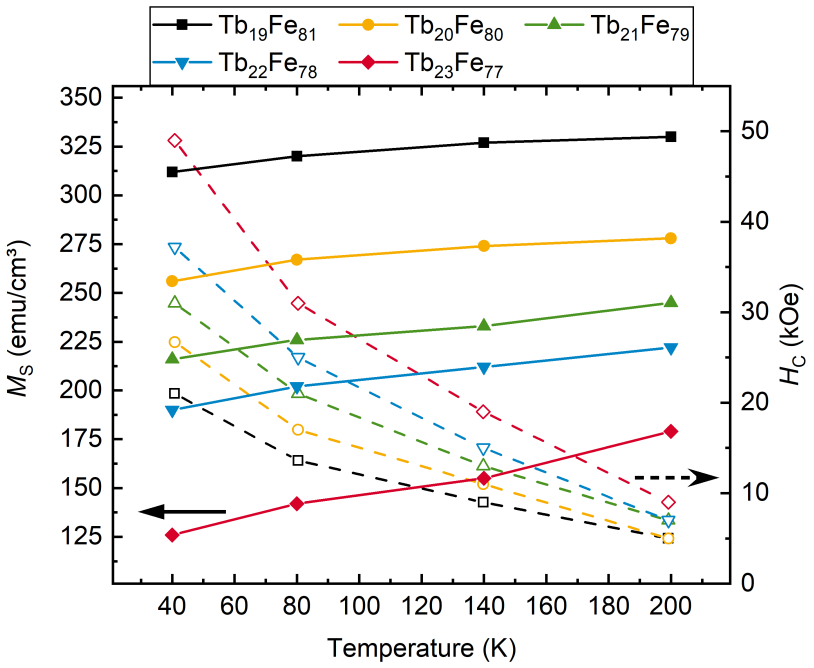

Figure 7.9: The evolution of saturation magnetization M_S (solid symbols, left axis) and coercivity H_C (open symbols, right axis) with temperature of different 10 nm thick Tb_xFe_{100-x} layers.

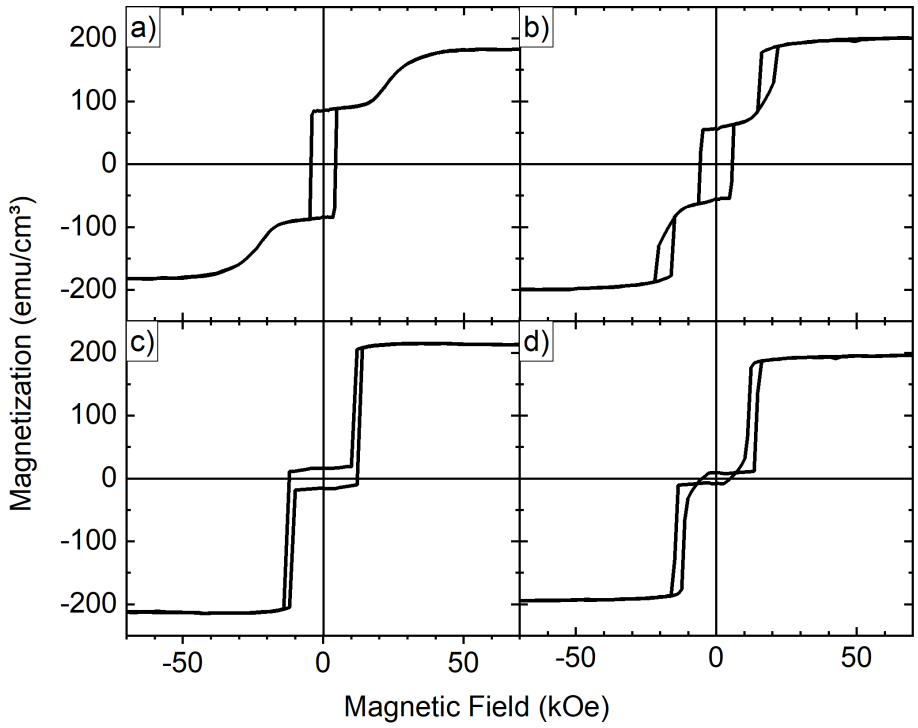

Figure 7.10: Comparison of the oop hysteresis loops of four nominally similar TbFe-based bilayer samples at room temperature: a) $Tb_{21}Fe_{79}/Tb_{36}Fe_{64}$, b) $Tb_{20}Fe_{80}/Tb_{36}Fe_{64}$, c) $Tb_{36}Fe_{64}/Tb_{21}Fe_{79}$ with added gradient interlayer, and d) $Tb_{19}Fe_{81}/Tb_{36}Fe_{64}$. The very different hysteresis loops are proof of the strong sensitivity of the magnetic behaviour on the layer and interlayer composition.

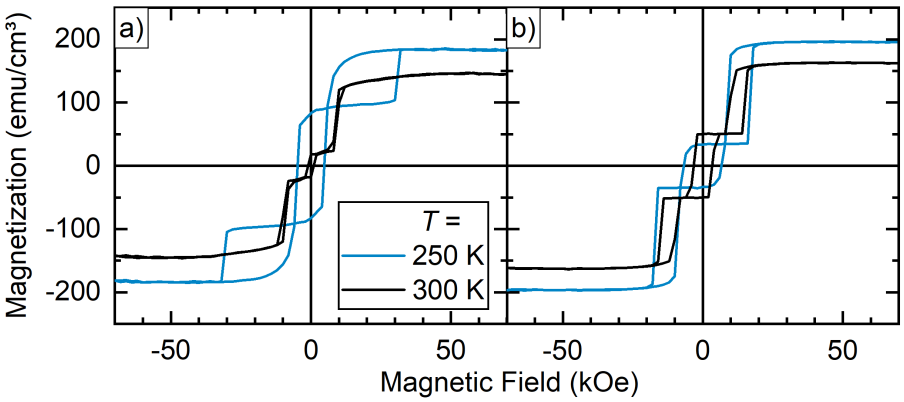

Figure 7.11: Comparison of the oop hysteresis loops of two different samples taken at 250 and 300 K. The layer stacks are a) $Tb_{36}Fe_{64}$ (10 nm)/$Tb_{19}Fe_{81}$ (10 nm) and b) $Tb_{19}Fe_{81}$ (9 nm)/$Tb_{23}Fe_{77}$ (2 nm)/$Tb_{36}Fe_{64}$ (9 nm). Both samples display a two-step reversal process with negative remanence at 250 K with a subsequent transition to a three-step reversal process at 300 K. Negative remanence values can be observed in strongly exchange-coupled systems such as these under certain conditions [315].

switching is gradual and non-hysteretic, so either the whole film is gradually tilted in its magnetization or a domain wall is slowly being propagated through the film by the change of the magnetic field. In Fig. 7.10 b), however, the switching is more sudden, suggesting that most of the film switches in an instant and that a domain wall can more easily propagate through the layer.

Figure 7.10 c) and d) show a two-step magnetic reversals, where each layer switches its magnetization only once. The interlayer exchange coupling is assumed to be lower here, since the switching of the Fe-dominated layer happens at lower magnetic field magnitudes and the Zeeman energy dominates the interlayer exchange coupling energy after the second switching event, when both layers are aligned in parallel. For the samples shown in Fig. 7.10 a) and b), the opposite is the case, as an antiparallel alignment and thus less favourable Zeeman energy is overcompensated by the more favourable antiparallel alignment of the two layers according to their strong interlayer exchange coupling.

Another interesting property is the negative remanence seen in Fig. 7.10 d). It is caused by the Fe-dominated TbFe layer having a larger magnetization than the Tb-dominated one, but still switching first. Even though such a behaviour seems unphysical due to the Zeeman energy, such a behaviour was already modeled in 1994 by O'Shea et al. [315] and also shown experimentally [316, 317]. It can appear in bilayer systems with antiparallel coupling where magnetization and K_u differ between the two layers. If the magnetization of the layer with lower K_u is higher, then its switching before zero field can be energetically favourable compared to the switching of the lower-magnetization layer. This seems to be the case for the sample shown in Fig. 7.10 d), but is not confined to this one sample.

A few other samples investigated in this work showed a two-step reversal process, and some of those also showed negative remanent magnetizations. However, most of these transition to a three-step reversal process as the temperature increases. Shown

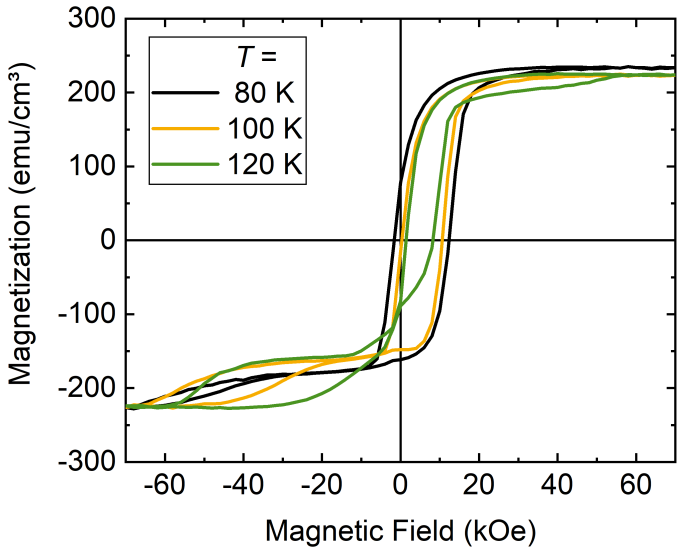

Figure 7.12: The double exchange bias behaviour seen in the field-cooled hysteresis loops of a $Tb_{36}Fe_{64}/Tb_{19}Fe_{81}$ sample at low temperatures. Compared to previous measurements, the DEB is stable at higher temperatures and shows a more stable biasing in the whole temperature range.

in Fig. 7.11 are two samples showing large negative remanence ratios M_R/M_S of -0.45 and -0.16 at 250 K. In both of these samples, it is the Tb-dominated layer that switches magnetization first, so it must have a lower K_u than the Fe-dominated layer at 250 K. At 300 K, however, the energy terms in these films have changed so much that a three-step magnetic reversal process is energetically favourable.

These investigations show that even small changes between samples can greatly influence the magnetic behaviour of the bilayer system. This has to be taken into consideration during the evaluation of the findings of this work, since it greatly influences reproducibility.

7.2.3 Investigation of inverted TbFe/TbFe bilayer structures

The bilayers of the samples previously investigated consisted of an Fe-dominated TbFe layer at the bottom and a Tb-dominated one on top. After investigating the influence of small differences in the samples on their magnetic behaviours, we decided to follow the layer structure that was used by Hebler et al. more closely. These consisted of a Tb-dominated TbFe film at the bottom and an Fe-dominated one on the top, i.e. an inversion of the samples investigated in chapter 7.2.1. If the layers did not influence each other, the results should be identical. However, with the knowledge of the sensitivity of the system even to small changes, it was expected that the order of layers would notably change the magnetic behaviour.

Indeed, a standard sample consisting of a $Tb_{36}Fe_{64}$ (10 nm)/$Tb_{19}Fe_{81}$ (10 nm) bilayer showed DEB at higher temperatures with the Tb-dominant layer at the bottom. The *M-H* hysteresis loops displayed in Fig. 7.12 show two clearly distinguishable subloops

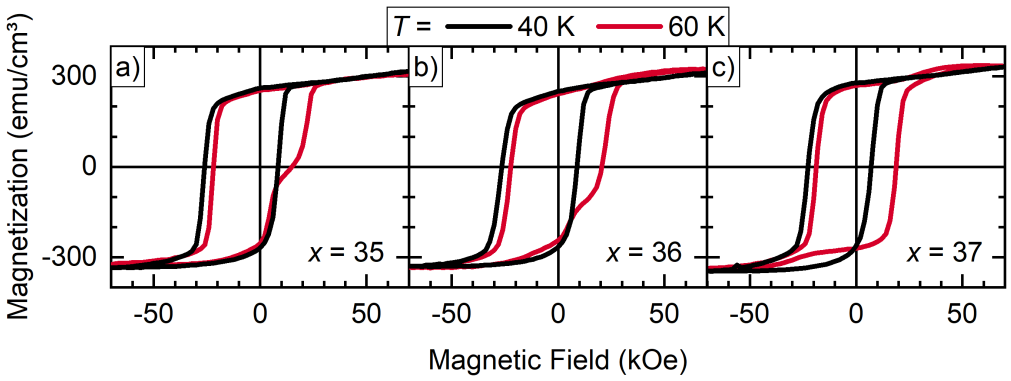

Figure 7.13: The comparison of field-cooled M-H loops of different $Tb_xFe_{100-x}/Tb_{19}Fe_{81}$ bilayers at low temperatures. All three samples show a completely pinned Tb-dominated layer at 40 K, but with increasing x, the Tb-dominated layer becomes less pinned at 60 K.

shifted in opposite directions up to temperatures of 120 K. Interestingly, the width of the inner loop is much reduced when compared to Fig. 7.3, which consist of the same layer structure, only inverted.

The differences between these samples could be explained by the difference in the growth dynamics: with less Fe in the bottom layer, there is less resputtering occurring when the second layer begins being deposited. This change is reinforced by the fact that fewer Tb atoms are deposited in the top layer, which would have a higher resputtering rate due to their higher atomic mass. This slight difference in resputtering rate would influence the interfacial region between the two layers, which in turn influences the DEB behaviour.

It is thus concluded that it is beneficial for the observation of DEB if the Tb-dominated layer is at the bottom of the bilayer. Accordingly, the Tb-dominated layer has been deposited first for all the remaining samples.

Varying the composition of the Tb-dominated bottom TbFe layer

Next, the influence of the bottom Tb-dominated layer on the magnetic behaviour was investigated. We slightly varied the Tb content x from 35 to 37 at.% and kept the top layer composition at $Tb_{19}Fe_{81}$. Figure 7.13 shows the M-H hysteresis loops at 40 K and 60 K, which is the maximum temperature at which DEB can be observed in these samples. This is a strong reduction compared to the previous sample (see Fig. 7.12), once more showing the differences that even nominally identical samples can display.

At 40 K, all three samples still show a completely exchange-biased loop of the Tb-dominated layer. The loop of the Fe-dominated layer cannot be clearly identified, but is expected to be partly visible in the sloped region at high positive fields. Interestingly, the shifting direction is indicative of a Tb-dominated pinning layer, as opposed to the more commonly observed Fe-dominated one.

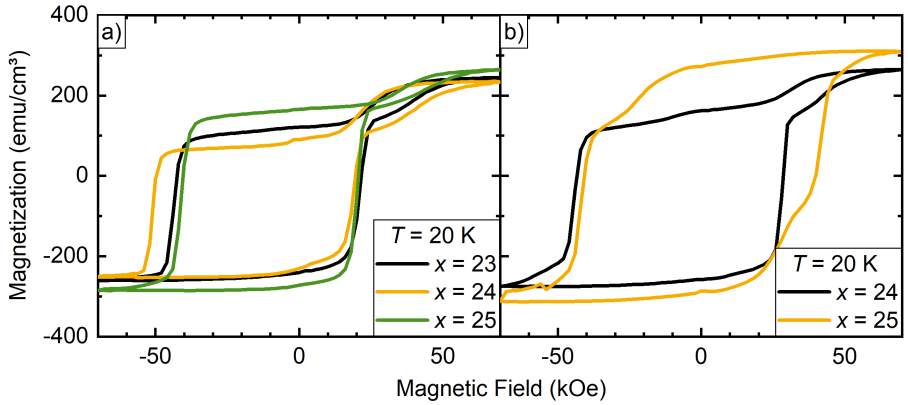

Figure 7.14: Comparison of the field-cooled hysteresis loops of samples containing an interlayer between a $Tb_{36}Fe_{64}$ (8 nm) and a $Tb_{19}Fe_{81}$ (8 nm) layer. The interlayer had varying composition x with Tb_xFe_{100-x} and a thickness of a) 4 nm and b) 8 nm. For all samples, the DEB behaviour is only seen at very low temperatures.

The influence of the changed Tb content is mainly visible in the M-H loops at 60 K. There, the higher Tb content in the bottom layer leads to a smaller part of the layer being pinned in one direction. For $x = 37$ (Fig. 7.13 c)), the loop is even completely symmetrical at 60 K, meaning that the whole layer is unpinned. The differences between these three samples are only small, though, so larger differences in the composition of the bottom Tb-dominated layer seem to be necessary to effect a larger change in magnetic behaviour.

Effect of added interlayers of different thickness and composition on inverted Tbfe/TbFe bilayers

The next focus of investigation was the effect that interlayers of different composition and thickness would have on the DEB behaviour of the TbFe-based bilayers. Five samples were deposited for this purpose. Three of those contained interlayers with a thickness of 4 nm and a thickness of 8 nm for both the Fe-dominated and the Tb-dominated layers. The remaining two had an interlayer that was 8 nm thick with the same thickness for the other two layers, so they were essentially trilayer samples.

The Tb composition of the interlayer in at.% is again referred to as x, so the layer stack is $Tb_{36}Fe_{64}$ (8 nm)/Tb_xFe_{100-x} (t)/$Tb_{19}Fe_{81}$ (8 nm). Unfortunately, the thicker interlayers were not beneficial for the emergence of DEB behaviour. Figure 7.14 shows the M-H hysteresis loops of these samples at 20 K, which was the highest temperature at which DEB was observable. The overall behaviour of all samples is quite similar, with a broad loop of the Tb-dominated layer shifted to negative fields and a small loop of the Fe-dominated layer at high positive fields. Once more, the shifting directions indicate a Tb-dominated pinning layer. The trilayer sample with $x = 25$ even shows an almost symmetrical hysteresis loop.

We can thus conclude that a thicker interlayer is not helpful for the formation of DEB. A thicker interlayer likely decreases the direct exchange coupling between the

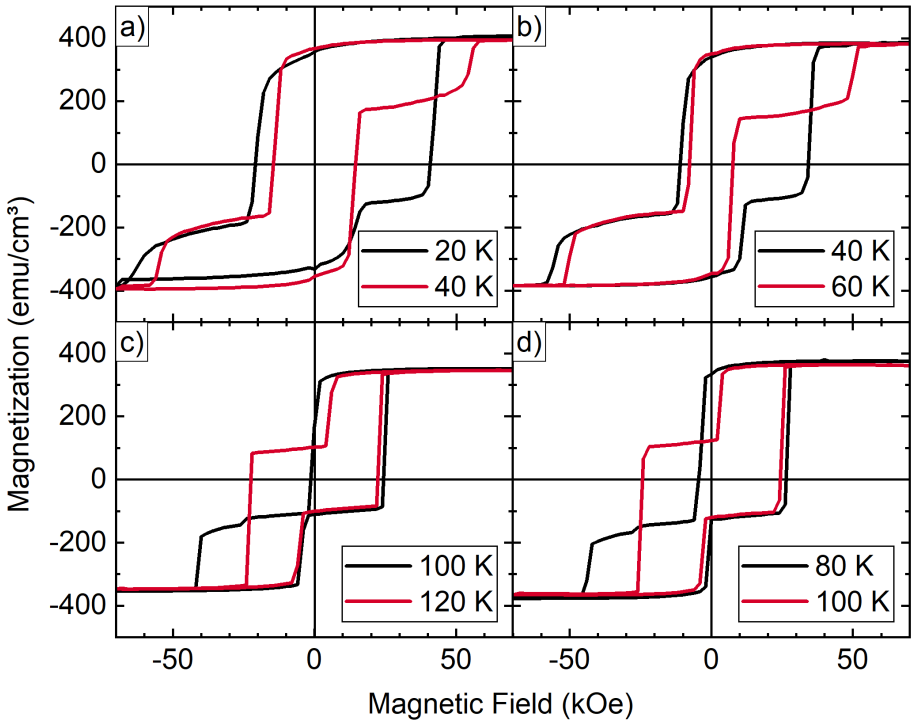

Figure 7.15: A comparison of low-temperature FC hysteresis loops of different TbFe-based film stacks deposited using RF sputtering for Tb. The samples investigated all contain a $Tb_{36}Fe_{64}$ bottom and a $Tb_{19}Fe_{81}$ top layer. In a), both films are 10 nm thick. A 2 nm thick interlayer between the two layers was additionally deposited for the other samples, consisting of b) a composition gradient from 36 to 19 at.% Tb, c) a $Tb_{23}Fe_{77}$ layer, and d) a $Tb_{25}Fe_{75}$ layer.

two TbFe layers, which cannot be completely compensated by the coupling to the interlayer itself with its vanishing magnetization. Further, a precise control of the interlayer composition would be required to reliably create a pinning effect on the two free layers.

In order to better control the deposition rate of Tb and thus the composition of the TbFe layers, a set of samples was deposited using an RF generator for the magnetron containing the Tb target. Using RF sputtering usually decreases the deposition rates, but in turn reduces the variation of deposition rate since small changes in sputtering power have less effect on the sputtering yield. Also, thin films deposited by RF sputtering usually show a smoother surface, which might influence the interface between the two TbFe layers in our samples.

Using this technique, we deposited a reference sample with the standard bilayer structure $Tb_{36}Fe_{64}$ (10 nm)/$Tb_{19}Fe_{81}$ (10 nm) as well as three samples with a reduced thickness of 9 nm for the two layers and different interlayers of 2 nm thickness. In these three samples, the thickness of the two free layers was reduced to 9 nm each to keep the same total film thickness equal. The interlayers were chosen to have a composition gradient or to have a fixed composition of 23 and 25 at.% Tb, respectively. The *M*-*H* hysteresis loops of these samples are shown in Fig. 7.15.

Both the sample without interlayer and the sample with a composition gradient transition from sharply defined DEB to a symmetric hysteresis loop already at very low temperatures (40 K and 60 K, respectively). However, the samples with the interlayer of fixed composition show a DEB that is stable to significantly higher temperatures. These also show very sharply defined switching fields, which indicates that no spin canting or "slow" domain wall propagation is involved in the magnetic reversal of the two free layers.

The usage of RF sputtering has most likely led to a much sharper interface between the different TbFe layers. As a consequence, the intermixing of the layers is much reduced and the sample without interlayer has almost no pinning potential at the TbFe/TbFe interface. The samples with an interlayer of fixed composition, on the other hand, showed a strong DEB, their interlayers being close to compensation and thick enough to exert a stable pinning on the free layers.

The outlier in this sample series is the sample with a composition gradient in the interlayer. If insufficient intermixing is the reason for the absence of DEB in Fig. 7.15 a), then the deposition of a composition gradient should compensate this. However, this is not the case. Accordingly, another factor must be important. Comparing Fig. 7.15 b) with c) and d), the thickness of the interlayer might be this factor. If intermixing is stronger, the interlayer region could potentially contain a wider region that is near compensation. If the interlayer region is too thin due to insufficient intermixing, then the region being close to compensation might be smaller than a few Ångström in width and thus essentially non-existent.

As a last sample series, we thus investigated the effect of thicker interlayers containing composition gradients on the DEB behaviour. As interlayers, we chose a 4 nm thick composition gradient, a 2 nm thick interlayer of fixed composition with composition gradients on either side, and an interlayer with three alternating composition gradients totalling about 6 nm. The thickness of the $Tb_{36}Fe_{64}$ and $Tb_{19}Fe_{81}$ layers was kept at 8 nm. The resulting composition profile of the samples is depicted in Fig. 7.16 b).

Figure 7.16 a) shows the hysteresis loops of these samples at the highest temperature at which DEB is observable. Comparing them to the samples with thick interlayers without a composition gradient (see Fig. 7.14), the gradients seem to be much better at creating DEB at higher temperatures. The addition of the region of fixed composition when compared to the sample containing only a straight composition gradient is minimal, the only difference being the slightly lower temperature at which the DEB is stable. On the other hand, the zigzag-gradient (right column in Fig. 7.16) only shows DEB at very low temperatures below 40 K, and interestingly has a Tb-dominated pinning layer as opposed to the Fe-dominated one of the other two samples. Considering that the average composition of the three gradients is on the Tb-dominated side, this is not too surprising.

In conclusion, we found that many small changes in the TbFe-based bilayer samples can have a strong effect on their magnetic properties, especially the emergence and stability of DEB. The intermixing at the interface of the two TbFe layers could be confirmed to be the reason behind the development of the double exchange bias phenomenon. Attempts at manipulating this interfacial region have shown that both

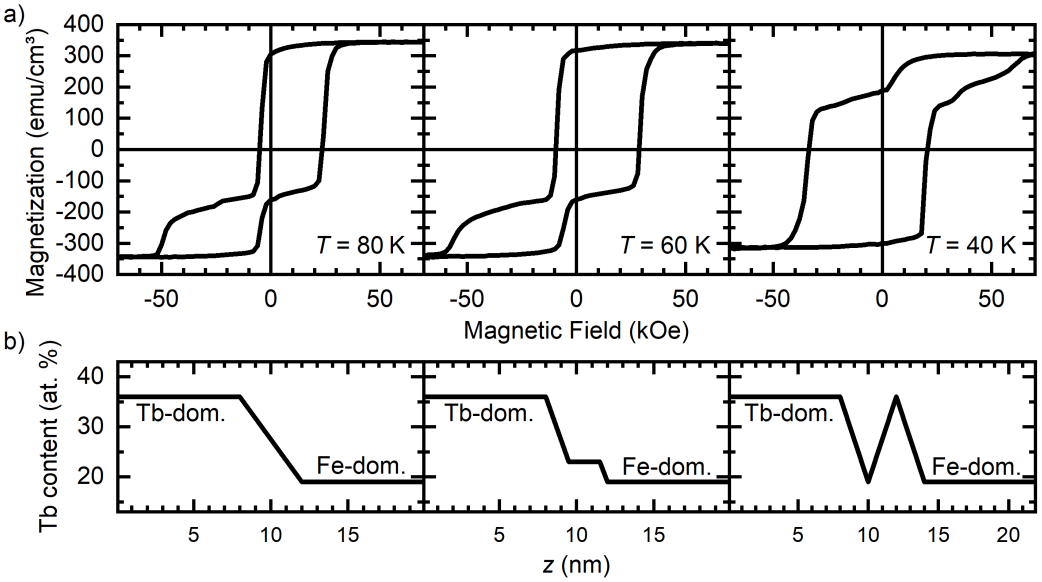

Figure 7.16: A comparison of the DEB behaviour of three samples with a thicker interlayer of 4-6 nm thickness. a) The FC hysteresis loops of the samples at the maximum temperature at which DEB was observable and b) their corresponding composition profiles along the thickness of the respective layer stack.

composition gradients as well as interlayers of fixed composition can lead to DEB behaviour, but sometimes to a lesser degree than a bilayer structure. Indeed, the most stable DEB, i.e. the one that was still observable at the highest temperatures, was seen for a simple bilayer structure of $Tb_{36}Fe_{64}/Tb_{19}Fe_{81}$. Large differences in magnetic behaviour of nominally identical samples showed the low reproducibility of these bilayer systems, which are caused by the extremely high sensitivity of the TbFe system on the precise composition of the two elements.

7.3 Ultraslow magnetic relaxation

During the investigation of the TbFe-based bilayer structures, one sample in particular showed a very peculiar magnetic behaviour at low temperatures. The sample consisted of a $Tb_{20}Fe_{80}/Tb_{36}Fe_{64}$ bilayer, with substrate, seed layer, and capping layers as depicted in Fig. 7.1. In the temperature range between 80 and 140 K, which is above the temperatures at which this sample showed exchange bias, the *M*-*H* loops showed an overcrossing of the hysteresis loop branches. This overcrossing happens just after the switching of the Tb-dominated layer. Figure 7.17 shows the symmetric hysteresis loops at 100, 120, 130, and 140 K, displaying this overcrossing behaviour.

The overcrossing branches indicate that an energetically unfavourable parallel alignment of the two TbFe layers exists after the switching of the Tb-dominated layer. At 100 K, this metastable configuration is present up to saturation, but the Fe-dominated layer slowly switches again when reducing the applied magnetic field, leading to an antiparallel alignment and a decrease in magnetization. Thus, the ascending branch shows a higher magnetization than the descending branch between 18 and 70 kOe. The

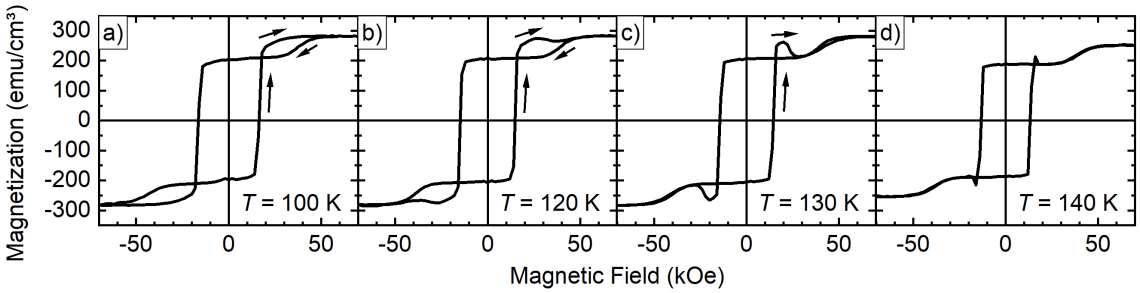

Figure 7.17: A depiction of the overcrossing behaviour observed for a $Tb_{20}Fe_{80}$ (10 nm)/$Tb_{36}Fe_{64}$ (10 nm) bilayer. In a), the magnetization goes to saturation after the overcrossing, while it decreases even with an increase in field in b) and c). In d), the overcrossing is strongly reduced, but still noticeable.

same can be observed for the other measurements depicted in Fig. 7.17, but the effect is reduced at higher temperatures.

For temperatures above 120 K, the Fe-dominated layer starts to revert its magnetization with increasing magnetic field after the overcrossing. This is illogical, since a higher magnetic field should render a parallel alignment of the two layers more stable, not less so. At 130 K, this switching is even completed when the field reaches 30 kOe, after which the applied field starts switching the Fe-dominated layer once more going towards saturation. At 140 K, the overcrossing is almost vanishingly small, but still observable.

Very fast measurement techniques like the magneto-optical Kerr effect (MOKE), where the sweeping of the magnetic field from maximum to minimum can happen within only a few seconds, can sometimes show an overcrossing if the magnetization dynamics are in the same range of speed as the measurement itself. However, SQUID-VSM is known for being a very slow measuring technique, where field stabilization and signal integration at each field step take a few seconds. Can this overcrossing behaviour then be real at all?

The overcrossing of hysteresis branches was first seen in the Stoner-Wohlfarth model, for angles between the easy axis and applied magnetic field near 90 ° [318]. This was generally considered "non-physical" and an error of the model, since a cycling of such a clockwise hysteresis would produce energy indefinitely, and subsequent models formulated conditions to eliminate the possibility of such results [319] or found more accurate ways to calculate hysteresis loops [320].

However, recent research has shown experimental proof that the overcrossing of hysteresis branches can actually exist [321, 322]. Even if the overcrossing was only marginal, this showed the possibility of a clockwise hysteresis, i.e. where magnetization of the descending branch is lower than that of the ascending branch. Field cycling through such a loop would allow to extract energy from the system indefinitely. The observed phenomenon does not violate thermodynamics, though, since the overcrossing can only be achieved as part of the large, counterclockwise hysteresis, so no net energy is created in the system during magnetic field cycling.

Figure 7.18 shows a schematic representation of the switching events that happen in the TbFe-based bilayer sample during a field sweep starting from negative saturation.

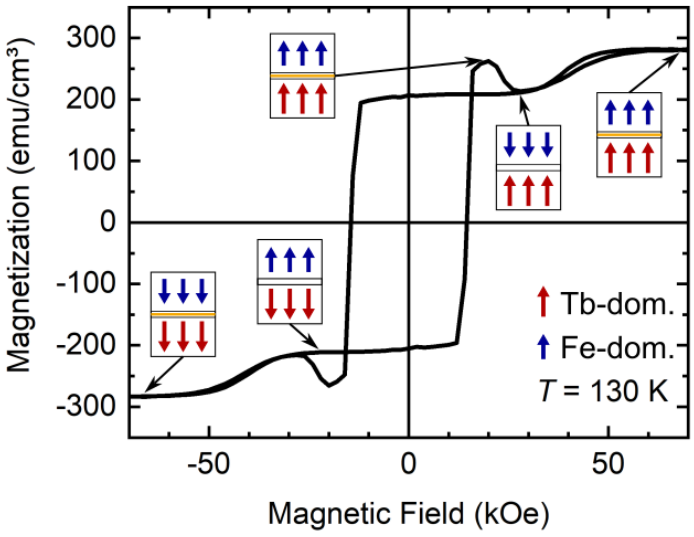

Figure 7.18: A schematic depiction of the magnetic alignment of the two TbFe layers at different points of the overcrossing hysteresis loop, starting at negative saturation. The Fe-dominated layer (blue arrows) has a lower magnetization than the Tb-dominated layer (red arrows), so the switching events can be identified beyond doubt. A yellow line in the interlayer region signifies a magnetic domain wall.

With both layers being aligned along the external field and thus parallel to each other, there is a magnetic domain wall present at the interface between the two. When reducing the magnitude of the magnetic field, the Fe-dominated layer switches its magnetization slowly, still being stabilized by Zeeman and anisotropy energies, ending in the annihilation of the domain wall in the antiparallel configuration of the two layers.

Applying a sufficiently large positive field, the Tb-dominated layer also switches its magnetization. Both layers have thus switched once, leaving their magnetizations parallel to each other. This again requires the existence of a magnetic domain wall, which is energetically unfavourable. Upon further field increase, the Fe-dominated switches again, transitioning the sample to its energetically favourable antiparallel state without domain wall. Only with further increase of the magnetic field can the magnetization of the Fe-dominated layer slowly be aligned with the external field, leading to the final parallel configuration at saturation.

Since the switching of the magnetization of the Fe-dominated layer against the external field with increasing magnetic field magnitude seen in Fig. 7.18 still seems illogical considering the sample layout, we considered that the increasing field is not actually the driving force here. Instead, we investigated how time would affect the magnetization of the bilayer system when the magnetic field is kept constant after the switching of the Tb-dominated layer.

These measurements were performed at different positive field values above the overcrossing point, which was at 16 kOe at 130 K, after the sample was previously saturated in the negative field direction. The constant field at which the sample was held is referred to as the relaxation field H_{relax}, and the sample was allowed to stay at this stable field for 10 minutes once the field was reached.

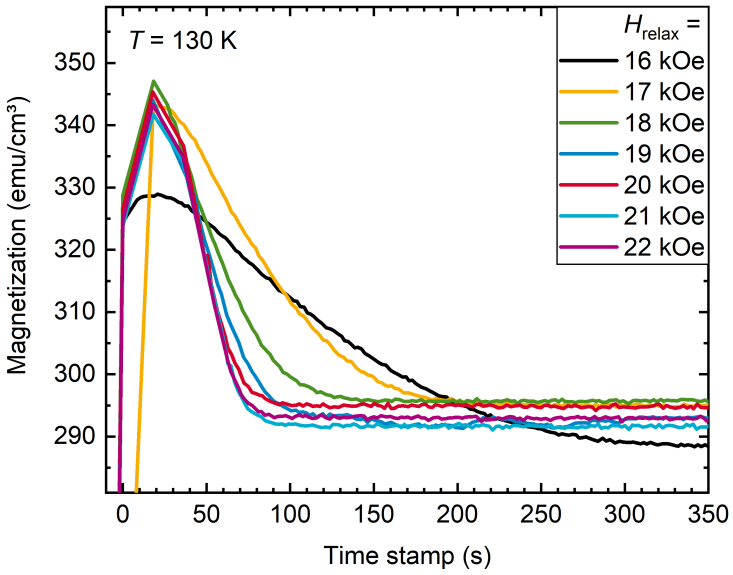

Figure 7.19: The relaxation of magnetization over time in a constant magnetic field at 130 K. The sample was previously saturated at -70 kOe, and all relaxation field values H_{relax} lie above the overcrossing point, which lies just below 16 kOe.

The resulting *M*-*t* measurements for different values of H_{relax} are shown in Fig. 7.19. Indeed, the decrease in magnetization is not caused by an increase in field, but by a slow relaxation into the stable antiparallel configuration (*in spite* of the field). For higher relaxation fields above 21 kOe, this state is reached about 90 seconds after the overcrossing. Incidentally, this is the same amount of time that passed between the crossover and the reaching of the antiparallel state in the hysteresis loop shown in Fig. 7.17 c).

For lower relaxation fields, the Fe-dominated layer takes longer to switch its magnetization. Just after the overcrossing, for $H_{\mathrm{relax}} = 16$ kOe, around 300 seconds pass until the antiparallel state between the two TbFe layer is reached. This is counterintuitive, since the Fe-dominated layer switches its magnetization to oppose the external field, which should be easier at lower field values. Accordingly, another effect must be the driving factor for this switching.

In the state of parallel alignment of the two TbFe layers, a domain wall exists at the interface between the two. Knowing that there is an interlayer region with a high coercivity, as discussed in the previous chapter, we have to assume that this domain wall is situated on the Tb-dominated side of the interlayer immediately after the Tb-dominated layer has switched its magnetization, which fits to previous observations by Schubert et al. [33]. In order for the stable antiparallel state to be reached, the domain wall has to propagate into and through the Fe-dominated layer. Thus, it first has to traverse the hard interlayer, which poses another energy barrier.

An increase in the magnetic field can then be thought of as a pushing force compressing the domain wall against the hard interlayer. With the domain wall compressed more strongly, a stronger torque is exerted on the magnetic moments in the inter-

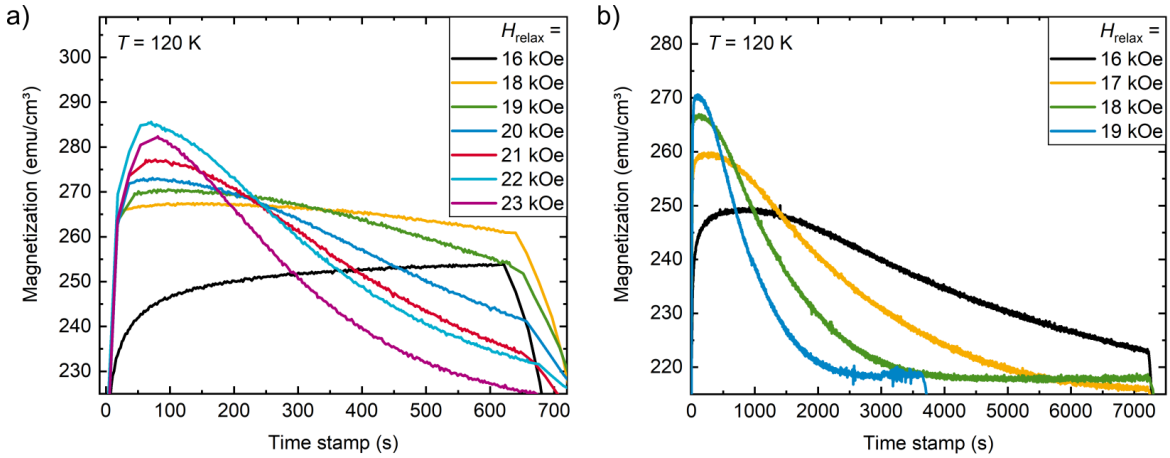

Figure 7.20: The magnetic relaxation measurements taken at 120 K. The duration of the measurements was a) 10 minutes and increased to b) 1 and 2 hours for the lower relaxation field values, as the relaxation was too slow to be observed in the first measurement.

layer. Finally, the domain wall traverses the interlayer and can progress through the Fe-dominated layer.

The question now is why this process can happen at all with time being the only variable. With all other forces being constant, there must be an inherent magnetic inertia in the system that allows only for a slow change of alignment of magnetic moments. This is reminiscent of magnetic viscosity, a phenomenon that also shows a slow change of magnetization after a change in magnetic field [323]. This change is generally larger for fields near H_C and linear in $log(t)$, but can also show a symmetric S-shape [324]. However, the ordinary magnetic viscosity leads to an alignment of the magnetic moments along the external field direction, which is the opposite of the behaviour observed here.

Another explanation might be the extraordinary magnetic viscosity that can be seen in systems with unidirectional anisotropy, such as exchange-biased systems [325]. This can change the equilibrium condition of magnetization, so that the system relaxes towards a certain magnetic state as determined by the exchange interactions within. These are mostly influenced by magnetization processes in ferrimagnetic or near antiferromagnetic regions in a sample, which are present in the sample at hand.

One material class that also shows gradual changes of magnetization over extended time spans is spin glasses. These rely on the frozen spins of frustrated magnetic clusters that are diluted in a non-magnetic matrix [326]. They show a non-exponential decay of magnetization over time in a field-cooled remanent state [327]. However, the TbFe sample consists of a completely ferrimagnetic material, so it cannot be considered a spin glass in a technical sense. Still, magnetic frustration is likely a very important factor for the relaxation behaviour.

As already mentioned, the sample region mostly responsible for the high viscosity is the interlayer region. When the Tb- and Fe-dominated layers are aligned in parallel, there must be a domain wall in between them, with magnetic moments of both Tb and Fe pointing at least partially in the in-plane direction. Paired with the random

distribution of in-plane components of the local anisotropy axes of the Tb atoms, the in-plane components of the domain walls will point largely in different directions. This leads to an immense amount of frustration in this thin region, which explains why the domain wall can not easily propagate.

Since the interlayer is thin as well as basically magnetically compensated, its magnetization dynamics do not alter the magnetization itself: this is done by the change of magnetization of the Fe-dominated layer. At this point, we cannot be certain whether the magnetic moments in this layer coherently rotate, are laterally split up in domains, or show a tilting gradient along the film normal. Measurements presented later in this chapter will illuminate this issue, but first, the influence of temperature on the relaxation dynamics shall be investigated.

Figure 7.20 shows the magnetic relaxation measurements at 120 K for different relaxation durations. The decrease in magnetization is slower than at 130 K, not reaching equilibrium after 10 min for the fields shown. These relaxation measurements now show clearly that relaxation fields closer to the overcrossing point lead to vastly higher relaxation times. The graph for $H_{\mathrm{relax}} = 16\,\mathrm{kOe}$ in Fig. 7.20 a), which is just above the overcrossing point, suggests that the magnetization approaches a higher magnetization value than the antiparallel one, which would only be possible if at least part of the Fe-dominated layer remained parallel to the Tb-dominated layer. However, if the relaxation duration is increased sufficiently (Fig. 7.20 b)), it becomes clear that also for this value of H_{relax}, the antiparallel state is the stable one. The initial increase of magnetization seen for low values of H_{relax} can be explained by the compression of the domain wall, which is situated in the Tb-dominated layer, thus allowing more magnetic moments to point along the field direction.

Contrary to the two temperatures at which relaxation measurements were just shown, the hysteresis loop taken at 100 K does not show a decrease in magnetization after the overcrossing. Does this mean that the parallel alignment is stable, even if an antiparallel state is reached after saturating the sample and reducing the field again to the same value? First relaxation measurements indeed seemed to indicate that the magnetization increases for relaxation field values up to 5 kOe above the overcrossing at 18 kOe. However, it was already shown that a slight increase in magnetization does not exclude a decrease at longer relaxation durations. Accordingly, the relaxation fields were increased further, up to 40 kOe.

The relaxation measurements, shown in Fig. 7.21, once more show a steady decrease in magnetization over time. Relaxation fields exceeding 27 kOe are needed in order for any decrease to be noticeable over the course of two hours, though. It can only be assumed that also with lower H_{relax}, a decrease and consequent approach of the magnetization towards the antiparallel value will happen for longer relaxation times. However, such measurements could take days to make the changes visible, as a relaxation measurement over ten hours with H_{relax} =29 kOe has shown that a complete relaxation would take at least two days.

To see if the relaxation has any major influence on the rest of the hysteresis loops, we then compared the minor loops (from - 70 kOe to H_{relax} and back) taken without relaxation ($t_{\mathrm{relax}} = 0$) with those measured alongside the relaxation measurements

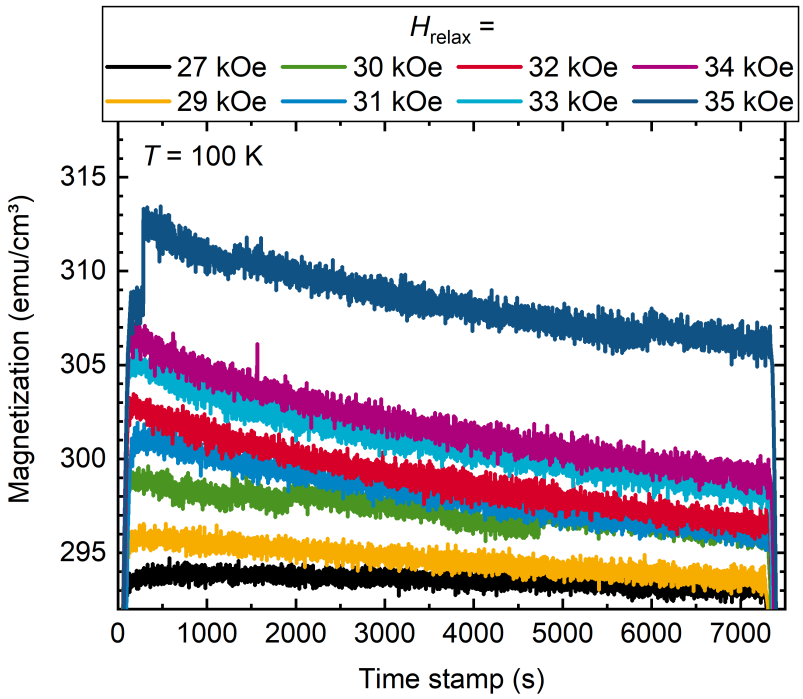

Figure 7.21: The relaxation measurements taken at 100 K for different values of H_{relax}. Even though the overcrossing point at this temperature lies at 18 kOe, a reduction of magnetization was only observed for relaxation fields above 27 kOe in this time range. The low slope indicates immense relaxation durations until the stable antiparallel configuration is reached.

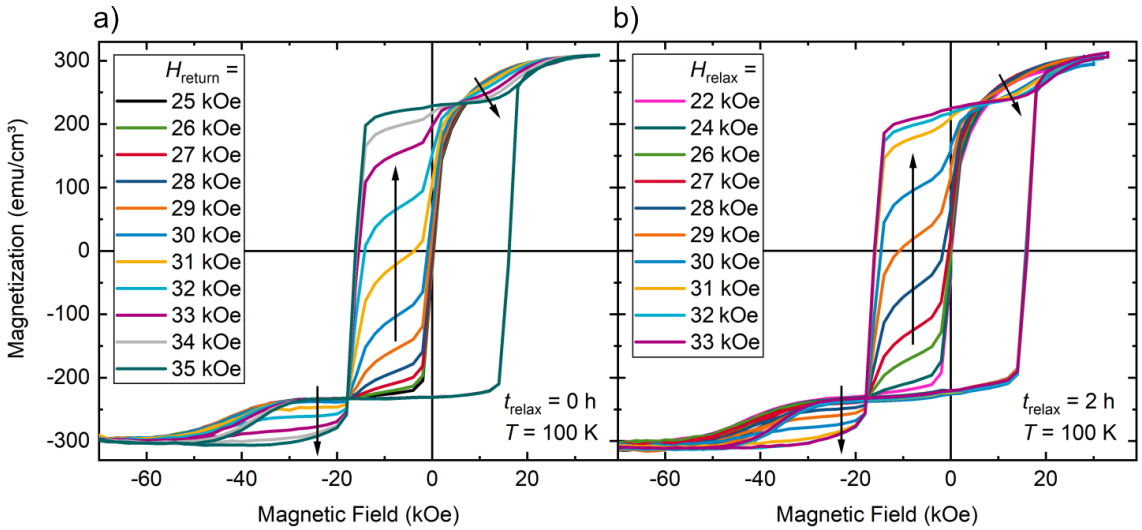

Figure 7.22: A comparison of a) minor hysteresis loops and b) the hysteresis loops measured during the relaxation measurements presented above. The arrows show the direction of the loops change with increasing values of maximum applied field. The only difference between the two measurement procedures is the waiting time t_{relax} at the maximum positive field, which was 0 in the case of a) and 2 hours in the case of b). The respective maximum fields are referred to as a) H_{return} and b) H_{relax}.

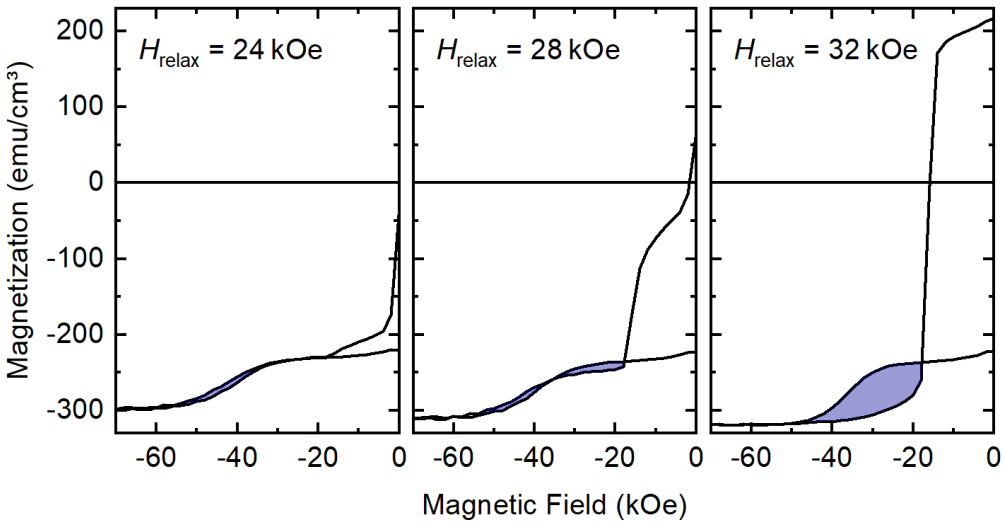

Figure 7.23: A depiction of the different overcrossing behaviours seen in the hysteresis loops of the relaxation measurements at 100 K. Depending on the relaxation field H_{relax}, a different fraction of the Tb-dominated layer is re-pinned to switch its magnetization at -18 kOe. Further, the degree of overcrossing, as quantified by the overcrossing area between the ascending and descending hysteresis branches between -18 and -70 kOe (shaded blue), is increased with H_{relax}.

($t_{\mathrm{relax}} = 2\,\mathrm{h}$). For the sake of simplicity, the maximum field of the minor loops without relaxation is referred to as the return field H_{return}, since there was no actual relaxation measurement done at this point. The two sets of measurements are shown in figs. 7.22 a) and b), respectively.

In both cases, a gradual change from a DEB loop towards a more symmetric loop with stronger overcrossing can be observed. This behaviour alone gives a lot of insight about the dynamics inside the interfacial region between the two TbFe layers. If the interlayer was completely homogeneous, the domain wall would penetrate the whole layer at the same time at a certain critical field or relaxation duration. This would in turn lead to a sharp transition from DEB to symmetric loop, which is not observed here. Instead, the interlayer must be quite inhomogeneous, which is not surprising for the amorphous structure.

An inhomogeneous interlayer would allow the domain wall to penetrate easier in some regions compared to others, meaning that the pinning direction of the interlayer is also switched in these regions. With increasing relaxation field, these regions grow laterally and re-pin a larger part of both TbFe layers in the opposite direction, thus gradually approaching the shape of the full hysteresis loop.

The comparison of three measurements with different relaxation fields in Fig. 7.23 shows this more clearly. It can be seen that ascending and descending branch are alike for low H_{relax}, but increasing the relaxation field leads to the onset of overcrossing at -18 kOe and an elevation of the descending branch magnetization at low negative fields, indicating that an increasingly larger part of the Tb-dominated layer is re-pinned. For $H_{\mathrm{relax}} = 32\,\mathrm{kOe}$, the loop is almost identical to the full loop, so re-pinning is almost complete in this measurement.

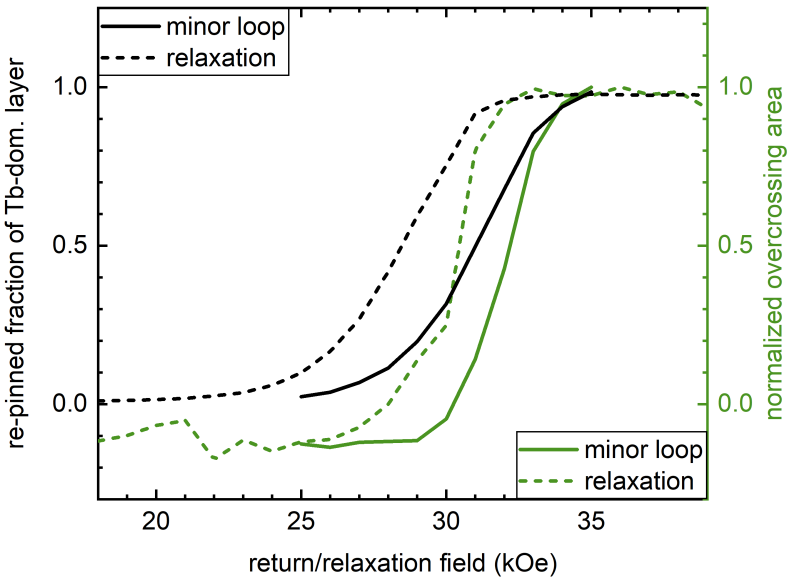

Figure 7.24: Comparison of the re-pinned fraction of the Tb-dominated layer (black) and the degree of overcrossing (green) between the minor loops and the relaxation measurement loops for various values of return field or relaxation field, respectively. The degree of overcrossing is represented by the overcrossing area normalized to its maximum value.

For $H_{\mathrm{return}}(t_{\mathrm{relax}} = 0) = H_{\mathrm{relax}}(t_{\mathrm{relax}} = 2\,\mathrm{h})$, the transitions towards the more symmetric shape in the measurements with relaxation is more pronounced than in the minor loops without relaxation. In order to compare the two different types of measurement, the fraction of the Tb-dominated layer that is re-pinned and the amount of overcrossing are measured in each loop.

The former was determined by comparing the magnetization levels at -4 kOe, when the switching of the originally biased Tb-dominated layer is completed. If the magnetization at this point is identical to that of the ascending branch, 0 % have been re-pinned, and if it is at the value of the descending branch of the full loop, 100 % have been re-pinned. This assumes that the Fe-dominated keeps its positive magnetization throughout the whole process. The amount of overcrossing was then measured as the area enclosed between the two hysteresis loop branches at negative field from the point of overcrossing at -18 kOe to saturation at -70 kOe (blue shade in Fig. 7.24).

The resulting values are shown in Fig. 7.24. Both types of measurement show a very similar behaviour, but the differences are easily seen: with a relaxation of two hours, the field necessary to achieve a certain amount of re-pinning is reduced by around 2.5 kOe. Interestingly, this field shift is constant, so it is independent of anything except the relaxation duration. This includes any amount of switching in the interlayer that is caused by just ramping up the field to H_{relax}. Accordingly, the interlayer domains grow at the same rate, no matter how big they are or how strong the magnetic field is.

Another conclusion from Fig. 7.24 is that the onset of overcrossing is later than that of re-pinning of the Tb-dominated layer, but its transition is completed at the same time. The overcrossing area is coupled to the fraction of the Fe-dominated layer that is aligned parallel to the Tb-dominated layer after the overcrossing. The delayed onset of

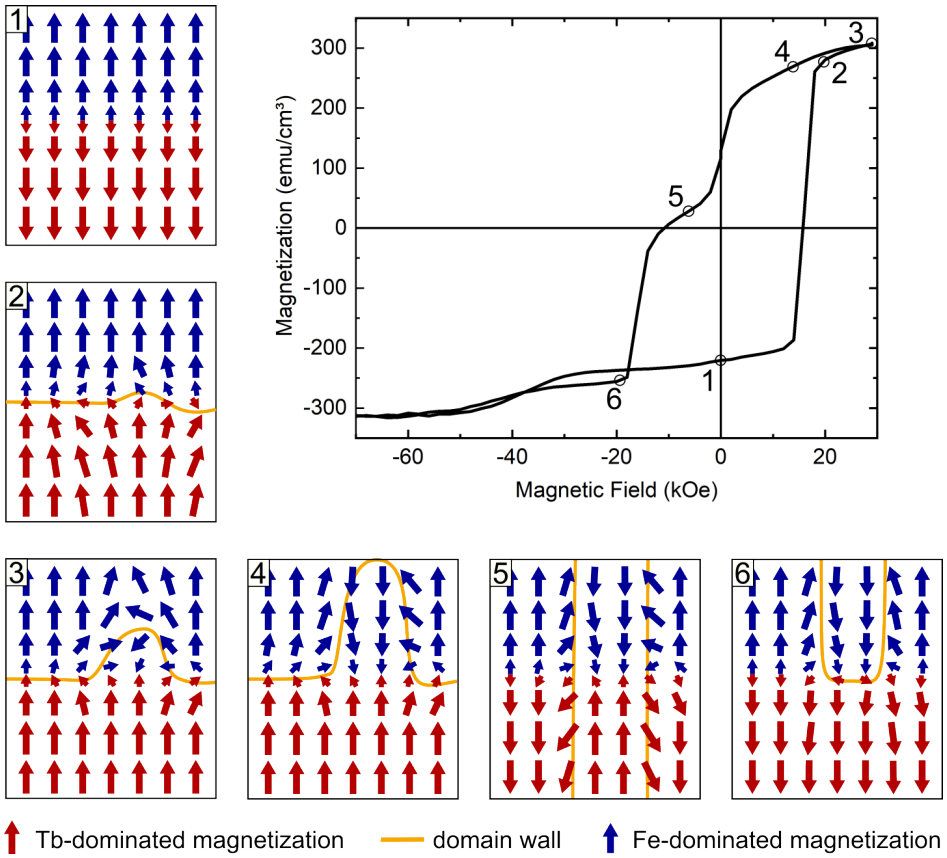

Figure 7.25: Detailed schematic of the alignment of magnetic moments and the magnetic domain wall in the TbFe bilayer at different points during an *M-H* measurement at 100K. During the relaxation at point 3, the domain wall can traverse the hard interlayer region and advance into the Fe-dominated layer, thereby reducing the net magnetization.

overcrossing indicates that the interlayer can start re-pinning the Tb-dominated layer without also re-pinning the Fe-dominated layer. However, it is also possible that the switching of the Tb-dominated layer also induces a switching of the Fe-dominated layer for low degrees of re-pinning, which would reduce the overcrossing area. Only when the domains in the interlayer are big and stable enough to withstand the switching of the Tb-dominated layer can an overcrossing be observed.

We can now reconstruct the landscape of magnetic moments in the sample with the details we learned from the minor loops and relaxation measurements. The behaviour and alignment of magnetic moments in the $Tb_{20}Fe_{80}/Tb_{36}Fe_{64}$ bilayer sample at different points of the hysteresis loop is depicted in Fig. 7.25. At point 1, the sample is in negative remanence and the two layers are in an antiparallel configuration, so no domain wall exists between the two.

When the Tb-dominated layer switches magnetization at +18 kOe at point 2, a new domain wall is created. Due to inhomogeneities in the interlayer region, this domain wall is not at the exact same vertical position everywhere. The increase of magnetization seen between point 2 and 3 is caused by the compression of the domain wall against the interlayer region, effectively aligning more of the Tb-dominated magneti-

zation with the field. At this point, the domain wall can also penetrate the interlayer region in some places.

When holding the magnetic field at point 3, the domain wall can propagate laterally through the interlayer region. Most of the magnetization of the Fe-dominated layer is still aligned with the external field, though, since Zeeman energy and anisotropy energy still stabilize this configuration. Accordingly, the magnetization will only marginally change. Only if the domain wall has penetrated sufficiently large portions of the interlayer will the exchange coupling energy dominate over the other energy contributions and the magnetization decrease slowly.

The same can be achieved when the external magnetic field is reduced, such as at point 4. Here, the stabilizing Zeeman energy decreases and allows the domain wall to also propagate through the Fe-dominated layer. With a further decrease in magnetic field, the Tb-dominated layer also switches its magnetization at point 5, but only in those regions where the domain wall stayed on the Tb-dominated side of the interlayer. The domain walls at this state are now vertical, separating lateral regions of different antiparallel alignment of the two layers. One part of the regions still has the same pinning as at point 1, but some was re-pinned to the opposite direction by a change of the interlayer region's magnetization direction.

Lastly, if also the re-pinned part of the Tb-dominated layer switches its magnetization at point 6, the domain wall is quickly closed around the re-pinned Fe-dominated layer regions. During this process, some part of the Fe-dominated layer can switch alongside the Tb-dominated layer, leading to the delayed onset of overcrossing as depicted in Fig. 7.24. The rest of the still unswitched magnetization of the Fe-dominated layer is visible as the overcrossing, causing a magnetization value that is lower than that seen for the complete antiparallel state at point 1. Again, the domain wall can slowly propagate through the interlayer region, given enough time, ultimately relaxing into the fully antiparallel state of the two layers.

In conclusion, we have shown that the interlayer exchange coupling in TbFe-based bilayers in conjunction with the formation of a nearly compensated interlayer and the high magnetic frustration can lead to very slow magnetization dynamics similar to magnetic viscosity or spin glass behaviour. Lower temperatures and lower relaxation fields showed a slower relaxation towards the stable antiparallel configuration of the two TbFe layers. A relaxation of two hours at a fixed field at 100 K was shown to have the same effect as applying a magnetic field that is 2.5 kOe higher.

Lastly, it should be mentioned that a very similar behaviour was also observed for other samples with the Tb-dominated layer on the bottom. Some of the low-temperature measurements of these samples displayed hysteresis loops where the highest magnetization values are not reached at the maximum field, but just after the point of overcrossing. In this case, the transient state of parallel alignment of the two layers is so energetically unfavourable that not even the high magnetic field of 70 kOe can fully align them.

CHAPTER 8

Further candidate materials for magnetic coupling phenomena

As has already been stated in chapter 3.1.2 about the properties of $L1_0$ FePt, there are also many other alloys with the $L1_0$ structure that show interesting and useful properties. Among those are FeNi, MnPt, and CrPt. However, $L1_0$ FeNi is remarkably difficult to fabricate in this structure, and CrPt is difficult to grow in the (001) direction.

In the frame of this work, we have tried to create a mixed $L1_0$ structure with four instead of two constituent elements, with the intention of combining and improving magnetic properties of different $L1_0$ phases. Especially when combining transition metals with ferro- and antiferromagnetic interactions, the combination of both in the same alloy could lead to rich and novel magnetic properties.

We also tried to achieve a good (001) ordering in $L1_0$ CrPt thin films grown on MgO(001) substrates, since a good control of crystalline orientation is needed in order to maximize the use of this system as a pinning layer in exchange bias applications.

8.1 Entropy-stabilized/mixed $L1_0$ structures

Two of the most useful antiferromagnetic $L1_0$ systems are MnPt and CrPt, which are useful as pinning layers in exchange bias systems. CrPt has good corrosion resistance, and MnPt displays a high spin Hall angle [328], making it interesting for spintronic applications. Additionally, both alloys have strong uniaxial magnetic anisotropy [144, 145].

Another very promising alloy is the ferromagnetic $L1_0$ FeNi, also called *tetrataenite*. It shows a high saturation magnetization of 1270 emu/cm^3, a high K_u of 1.3 MJ/m^3, a coercivity of 4 kOe, and a reasonably high T_C of 550 °C [152, 329, 330], making it an extremely promising candidate for replacing modern supermagnets, which rely heavily on the usage of (heavy) rare-earth elements. However, this system is notoriously difficult to synthesize even in thin film form, often relying on deposition of elemental monolayers [331–334] or denitriding [335–337]. These samples still often display rather

low order parameters, and many samples that have been analyzed so far actually stem from meteorites [130, 151].

Since stabilizing binary FeNi in the $L1_0$ structure is difficult, another way of going towards a permanent magnet with similar properties could be to slowly add Ni to the better understood $L1_0$ FePt system. This can be grown reliably with a high order parameter, which could be exploited by partly substituting Pt by Ni.

Additionally, one can use the new concept of entropy-stabilization of alloys. This relatively novel approach to creating solid solutions was first described at the example of so-called high-entropy alloys, meaning alloys consisting of at least 5 different elements [338]. The idea behind this is that the increased mixing entropy in these alloys helps stabilize a solid solution of the constituent elements, thus stabilizing a single phase with a simple structure [339]. It has already been shown that an $L1_0$ structure can be stabilized in this manner, using the mixture FeCoNiMnCu together with Pt [340], so other attempts might also prove feasible.

8.1.1 Magnetic and structural investigation

In this work, we prepared two mixed alloys by magnetron sputtering: Fe(PtPdNi) and (FeCrMn)Pt. Both of these consist of elements that can form the $L1_0$ structure with the unmixed alloying partner, which should ideally help the formation of the ordered alloy. Since there are only 3 elements combined for one sublattice, this is not a high-entropy alloy, strictly speaking. Instead, we will refer to this simply as a mixed or entropy-stabilized alloy.

The ratios of the elements were chosen such that 50 at.% are made up of the unmixed element, i.e. Pt in the case of (FeCrMn)Pt and Fe in the case of Fe(PtPdNi). The composition of the mixed part was set to be equiatomic. The sputtering rates were then calibrated as such. The sputtering pressure was set to 5 µbar and the samples deposited on MgO substrates at room temperature, with a nominal total film thickness of 20 nm. Another (FeCrMn)Pt sample with a 20 nm thick film was deposited at a nominal deposition temperature of 800 °C, similar to the $L1_0$ FePt films also investigated in this work.

The X-ray diffractogram of the Fe(PtPdNi) sample is shown in Fig. 8.1. It is quite clear that no signal other than that of the substrate is visible in the diagram. The formation of an $L1_0$ structure at room temperature was not expected, since high deposition temperatures are usually needed for its formation in FePt and FePd alloys. However, there are also no traces of any other phases, so it can be concluded that no significant phase separation or polycrystalline growth happened in the film. Instead, the film can be assumed to have an amorphous or nanocrystalline structure. To induce the formation of any structure, higher deposition temperatures or some form of post-deposition heat treatment are needed.

Figure 8.2 shows the θ-2θ XRD measurements of the (FeCrMn)Pt samples, deposited at different temperatures. The sample deposited at room temperature only shows the (002) reflection peak of the MgO substrate, highlighted in blue, and a small signal on its left shoulder, at around 40 °. This peak position can be associated with the

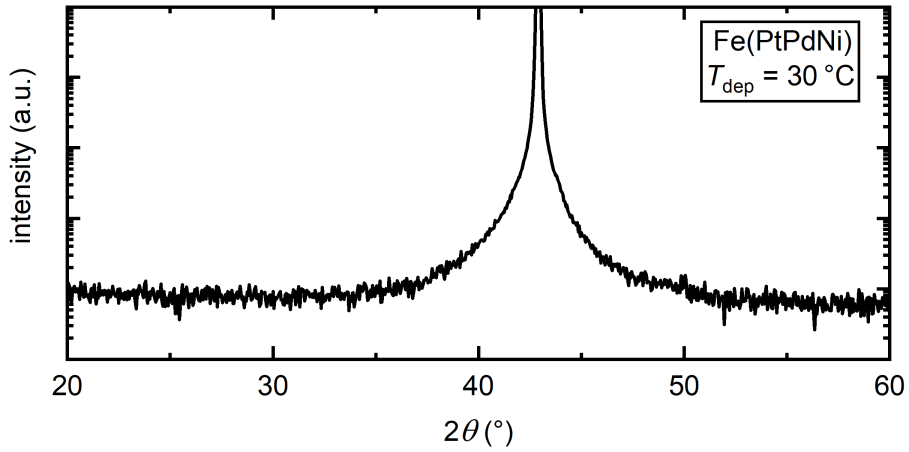

Figure 8.1: θ-2θ diffractogram of the Fe(PtPdNi) sample deposited at room temperature. No signal except the substrate peak at 42.92 ° can be observed, indicating an amorphous or nanocrystalline structure in the film.

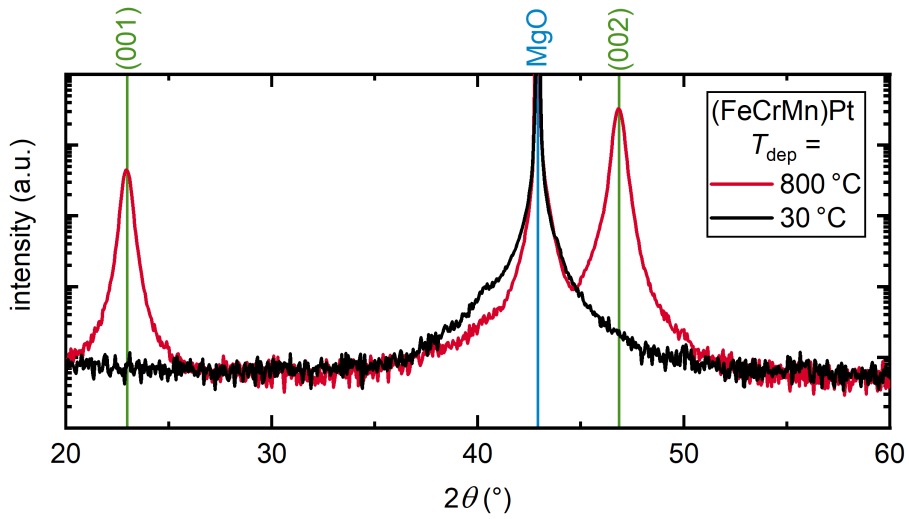

Figure 8.2: Comparison of the θ-2θ diffractograms of (FeCrMn)Pt samples deposited at room temperature and at a nominal deposition temperature of 800 °C. While the sample deposited at room temperature shows almost no structure, two clear (00l) reflection peaks can be seen for the sample deposited at high temperature.

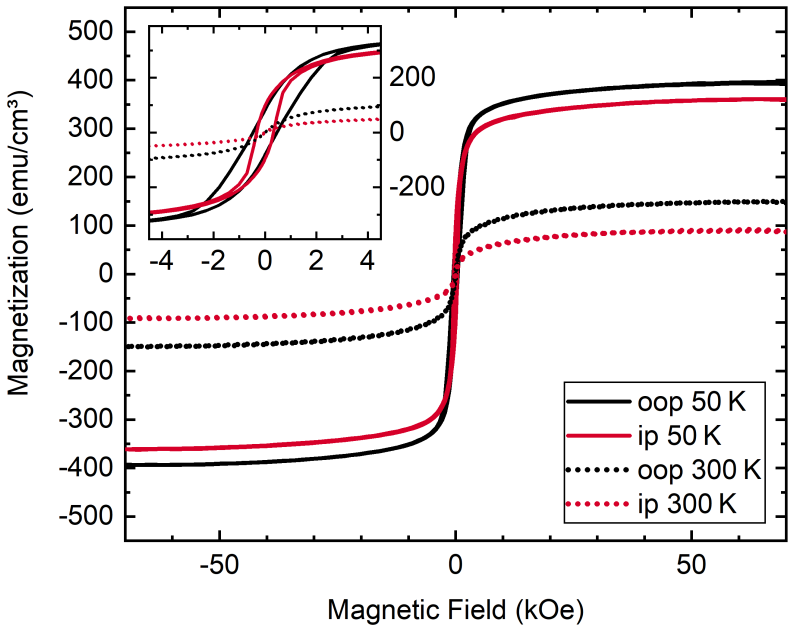

Figure 8.3: Comparison of the ip and oop hysteresis loops of the structured (FeCrMn)Pt sample at 50 K and 300 K. The similarity of the two measurement directions indicates a magnetically isotropic behaviour in the whole temperature range. The inset shows a zoomed-in image of the low-field region of the loop, making the differences between the two temperatures better visible.

(111) reflection peak of $L1_0$ MnPt or the cubic $L1_2$ phases of $CrPt_3$ and $FePt_3$. The (111) reflection peaks of $L1_0$ FePt and CrPt are situated at slightly higher angles, namely around 41 °. The existence of this peak, albeit small, likely indicates that some degree of structural formation was possible in this alloy even when deposited at room temperature.

The sample deposited at 800 °C, on the other hand, shows two strong peaks at 22.9 and 46.8°. These angular positions are in the region where most $L1_0$ structures show their (001) and (002) reflection peaks. Assuming this structure has also grown in the c lattice direction, we have assigned the same labels to the two peaks, and consequently calculated the lattice parameter to be 3.87 Å. Note, however, that this is just a preliminary designation, as the precise structure is not yet known. If these allocations are correct, then we can also conclude that the order parameter is rather low, since the peak intensity of the (001) reflection peak is significantly lower than that of the (002) reflection peak, by a factor of 10. Another reason for this could be that the peaks have been mislabelled, which will be investigated in measurements following later.

Since only the sample deposited at high temperature showed a good structure in the XRD measurements, all following measurements were only done on this sample. Accordingly, this sample will simply be referred to as the (FeCrMn)Pt sample from now on.

Next, the magnetic properties of the sample were investigated. The M-H hysteresis loops were measured at different temperatures both in oop and ip direction. A comparison between the measurements at 50 K and at room temperature is depicted

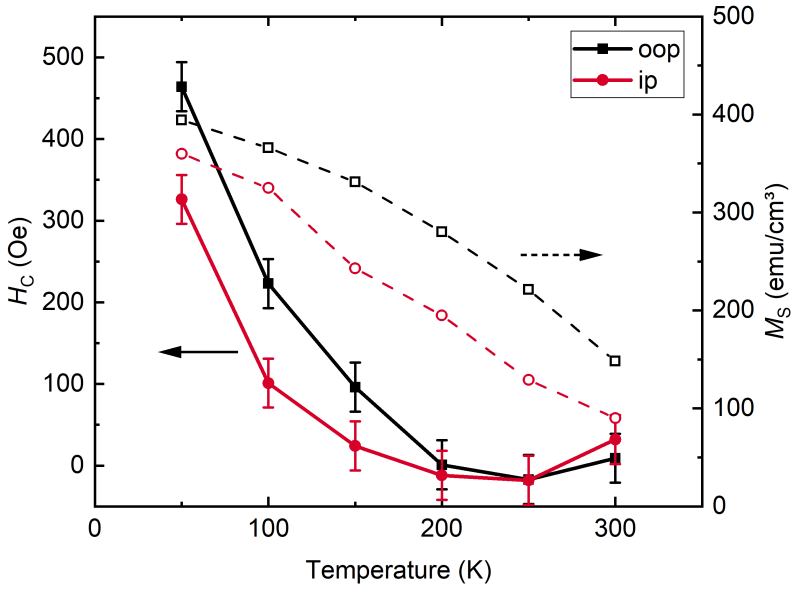

Figure 8.4: The change of coercivity H_C (solid symbols, left axis) and saturation magnetization Ms (open symbols, right axis) of the structured (FeCrMn)Pt sample with temperature.

in Fig. 8.3. As expected, the magnetization values increase for lower temperatures. The coercivity stays extremely low compared to other $L1_0$ structures, and also the difference between ip and oop direction is minimal, suggesting an almost completely isotropic material.

The difference between the ip and oop magnetizations at room temperature seems puzzling, but can be explained by the likely existence of a soft phase artefact as mentioned in chapter 4.1. This could not be subtracted as the hysteresis loops themselves are quite soft magnetic in their nature. Also, the background subtraction assumes a slope of zero at maximum field, which might not hold completely true for either measurement.

The evolution of the coercivity and the saturation magnetization of the (FeCrMn)Pt sample with temperature is shown in Fig. 8.4. As can be seen, both parameters are generally lower for the ip measurements and drop with increasing temperatures. The decrease of coercivity is fast, almost reaching zero at 250 K. Note that in this case, the effect of currents trapped in the magnet of the SQUID-VSM is not negligible, leading to an magnetic field offset of around 30 Oe, displayed by the error bars. It is thus likely and plausible that the coercivity decreases until 300 K and does not actually increase as seen in the diagram.

The magnetization decreases steadily towards room temperature, as already observed. The curvature suggests a Curie temperature around 350 K, but the comparison with the M-T measurements shown in Fig. 8.5 suggest that it is around room temperature. The magnitude of the saturation magnetization also displays the low Fe content in the alloy, and the Cr and Mn magnetic moments do not contribute significantly to the magnetization.

To get more information about the magnetic properties, we conducted M-T measurements with field-cooling (FC) and zero-field-cooling (ZFC) techniques using a guiding

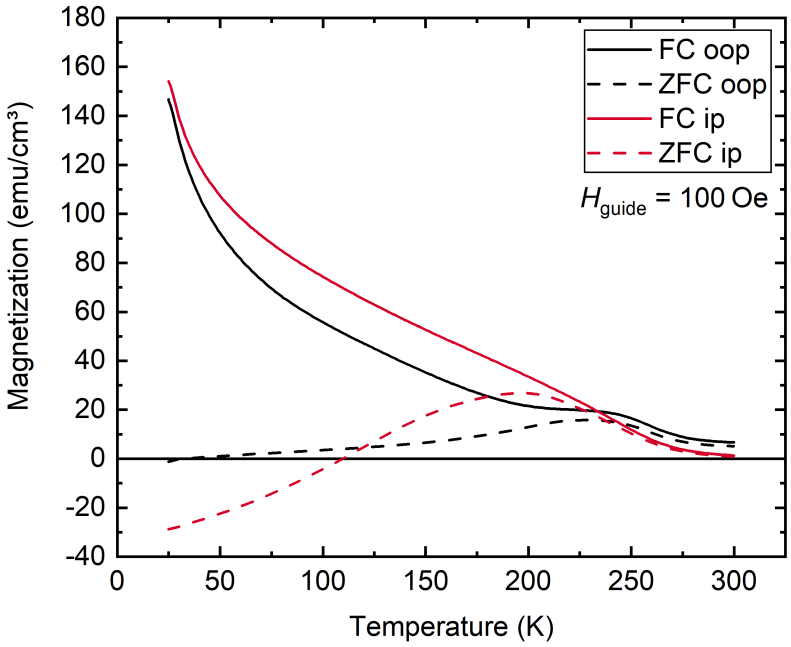

Figure 8.5: The field-cooled (FC) and zero-field-cooled (ZFC) M-T measurements of the structured (FeCrMn)Pt sample. A small bump can be seen around 240 K for the oop measurements and around 200 K for the ip measurements. The initial negative magnetization seen for the ZFC measurements is caused by a small effective negative field present during the cooling process due to trapped flux in the SQUID magnet, freezing the negative magnetization of the sample at that field at room temperature (see Fig. 8.3).

field of 100 Oe during the measurement. Before cooling, the samples were saturated in positive direction and the field subsequently set either to zero (ZFC) or to 70 kOe (FC), depending on the type of cooling condition wanted for the measurement. The four measurements are shown in Fig. 8.5, and display a nontrivial behaviour.

Both FC measurements display a high magnetization at low temperatures, caused by the magnetic moments that were frozen due to the field applied during cooling. Both the oop and the ip measurement display a bump in magnetization when increasing the temperature, the one for the ip measurement being only a slight variation in the negative slope between 200 and 250 K. The bump for the oop measurement is more noticeable, being situated at around 240 K.

Both of these bumps also exist in the ZFC measurements, where they actually form maxima of magnetization. The oop measurement starts in an almost completely demagnetized state and only very slightly increases in magnetization until the maximum is reached at 228 K, after which it can be said to behave like the FC measurement. The ip measurement actually starts with a negative magnetization and behaves very similarly, reaching a maximum at 196 K and following the FC curve after that.

The negative magnetization that is observed for the ZFC ip measurement at very low temperatures is most likely caused by the already mentioned field offset of the SQUID-VSM magnet. When reducing the magnetic field from high positive values to zero, superconductive currents can be trapped inside the magnet and apply a small negative

field on the sample, often around -20 to -50 Oe. This negative field can slightly align the soft magnetic moments at room temperature, and this state can then be frozen by cooling. This leads to the negative magnetization measured at very low temperatures for this measurement. A confirmation of this can be seen by the point where the measurement graph crosses zero, which is at 110 K. Comparing this to Fig. 8.4, we can see that the ip coercivity at 100 K is around 100 Oe, which is the value of the guiding field used for the M-T measurements. As a consequence, we can say that the guiding field is able to cause magnetic reversal in this sample, turning the magnetic moments into the positive direction.

The magnetization bump observed for the M-T measurements are expected for the ZFC measurements, as the increasing temperature allows the guiding field to start aligning the randomly oriented magnetizations little by little, working against the magnetic anisotropy. This continues until the system is "unfrozen" and the ZFC measurement becomes the same as the FC measurement.

However, the fact that there is also a trace of the bump visible in the FC measurements suggests that there are also antiferromagnetic interactions present in the alloy. These would hinder the increase of M towards lower temperature, leading to a decrease in slope.

This is also not very surprising, as Cr itself is an antiferromagnetic element, and Fe shows a frustrated noncollinear alignment of magnetic moments in combination with both Cr or Mn [341–343]. The complicated nature of the magnetic interaction between the three elements in the (FeCrMn)Pt alloy likely leads to a complex alignment of the magnetic moments, and possibly to spin-glass-like behaviour. However, these would require much more investigation of the magnetization dynamics, especially at low temperatures.

All these observations show that this material is not a hard magnet as $L1_0$ FePt, but rather a magnetically frustrated system with very low magnetic anisotropy. Because of this finding, the structure of the (FeCrMn)Pt film was analyzed in more detail. Reciprocal space maps (RSM) have been recorded in order to get a broader insight into the structure of the alloy, as multiple dimensions of the lattice can be investigated in this manner.

Figure 8.6 shows the RSM of the (FeCrMn)Pt sample over a large range of angles. One can see the strong signal of the cubic MgO substrate and additionally another seemingly cubic pattern. Since the $L1_0$ structure is characterized by its tetragonal lattice, this is a first indicator that the (FeCrMn)Pt film has not actually grown in this structure. Evaluating all the visible diffraction peaks and averaging the results, we receive a lattice parameter of 3.86 Å in both the vertical and lateral direction, thus confirming that the structure is cubic and not tetragonal. However, even though the lattice parameters in the two directions are identical, there could still be a chemical order in the sense of the $L1_0$ structure, i.e. alternating layers of Pt and a mixture of Fe, Cr, and Mn.

In order to test this possibility, one can take a look at the presence and intensity of various diffraction peaks with different Miller indices (h k l). In a lattice with $L1_0$ ordering, all (00l) reflections are allowed, but all reflections with a mixed parity of h

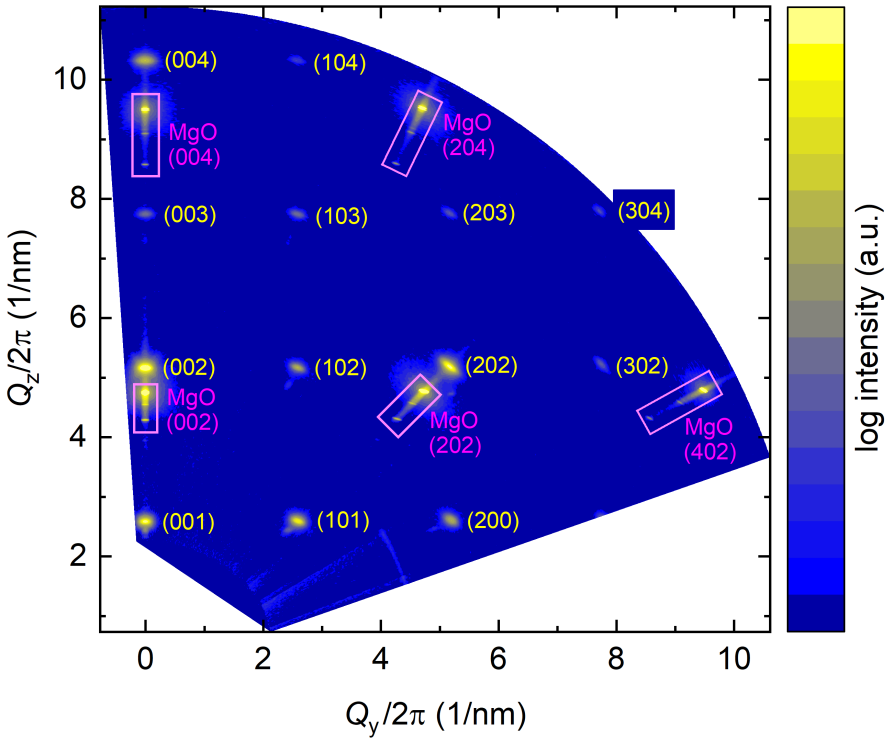

Figure 8.6: Reciprocal space map (RSM) of the structured (FeCrMn)Pt sample. The intense signal of the MgO substrate (pink rectangles) is overlaid by another signal with quadratic symmetry caused by the (FeCrMn)Pt film.

and k, such as the (101) reflection peak, are forbidden. Assuming an even distribution of Fe, Cr, and Mn among the crystal, the same would hold true for the (FeCrMn)Pt film if the film was $L1_0$-ordered. At the least, one would assume a strongly decreased intensity for the forbidden peaks when compared to the allowed peaks.

Figure 8.7 shows the cross-sections of the RSM along the directions where $l = 1$ (top graph in green) and where $h = 1$ (right graph in red). The cross-section along $h = 0$ is equivalent to a regular θ-2θ scan as shown in Fig. 8.2, where the reduced intensity of the (001) reflection peak was already observed. The red graph containing the (10l) reflection peaks only shows the regular decrease of peak intensity with increasing diffraction angle. The green graph displaying the (h01) reflection peaks also only shows that the intensity of the peaks decrease with increasing diffraction angle, but not that the (101) reflection peak in the center is significantly reduced in intensity.

Accordingly, it follows that the (FeCrMn)Pt film is with certainty not in the $L1_0$ structure. Another, structurally similar structure is the cubic $L1_2$ phase, but this is made up of a 1:3 stoichiometry such as in $CrPt_3$. An investigation of the film by TEM was then undertaken to test this possibility further.

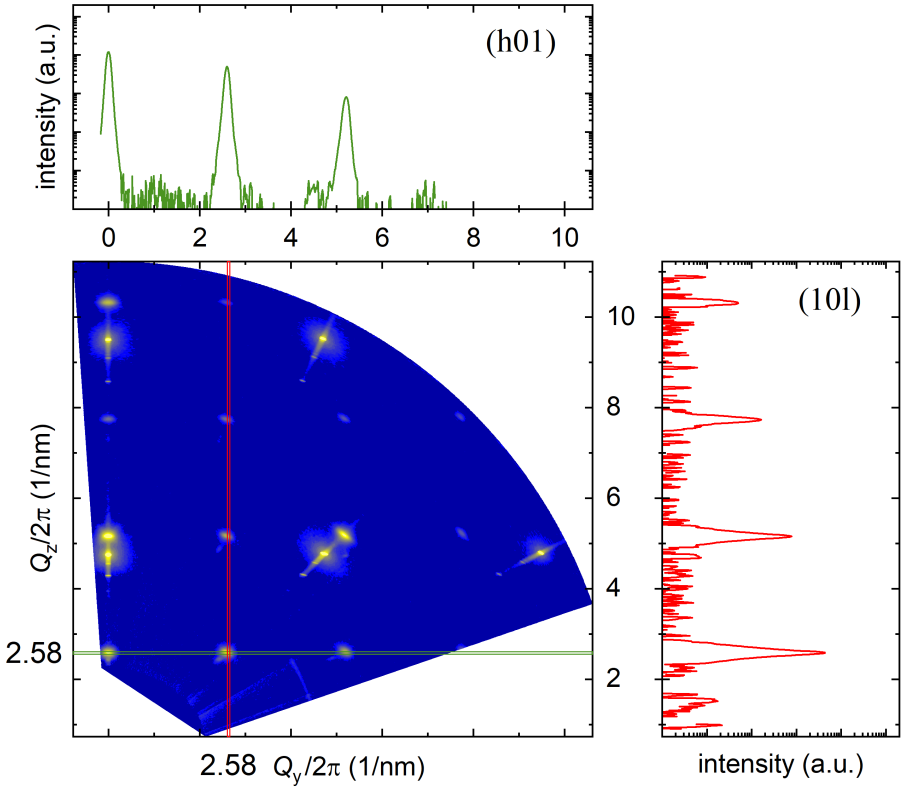

Figure 8.7: Line intensity profiles of the RSM shown above. The green graph on top shows the (h01) reflection peaks, the red one on the right the (10l) reflection peaks. The linear decrease of the logarithmic intensity with increasing angle indicates that no peaks are *forbidden* by the structure of the film.

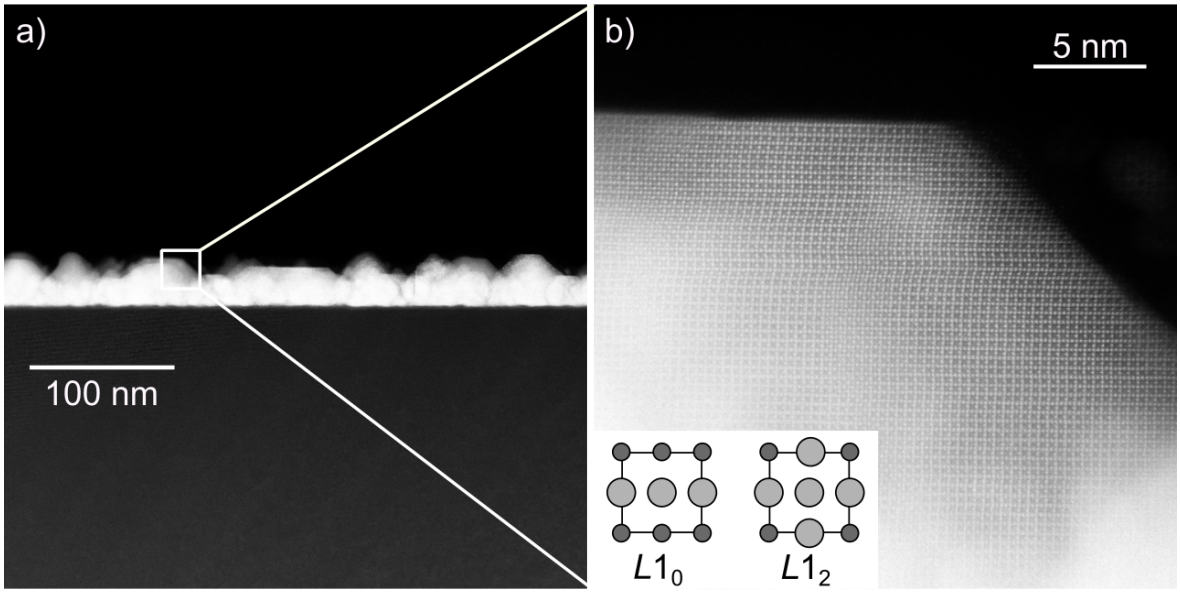

Figure 8.8: TEM cross-section micrograph of the (FeCrMn)Pt film in dark-field mode. a) The granular structure of the nominally 20 nm thick film is clearly visible. b) The structure within the grains of the film does not show the alternating contrast as expected of an $L1_0$ film, but the grid of an $L1_2$ structure, as shown in the inset. Antiphase boundaries are also visible in the grain, e.g. expanding to the bottom left from the top right corner of the grain.

8.1.2 Investigation by TEM

A dark-field cross-section TEM image of the (FeCrMn)Pt sample is shown in Fig. 8.8. It shows the granular structure of the nominally 20 nm thick film as is also common for $L1_0$ FePt films deposited at high temperature.

Figure 8.8 b) shows a High-Resolution STEM image of one grain of the layer. It clearly shows that the surface of the grain is terminated in the low-index (001) and (101) Miller planes, and a very regular structure can be seen in the grain, consisting of a high-contrast grid with low-contrast elements in the gaps. In order to interpret this, the two structures of interest need to be considered.

The main difference between the $L1_0$ and the $L1_2$ structures is the layering in the (001) lattice direction. The $L1_0$ phase is made up of alternating layers of elements, while the 1:3 stoichiometry of the $L1_2$ phase leads to the replacement of half of the atoms of one layer by the atoms of the dominant element in the alloy. The alternating layers in the (001) direction thus consist of either only the dominant element or an alternating pattern of both elements.

This difference is depicted in the inset of Fig. 8.8 b). It can now be easily concluded that the film indeed displays the $L1_2$ structure, with the high-contrast element, in this case Pt, being the dominant element.

The next important question is why the alloy would form such a structure that is dominated by Pt even though it nominally makes up 50 at.% of the film. Accordingly, EDX and EELS measurements were performed to give us insight into the actual stoichiometry of and elemental distribution within the (FeCrMn)Pt film.

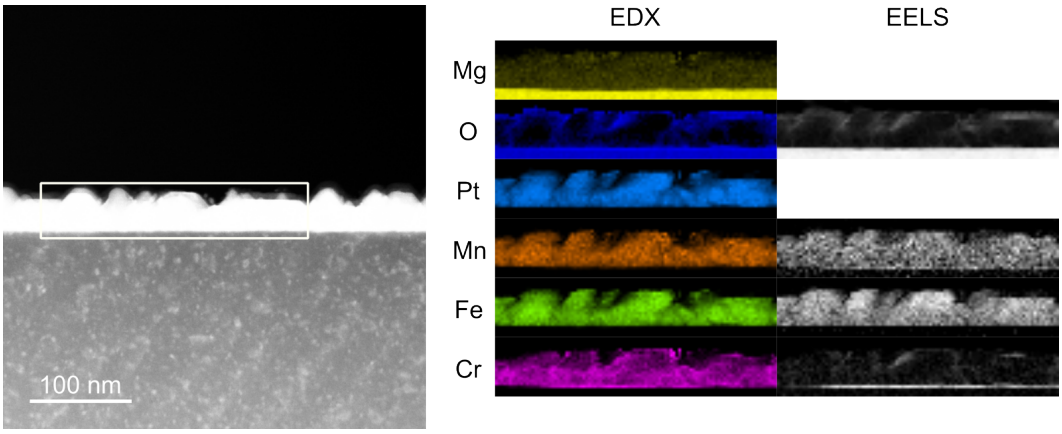

Figure 8.9: EDX and EELS mappings of the sample area shown on the left. Cr seems to be diminished inside the grains, while it shares areas with oxygen on the surface of the grains and on the film-substrate interface, indicating the formation of chromium oxide.

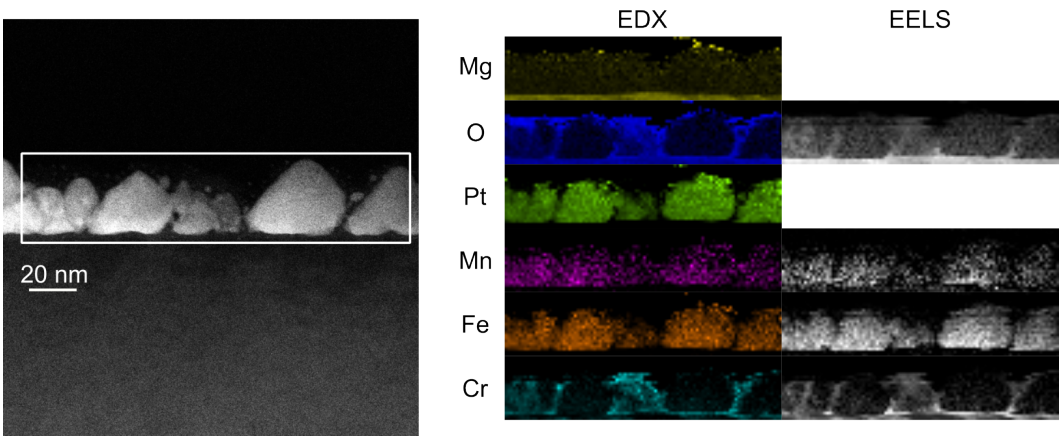

Figure 8.10: Higher-magnification EDX and EELS maps of a thinner part of the (FeCrMn)Pt sample. Again, the accumulation of Cr and O outside of the grains indicates the formation of chromium oxide. The Mn content in the grains also seems reduced.

One of these measurements is shown in Fig. 8.9. The investigated region, as highlighted in Fig. 8.9 a), is the same as in Fig. 8.8, only the contrast is increased due to longer exposure. The EDX/EELS maps in Fig. 8.9 b) show that the grains consist mostly of Fe, Mn, and Pt. The Cr signal in the grains is weak in the EDX map and even weaker in the EELS maps. It is instead mostly concentrated on the surface of the grains or below them. The presence of the oxygen signal in the same areas suggests the formation of chromium oxide in this sample.

Because of the discrepancy between the Cr signals in EDX and EELS, we investigated another region of the film in the same manner. The second measurement is shown in Fig. 8.10. The film in this region has been thinned to a higher degree, so the individual grains can be differentiated more easily.

The results of the first EDX/EELS mapping are confirmed in these measurements: within the grains, the strongest signal is that of Pt, while Fe and especially Mn show a significantly weaker signal. The EDX and EELS measurements for Cr are more congruent this time, both showing that Cr is mostly absent from the big grains and is

instead accumulated at the surface of the grains. Once more, the oxygen signal in the same regions suggests the formation of chromium oxide.

The overall composition of the (FeCrMn)Pt film as given by the integrated EDX signals is $Fe_{22}Cr_{12}Mn_8Pt_{58}$, which deviates strongly from the nominal composition of $Fe_{16.7}Cr_{16.7}Mn_{16.6}Pt_{50}$. The reason for the reduced of content of Cr and Mn is unknown, but is likely linked with an error in the calibration of the deposition rates. Both elements are not commonly deposited in the BESTEC sputter system used here, so an incorrectly calibrated quartz balance could well be the reason for the discrepancy.

Consequently, we can say that the film of the (FeCrMn)Pt sample consists of highly textured $L1_2$ (FeMn)Pt_3 grains with an amorphous region of CrO_x surrounding the grains. Even though the intended $L1_0$ structure was not achieved, the possibility of creating a highly ordered structure with a mixed composition was demonstrated. Assuming the deposition rates can be correctly calibrated, it is thought that other mixed alloys, possibly in the $L1_0$ structure, can also be fabricated.

8.2 $L1_0$ CrPt and $L1_2$ $CrPt_3$

The antiferromagnetic $L1_0$ phase of CrPt can be created by deposition at high temperature or by post-annealing of samples deposited at room temperature. However, such samples mostly show a (111) growth direction when deposited at high temperatures, only showing a partial (001) growth at deposition temperatures above 600 °C on thermally oxidized Si and quartz substrates [145, 344]. Samples deposited at room temperature and subsequently post-annealed can also develop a (001) growth texture, but this is also accompanied by simultaneous (111) grain growth. Further, films with a minimum thickness of around 100 nm are required to observe this on thermally oxidized Si substrates [145].

In order to receive an in-plane alignment of the Cr magnetic moments in the $L1_0$ CrPt alloy, a pure (001) growth should be achieved. Also, thin CrPt films are desired for applications not only for the minimization of total device thickness, but also reduction of cost. We tried to achieve $L1_0$ order with (001) growth in thin CrPt films by depositing a nominally 20 nm thick CrPt film at a nominal deposition temperature of 400 °C and post-annealing it at 700 °C. The film was deposited on an MgO (001) substrate using sputter deposition with an Ar pressure of 5 µbar.

After investigation by XRD, the sample was post-annealed at 700 °C for 1 h in forming gas atmosphere with 10 % H_2 content. The heat treatment was repeated after the investigation was completed, so the sample was post-annealed at 700 °C for a total of 2 h. Once the next XRD investigation was done, a last post-annealing was performed, this time increasing the duration to 2 h, so the sample experienced a total of 4 h of heat treatment at 700 °C. This is of course not identical to a single heat treatment with a duration of 4 h, because the sample experiences the heating and cooling multiple times, but this designation is still used for the sake of brevity. Since CrPt is an antiferromagnet, no focus was put on the magnetic measurements.

The θ-2θ X-ray diffractograms of the samples at the various stages are depicted in Fig. 8.11. In the as-prepared stage, the sample displays the existence of both the (002) and

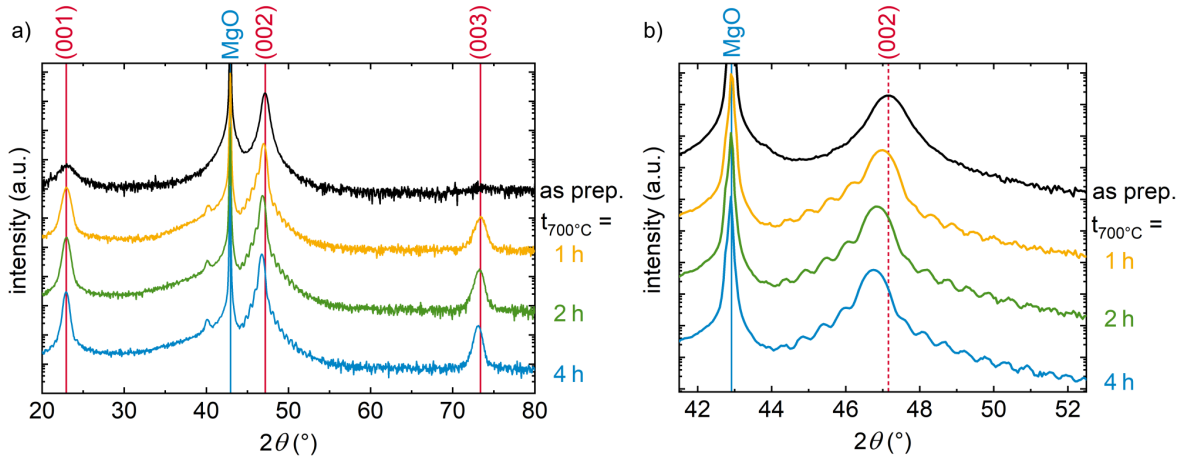

Figure 8.11: a) θ-2θ scans of the CrPt films in the as-deposited state and after certain total post-annealing durations at 700 °C. The appearance of the (001) and (003) reflection peaks indicate increased ordering after the heat treatment. b) A zoom of the (002) reflection peak area of the θ-2θ measurements. A shift away from the (002) peak position of the as-prepared sample (dashed line) and the appearance of Laue oscillations after the post-annealing treatment is observable.

the (001) reflection peaks, but the (001) peak is very low in intensity. This indicates a low order parameter under the assumption that it is the $L1_0$ phase. After post-annealing the sample at 700 °C for 1 h, the sample already shows not only an increased (001) and (003) reflection peak intensity, but also Laue oscillations around the (002) reflection peak. These become slightly more pronounced for longer heat treatment, as can be seen in Fig. 8.11, extending further from the main peak. These oscillations indicate that a large part of the film consists of the same crystallographic phase and consists of the same number of unit cells stacked along the scattering direction, i.e. has the same thickness [345].

Interestingly, the (002) peak of the measurements moves further away from the position of the (002) reflection peak of the as-prepared CrPt sample, appearing at lower angles. This indicates that the c lattice parameter increases with increasing post-annealing duration. The evolution of c is depicted in Fig. 8.12 a), showing that it does not approach the bulk value as expected, but instead seems to approach another value around 3.89 Å.

In order to gain more information on the structure, we performed an RSM measurement on the sample, depicted in Fig. 8.12 b). The evaluation of this gives us information about the in-plane lattice parameter a as well as the vertical c. The position of the (202) reflection peak revealed that the sample is actually not tetragonal, but cubic. Further, the existence of reflection peaks with Miller indices h and k of mixed parity is also an indication that the structure is not $L1_0$. The intensities rather indicate that the sample has the cubic $L1_2$ structure.

Indeed, the lattice parameter of 3.88 Å fits to that of $L1_2$ $CrPt_3$, which lies between 3.88 and 3.89 Å [346, 347]. An EDX measurements of the sample gives a composition of $Cr_{40}Pt_{60}$. In addition, there could be a part of the Cr that forms an oxide at the interface with the MgO substrate or at the surface, as was shown previously for the

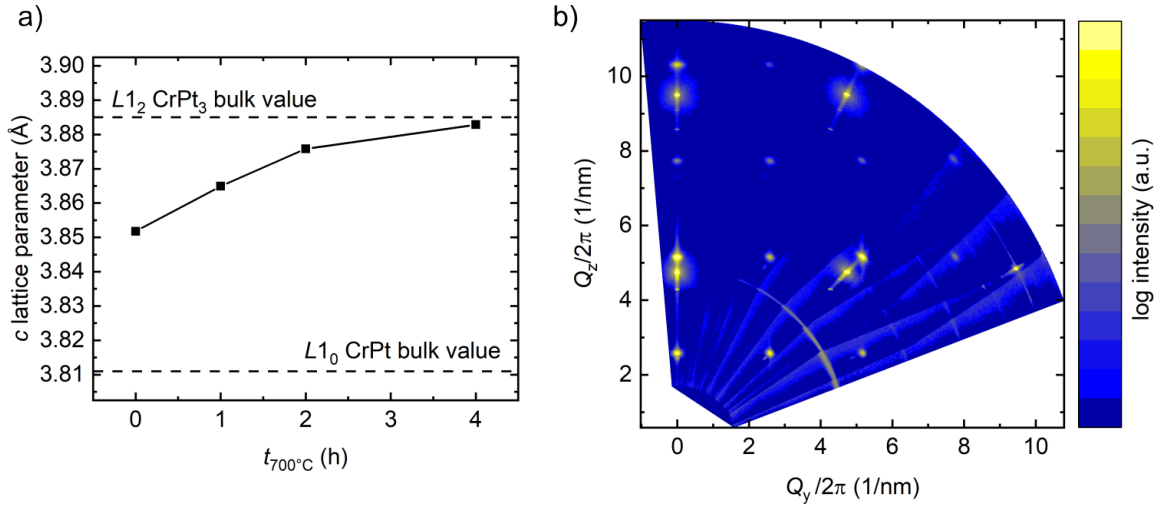

Figure 8.12: a) The evolution of the c lattice parameter of the CrPt film with increased total annealing duration at 700 °C. b) The RSM of the CrPt film shows a signal with quadratic symmetry in addition to the high-intensity signal of the MgO substrate, indicating that not the $L1_0$ structure has developed in the film, but the $L1_2$ structure. The straight lines in the background are measurement artefacts, and the partially visible arcs are caused by the substrate.

(FeCrMn)Pt sample in chapter 8.1.2. This would further reduce the amount of Cr in the film. With the stable composition range of $L1_0$ CrPt being only around 48 - 52 at.% Cr, we can now conclude with certainty that the sample has the $L1_2$ $CrPt_3$ structure.

$CrPt_3$ in the $L1_2$ structure is a ferrimagnetic alloy with oppositely aligned magnetic moments of Cr and Pt [348]. It shows a saturation magnetization around 150-200 emu/cm^3 [349–351] and coercivities of up to 12 kOe along the magnetic easy axis [351, 352]. The magnetic easy axis is along the (111) direction [346, 353, 354], and films grown with a (111) orientation can show a K_u of up to 0.8 MJ/m^3 [349]. A deposition or post-annealing temperature of 850 °C is most often used throughout the literature in order to induce a high crystalline order in the $CrPt_3$ alloy, but the results shown here prove that a combination of co-deposition of Cr and Pt at a nominal deposition temperature of 400 °C and post-annealing at 700 °C can also induce a high degree of crystallinity in the $L1_2$ $CrPt_3$ phase. In order to determine the order parameter, the (112) and (113) reflection peaks would need to be investigated, though [355].

Since the films investigated here display a (001) growth direction, no PMA is expected to exist in these thin films. This is also proven by the M-H hysteresis loops measured at room temperature, which are shown in Fig. 8.13. Instead of PMA, there is only a very slight in-plane anisotropy visible in the hysteresis loops. This can be explained by the angle between the (111) easy axis and the two measurement directions: the angles are around 54.7° to the oop and 45.3° to the ip direction. Together with the shape anisotropy, the easy axis is thus slightly more aligned towards the sample plane, but the difference is only minor and mainly seen by the higher M_R. The coercivity is only around 1 kOe, also being a bit higher in the ip direction. The saturation magnetization of around 200 emu/cm^3 fits the higher end of those reported in the literature, probably resulting from the surplus of Cr.

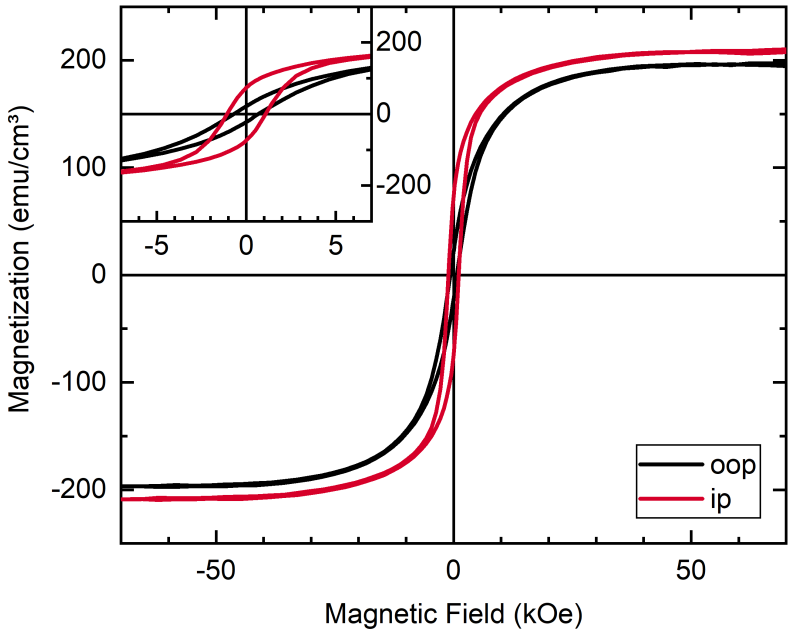

Figure 8.13: The *M-H* hysteresis loops of the $CrPt_3$ film at room temperature in the oop and ip directions. The inset on the top left shows a zoom of the low-field region, making the difference between the two loops better visible.

In conclusion, we were not able to induce an $L1_0$ structure in the CrPt sample, but the main reason for this is the composition deviating so much from the calibrated one. Similar to the (FeCrMn)Pt sample, an incorrectly calibrated quartz balance is most likely the cause for this. Unfortunately, both samples were deposited before this error was discovered. Still, we were able to induce a higher degree ordering of the sample by post-annealing, which can be seen by the increase of the (001) reflection peak intensity. Further, the appearance of Laue oscillations indicates that the $CrPt_3$ film is rather smooth and very uniform in its thickness. If appropriate substrates are used, an epitaxial (111) growth could very likely be achieved using the same temperatures as described here.

CHAPTER 9

Summary

The work presented here comprises three main aspects: i) the magnetic hardening of thin $L1_0$ FePt films with Tb by post-annealing, ii) inducing the $L1_0$ phase in mixed alloys and the CrPt alloy, and iii) investigating the low-temperature behaviour of TbFe-based bilayers, caused by exchange coupling.

Due to its outstanding magnetic properties, the $L1_0$ phase of FePt is the material used in the first conventionally available HDDs using the HAMR technique. Magnetically harder alloys, i.e. those with a higher K_u and H_C, are thermally more stable and are thus useful for an increased bit density in such hard drives, since magnetic grains can be made smaller. The grain boundary diffusion (GBD) process is often used to enhance the H_C of modern supermagnets, utilizing the antiferromagnetic exchange coupling between rare-earth elements such as Tb or Dy and the ferromagnetic main phase to increase its coercivity. The feasibility of such an approach on thin $L1_0$ FePt films was tested.

We deposited FePt thin films with $L1_0$ ordering by magnetron sputter co-deposition of elemental Fe and Pt targets on (100)-oriented MgO substrates at a nominal deposition temperature of 800 °C. Since such films usually do not show grain boundaries due to the epitaxial growth, 20 and 30 nm were chosen as the film thickness since the island-like growth leads to the existence of trenches between partially coalesced FePt grains at such thicknesses. The additionally deposited Tb of 10 nm thickness could then fill these trenches in lieu of grain boundaries, possibly enhancing the separation and hardening of magnetic grains when heat-treated ex-situ.

The first measurement series tested the influence of different post-annealing temperatures on the magnetic properties (H_C and M_S) of two Tb-free and two Tb-containing FePt samples. In order to ensure comparability, the same sample pieces were used throughout these measurements. Of the four samples investigated, only the 20 nm thick FePt film with added Tb layer showed an increase of coercivity. This increase was most pronounced for annealing temperatures between 650 and 750 °C. XRD measurements confirmed that the FePt film had the $L1_0$ structure with the c-axis perpendicular to the film plane, and sign of intermixing of Tb into the FePt film could be observed, suggesting that the observed change in coercivity is caused only by incorporation of the

Tb into the $L1_0$ FePt structure. Investigation by AFM and SEM showed the different microstructures of the samples: the samples with reduced coercivity showed largely interconnected grains with small, disconnected trenches, while the high-coercivity sample displayed a high degree of grain separation. It was then argued that this is the reason for the observed magnetic behaviour, since the isolation of grains is an efficient way of suppressing domain wall propagation, which is the main mode of magnetic reversal in these thin films.

Further post-annealing treatments at fixed temperatures with increasing annealing duration were performed on different pieces of the Tb-series of samples. The results of these treatments did also not reproduce the behaviour of the first series of measurements. We observed a partial hardening of the 20 nm thick FePt film with added Tb layer upon post-annealing at 650 °C, but none at 700 °C. Instead, the 20 nm thick FePt film without Tb layer showed an enhanced coercivity upon annealing at the latter temperature for increased duration.

No increase of H_C was not observed for the Gd-containing sample series treated with the same post-annealing procedure as the first Tb-containing sample series. Instead, these samples only showed a general decrease in coercivity independent of the presence of a Gd layer.

This observation led to the conclusion that the presence of a Tb or Gd layer is not a prerequisite for the occurrence of magnetic hardening upon post-annealing. Instead, the microstructure of the sample in the as-prepared state is the most important factor determining the change of the coercivity with heat treatment. Well separated grains tend to become more isolated when the film is heated, thus increasing the field necessary to switch their magnetization. Phenomenologically, the necessary microstructure can be estimated to equate a coercivity of about 10 kOe in the as-prepared state, meaning that any portion of the film that requires magnetic fields of at least this value to be switched has the necessary microstructure to become magnetically hardened upon post-annealing.

It was further shown that even though the substrates were only 10 mm wide, there were substantial differences in H_C observable between different sample pieces cut from the same substrate, indicating a low homogeneity of these films deposited at high temperature. These differences account for the different behaviours of the samples seen during the various measurement series. As a consequence, it cannot be said with certainty what influence, if any, the presence of Tb had in the observed magnetic hardening. To achieve this, one would need to compare samples with identical microstructure and thus magnetic properties in the as-prepared state, with the only difference being the presence or absence of a Tb layer.

The second part of this work concerned itself with different types of unusual magnetic behaviour of field-cooled TbFe-based bilayers at low temperatures. The samples consisted of two Tb_xFe_{100-x} films of different compositions, one being Tb-dominated, the other Fe-dominated. These were shown to display a double exchange bias at low temperatures after field cooling, caused by the formation of a magnetically hard interlayer between the two nominal layers. The DEB behaviour was investigated in dependence of the film compositions as well as the properties of an intentionally deposited inter-

layer. It was shown that the interlayer can be Tb- or Fe-dominated and that changing the layer composition greatly affects the stability of the DEB.

The high sensitivity of the system on precise composition was elucidated by the comparison of similar samples showing vastly different behaviour at room temperature, i.e. two- and three-step magnetic reversal at RT. For some samples, a two-step hysteresis loop with a substantial negative remanence M_R was observed at 250 K, transitioning to a three-step loop with positive M_R at room temperature. This behaviour is mainly influenced by the values of K_u and M_S of the two layers, with the less anisotropic layer switching first. In such cases where this is also the layer with higher M_S, a negative remanence can be observed.

It was also shown that the order of layers also influences the magnetic behaviour. With the Tb-dominated layer at the bottom, we were able to achieve DEB with clearly separated hysteresis loops at temperatures between 80 and 120 K, which is higher than for any bilayer with the Fe-dominated TbFe layer on the bottom.

Another surprising phenomenon was discovered in a $Tb_{20}Fe_{80}(10\,nm)/Tb_{36}Fe_{54}(10\,nm)$ bilayer between 80 and 140 K. The *M-H* hysteresis loops displayed an overcrossing of branches in the first and third quadrant, thus giving a clockwise partial hysteresis. Some of these also suggested that the magnetization of the sample was decreasing with an increase of the magnetic field. Further investigation showed that this is not in fact a violation of thermodynamic laws, but a result of an ultraslow magnetic relaxation process, comparable to spin glass behaviour or magnetic viscosity. Relaxation measurement were presented, where the magnetic field was held constant while the change of magnetization was documented for multiple minutes up to hours. It was found that the decay of magnetization was not exponential and was slower for lower temperatures and lower magnetic fields. At 100 K, a complete relaxation was shown to possibly take multiple days, given the proper relaxation field value.

Comparing regular partial hysteresis measurements, where the sample was not allowed to relax, to those where a relaxation duration of two hours was included, we observed that the relaxation could substitute for the appliance of a higher magnetic field. A relaxation duration of 2 h at a given magnetic field was equivalent to a magnetic field that is 2.5 kOe higher with regards to the resulting overcrossing and re-biasing. A simple phenomenological explanation of the magnetization reversal process was then presented, showcasing the importance of the magnetic hardness and frustration of the interlayer region and its inhomogeneity for the observed behaviour of overcrossing and relaxation of magnetization.

In the last chapter, the induction of the $L1_0$ structure in a variety of different alloys with different approaches was investigated. Since many $L1_0$ structures, such as MnPt, CrPt, or FeNi, show promising magnetic properties useful for a variety of purposes, we tried combining different elements forming the $L1_0$ structure to possibly attain novel magnetic materials in said structure. Such a structure could help stabilize the much-coveted but difficult-to-synthesize hard magnet FeNi or show otherwise interesting magnetic behaviour. The mixed alloys Fe(PtPdNi) and (FeCrMn)Pt showed no discernable order when sputter-deposited at room temperature, but the latter was shown to display a strong crystalline order when deposited at a nominal deposition

temperature of 800 °C. However, due to deviations from the intended stoichiometry, the actual structure was not the intended tetragonal $L1_0$, but the cubic $L1_2$ phase. Further, the Cr tended to segregate from the grains and form an oxide on the grain surface. The magnetic measurements of this sample showed some degree of magnetic frustration, which was not unexpected because of the combination of an elemental ferromagnet (Fe) with an elemental antiferromagnet (Mn). Nevertheless, it was shown that structurally ordered films can be created from mixed alloys. As such, an $L1_0$ structure does not seem unattainable if the proper composition can be achieved.

We further tried to achieve a (001) directional growth of the $L1_0$ phase of CrPt on MgO substrates by first sputter-depositing them at a nominal temperature of 400 °C and then post-annealing them at 700 °C. While we were able to produce a nicely structured film showing Laue oscillations in the X-ray diffractograms, the film was not in the $L1_0$, but in the $L1_2$ phase. This was caused by a discrepancy in the composition of the film, which showed a substantial deficiency in Cr. Once more, it is thought that a more precise control of the film composition a nicely ordered $L1_0$ CrPt film can probably be attained.

Supplementary

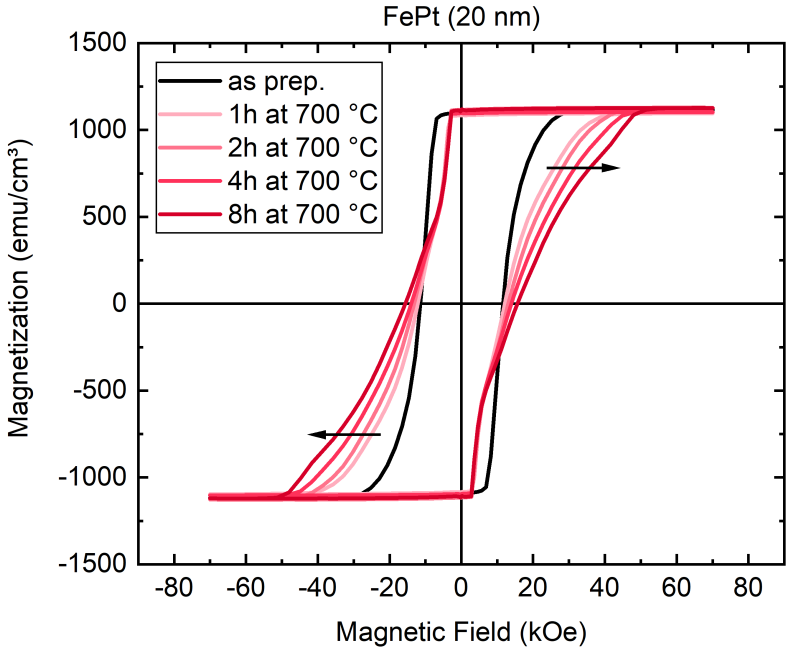

Figure S1: An overlay of the measurements of a 20 nm thick $L1_0$ FePt film in the as-prepared state and after different amounts of total post-annealing time at 700 °C. The arrows highlight the shift with increasing total annealing duration. By the point where the loops cross at about 10 kOe, we can see that a part was shifted to lower and a part to higher switching fields. This is an indication that the respective fractions (i.e. the grains) of the FePt layer have changed their coercivity. Those that started with a coercivity below the crossing point at 10 kOe had their coercivity reduced, switching at lower fields in the post-annealed sample. The grains that had a higher resistance to switching, i.e. that switched above 10 kOe in the as-prepared state, had their respective coercivity increased. This can be explained by the microstructural changes in the sample. The low-coercivity grains were already partially conjoined in the as-prepared state, further growing together by the heat treatment. On the other hand, the high-coercivity grains were already rather isolated before the post-annealing treatment, and only got more isolated and hardened by it. This change seems to be stronger the further the initial coercivity lies above 10 kOe.

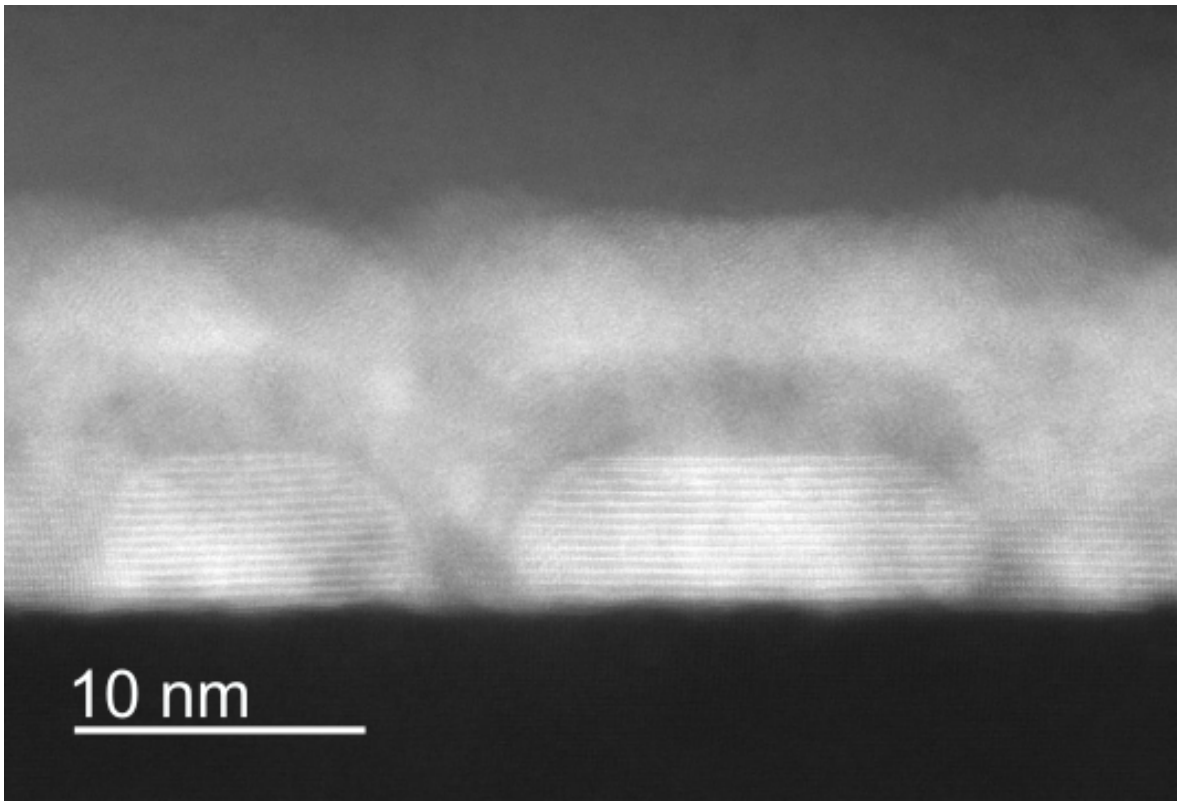

Figure S2: A TEM micrograph of a Mg0(sub.)/FePt(2 nm)/Gd(3 nm)/Si_3N_4(5 nm) sample, showcasing the granular island-like growth of $L1_0$ FePt at elevated temperatures. The nominally 2 nm thick FePt film was deposited at a nominal deposition temperature of 800 °C and consists of ordered, disconnected islands that are around 5 nm thick. The horizontal lines confirm the $L1_0$-ordering and c-direction growth of the FePt layer.

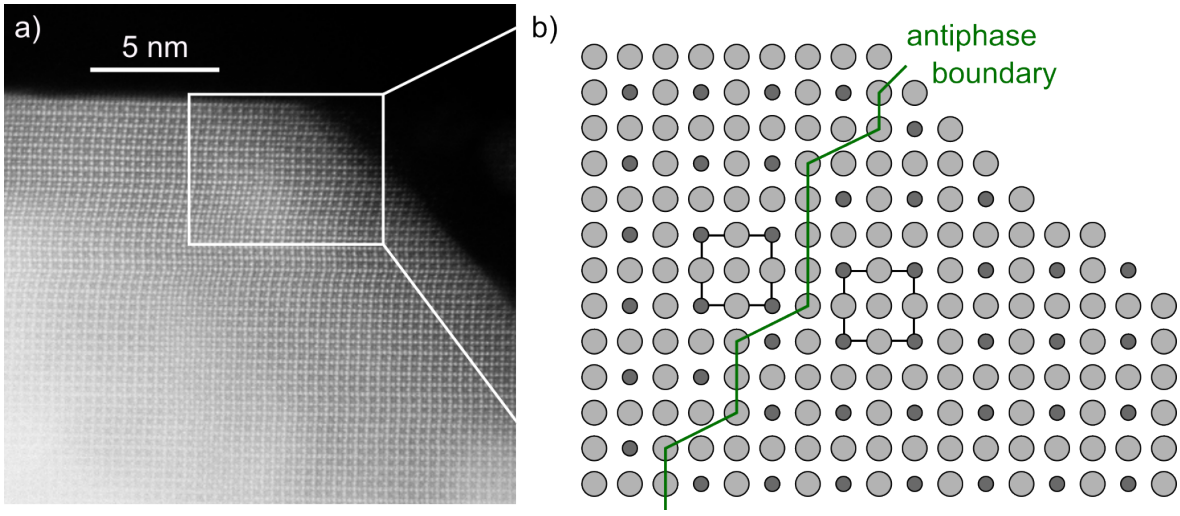

Figure S3: a) A more detailed look at the grain of the mixed (FeCrMn)Pt sample in a TEM micrograph. An antiphase boundary where the stacking order is effectively shifted by half a unit cell in the c-direction can be seen starting at the top right corner of the grain. For clarity, it is schematically depicted in b). It is caused by the coalescence of two grains with different starting layers during the layer growth. The shift of half a unit cell is more easily seen by comparing the unit cell positions in the two halves of the grain, highlighted by the black squares.

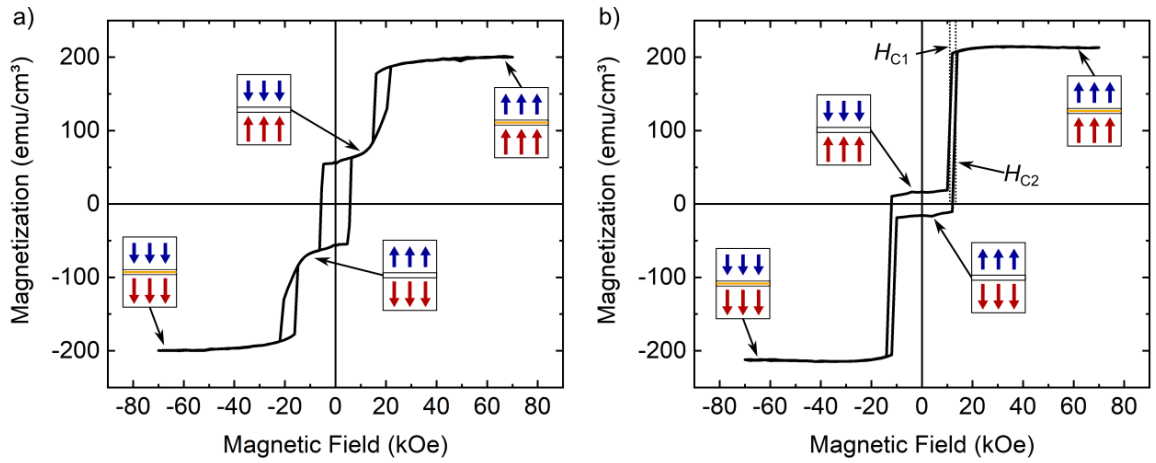

Figure S4: A comparison of the a) three-step and b) two-step reversal behaviour seen for TbFe-based bilayers at room temperature. In a), coming from the parallel alignment of both layers at saturation, the layer with lower magnetization and lower K_u switches first, leading to an antiparallel alignment. At the second switching event at low negative field, both layers switch simultaneously, conserving the antiparallel state stable at this field. With a stronger negative field, the low-magnetization layer switches once more, so the magnetization of both layers is once more parallel. In b), the field H_{C1} at which the lower-magnetization switches is lower than the switching field H_{C2} of the higher-magnetization layer. Accordingly, the parallel configuration is already stable after the second switching event, and the resulting hysteresis loop shows the two-step reversal behaviour.

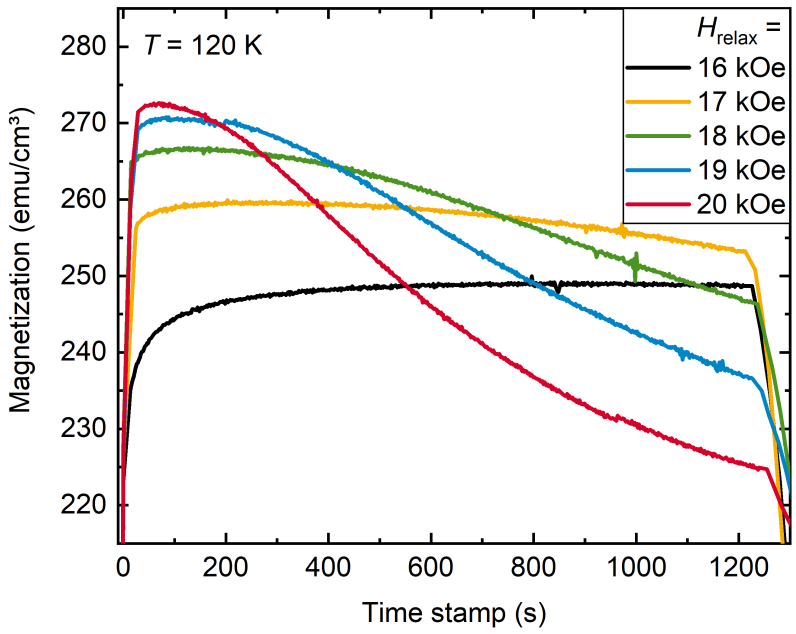

Figure S5: A magnetic relaxation measurement of a sub./Pt(5 nm)/$Tb_{20}Fe_{80}$(10 nm)/-$Tb_{36}Fe_{64}$(10 nm)/Pt(5 nm) sample at 120 K with various relaxation field values H_{relax}. The relaxation duration of 20 min was not enough to observe a decrease of magnetization for $H_{relax} = 16$ kOe, and no transition to a concave slope could be seen for $H_{relax} = 17$ and 18 kOe, which is why the measurement was repeated with an increased relaxation duration of 1 hour, as displayed in Fig. 7.20 b).

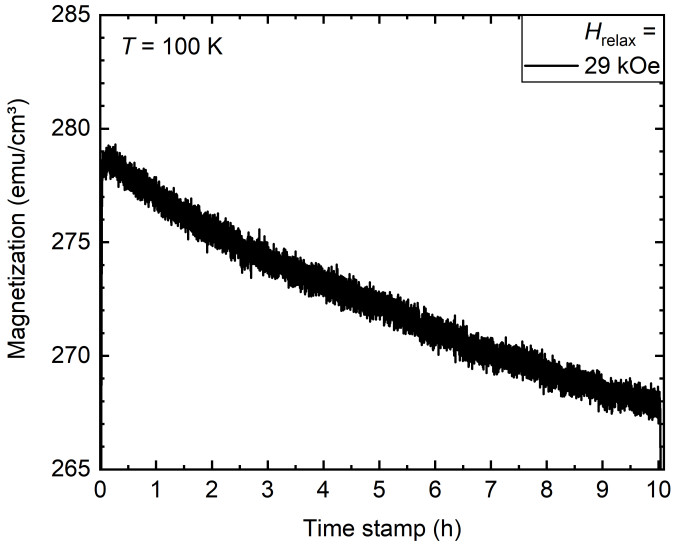

Figure S6: A magnetic relaxation measurement of a sub./Pt(5 nm)/$Tb_{20}Fe_{80}$(10 nm)/-$Tb_{36}Fe_{64}$(10 nm)/Pt(5 nm) sample at 100 K with a relaxation field of $H_{\mathrm{relax}} = 29$ kOe. The long relaxation time of 10 h was chosen since the slope is so low. Linear extrapolation of the slope suggests that the stable magnetization value at this field (around 248 emu/cm^3) would be reached after about 44 hours, but since the decay is not linear, this would take significantly longer.

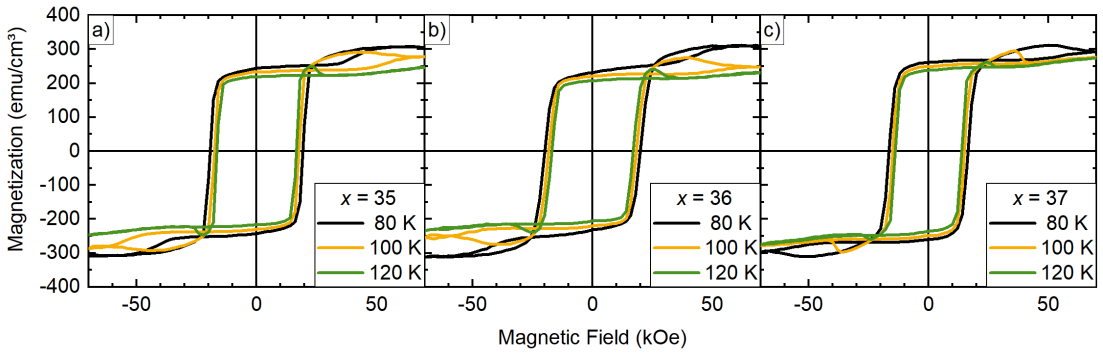

Figure S7: The hysteresis loops of three more TbFe-bases bilayers showing overcrossing hysteresis branches in the first and third quadrant. The layer stack of these samples is sub./Pt(5 nm)/Tb_xFe_{100-x}(10 nm)/$Tb_{19}Fe_{81}$(10 nm)/Pt(5 nm), with the respective values of x being given in the diagrams. For many of the measurements, the highest value of magnetization is reached after the overcrossing and not at maximum external field. This indicates that the transient state of parallel alignment of the two TbFe layers cannot be achieved by even the strong applied field of 70 kOe, but can temporarily exist due to the slow magnetization dynamics after the switching of the Tb-dominant layer.

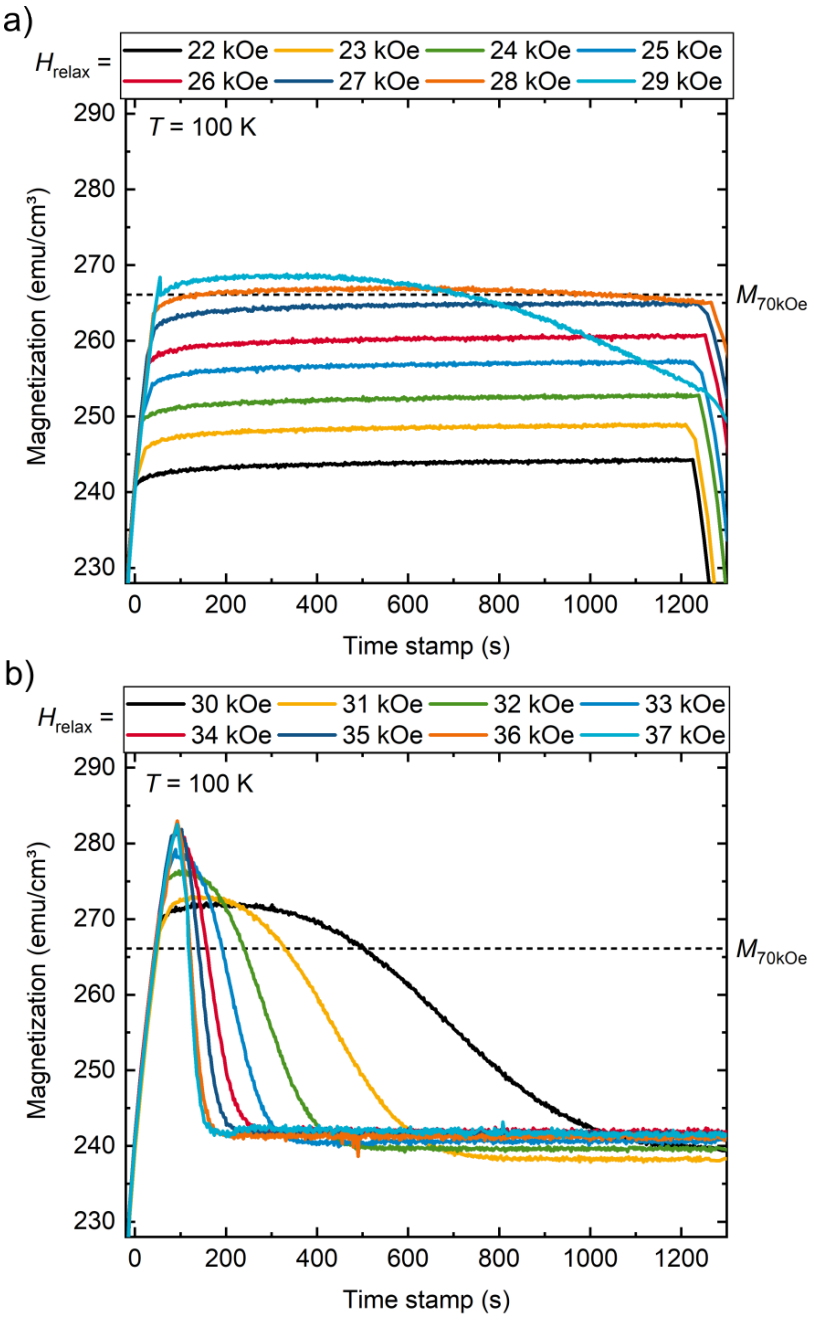

Figure S8: Magnetic relaxation measurements of the sample displayed in Fig. S7 c) taken at 100 K with various relaxation fields H_{relax}. Time stamp 0 is equivalent to the start of the overcrossing, i.e. when the field reaches 22 kOe. The magnetization of the sample at a field of 70 kOe ($M_{70\mathrm{kOe}}$) is highlighted by a dashed line for reference. The upwards slope of the magnetization seems identical for all measurements not crossing $M_{70\mathrm{kOe}}$. Once this value is surpassed for $H_{\mathrm{relax}} \geq 28$ kOe, the magnetization begins to relax towards the stable value at that field, around 240 emu/cm^3. The relaxation is faster and the overshooting of magnetization higher for larger H_{relax} up until 36 kOe.

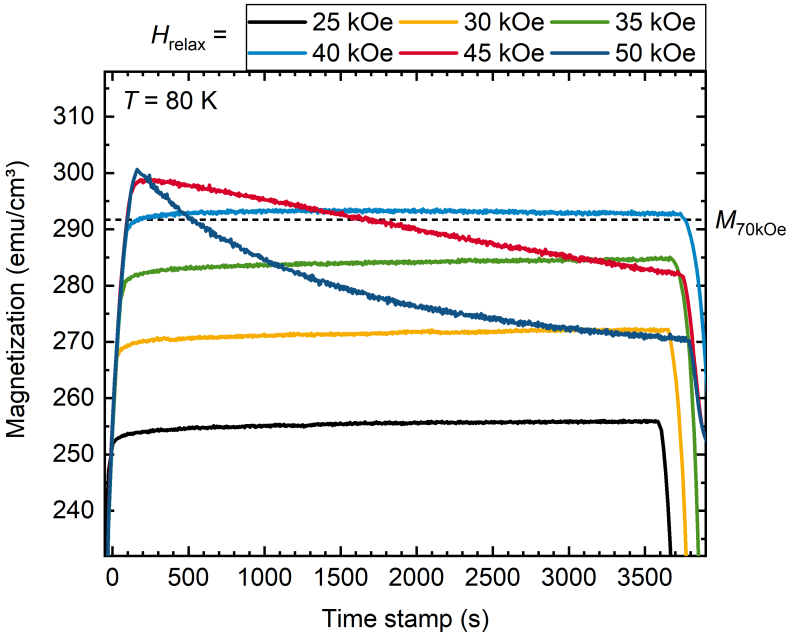

Figure S9: Magnetic relaxation measurements of the sample displayed in Fig. S7 c) taken at 80 K with various relaxation fields H_{relax}. Time stamp 0 is equivalent to the start of the overcrossing, i.e. when the field reaches 25 kOe. The magnetization of the sample at a field of 70 kOe ($M_{70\mathrm{kOe}}$) is highlighted by a dashed line for reference. Again, the upwards slope of the magnetization seems identical for all measurements not crossing $M_{70\mathrm{kOe}}$. The magnetization only barely starts decreasing for $H_{\mathrm{relax}} = 40$ kOe, while it is faster for higher relaxation fields.

Bibliography

[1] J. Fontana R. E., R. G. Biskeborn, M. Lantz, and G. M. Decad, "Tape in the cloud—Technology developments and roadmaps supporting 80 TB cartridge capacities", AIP Advances **9**, 125222 (2019) 10.1063/1.5130404.

[2] D. Weller, A. Moser, L. Folks, M. E. Best, W. Lee, M. F. Toney, M. Schwickert, J.-U. Thiele, and M. F. Doerner, "High K_u materials approach to 100 Gbits/in^2", IEEE Transactions on Magnetics **36**, 10–15 (2000) 10.1109/20.824418.

[3] M. Albrecht, G. Hu, I. L. Guhr, T. C. Ulbrich, J. Boneberg, P. Leiderer, and G. Schatz, "Magnetic multilayers on nanospheres", Nature Materials **4**, 203–206 (2005) 10.1038/nmat1324.

[4] M. Albrecht, C. T. Rettner, A. Moser, M. E. Best, and B. D. Terris, "Recording performance of high-density patterned perpendicular magnetic media", Applied Physics Letters **81**, 2875–2877 (2002) 10.1063/1.1512946.

[5] R. Wood, "Shingled Magnetic Recording (SMR) and Two-Dimensional Magnetic Recording (TDMR)", Journal of Magnetism and Magnetic Materials **561**, 169670 (2022) https://doi.org/10.1016/j.jmmm.2022.169670.

[6] J.-G. Zhu, X. Zhu, and Y. Tang, "Microwave Assisted Magnetic Recording", IEEE Transactions on Magnetics **44**, 125–131 (2008) 10.1109/TMAG.2007.911031.

[7] M. H. Kryder, E. C. Gage, T. W. McDaniel, W. A. Challener, R. E. Rottmayer, G. Ju, Y.-T. Hsia, and M. F. Erden, "Heat Assisted Magnetic Recording", Proceedings of the IEEE **96**, 1810–1835 (2008) 10.1109/JPROC.2008.2004315.

[8] D. Suess, C. Vogler, C. Abert, F. Bruckner, R. Windl, L. Breth, and J. Fidler, "Fundamental limits in heat-assisted magnetic recording and methods to overcome it with exchange spring structures", Journal of Applied Physics **117**, 163913 (2015) 10.1063/1.4918609.

[9] H. Li and J.-G. Zhu, "The Role of Media Property Distribution in HAMR SNR", IEEE Transactions on Magnetics **49**, 3568–3571 (2013) 10.1109/TMAG.2012.2234086.

[10] D. Weller, G. Parker, O. Mosendz, E. Champion, B. Stipe, X. Wang, T. Klemmer, G. Ju, and A. Ajan, "A HAMR Media Technology Roadmap to an Areal Density of 4 Tb/in^2 ", IEEE Transactions on Magnetics **50**, 1–8 (2014) 10.1109/TMAG.2013.2281027.

[11] D. Weller, G. Parker, O. Mosendz, A. Lyberatos, D. Mitin, N. Y. Safonova, and M. Albrecht, "Review Article: FePt heat assisted magnetic recording media", Journal of Vacuum Science & Technology B **34**, 060801 (2016) 10.1116/1.4965980.

[12] R. F. L. Evans, R. W. Chantrell, U. Nowak, A. Lyberatos, and H.-J. Richter, "Thermally induced error: Density limit for magnetic data storage", Appl. Phys. Lett. **100**, 102402 (2012) 10.1063/1.3691196.

[13] H. J. Richter, A. Lyberatos, U. Nowak, R. F. L. Evans, and R. W. Chantrell, "The thermodynamic limits of magnetic recording", Journal of Applied Physics **111**, 033909 (2012) 10.1063/1.3681297.

[14] K. Hono, Y. K. Takahashi, G. Ju, J.-U. Thiele, A. Ajan, X. Yang, R. Ruiz, and L. Wan, "Heat-assisted magnetic recording media materials", MRS Bulletin **43**, 93–99 (2018) 10.1557/mrs.2018.5.

[15] C. Vogler, C. Abert, F. Bruckner, D. Suess, and D. Praetorius, "Heat-assisted magnetic recording of bit-patterned media beyond 10 Tb/in^2", Applied Physics Letters **108**, 102406 (2016) 10.1063/1.4943629.

[16] F. Steinbach, N. Stetzuhn, D. Engel, U. Atxitia, C. von Korff Schmising, and S. Eisebitt, "Accelerating double pulse all-optical write/erase cycles in metallic ferrimagnets", Applied Physics Letters **120**, 112406 (2022) 10.1063/5.0080351.

[17] C. D. Stanciu, F. Hansteen, A. Kimel, A. Kirilyuk, A. Tsukamoto, A. Itoh, and T. Rasing, "All-Optical Magnetic Recording with Circularly Polarized Light", Physical Review Letters **99**, 047601 (2007) 10.1103/PhysRevLett.99.047601.

[18] A. Hassdenteufel, B. Hebler, C. Schubert, A. Liebig, M. Teich, M. Helm, M. Aeschlimann, M. Albrecht, and R. Bratschitsch, "Thermally Assisted All-Optical Helicity Dependent Magnetic Switching in Amorphous $Fe_{100-x}Tb_x$ Alloy Films", Adv. Mater. **25**, 3122–3128 (2013) 10.1002/adma.201300176.

[19] M. J. G. Peeters, Y. M. van Ballegooie, and B. Koopmans, "Influence of magnetic fields on ultrafast laser-induced switching dynamics in Co/Gd bilayers", Phys. Rev. B **105**, 014429 (2022) 10.1103/PhysRevB.105.014429.

[20] J. Gorchon, C.-H. Lambert, Y. Yang, A. Pattabi, R. B. Wilson, S. Salahuddin, and J. Bokor, "Single shot ultrafast all optical magnetization switching of ferromagnetic Co/Pt multilayers", in 2017 fifth berkeley symposium on energy efficient electronic systems & steep transistors workshop (e3s) (2017), pp. 1–2, 10.1109/E3S.2017.8246170.

[21] S. Mangin, M. Gottwald, C.-H. Lambert, D. Steil, V. Uhlíř, L. Pang, M. Hehn, S. Alebrand, M. Cinchetti, G. Malinowski, Y. Fainman, M. Aeschlimann, and E. E. Fullerton, "Engineered materials for all-optical helicity-dependent magnetic switching", Nature Materials **13**, 286–292 (2014) 10.1038/nmat3864.

[22] C.-H. Lambert, S. Mangin, B. S. D. C. S. Varaprasad, Y. K. Takahashi, M. Hehn, M. Cinchetti, G. Malinowski, K. Hono, Y. Fainman, M. Aeschlimann, and E. E. Fullerton, "All-optical control of ferromagnetic thin films and nanostructures", Science **345**, 1337–1340 (2014) 10.1126/science.1253493.

[23] S. Bhatti, R. Sbiaa, A. Hirohata, H. Ohno, S. Fukami, and S. N. Piramanayagam, "Spintronics based random access memory: a review", Materials Today **20**, 530–548 (2017) https://doi.org/10.1016/j.mattod.2017.07.007.

[24] J. C. S. Kools, "Exchange-biased spin-valves for magnetic storage", IEEE Transactions on Magnetics **32**, 3165–3184 (1996) 10.1109/20.508381.

[25] Y. Huai, "Spin-Transfer Torque MRAM (STT-MRAM): Challenges and Prospects", AAPPS Bulletin (2008).

[26] T. Seki, S. Mitani, K. Yakushiji, and K. Takanashi, "Spin-polarized current-induced magnetization reversal in perpendicularly magnetized L1-FePt layers", Applied Physics Letters **88**, 172504 (2006) 10.1063/1.2198819.

[27] T. Seki, Y. Hasegawa, S. Mitani, S. Takahashi, H. Imamura, S. Maekawa, J. Nitta, and K. Takanashi, "Giant spin Hall effect in perpendicularly spin-polarized FePt/Au devices", Nature Materials **7**, 125–129 (2008) 10.1038/nmat2098.

[28] X. Zhao, J. Wen, B. Yang, H. Zhu, Q. Cao, D. Wang, Z. Qian, and Y. Du, "Electric Field Manipulated Multilevel Magnetic States Storage in FePt/(011) PMN-PT Heterostructure", ACS Applied Materials & Interfaces **9**, PMID: 28948771, 36038–36044 (2017) 10.1021/acsami.7b11015.

[29] M. Stiehl, S. Wust, N. Schmidt, T. Dannegger, J. Seyd, M. Berritta, P. M. Oppeneer, M. Albrecht, U. Nowak, and M. Aeschlimann, "All-optical switching in Cr- and Mn-doped $L1_0$ FePt thin films", Phys. Rev. Appl. **21**, 054064 (2024) 10.1103/PhysRevApplied.21.054064.

[30] Y. K. Takahashi, R. Medapalli, S. Kasai, J. Wang, K. Ishioka, S. H. Wee, O. Hellwig, K. Hono, and E. E. Fullerton, "Accumulative Magnetic Switching of Ultrahigh-Density Recording Media by Circularly Polarized Light", Phys. Rev. Appl. **6**, 054004 (2016) 10.1103/PhysRevApplied.6.054004.

[31] R. John, M. Berritta, D. Hinzke, C. Müller, T. Santos, H. Ulrichs, P. Nieves, J. Walowski, R. Mondal, O. Chubykalo-Fesenko, J. McCord, P. M. Oppeneer, U. Nowak, and M. Münzenberg, "Magnetisation switching of FePt nanoparticle recording medium by femtosecond laser pulses", Scientific Reports **7**, 4114 (2017) 10.1038/s41598-017-04167-w.

[32] M. O. A. Ellis, E. E. Fullerton, and R. W. Chantrell, "All-optical switching in granular ferromagnets caused by magnetic circular dichroism", Scientific Reports **6**, 30522 (2016) 10.1038/srep30522.

[33] C. Schubert, B. Hebler, H. Schletter, A. Liebig, M. Daniel, R. Abrudan, F. Radu, and M. Albrecht, "Interfacial exchange coupling in Fe-Tb/[Co/Pt] heterostructures", Physical Review B **87**, 054415 (2013) 10.1103/PhysRevB.87.054415.

[34] S. Romer, M. A. Marioni, K. Thorwarth, N. R. Joshi, C. E. Corticelli, H. J. Hug, S. Oezer, M. Parlinska-Wojtan, and H. Rohrmann, "Temperature dependence of large exchange-bias in TbFe-Co/Pt", Applied Physics Letters **101**, 222404 (2012) 10.1063/1.4767142.

[35] M. A. Ruderman and C. Kittel, "Indirect Exchange Coupling of Nuclear Magnetic Moments by Conduction Electrons", Phys. Rev. **96**, 99–102 (1954) 10.1103/PhysRev.96.99.

[36] T. Kasuya, "A Theory of Metallic Ferro- and Antiferromagnetism on Zener's Model", Progress of Theoretical Physics **16**, 45–57 (1956) 10.1143/PTP.16.45.

[37] K. Yosida, "Magnetic Properties of Cu-Mn Alloys", Phys. Rev. **106**, 893–898 (1957) 10.1103/PhysRev.106.893.

[38] P. Bruno and C. Chappert, "Ruderman-Kittel theory of oscillatory interlayer exchange coupling", Phys. Rev. B **46**, 261–270 (1992) 10.1103/PhysRevB.46.261.

[39] S. S. P. Parkin, "Systematic variation of the strength and oscillation period of indirect magnetic exchange coupling through the 3d, 4d, and 5d transition metals", Phys. Rev. Lett. **67**, 3598–3601 (1991) 10.1103/PhysRevLett.67.3598.

[40] M. N. Baibich, J. M. Broto, A. Fert, F. N. Van Dau, F. Petroff, P. Etienne, G. Creuzet, A. Friederich, and J. Chazelas, "Giant Magnetoresistance of (001)Fe/(001)Cr Magnetic Superlattices", Phys. Rev. Lett. **61**, 2472–2475 (1988) 10.1103/PhysRevLett.61.2472.

[41] G. Binasch, P. Grünberg, F. Saurenbach, and W. Zinn, "Enhanced magnetoresistance in layered magnetic structures with antiferromagnetic interlayer exchange", Phys. Rev. B **39**, 4828–4830 (1989) 10.1103/PhysRevB.39.4828.

[42] B. Dieny, V. S. Speriosu, S. S. P. Parkin, B. A. Gurney, D. R. Wilhoit, and D. Mauri, "Giant magnetoresistive in soft ferromagnetic multilayers", Phys. Rev. B **43**, 1297–1300 (1991) 10.1103/PhysRevB.43.1297.

[43] R. Skomski and J. M. D. Coey, "Magnetic anisotropy — How much is enough for a permanent magnet?", Scripta Materialia **112**, 3–8 (2016) https://doi.org/10.1016/j.scriptamat.2015.09.021.

[44] E. F. Kneller and R. Hawig, "The exchange-spring magnet: a new material principle for permanent magnets", IEEE Transactions on Magnetics **27**, 3588–3560 (1991) 10.1109/20.102931.

[45] T. Leineweber and H. Kronmüller, "Magnetisation Reversal Modes in Inhomogeneous Magnets", physica status solidi (b) **201**, 291–301 (1997) https://doi.org/10.1002/1521-3951(199705)201:1<291::AID-PSSB291>3.0.CO;2-X.

[46] E. E. Fullerton, J. S. Jiang, and S. D. Bader, "Hard/soft magnetic heterostructures: model exchange-spring magnets", Journal of Magnetism and Magnetic Materials **200**, 392–404 (1999) https://doi.org/10.1016/S0304-8853(99)00376-5.

[47] S.-s. Yan, J. A. Barnard, F.-t. Xu, J. L. Weston, and G. Zangari, "Critical dimension of the transition from single switching to an exchange spring process in hard/soft exchange-coupled bilayers", Phys. Rev. B **64**, 184403 (2001) 10.1103/PhysRevB.64.184403.

[48] G.-h. Guo, G.-f. Zhang, S.-y. Song, D. W. Wang, G. J. Bowden, and P. A. J. de Groot, "Irreversible magnetic exchange-spring processes in antiferromagnetic exchange-coupled bilayer systems", Applied Physics Letters **93**, 102505 (2008) 10.1063/1.2972028.

[49] G.-h. Guo, G.-f. Zhang, and X.-g. Wang, "Crossover from reversible to irreversible magnetic exchange-spring processes in antiferromagnetically exchange-coupled soft/hard bilayer structures", Journal of Applied Physics **108**, 043919–043919 (2010) 10.1063/1.3478752.

[50] X.-g. Wang, G.-h. Guo, and G.-f. Zhang, "Transition from reversible to irreversible magnetic exchange-spring processes in antiferromagnetically exchange-coupled hard/soft/hard trilayer structures", Journal of Magnetism and Magnetic Materials **323**, 1722–1726 (2011) https://doi.org/10.1016/j.jmmm.2011.02.007.

[51] R. Skomski and J. M. D. Coey, "Giant energy product in nanostructured two-phase magnets", Phys. Rev. B **48**, 15812–15816 (1993) 10.1103/PhysRevB.48.15812.

[52] G. Vashisht, R. Goyal, M. Bala, S. Ojha, and S. Annapoorni, "Studies of Exchange Coupling in FeCo/$L1_0$-FePt Bilayer Thin Films", IEEE Transactions on Magnetics **55**, 1–5 (2019) 10.1109/TMAG.2018.2876167.

[53] D. Suess, T. Schrefl, R. Dittrich, M. Kirschner, F. Dorfbauer, G. Hrkac, and J. Fidler, "Exchange spring recording media for areal densities up to 10Tbit/in^2", Journal of Magnetism and Magnetic Materials **290-291**, Proceedings of the Joint European Magnetic Symposia (JEMS' 04), 551–554 (2005) https://doi.org/10.1016/j.jmmm.2004.11.525.

[54] D. Suess, J. Lee, J. Fidler, and T. Schrefl, "Exchange-coupled perpendicular media", Journal of Magnetism and Magnetic Materials **321**, Current Perspectives: Perpendicular Recording, 545–554 (2009) https://doi.org/10.1016/j.jmmm.2008.06.041.

[55] D. Suess, T. Schrefl, S. Fähler, M. Kirschner, G. Hrkac, F. Dorfbauer, and J. Fidler, "Exchange spring media for perpendicular recording", Applied Physics Letters **87**, 012504 (2005) 10.1063/1.1951053.

[56] D. Makarov, J. Lee, C. Brombacher, C. Schubert, M. Fuger, D. Suess, J. Fidler, and M. Albrecht, "Perpendicular FePt-based exchange-coupled composite media", Applied Physics Letters **96**, 062501–062501 (2010) 10.1063/1.3309417.

[57] T. Dutta, S. N. Piramanayagam, T. H. Ru, M. S. M. Saifullah, C. S. Bhatia, and H. Yang, "Exchange coupled CoPt/FePtC media for heat assisted magnetic recording", Applied Physics Letters **112**, 142411 (2018) 10.1063/1.5012815.

[58] W. H. Meiklejohn and C. P. Bean, "New Magnetic Anisotropy", Phys. Rev. **105**, 904–913 (1957) 10.1103/PhysRev.105.904.

[59] R. L. Stamps, "Mechanisms for exchange bias", Journal of Physics D: Applied Physics **33**, R247 (2000) 10.1088/0022-3727/33/23/201.

[60] A. P. Malozemoff, "Random-field model of exchange anisotropy at rough ferromagnetic-antiferromagnetic interfaces", Phys. Rev. B **35**, 3679–3682 (1987) 10.1103/PhysRevB.35.3679.

[61] A. P. Malozemoff, "Heisenberg-to-Ising crossover in a random-field model with uniaxial anisotropy", Phys. Rev. B **37**, 7673–7679 (1988) 10.1103/PhysRevB.37.7673.

[62] D. Mauri, H. C. Siegmann, P. S. Bagus, and E. Kay, "Simple model for thin ferromagnetic films exchange coupled to an antiferromagnetic substrate", Journal of Applied Physics **62**, 3047–3049 (1987) 10.1063/1.339367.

[63] T. C. Schulthess and W. H. Butler, "Consequences of Spin-Flop Coupling in Exchange Biased Films", Phys. Rev. Lett. **81**, 4516–4519 (1998) 10.1103/PhysRevLett.81.4516.

[64] M. D. Stiles and R. D. McMichael, "Model for exchange bias in polycrystalline ferromagnet-antiferromagnet bilayers", Phys. Rev. B **59**, 3722–3733 (1999) 10.1103/PhysRevB.59.3722.

[65] U. Nowak, K. D. Usadel, J. Keller, P. Miltényi, B. Beschoten, and G. Güntherodt, "Domain state model for exchange bias. I. Theory", Phys. Rev. B **66**, 014430 (2002) 10.1103/PhysRevB.66.014430.

[66] T. Mewes and R. L. Stamps, "Exchange bias of antiferromagnets with random anisotropies and perfectly compensated interfaces", Applied Physics Letters **84**, 3840–3842 (2004) 10.1063/1.1745112.

[67] T. J. Moran, J. M. Gallego, and I. K. Schuller, "Increased exchange anisotropy due to disorder at permalloy/CoO interfaces", Journal of Applied Physics **78**, 1887–1891 (1995) 10.1063/1.360225.

[68] J. Nogués, T. J. Moran, D. Lederman, I. K. Schuller, and K. V. Rao, "Role of interfacial structure on exchange-biased FeF_2-Fe", Phys. Rev. B **59**, 6984–6993 (1999) 10.1103/PhysRevB.59.6984.

[69] A. E. Berkowitz and J. H. Greiner, "Exchange Anisotropy and Strain Interactions in the Ni-NiO System", Journal of Applied Physics **36**, 3330–3341 (1965) 10.1063/1.1702976.

[70] J. Bransky, I. Bransky, and A. A. Hirsch, "Exchange Anisotropy in Thin Cobalt Films Deposited on a CoO Single-Crystal Substrate", Journal of Applied Physics **41**, 183–185 (1970) 10.1063/1.1658318.

[71] W. Feng, N.-Y. Jiang, S.-D. Huang, H.-M. Chen, C.-W. Cheng, G. Chern, and C.-C. Yu, ""External forces" are indispensable for the occurrence of exchange bias?", Journal of Applied Physics **111**, 033904 (2012) 10.1063/1.3681174.

[72] J. Jia, Y. Chen, B. Wang, B. Han, Y. Wu, Y. Wang, and J. Cao, "The double-shifted magnetic hysteresis loops and domain structure in perpendicular [Co/Ni]N/IrMn exchange biased systems", Journal of Physics D: Applied Physics **52**, 065001 (2018) 10.1088/1361-6463/aaf0f9.

[73] A. D. Talantsev, M. V. Bahmetiev, and R. B. Morgunov, "Robust evaluation of coercivity in exchange biased films", Measurement **204**, 112074 (2022) https://doi.org/10.1016/j.measurement.2022.112074.

[74] C. Gritsenko, A. Omelyanchik, A. Berg, I. Dzhun, N. Chechenin, O. Dikaya, O. A. Tretiakov, and V. Rodionova, "Inhomogeneous magnetic field influence on magnetic properties of NiFe/IrMn thin film structures", Journal of Magnetism and Magnetic Materials **475**, 763–766 (2019) https://doi.org/10.1016/j.jmmm.2018.10.013.

[75] P. J. van der Zaag, Y. Ijiri, J. A. Borchers, L. F. Feiner, R. M. Wolf, J. M. Gaines, R. W. Erwin, and M. A. Verheijen, "Difference between Blocking and Néel Temperatures in the Exchange Biased Fe_3O_4/CoO System", Phys. Rev. Lett. **84**, 6102–6105 (2000) 10.1103/PhysRevLett.84.6102.

[76] P. J. van der Zaag, A. R. Ball, L. F. Feiner, R. M. Wolf, and P. A. A. van der Heijden, "Exchange biasing in MBE grown Fe_3O_4/CoO bilayers: The antiferromagnetic layer thickness dependence", Journal of Applied Physics **79**, 5103–5105 (1996) 10.1063/1.361315.

[77] T. Ambrose and C. L. Chien, "Dependence of exchange coupling on antiferromagnetic layer thickness in NiFe/CoO bilayers", Journal of Applied Physics **83**, 6822–6824 (1998) 10.1063/1.367863.

[78] A. J. Devasahayam and M. H. Kryder, "The dependence of the antiferromagnet/ferromagnet blocking temperature on antiferromagnet thickness and deposition conditions", Journal of Applied Physics **85**, 5519–5521 (1999) 10.1063/1.369880.

[79] H. Shim, P. Dutta, M. S. Seehra, and J. Bonevich, "Size dependence of the blocking temperatures and electron magnetic resonance spectra in NiO nanoparticles", Solid State Communications **145**, 192–196 (2008) https://doi.org/10.1016/j.ssc.2007.10.026.

[80] Q. Chen and Z. J. Zhang, "Size-dependent superparamagnetic properties of $MgFe_2O_4$ spinel ferrite nanocrystallites", Applied Physics Letters **73**, 3156–3158 (1998) 10.1063/1.122704.

[81] E. Fulcomer and S. H. Charap, "Thermal fluctuation aftereffect model for some systems with ferromagnetic-antiferromagnetic coupling", Journal of Applied Physics **43**, 4190–4199 (1972) 10.1063/1.1660894.

[82] K. Nishioka, S. Shigematsu, T. Imagawa, and S. Narishige, "Thickness effect on ferro/antiferromagnetic coupling of Co/CrMnPt systems", Journal of Applied Physics **83**, 3233–3238 (1998) 10.1063/1.367090.

[83] A. N. Dobrynin, P. Warin, A. Vorobiev, and D. Givord, "On the origin of positive exchange bias and coercivity enhancement in proximity to the blocking temperature", Journal of Magnetism and Magnetic Materials **520**, Magnetic materials and their applications: in Memory of Dominique Givord, 166707 (2021) https://doi.org/10.1016/j.jmmm.2020.166707.

[84] M. G. Blamire, M. Ali, C.-W. Leung, C. H. Marrows, and B. J. Hickey, "Exchange Bias and Blocking Temperature in Co/FeMn/CuNi Trilayers", Phys. Rev. Lett. **98**, 217202 (2007) 10.1103/PhysRevLett.98.217202.

[85] K. G. West, D. N. H. Nam, J. W. Lu, N. D. Bassim, Y. N. Picard, R. M. Stroud, and S. A. Wolf, "Exchange bias in a single phase ferrimagnet", Journal of Applied Physics **107**, 113915 (2010) 10.1063/1.3374639.

[86] S. Gondh, M. M. Patidar, K. Kumar, M. P. Saravanan, V. Ganesan, and A. K. Pramanik, "Large exchange bias and low-temperature glassy state in the frustrated triangular-lattice antiferromagnet $Ba_3NiIr_2O_9$", Phys. Rev. B **104**, 014401 (2021) 10.1103/PhysRevB.104.014401.

[87] J. Nogués, D. Lederman, T. J. Moran, and I. K. Schuller, "Positive Exchange Bias in FeF_2-Fe Bilayers", Phys. Rev. Lett. **76**, 4624–4627 (1996) 10.1103/PhysRevLett.76.4624.

[88] S. K. Mishra, F. Radu, H. A. Dürr, and W. Eberhardt, "Training-Induced Positive Exchange Bias in NiFe/IrMn Bilayers", Phys. Rev. Lett. **102**, 177208 (2009) 10.1103/PhysRevLett.102.177208.

[89] B. M. Wang, Y. Liu, P. Ren, B. Xia, K. B. Ruan, J. B. Yi, J. Ding, X. G. Li, and L. Wang, "Large Exchange Bias after Zero-Field Cooling from an Unmagnetized State", Phys. Rev. Lett. **106**, 077203 (2011) 10.1103/PhysRevLett.106.077203.

[90] A. Migliorini, B. Kuerbanjiang, T. Huminiuc, D. Kepaptsoglou, M. Muñoz, J. L. F. Cuñado, J. Camarero, C. Aroca, G. Vallejo-Fernández, V. K. Lazarov, and J. L. Prieto, "Spontaneous exchange bias formation driven by a structural phase transition in the antiferromagnetic material", Nature Materials **17**, 28–35 (2018) 10.1038/nmat5030.

[91] B. Liu, B. Wang, T. Nie, Y. Xie, H. Yang, G. Li, J. Pan, and R.-W. Li, "Effect of isothermal crystallization in antiferromagnetic IrMn on the formation of spontaneous exchange bias", Applied Physics Letters **118**, 252404 (2021) 10.1063/5.0053339.

[92] L. Bufaiçal and E. M. Bittar, "Essential aspects of the spontaneous exchange bias effect", Journal of Magnetism and Magnetic Materials **599**, 172109 (2024) https://doi.org/10.1016/j.jmmm.2024.172109.

[93] T. Hajiri, H. Goto, and H. Asano, "Scaling the electrical current switching of exchange bias in fully epitaxial antiferromagnet/ferromagnet bilayers", Phys. Rev. B **102**, 014404 (2020) 10.1103/PhysRevB.102.014404.

[94] J. Zehner, D. Wolf, M. U. Hasan, M. Huang, D. Bono, K. Nielsch, K. Leistner, and G. S. D. Beach, "Magnetoionic control of perpendicular exchange bias", Phys. Rev. Mater. **5**, L061401 (2021) 10.1103/PhysRevMaterials.5.L061401.

[95] J. Gompertz, R. Carpenter, S. Hassan, M. Ormston, and K. O'Grady, "Magnetization Asymmetry in Exchange Bias Systems", IEEE Transactions on Magnetics **58**, 1–5 (2022) 10.1109/TMAG.2021.3080699.

[96] S. Jenkins, R. W. Chantrell, and R. F. L. Evans, "Exchange bias in multigranular noncollinear $IrMn_3$/CoFe thin films", Phys. Rev. B **103**, 014424 (2021) 10.1103/PhysRevB.103.014424.

[97] K. O'Grady, L. E. Fernandez-Outon, and G. Vallejo-Fernandez, "A new paradigm for exchange bias in polycrystalline thin films", Journal of Magnetism and Magnetic Materials **322**, 883–899 (2010) https://doi.org/10.1016/j.jmmm.2009.12.011.

[98] M. Merkel, R. Huhnstock, M. Reginka, D. Holzinger, M. Vogel, A. Ehresmann, J. Zehner, and K. Leistner, "Interrelation between polycrystalline structure and time-dependent magnetic anisotropies in exchange-biased bilayers", Phys. Rev. B **102**, 144421 (2020) 10.1103/PhysRevB.102.144421.

[99] T. J. Klemmer, V. R. Inturi, M. K. Minor, and J. A. Barnard, "Exchange induced unidirectional anisotropy observed using Cr–Al antiferromagnetic films", Applied Physics Letters **70**, 2915–2917 (1997) 10.1063/1.119052.

[100] C. Leighton, J. Nogués, B. J. Jönsson-Åkerman, and I. K. Schuller, "Coercivity Enhancement in Exchange Biased Systems Driven by Interfacial Magnetic Frustration", Phys. Rev. Lett. **84**, 3466–3469 (2000) 10.1103/PhysRevLett.84.3466.

[101] J.-g. Hu, G. Jin, A. Hu, and Y.-q. Ma, "Temperature dependence of exchange bias and coercivity in ferromagnetic/antiferromagnetic bilayers", The European Physical Journal B - Condensed Matter and Complex Systems **40**, 265–271 (2004) 10.1140/epjb/e2004-00272-0.

[102] R. Jungblut, R. Coehoorn, M. T. Johnson, J. aan de Stegge, and A. Reinders, "Orientational dependence of the exchange biasing in molecular-beam-epitaxy-grown $Ni_{80}Fe_{20}/Fe_{50}Mn_{50}$ bilayers (invited)", Journal of Applied Physics **75**, 6659–6664 (1994) 10.1063/1.356888.

[103] K. A. Seu, H. Huang, J. F. Lesoine, H. D. Showman, J. Egelhoff W. F., L. Gan, and A. C. Reilly, "Co layer thickness dependence of exchange biasing for IrMn/Co and FeMn/Co", Journal of Applied Physics **93**, 6611–6613 (2003) 10.1063/1.1555332.

[104] D. Mauri, E. Kay, D. Scholl, and J. K. Howard, "Novel method for determining the anisotropy constant of MnFe in a NiFe/MnFe sandwich", Journal of Applied Physics **62**, 2929–2932 (1987) 10.1063/1.339374.

[105] C. Y. Tsai, J.-H. Hsu, P. Saravanan, and K. F. Lin, "Study on the occurrence of spontaneously established perpendicular exchange bias in $Co_{49}Pt_{51}$/IrMn bilayers", Journal of Applied Physics **115**, 17D726 (2014) 10.1063/1.4868915.

[106] W. Zhang and K. M. Krishnan, "Epitaxial exchange-bias systems: from fundamentals to future spin-orbitronics", Materials Science and Engineering: R: Reports **105**, 1–20 (2016) https://doi.org/10.1016/j.mser.2016.04.001.

[107] C. Y. Tsai, J.-H. Hsu, and K. F. Lin, "Perpendicular exchange bias behaviors of CoPt/IrMn and CoPt/FeMn bilayers: A comparative study", Journal of Applied Physics **117**, 17D153 (2015) 10.1063/1.4919116.

[108] W. Zhang, M. E. Bowden, and K. M. Krishnan, "Competing effects of magnetocrystalline anisotropy and exchange bias in epitaxial Fe/IrMn bilayers", Applied Physics Letters **98**, 092503 (2011) 10.1063/1.3561516.

[109] M. Takahashi and M. Tsunoda, "Magnetic anisotropy of antiferromagnet and its role on the exchange bias in ferromagnetic/antiferromagnetic bilayers", Journal of Physics D: Applied Physics **35**, 2365 (2002) 10.1088/0022-3727/35/19/307.

[110] W. C. Cain and M. H. Kryder, "Investigation of the exchange mechanism in NiFe-TbCo bilayers", Journal of Applied Physics **67**, 5722–5724 (1990) 10.1063/1.346107.

[111] P. J. van der Zaag, R. M. Wolf, A. R. Ball, C. Bordel, L. F. Feiner, and R. Jungblut, "A study of the magnitude of exchange biasing in [111] Fe_3O_4/CoO bilayers", Journal of Magnetism and Magnetic Materials **148**, 346–348 (1995) https://doi.org/10.1016/0304-8853(95)00266-9.

[112] S. Mangin, G. Marchal, and B. Barbara, "Evidence of Exchange-Bias-Like Phenomenon in GdFe/TbFe/GdFe Domain Wall Junctions", Phys. Rev. Lett. **82**, 4336–4339 (1999) 10.1103/PhysRevLett.82.4336.

[113] S. Mangin, F. Montaigne, and A. Schuhl, "Interface domain wall and exchange bias phenomena in ferrimagnetic/ferrimagnetic bilayers", Phys. Rev. B **68**, 140404 (2003) 10.1103/PhysRevB.68.140404.

[114] D. Paccard, C. Schlenker, O. Massenet, R. Montmory, and A. Yelon, "A New Property of Ferromagnetic-Antiferromagnetic Coupling", physica status solidi (b) **16**, 301–311 (1966) https://doi.org/10.1002/pssb.19660160131.

[115] C. Schlenker, S. S. P. Parkin, J. C. Scott, and K. Howard, "Magnetic disorder in the exchange bias bilayered FeNi-FeMn system", Journal of Magnetism and Magnetic Materials **54-57**, 801–802 (1986) https://doi.org/10.1016/0304-8853(86)90260-X.

[116] T. Miyazaki and N. Tezuka, "Giant magnetic tunneling effect in Fe/Al_2O_3/Fe junction", J. Magn. Magn. Mater. **139**, L231–L234 (1995) https://doi.org/10.1016/0304-8853(95)90001-2.

[117] J. M. Daughton, "GMR applications", Journal of Magnetism and Magnetic Materials **192**, 334–342 (1999) https://doi.org/10.1016/S0304-8853(98)00376-X.

[118] S. Yan, Z. Zhou, Y. Yang, Q. Leng, and W. Zhao, "Developments and applications of tunneling magnetoresistance sensors", Tsinghua Science and Technology **27**, 443–454 (2022) 10.26599/TST.2021.9010061.

[119] O. Akdogan, A. Dobrynin, D. Le Roy, N. M. Dempsey, and D. Givord, "Superferrimagnetism in hard Nd-Fe-B thick films, an original concept for coercivity enhancement", Journal of Applied Physics **115**, 17A764 (2014) 10.1063/1.4869067.

[120] N. R. Anderson and R. E. Camley, "Temperature-dependent magnetization in bimagnetic nanoparticles with antiferromagnetic interfacial exchange", Phys. Rev. B **94**, 134432 (2016) 10.1103/PhysRevB.94.134432.

[121] K. Matchida, S. Suzuki, T. Kawasaki, D.-S. Li, T. Kitamon, K. Nakamura, and Y. Shimizu, "High-coercive Nd-Fe-B sintered magnets diffused with Dy or Tb metal and their applications", in 2005 IEEE International Magnetics Conference (INTERMAG) (2005), pp. 947–948, 10.1109/INTMAG.2005.1463902.

[122] J. Wang, H. Sepehri-Amin, H. Tajiri, T. Nakamura, K. Masuda, Y. K. Takahashi, T. Ina, T. Uruga, I. Suzuki, Y. Miura, and K. Hono, "Impact of carbon segregant on microstructure and magnetic properties of FePt-C nanogranular films on MgO (001) substrate", Acta Materialia **166**, 413–423 (2019) https://doi.org/10.1016/j.actamat.2019.01.001.

[123] T. Seki, S. Iihama, T. Taniguchi, and K. Takanashi, "Large spin anomalous Hall effect in $L1_0$-FePt: Symmetry and magnetization switching", Phys. Rev. B **100**, 144427 (2019) 10.1103/PhysRevB.100.144427.

[124] J. Yu, R. González-Hernández, L. Liu, J. Deng, H. Y. Yoong, H. Wang, W. Lin, H. Liu, F. Poh, J. Sinova, and J. Chen, "Thickness dependence of anomalous Hall conductivity in $L1_0$-FePt thin film", Journal of Physics D: Applied Physics **52**, 43LT02 (2019) 10.1088/1361-6463/ab360a.

[125] B. Zhao, H. Xue, G. Wu, Z. Zhu, Y. Ren, Q. Y. Jin, and Z. Zhang, "Interlayer modulation on the dynamic magnetic properties of $L1_0$-FePt/NM/$[CoNi]_5$ composite film structures", Applied Physics Letters **115**, 062401 (2019) 10.1063/1.5099182.

[126] S. Yoshimura, S. Omiya, G. Egawa, H. Saito, and J. Bai, "Control of magnetic anisotropy field of (001) oriented $L1_0$-Fe(Pd_xPt_{1-x}) films for MRAM application", Journal of Physics: Conference Series **266**, 012114 (2011) 10.1088/1742-6596/266/1/012114.

[127] R. Sbiaa, H. Meng, and S. N. Piramanayagam, "Materials with perpendicular magnetic anisotropy for magnetic random access memory", physica status solidi (RRL) – Rapid Research Letters **5**, 413–419 (2011) https://doi.org/10.1002/pssr.201105420.

[128] J. M. Slaughter, "Materials for Magnetoresistive Random Access Memory", Annual Review of Materials Research **39**, 277–296 (2009) 10.1146/annurev-matsci-082908-145355.

[129] M. Yoshikawa, E. Kitagawa, T. Nagase, T. Daibou, M. Nagamine, K. Nishiyama, T. Kishi, and H. Yoda, "Tunnel Magnetoresistance Over 100% in MgO-Based Magnetic Tunnel Junction Films With Perpendicular Magnetic $L1_0$-FePt Electrodes", IEEE Transactions on Magnetics **44**, 2573–2576 (2008) 10.1109/TMAG.2008.2003059.

[130] M. Kotsugi, H. Maruyama, N. Ishimatsu, N. Kawamura, M. Suzuki, M. Mizumaki, K. Osaka, T. Matsumoto, T. Ohkochi, T. Ohtsuki, T. Kojima, M. Mizuguchi, K. Takanashi, and Y. Watanabe, "Structural, magnetic and electronic state characterization of $L1_0$-type ordered FeNi alloy extracted from a natural meteorite", Journal of Physics: Condensed Matter **26**, 064206 (2014) 10.1088/0953-8984/26/6/064206.

[131] D. E. Laughlin, K. Srinivasan, M. Tanase, and L. Wang, "Crystallographic aspects of $L1_0$ magnetic materials", Scripta Materialia **53**, 383–388 (2005) https://doi.org/10.1016/j.scriptamat.2005.04.039.

[132] P. Ravindran, A. Kjekshus, H. Fjellvåg, P. James, L. Nordström, B. Johansson, and O. Eriksson, "Large magnetocrystalline anisotropy in bilayer transition metal phases from first-principles full-potential calculations", Phys. Rev. B **63**, 144409 (2001) 10.1103/PhysRevB.63.144409.

[133] C. Creemers, S. Helfensteyn, J. Luyten, and M. Schurmans, "Synergy between material, surface science experiments and simulations", in (Springer, 2007), pp. 109–169, 10.1007/978-0-387-34565-9_5.

[134] M. Ohtake, S. Ouchi, F. Kirino, and M. Futamoto, "$L1_0$ ordered phase formation in FePt, FePd, CoPt, and CoPd alloy thin films epitaxially grown on MgO(001) single-crystal substrates", Journal of Applied Physics **111**, 07A708 (2012) 10.1063/1.3672856.

[135] X. H. Li, B. T. Liu, W. Li, H. Y. Sun, D. Q. Wu, and X. Y. Zhang, "Atomic ordering kinetics of FePt thin films: Nucleation and growth of $L1_0$ ordered domains", Journal of Applied Physics **101**, 093911 (2007) 10.1063/1.2730568.

[136] W. Li and L. Chen, "Grain growth mechanism and magnetic properties in $L1_0$-FePt thin films", AIP Advances **7**, 085203 (2017) 10.1063/1.4991423.

[137] C. Suryanarayana and M. G. Norton, *X-Ray Diffraction: A Practical Approach*, First (Springer New York, NY, 1998).

[138] M. Albrecht and C. Brombacher, "Rapid thermal annealing of FePt thin films", physica status solidi (a) **210**, 1272–1281 (2013) https://doi.org/10.1002/pssa.201228718.

[139] E. Yang, D. E. Laughlin, and J.-G. Zhu, "Correction of Order Parameter Calculations for FePt Perpendicular Thin Films", IEEE Transactions on Magnetics **48**, 7–12 (2012) 10.1109/TMAG.2011.2164547.

[140] D. J. Sellmyer, C. P. Luo, M. L. Yan, and Y. Liu, "High-anisotropy nanocomposite films for magnetic recording", IEEE Transactions on Magnetics **37**, 1286–1291 (2001) 10.1109/20.950820.

[141] M. F. Toney, M. G. Samant, T. Lin, and D. Mauri, "Thickness dependence of exchange bias and structure in MnPt and MnNi spin valves", Applied Physics Letters **81**, 4565–4567 (2002) 10.1063/1.1528279.

[142] A. Edström, J. Chico, A. Jakobsson, A. Bergman, and J. Rusz, "Electronic structure and magnetic properties of $L1_0$ binary alloys", Phys. Rev. B **90**, 014402 (2014) 10.1103/PhysRevB.90.014402.

[143] D. Solina, W. Schmidt, R. Kaltofen, C. Krien, C.-H. Lai, and A. Schreyer, "The magnetic structure of $L1_0$ ordered MnPt at room temperature determined using polarized neutron diffraction", Materials Research Express **6**, 076105 (2019) 10.1088/2053-1591/ab1318.

[144] R. Umetsu, A. Sakuma, and K. Fukamichi, "Magnetic anisotropy energy of antiferromagnetic L10-type equiatomic Mn alloys", Applied Physics Letters **89**, 052504–052504 (2006) 10.1063/1.2236103.

[145] R. Zhang, R. Skomski, X.-Z. Li, Z. Li, P. Manchanda, A. Kashyap, R. Kirby, S.-H. Liou, and D. Sellmyer, "$L1_0$ CrPt phase formation and magnetic properties", Journal of Applied Physics **111**, 7–720 (2012) 10.1063/1.3677928.

[146] N. Cheng, J. Ahn, and K. M. Krishnan, "Epitaxial growth and exchange biasing of PdMn/Fe bilayers grown by ion-beam sputtering", Journal of Applied Physics **89**, 6597–6599 (2001) 10.1063/1.1360677.

[147] D. Goll and T. Bublat, "Large-area hard magnetic L10-FePt and composite L10-FePt based nanopatterns", physica status solidi (a) **210**, 1261–1271 (2013) https://doi.org/10.1002/pssa.201329017.

[148] C. Leroux, M. C. Cadeville, V. Pierron-Bohnes, G. Inden, and F. Hinz, "Comparative investigation of structural and transport properties of $L1_0$ NiPt and CoPt phases; the role of magnetism", Journal of Physics F: Metal Physics **18**, 2033 (1988) 10.1088/0305-4608/18/9/021.

[149] H. Shima, K. Oikawa, A. Fujita, K. Fukamichi, K. Ishida, S. Nakamura, and T. Nojima, "Magnetocrystalline anisotropy energy in $L1_0$-type CoPt single crystals", Journal of Magnetism and Magnetic Materials **290-291**, Proceedings of the Joint European Magnetic Symposia (JEMS' 04), 566–569 (2005) https://doi.org/10.1016/j.jmmm.2004.11.536.

[150] N. I. Vlasova, G. S. Kandaurova, and N. N. Shchegoleva, "Effect of the polytwinned microstructure parameters on magnetic domain structure and hysteresis properties of the CoPt-type alloys", Journal of Magnetism and Magnetic Materials **222**, 138–158 (2000) https://doi.org/10.1016/S0304-8853(00)00506-0.

[151] E. Poirier, F. E. Pinkerton, R. Kubic, R. K. Mishra, N. Bordeaux, A. Mubarok, L. H. Lewis, J. I. Goldstein, R. Skomski, and K. Barmak, "Intrinsic magnetic properties of L1 FeNi obtained from meteorite NWA 6259", Journal of Applied Physics **117**, 17E318 (2015) 10.1063/1.4916190.

[152] J. Paulevé, A. Chamberod, K. Krebs, and A. Bourret, "Magnetization Curves of Fe–Ni (50–50) Single Crystals Ordered by Neutron Irradiation with an Applied Magnetic Field", Journal of Applied Physics **39**, 989–990 (1968) 10.1063/1.1656361.

[153] T. Sands, J. P. Harbison, M. L. Leadbeater, J. Allen S. J., G. W. Hull, R. Ramesh, and V. G. Keramidas, "Epitaxial ferromagnetic τ-MnAl films on GaAs", Applied Physics Letters **57**, 2609–2611 (1990) 10.1063/1.103826.

[154] T. Klemmer, D. Hoydick, H. Okumura, B. Zhang, and W. A. Soffa, "Magnetic hardening and coercivity mechanisms in $L1_0$ ordered FePd ferromagnets", Scripta Metallurgica et Materialia **33**, Proceedings of an Acta Metallurgica Meeting on Novel Magnetic Structures and Properties, 1793–1805 (1995) https://doi.org/10.1016/0956-716X(95)00413-P.

[155] J. Lyubina, B. Rellinghaus, O. Gutfleisch, and M. Albrecht, "Chapter 5 - Structure and magnetic properties of $L1_0$-ordered Fe-Pt alloys and nanoparticles", in *Handbook of magnetic materials*, Vol. 19, edited by K. H. J. Buschow, Handbook of Magnetic Materials (Elsevier, 2011), pp. 291–395.

[156] T. Burkert, O. Eriksson, S. I. Simak, A. V. Ruban, B. Sanyal, L. Nordström, and J. M. Wills, "Magnetic anisotropy of $L1_0$ FePt and $Fe_{1-x}Mn_xPt$", Phys. Rev. B **71**, 134411 (2005) 10.1103/PhysRevB.71.134411.

[157] O. Yamada, H. Tokuhara, F. Ono, M. Sagawa, and Y. Matsuura, "Magnetocrystalline anisotropy in $Nd_2Fe_{14}B$ intermetallic compound", Journal of Magnetism and Magnetic Materials **54-57**, 585–586 (1986) https://doi.org/10.1016/0304-8853(86)90718-3.

[158] M. Katter, J. Weber, W. Assmus, P. Schrey, and W. Rodewald, "A new model for the coercivity mechanism of $Sm_2(Co,Fe,Cu,Zr)_{17}$ magnets", IEEE Transactions on Magnetics **32**, 4815–4817 (1996) 10.1109/20.539161.

[159] J. M. D. Coey, "Hard Magnetic Materials: A Perspective", IEEE Transactions on Magnetics **47**, 4671–4681 (2011) 10.1109/TMAG.2011.2166975.

[160] M. T. Kief and R. H. Victora, "Materials for heat-assisted magnetic recording", MRS Bulletin **43**, 87–92 (2018) 10.1557/mrs.2018.2.

[161] T. Shima, K. Takanashi, Y. K. Takahashi, and K. Hono, "Coercivity exceeding 100kOe in epitaxially grown FePt sputtered films", Applied Physics Letters **85**, 2571–2573 (2004) 10.1063/1.1794863.

[162] R. A. Ristau, K. Barmak, L. H. Lewis, K. R. Coffey, and J. K. Howard, "On the relationship of high coercivity and L1 ordered phase in CoPt and FePt thin films", Journal of Applied Physics **86**, 4527–4533 (1999) 10.1063/1.371397.

[163] S. Sun, C. Murray, D. Weller, L. Folks, and A. Moser, "Monodisperse FePt Nanoparticles and Ferromagnetic FePt Nanocrystal Superlattices", Science **287**, 1989–92 (2000) 10.1126/science.287.5460.1989.

[164] D. Weller and M. F. Doerner, "Extremely High-Density Longitudinal Magnetic Recording Media", Annual Review of Materials Science **30**, 611–644 (2000) 10.1146/annurev.matsci.30.1.611.

[165] Y. Peng, T. J. Klemmer, G. Ju, E. Gage, M. A. Seigler, W. A. Challener, D. C. Karns, X. Zhu, N. Gokemeijer, C. Peng, K. Pelhos, B. Lu, T. Rausch, X. W. Wu, L. Li, Y. T. Hsia, D. Buechel, R. D. Hempstead, and R. Rottmayer, "Heat Assisted Magnetic Recording on High Anisotropy Nanocomposite Media", in 2008 8th ieee conference on nanotechnology (2008), pp. 603–604, 10.1109/NANO.2008.180.

[166] M. L. Yan, H. Zeng, N. Powers, and D. J. Sellmyer, "$L1_0$, (001)-oriented FePt:B_2O_3 composite films for perpendicular recording", Journal of Applied Physics **91**, 8471–8473 (2002) 10.1063/1.1451902.

[167] T. Shima, K. Takanashi, Y. K. Takahashi, and K. Hono, "Preparation and magnetic properties of highly coercive FePt films", Applied Physics Letters **81**, 1050–1052 (2002) 10.1063/1.1498504.

[168] J. Wang, H. Sepehri-Amin, Y. K. Takahashi, T. Ohkubo, and K. Hono, "Magnetic in-plane components of FePt nanogranular film on polycrystalline MgO underlayer for heat-assisted magnetic recording media", Acta Materialia **177**, 1–8 (2019) https://doi.org/10.1016/j.actamat.2019.07.017.

[169] B. C. Lim, J. S. Chen, and G. M. Chow, "Interfacial Effects of MgO Buffer Layer on Perpendicular Anisotropy of$L1_0$FePt Films", IEEE Transactions on Magnetics **42**, 3017–3019 (2006) 10.1109/TMAG.2006.878402.

[170] E. Yang and D. E. Laughlin, "$L1_0$ FePt-oxide columnar perpendicular media with high coercivity and small grain size", Journal of Applied Physics **104**, 023904 (2008) 10.1063/1.2956691.

[171] C. Xu, B. S. D. C. S. Varaprasad, D. E. Laughlin, and J.-G. Zhu, "Bias sputtering of granular $L1_0$-FePt films with hexagonal boron nitride grain boundaries", Scientific Reports **13** (2023) 10.1038/s41598-023-38106-9.

[172] S. Okamoto, N. Kikuchi, O. Kitakami, T. Miyazaki, Y. Shimada, and K. Fukamichi, "Chemical-order-dependent magnetic anisotropy and exchange stiffness constant of FePt (001) epitaxial films", Phys. Rev. B **66**, 024413 (2002) 10.1103/PhysRevB.66.024413.

[173] C. L. Platt, K. W. Wierman, E. B. Svedberg, R. van de Veerdonk, J. K. Howard, A. G. Roy, and D. E. Laughlin, "L–1_0 ordering and microstructure of FePt thin films with Cu, Ag, and Au additive", Journal of Applied Physics **92**, 6104–6109 (2002) 10.1063/1.1516870.

[174] C. Brombacher, H. Schletter, M. Daniel, P. Matthes, N. Jöhrmann, M. Maret, D. Makarov, M. Hietschold, and M. Albrecht, "FePtCu alloy thin films: Morphology, $L1_0$ chemical ordering, and perpendicular magnetic anisotropy", Journal of Applied Physics **112**, 073912 (2012) 10.1063/1.4757038.

[175] I. A. Vladymyrskyi, A. E. Gafarov, A. P. Burmak, S. I. Sidorenko, G. L. Katona, N. Y. Safonova, F. Ganss, G. Beddies, M. Albrecht, Y. N. Makogon, and D. L. Beke, "Low-temperature formation of the FePt phase in the presence of an intermediate Au layer in Pt /Au /Fe thin films", Journal of Physics D: Applied Physics **49**, 035003 (2015) 10.1088/0022-3727/49/3/035003.

[176] D.-H. Wei, "Perpendicular Magnetization Behavior of Low- Temperature Ordered FePt Films with Insertion of Ag Nanolayers", Materials **9** (2016) 10.3390/ma9030209.

[177] D.-H. Wei, S.-C. Chen, C.-J. Yang, R.-T. Huang, C.-L. Dong, and Y.-D. Yao, "Formation of FePt–MgO Nanocomposite Films at Reduced Temperature", Journal of Composites Science **6** (2022) 10.3390/jcs6060158.

[178] Y. Endo, N. Kikuchi, O. Kitakami, and Y. Shimada, "Lowering of ordering temperature for fct Fe–Pt in Fe/Pt multilayers", Journal of Applied Physics **89**, 7065–7067 (2001) 10.1063/1.1357150.

[179] T. Shima, T. Moriguchi, S. Mitani, and K. Takanashi, "Low-temperature fabrication of $L1_0$ ordered FePt alloy by alternate monatomic layer deposition", Applied Physics Letters **80**, 288–290 (2002) 10.1063/1.1432446.

[180] Y.-C. Wu, L.-W. Wang, and C.-H. Lai, "Low-temperature ordering of (001) granular FePt films by inserting ultrathin SiO_2 layers", Applied Physics Letters **91**, 072502 (2007) 10.1063/1.2770652.

[181] Y. F. Ding, J. S. Chen, E. Liu, C. J. Sun, and G. M. Chow, "Effect of lattice mismatch on chemical ordering of epitaxial $L1$ FePt films", Journal of Applied Physics **97**, 10H303 (2005) 10.1063/1.1851419.

[182] H. Xu, H. Heinrich, and J. Wiezorek, "Microstructural changes during annealing of FePd-based thin films", Intermetallics **11**, 963–969 (2003) 10.1016/S0966-9795(03)00100-6.

[183] M. Watanabe, T. Masumoto, D. H. Ping, and K. Hono, "Microstructure and magnetic properties of FePt–Al–O granular thin films", Applied Physics Letters **76**, 3971–3973 (2000) 10.1063/1.126838.

[184] H. Zeng, M. L. Yan, N. Powers, and D. J. Sellmyer, "Orientation-controlled nonepitaxial $L1_0$ CoPt and FePt films", Applied Physics Letters **80**, 2350–2352 (2002) 10.1063/1.1464663.

[185] C. Brombacher, C. Schubert, M. Daniel, A. Liebig, G. Beddies, T. Schumann, W. Skorupa, J. Donges, S. Häberlein, and M. Albrecht, "Chemical ordering of FePt films using millisecond flash-lamp annealing", Journal of Applied Physics **111**, 023902 (2012) 10.1063/1.3677991.

[186] K. Barmak, J. Kim, S. Shell, E. B. Svedberg, and J. K. Howard, "Calorimetric studies of the A1 to L1 transformation in FePt and CoPt thin films", Applied Physics Letters **80**, 4268–4270 (2002) 10.1063/1.1483924.

[187] Y. Mimura, N. Imamura, and T. Kobayashi, "Magnetic properties and curie point writing in amorphous metallic films", IEEE Transactions on Magnetics **12**, 779–781 (1976) 10.1109/TMAG.1976.1059199.

[188] H. Baker, ed., *ASM Handbook Volume 3 Alloy Phase diagrams* (ASM international, 1992).

[189] M. P. Dariel, J. T. Holthuis, and M. R. Pickus, "The terbium-iron phase diagram", Journal of the Less Common Metals **45**, 91–101 (1976) https://doi.org/10.1016/0022-5088(76)90200-9.

[190] E. P. Wohlfarth, ed., *Ferromagnetic Materials*, Vol. 1 (North-Holland Publishing Company, 1980).

[191] J. H. Zhu, C. T. Liu, L. M. Pike, and P. K. Liaw, "A thermodynamic interpretation of the size-ratio limits for laves phase formation", Metallurgical and Materials Transactions A **30**, 1449–1452 (1999) 10.1007/s11661-999-0292-5.

[192] R. Grössinger, R. S. Turtelli, and N. Mehmood, "Materials with high magnetostriction", IOP Conference Series: Materials Science and Engineering **60**, 012002 (2014) 10.1088/1757-899X/60/1/012002.

[193] J. M. D. Coey, *Magnetism and magnetic materials* (Cambridge University Press, 2009).

[194] T. Miyazaki, T. Saito, and Y. Fujino, "Magnetostrictive properties of sputtered binary Tb-Fe and pseudo-binary (Tb-Dy)-Fe alloy films", Journal of Magnetism and Magnetic Materials **171**, 320–328 (1997) https://doi.org/10.1016/S0304-8853(97)00076-0.

[195] M. Pasquale, A. Infortuna, L. Martino, C. Sasso, C. Beatrice, and S. H. Lim, "Magnetic properties of TbFe thin films under applied stress", Journal of Magnetism and Magnetic Materials **215-216**, 769–771 (2000) https://doi.org/10.1016/S0304-8853(00)00283-3.

[196] A. E. Clark and H. S. Belson, "Giant Room-Temperature Magnetostrictions in $TbFe_2$ and $DyFe_2$", Phys. Rev. B **5**, 3642–3644 (1972) 10.1103/PhysRevB.5.3642.

[197] L. Daniel and M. Domenjoud, "Anhysteretic Magneto-Elastic Behaviour of Terfenol-D: Experiments, Multiscale Modelling and Analytical Formulas", Materials **14** (2021) 10.3390/ma14185165.

[198] F. Jerems, C. M. Mahon, A. G. Jenner, and R. D. Greenough, "Amorphous magnetic materials for transducers", Ferroelectrics **228**, 333–341 (1999) 10.1080/00150199908226146.

[199] H. König, "Die kleinsten ferromagnetischen Elementarbereiche des Eisens", Naturwissenschaften **33**, 71–75 (1946) 10.1007/BF00592115.

[200] A. Brenner, D. E. Couch, and E. K. Williams, "Electrodeposition of alloys of phosphorus with nickel or cobalt", Journal of research of the National Bureau of Standards **44**, 109 (1950).

[201] P. Hansen, "Chapter 4 - Magnetic amorphous alloys", in *Handbook of magnetic materials*, Vol. 6, edited by K. H. J. Buschow, Handbook of Magnetic Materials (Elsevier, 1991), pp. 289–452, https://doi.org/10.1016/S1567-2719(05)80058-7.

[202] S. Kobe and A. R. Ferchmin, "Amorphous magnetism and magnetic materials: bibliography 1950-1976", Journal of Materials Science **12**, 1713–1749 (1977) 10.1007/BF00566234.

[203] G. S. Cargill III, "Ferromagnetism in amorphous solids", AIP Conference Proceedings **24**, 138–144 (1975) 10.1063/1.30020.

[204] R. Harris, M. Plischke, and M. J. Zuckermann, "New Model for Amorphous Magnetism", Phys. Rev. Lett. **31**, 160–162 (1973) 10.1103/PhysRevLett.31.160.

[205] J. M. D. Coey and P. W. Readman, "New Spin Structure in an Amorphous Ferric Gel", Nature **246**, The spelling speromagnetic should appear throughout this article [see Nature (London) 246, 445 (1973)], 476–478 (1973) 10.1038/246476a0.

[206] R. J. Gambino, P. Chaudhari, and J. J. Cuomo, "Amorphous Magnetic Materials", AIP Conference Proceedings **18**, 578–592 (1974) 10.1063/1.3141775.

[207] G. S. Cargill, "Structure of Metallic Alloy Glasses", in *Solid state physics*, Vol. 30, edited by H. Ehrenreich, F. Seitz, and D. Turnbull, Solid State Physics (Academic Press, 1975), pp. 227–320, https://doi.org/10.1016/S0081-1947(08)60337-9.

[208] J. M. D. Coey, J. Chappert, J. P. Rebouillat, and T. S. Wang, "Magnetic Structure of an Amorphous Rare-Earth Transition-Metal Alloy", Phys. Rev. Lett. **36**, 1061–1064 (1976) 10.1103/PhysRevLett.36.1061.

[209] P. Chaudhari and D. C. Cronemeyer, "The temperature dependence of the uniaxial anisotropy of $Gd_{1-x-y}Co_xMo_y$ amorphous alloy films on glass substrates", AIP Conference Proceedings **29**, 113–114 (1976) 10.1063/1.30542.

[210] R. W. Cochrane, R. Harris, and M. J. Zuckermann, "The role of structure in the magnetic properties of amorphous alloys", Physics Reports **48**, 1–63 (1978) https://doi.org/10.1016/0370-1573(78)90012-1.

[211] P. Chaudhari, J. J. Cuomo, and R. J. Gambino, "Amorphous metallic films for magneto-optic applications", Applied Physics Letters **22**, 337–339 (1973) 10.1063/1.1654662.

[212] J. M. D. Coey, "Amorphous magnetic order", Journal of Applied Physics **49**, 1646–1652 (1978) 10.1063/1.324880.

[213] S. Blundell, *Magnetism in condensed matter* (Oxford University Press, 2001).

[214] L. Peters, S. Ghosh, B. Sanyal, C. van Dijk, J. Bowlan, W. de Heer, A. Delin, I. Di Marco, O. Eriksson, M. I. Katsnelson, B. Johansson, and A. Kirilyuk, "Magnetism and exchange interaction of small rare-earth clusters; Tb as a representative", Scientific Reports **6**, 19676 (2016) 10.1038/srep19676.

[215] E. Trémolet de Lacheisserie, D. Gignoux, and M. Schlenker, *Magnetism: Materials and Applications*, Grenoble sciences (Springer, 2005).

[216] D. Li, S. Suzuki, T. Kawasaki, and K.-i. Machida, "Grain Interface Modification and Magnetic Properties of Nd–Fe–B Sintered Magnets", Japanese Journal of Applied Physics **47**, 7876 (2008) 10.1143/JJAP.47.7876.

[217] C. Fang, Z. Yan, X. Zhang, J. Xiao, F. Wang, and X. Xu, "Effect of element doping on the structural stability, magnetic properties and electronic structure of $SmCo_5$-based rare earth permanent magnets", Journal of Magnetism and Magnetic Materials **609**, 172492 (2024) https://doi.org/10.1016/j.jmmm.2024.172492.

[218] T. Ruckert, J. Tappert, R. A. Brand, and W. Keune, "Mössbauer-effect study of amorphous $Tb_{1-x}Fe_x$ films", Journal of Magnetism and Magnetic Materials **165**, Symposium E: Magnetic Ultrathin Films, Multilayers and Surfaces, 411–413 (1997) https://doi.org/10.1016/S0304-8853(96)00572-0.

[219] J. P. Eymery, A. Fnidiki, R. Krishnan, M. Tessier, and J. P. Vitton, "Conversion-electron Mössbauer spectroscopy studies in amorphous Tb-Fe films", Phys. Rev. B **38**, 11931–11933 (1988) 10.1103/PhysRevB.38.11931.

[220] J. Azoulay and L. Ley, "The magnetic moment of iron in Gd-Fe intermetallic compounds", Solid State Communications **31**, 131–134 (1979) https://doi.org/10.1016/0038-1098(79)90420-4.

[221] W. E. Henry, "Saturation Magnetization and Ferromagnetic Interaction in Terbium Metal", Journal of Applied Physics **30**, S99–S100 (1959) 10.1063/1.2185983.

[222] W. C. Thoburn, S. Legvold, and F. H. Spedding, "Magnetic Properties of Terbium Metal", Phys. Rev. **112**, 56–58 (1958) 10.1103/PhysRev.112.56.

[223] J. Vogel, M. Sacchi, R. J. H. Kappert, J. C. Fuggle, J. B. Goedkoop, N. B. Brookes, G. van der Laan, and E. E. Marinero, "Magnetic properties of Fe and Tb in Tb_xFe_{1-x} amorphous films studied with soft X-ray circular and linear dichroism", Journal of Magnetism and Magnetic Materials **150**, 293–303 (1995) https://doi.org/10.1016/0304-8853(95)00284-7.

[224] M. Trhlík, P. De Moor, J. John, T. Limbach, P. Schuurmans, B. Sedlák, N. Severijns, W. Vanderpoorten, L. Vanneste, and J. Wouters, "Tb magnetic moment behaviour in amorphous Tb-Fe alloy: A nuclear orientation study", Solid State Communications **87**, 59–61 (1993) https://doi.org/10.1016/0038-1098(93)90536-V.

[225] B. Hebler, A. Hassdenteufel, P. Reinhardt, H. Karl, and M. Albrecht, "Ferrimagnetic Tb–Fe Alloy Thin Films: Composition and Thickness Dependence of Magnetic Properties and All-Optical Switching", Frontiers in Materials **3** (2016) 10.3389/fmats.2016.00008.

[226] T. C. Hufnagel, S. Brennan, P. Zschack, and B. M. Clemens, "Structural anisotropy in amorphous Fe-Tb thin films", Phys. Rev. B **53**, 12024–12030 (1996) 10.1103/PhysRevB.53.12024.

[227] J. Zweck and R. Trautsch, "Magnetically Induced Changes in the Physical Microstructure of Anisotropic Amorphous FeTb Alloys", Crystal Research and Technology **35**, 689–705 (2000) https://doi.org/10.1002/1521-4079(200007)35:6/7<689::AID-CRAT689>3.0.CO;2-O.

[228] V. G. Harris and T. Pokhil, "Selective-Resputtering-Induced Perpendicular Magnetic Anisotropy in Amorphous TbFe Films", Phys. Rev. Lett. **87**, 067207 (2001) 10.1103/PhysRevLett.87.067207.

[229] V. G. Harris and T. Pokhil, "Evidence for selective resputtering as the growth mechanism of pair-order anisotropy in amorphous TbFe films", Bulletin of Materials Science **22**, 503–508 (1999) 10.1007/BF02749962.

[230] X. Yan, M. Hirscher, T. Egami, and E. E. Marinero, "Direct observation of anelastic bond-orientational anisotropy in amorphous $Tb_{26}Fe_{62}Co_{12}$ thin films by x-ray diffraction", Phys. Rev. B **43**, 9300–9303 (1991) 10.1103/PhysRevB.43.9300.

[231] V. G. Harris, K. D. Aylesworth, B. N. Das, W. T. Elam, and N. C. Koon, "Structural origins of magnetic anisotropy in sputtered amorphous Tb-Fe films", Phys. Rev. Lett. **69**, 1939–1942 (1992) 10.1103/PhysRevLett.69.1939.

[232] R. Skomski and D. J. Sellmyer, "Anisotropy of rare-earth magnets", Journal of Rare Earths **27**, 675–679 (2009) https://doi.org/10.1016/S1002-0721(08)60314-2.

[233] Y. Suzuki, S. Takayama, F. Kirino, and N. Ohta, "Single ion model for perpendicular magnetic anisotropy in RE-TM amorphous films", IEEE Transactions on Magnetics **23**, 2275–2277 (1987) 10.1109/TMAG.1987.1065290.

[234] P. Hansen and H. Heitmann, "Media for erasable magnetooptic recording", IEEE Transactions on Magnetics **25**, 4390–4404 (1989) 10.1109/20.45318.

[235] S.-N. Cheng, M. H. Kryder, and M. C. A. Mathur, "Stress related anisotropy studies in DC-magnetron sputtered TbCo and TbFe films", IEEE Transactions on Magnetics **25**, 4018–4020 (1989) 10.1109/20.42509.

[236] H. Takagi, S. Tsunashima, S. Uchiyama, and T. Fujii, "Stress induced anisotropy in amorphous Gd-Fe and Tb-Fe sputtered films", Journal of Applied Physics **50**, 1642–1644 (1979) 10.1063/1.327223.

[237] F. Hellman and E. M. Gyorgy, "Growth-induced magnetic anisotropy in amorphous Tb-Fe", Phys. Rev. Lett. **68**, 1391–1394 (1992) 10.1103/PhysRevLett.68.1391.

[238] W. Meiklejohn, F. Luborsky, and P. Frischmann, "On the origin of K_U in amorphous RE-TM magnetooptic recording materials", IEEE Transactions on Magnetics **23**, 2272–2274 (1987) 10.1109/TMAG.1987.1065652.

[239] J.-C. Shih, T.-S. Chin, Z.-G. Sun, H.-W. Zhang, and B.-G. Shen, "Domain structure of TbFe magnetostrictive films by MFM", IEEE Transactions on Magnetics **37**, 2681–2683 (2001) 10.1109/20.951273.

[240] R. B. van Dover, M. Hong, E. M. Gyorgy, J. Dillon J. F., and S. D. Albiston, "Intrinsic anisotropy of Tb-Fe films prepared by magnetron Co sputtering", Journal of Applied Physics **57**, 3897–3899 (1985) 10.1063/1.334908.

[241] Y. Takeno, M. Suwabe, T. Sakurai, and K. Goto, "Influence of Substrate Temperature on Magnetic Properties and Domains of Amorphous $Tb_{31}Fe_{69}$ Films", Japanese Journal of Applied Physics **25**, L657 (1986) 10.1143/JJAP.25.L657.

[242] H. Kobayashi, T. Ono, A. Tsushima, and T. Suzuki, "Large uniaxial magnetic anisotropy in amorphous Tb-Fe evaporated thin films", Applied Physics Letters **43**, 389–390 (1983) 10.1063/1.94354.

[243] C. Prados, E. Marinero, and A. Hernando, "Magnetic interactions and anisotropy in amorphous TbFe films", Journal of Magnetism and Magnetic Materials **165**, Symposium E: Magnetic Ultrathin Films, Multilayers and Surfaces, 414–416 (1997) https://doi.org/10.1016/S0304-8853(96)00573-2.

[244] A. Hernando, C. Prados, and C. Prieto, "Anisotropy, magnetostriction and local chemical order in amorphous Tb_xFe_{1-x} ($0.1 < x < 0.55$) thin films", Journal of Magnetism and Magnetic Materials **157-158**, European Magnetic Materials and Applications Conference, 501–503 (1996) https://doi.org/10.1016/0304-8853(95)01124-2.

[245] C. Schubert, *Magnetic Order and Coupling Phenomena: A Study of Magnetic Structure and Magnetization Reversal Processes in Rare-Earth-Transition-Metal Based Alloys and Heterostructures*, Springer Theses (Springer Cham, 2014).

[246] M. Mansuripur and M. Ruane, "Mean-field analysis of amorphous rare earth-transition metal alloys for thermomagnetic recording", IEEE Transactions on Magnetics **22**, 33–43 (1986) 10.1109/TMAG.1986.1064266.

[247] N. Smith and W. C. Cain, "Micromagnetic model of an exchange coupled NiFe-TbCo bilayer", Journal of Applied Physics **69**, 2471–2479 (1991) 10.1063/1.348684.

[248] C.-C. Lin, C.-H. Lai, R.-F. Jiang, and H.-P. D. Shieh, "High interfacial exchange energy in TbFeCo exchange-bias films", Journal of Applied Physics **93**, 6832–6834 (2003) 10.1063/1.1556932.

[249] L. You, T. Kato, S. Tsunashima, and S. Iwata, "Thermomagnetic writing on deep submicron-patterned TbFe films by nanosecond current pulse", Journal of Magnetism and Magnetic Materials **321**, Current Perspectives: Spintronics, 1015–1018 (2009) https://doi.org/10.1016/j.jmmm.2008.10.026.

[250] J. E. Greene, "Tracing the 5000-year recorded history of inorganic thin films from ≈3000 BC to the early 1900s AD", Applied Physics Reviews **1**, 041302 (2014) 10.1063/1.4902760.

[251] S. Swann, "Magnetron sputtering", Physics in Technology **19**, 67 (1988) 10.1088/0305-4624/19/2/304.

[252] W. R. Grove, "VII. On the electro-chemical polarity of gases", Philosophical Transactions of the Royal Society of London **142**, 87–101 (1852) 10.1098/rstl.1852.0008.

[253] A. G. Spencer, C. A. Bishop, and R. P. Howson, "The design and performance of planar magnetron sputtering cathodes", Vacuum **37**, 363–366 (1987) https://doi.org/10.1016/0042-207X(87)90026-1.

[254] H. Ghazal and N. Sohail, "Sputtering Deposition", in *Thin films*, edited by D. Yang (IntechOpen, Rijeka, 2022) Chap. 2, 10.5772/intechopen.107353.

[255] P. J. Kelly and R. D. Arnell, "Magnetron Sputtering: A Review of Recent Developments and Applications", Vacuum **56**, 159–172 (2000).

[256] B. Window and N. Savvides, "Unbalanced dc magnetrons as sources of high ion fluxes", J. Vac. Sci. Technol. A **4**, 453–456 (1986) 10.1116/1.573904.

[257] H. R. Koenig and L. I. Maissel, "Application of RF Discharges to Sputtering", IBM Journal of Research and Development **14**, 168–171 (1970) 10.1147/rd.142.0168.

[258] V. M. Mecea, "From Quartz Crystal Microbalance to Fundamental Principles of Mass Measurements", Analytical Letters - ANAL LETT **38** (2005) 10.1081/AL-200056171.

[259] A. Hotta, T. Ono, M. Hatayama, K. Tsumura, N. Kikuchi, S. Okamoto, O. Kitakami, and T. Shimatsu, "Magnetic anisotropy and order structure of L1-FePt(001) single-crystal films grown epitaxially on (001) planes of MgO, $SrTiO_3$, and $MgAl_2O_4$ substrates", Journal of Applied Physics **115**, 17B712 (2014) 10.1063/1.4862840.

[260] J. Deng, K. Dong, P. Yang, Y. Peng, G. Ju, J. Hu, G. M. Chow, and J. Chen, "Large lattice mismatch effects on the epitaxial growth and magnetic properties of FePt films", Journal of Magnetism and Magnetic Materials **446**, 125–134 (2018) https://doi.org/10.1016/j.jmmm.2017.09.014.

[261] K. F. Dong, H. H. Li, and J. S. Chen, "Lattice mismatch-induced evolution of microstructural properties in FePt films", Journal of Applied Physics **113**, 233904 (2013) 10.1063/1.4811348.

[262] A. Itabashi, M. Ohtake, S. Ouchi, F. Kirino, and M. Futamoto, "Structure Characterization of FePd, FePt, and CoPt Alloy Thin Films Epitaxially Grown on $SrTiO_3$(001) Single-Crystal Substrates", Journal of the Magnetics Society of Japan **37**, 202–205 (2013) 10.3379/msjmag.1303R017.

[263] I. Suzuki, S. Kubo, H. Sepehri-Amin, and Y. K. Takahashi, "Dependence of the Growth Mode in Epitaxial FePt Films on Surface Free Energy", ACS Appl. Mater. Interfaces **13**, 16620–16627 (2021) 10.1021/acsami.0c22510.

[264] A. Sakuma, "First Principle Calculation of the Magnetocrystalline Anisotropy Energy of FePt and CoPt Ordered Alloys", Journal of the Physical Society of Japan **63**, 3053–3058 (1994) 10.1143/JPSJ.63.3053.

[265] J. S. Chen, B. C. Lim, and J. P. Wang, "Controlling the crystallographic orientation and the axis of magnetic anisotropy in $L1_0$ FePt films", Applied Physics Letters **81**, 1848–1850 (2002) 10.1063/1.1504489.

[266] Y. K. Takahashi, K. Hono, T. Shima, and K. Takanashi, "Microstructure and magnetic properties of FePt thin films epitaxially grown on MgO (001) substrates", Journal of Magnetism and Magnetic Materials **267**, 248–255 (2003) https://doi.org/10.1016/S0304-8853(03)00377-9.

[267] V. Mazauric and S. Nasu, "Wetting and Prewetting of Non-conservative Antiphase Boundary in the $L1_0$ Structure", Materials Transactions, JIM **35**, 491–500 (1994) 10.2320/matertrans1989.35.491.

[268] A. Guinier, "X-Ray Diffraction in Crystals, Imperfect Crystals, and Amorphous Bodies", in (Dover Publications, 1994) Chap. 5.

[269] U. Holzwarth and N. Gibson, "The Scherrer equation versus the 'Debye-Scherrer equation'", Nature Nanotechnology **6**, 534–534 (2011) 10.1038/nnano.2011.145.

[270] M. Birkholz, *Thin Film Analysis by X-ray Scattering* (Wiley-VCH, 2005).

[271] R. L. Fagaly, "Superconducting quantum interference device instruments and applications", Review of Scientific Instruments **77**, 101101 (2006) 10.1063/1.2354545.

[272] R. Doll and M. Naebauer, "Experimental Proof of Magnetic Flux Quantization in a Superconducting Ring", Phys. Rev. Lett. **7**, 51–52 (1961).

[273] D. Drung, C. Assmann, J. Beyer, A. Kirste, M. Peters, F. Ruede, and T. Schurig, "Highly sensitive and easy-to-use SQUID sensors", IEEE Trans. Appl. Supercond. **17**, 699–704 (2007).

[274] M. M. Budnyk, Y. D. Minov, V. Lyakhno, V. A. Desnenko, A. S. Linnik, and O. B. Shopen, "Development of improved superconductive axial gradiometers for SQUID biomagnetic application", Fizika Nizkikh Temperatur **44**, 308–313 (2018) 10.1063/1.5024543.

[275] A.-O. Mandru, O. Yıldırım, M. A. Marioni, H. Rohrmann, M. Heigl, O.-T. Ciubotariu, M. Penedo, X. Zhao, M. Albrecht, and H. J. Hug, "Pervasive artifacts revealed from magnetometry measurements of rare earth-transition metal thin films", Journal of Vacuum Science & Technology A **38**, 023409 (2020) 10.1116/1.5135504.

[276] G. Binnig, C. F. Quate, and C. Gerber, "Atomic Force Microscope", Phys. Rev. Lett. **56**, 930–933 (1986) 10.1103/PhysRevLett.56.930.

[277] B. Voigtländer, *Atomic Force Microscopy* (Springer, 2019).

[278] M. Siegbahn, "Relations between the K and L Series of the High-Frequency Spectra", Nature **96**, 676–676 (1916) 10.1038/096676b0.

[279] R. Jenkins, R. Manne, R. Robin, and C. Senemaud, "Nomenclature, symbols, units and their usage in spectrochemical analysis - VIII. Nomenclature system for X-ray spectroscopy (Recommendations 1991)", Pure and Applied Chemistry **63**, 735–746 (1991) doi:10.1351/pac199163050735.

[280] A. Linnemann and S. Kühl, *Grundlagen der Licht- und Elektronenmikroskopie* (UTB, 2017).

[281] C. Cremer, "Lichtmikroskopie unterhalb des Abbe-Limits", Physik in unserer Zeit **42**, 21–29 (2011) https://doi.org/10.1002/piuz.201101251.

[282] M. Sagawa, S. Fujimura, H. Yamamoto, Y. Matsuura, and K. Hiraga, "Permanent magnet materials based on the rare earth-iron-boron tetragonal compounds", IEEE Transactions on Magnetics **20**, 1584–1589 (1984) 10.1109/TMAG.1984.1063214.

[283] M. Sagawa, S. Hirosawa, K. Tokuhara, H. Yamamoto, S. Fujimura, Y. Tsubokawa, and R. Shimizu, "Dependence of coercivity on the anisotropy field in the $Nd_2Fe_{14}B$-type sintered magnets", Journal of Applied Physics **61**, 3559–3561 (1987) 10.1063/1.338725.

[284] M. PAN, P. ZHANG, X. LI, H. GE, Q. WU, Z. JIAO, and T. LIU, "Effect of Terbium addition on the coercivity of the sintered NdFeB magnets", Journal of Rare Earths **28**, 399–402 (2010) https://doi.org/10.1016/S1002-0721(10)60300-6.

[285] Z. Tie-song, J. Han-min, G. Guang-hua, H. Xiu-feng, and C. Hong, "Magnetic properties of R ions in RCo_5 compounds (R=Pr, Nd, Sm, Gd, Tb, Dy, Ho, and Er)", Phys. Rev. B **43**, 8593–8598 (1991) 10.1103/PhysRevB.43.8593.

[286] WTO, *DS431: China — Measures Related to the Exportation of Rare Earths, Tungsten and Molybdenum*, Accessed Nov. 25, 2024, (2015) https://www.wto.org/english/tratop_e/dispu_e/cases_e/ds431_e.htm.

[287] Z. Samardžija, P. McGuiness, M. Soderžnik, S. Kobe, and M. Sagawa, "Microstructural and compositional characterization of terbium-doped Nd–Fe–B sintered magnets", Materials Characterization **67**, 27–33 (2012) https://doi.org/10.1016/j.matchar.2012.02.017.

[288] T.-H. Kim, T. T. Sasaki, T. Ohkubo, Y. Takada, A. Kato, Y. Kaneko, and K. Hono, "Microstructure and coercivity of grain boundary diffusion processed Dy-free and Dy-containing NdFeB sintered magnets", Acta Materialia **172**, 139–149 (2019) https://doi.org/10.1016/j.actamat.2019.04.032.

[289] Y. Lu, S. Zhong, M. Yang, C. Wang, L. Yang, L. Li, and B. Yang, "Nd-Fe-B Magnets: The Gradient Change of Microstructures and the Diffusion Principle after Grain Boundary Diffusion Process", Materials **12** (2019) 10.3390/ma12233881.

[290] H. Sepehri-Amin, T. Ohkubo, and K. Hono, "Grain boundary structure and chemistry of Dy-diffusion processed Nd–Fe–B sintered magnets", Journal of Applied Physics **107**, 09A745 (2010) 10.1063/1.3351247.

[291] H. X. Zeng, Z. W. Liu, J. S. Zhang, X. F. Liao, and H. Y. Yu, "Towards the diffusion source cost reduction for NdFeB grain boundary diffusion process", Journal of Materials Science & Technology **36**, 50–54 (2020) https://doi.org/10.1016/j.jmst.2019.08.009.

[292] Y. Gu, S. Hua, M. Pan, and X. Huang, "Enhancing the Magnetic Properties and Corrosion Resistance of Sintered NdFeB Magnets by Diffusion Process", International Journal of Electrochemical Science **15**, 3268–3273 (2020) https://doi.org/10.20964/2020.04.06.

[293] W. Chen, Y. L. Huang, J. M. Luo, Y. H. Hou, X. J. Ge, Y. W. Guan, Z. W. Liu, Z. C. Zhong, and G. P. Wang, "Microstructure and improved properties of sintered Nd-Fe-B magnets by grain boundary diffusion of non-rare earth", Journal of Magnetism and Magnetic Materials **476**, 134–141 (2019) https://doi.org/10.1016/j.jmmm.2018.12.048.

[294] H. X. Zeng, Q. X. Wang, J. S. Zhang, X. F. Liao, X. C. Zhong, H. Y. Yu, and Z. W. Liu, "Grain boundary diffusion treatment of sintered NdFeB magnets by low cost La-Al-Cu alloys with various Al/Cu ratios", Journal of Magnetism and Magnetic Materials **490**, 165498 (2019) https://doi.org/10.1016/j.jmmm.2019.165498.

[295] H. Zeng, Z. Liu, W. Li, J. Zhang, L. Zhao, X. Zhong, H. Yu, and B. Guo, "Significantly enhancing the coercivity of NdFeB magnets by ternary Pr-Al-Cu alloys diffusion and understanding the elements diffusion behavior", Journal of Magnetism and Magnetic Materials **471**, 97–104 (2019) https://doi.org/10.1016/j.jmmm.2018.09.080.

[296] K. Lu, X. Bao, Y. Zhou, X. Lv, Y. Ding, M. Zhang, C. Wang, and X. Gao, "Effect of Al/Cu on the magnetic properties and microstructure of Nd-Fe-B sintered magnet by diffusing Pr-Tb-(Cu, Al) alloys", Journal of Magnetism and Magnetic Materials **500**, 166384 (2020) https://doi.org/10.1016/j.jmmm.2019.166384.

[297] Y. Xie, Y. Yang, T. Zhang, Y. Fu, Q. Jiang, S. Ma, Z. Zhong, W. Cui, and Q. Wang, "Microstructure evolution and coercivity enhancement in Nd-Fe-B thin films diffusion-processed by R-Al alloys (R=Nd, Pr)", AIP Advances **8**, 056202 (2017) 10.1063/1.5006110.

[298] K. Loewe, D. Benke, C. Kübel, T. Lienig, K. P. Skokov, and O. Gutfleisch, "Grain boundary diffusion of different rare earth elements in Nd-Fe-B sintered magnets by experiment and FEM simulation", Acta Materialia **124**, 421–429 (2017) https://doi.org/10.1016/j.actamat.2016.11.034.

[299] A. Fick, "Ueber Diffusion", Annalen der Physik **170**, 59–86 (1855) https://doi.org/10.1002/andp.18551700105.

[300] J.-W. Liao, U. Atxitia, R. F. L. Evans, R. W. Chantrell, and C.-H. Lai, "Atomistic modeling of magnetization reversal modes in $L1_0$ FePt nanodots with magnetically soft edges", Phys. Rev. B **90**, 174415 (2014) 10.1103/PhysRevB.90.174415.

[301] Y. Zhang, A. Kalitsov, J. Ciston, O. Mryasov, B. Ozdol, J. Zhu, S. Jain, B. Zhang, B. Livshitz, A. Chernyshov, A. Ajan, P. Dorsey, G. Bertero, R. Acharya, A. Greene, and S. Myers, "Microstructure and magnetic properties of ultrathin FePt granular films", AIP Advances **8**, 125018 (2018) 10.1063/1.5022781.

[302] N. Schmidt, S. Laureti, F. Radu, H. Ryll, C. Luo, F. D'Acapito, S. Tripathi, E. Goering, D. Weller, and M. Albrecht, "Structural and magnetic properties of FePt-Tb alloy thin films", Physical Review B **100** (2019) 10.1103/PhysRevB.100.064428.

[303] Y.-K. Chung, S.-A. Kim, J.-H. Koo, H.-C. Oh, E.-O. Chi, J.-H. Hahn, and C. Park, "Crystallization Behavior of Amorphous Si_3N_4 and Particle Size Control of the Crystallized -Si_3N_4", Journal of Nanoscience and Nanotechnology **16**, 5403–5409 (2016) doi:10.1166/jnn.2016.12220.

[304] S. Zhu, M. Sun, B. Mei, L. Yang, C. Yuyi, Z. Shi, J. Bai, X. Wang, Z. Jiang, C. Liu, B. Huang, J. Ge, and W. Xing, "Intrinsic Spin Shielding Effect in Platinum–Rare Earth Alloy Boosts Oxygen Reduction Activity", National Science Review **10** (2023) 10.1093/nsr/nwad162.

[305] T. Xu, J. Liu, X. Zhang, Q. Zhang, H.-A. Zhou, Y. Dong, P. Gargiani, M. Valvidares, Y. Zhou, and W. Jiang, "Systematic Control of the Interlayer Exchange Coupling in Perpendicularly Magnetized Synthetic Antiferromagnets", Phys. Rev. Appl. **18**, 054051 (2022) 10.1103/PhysRevApplied.18.054051.

[306] B. Hebler, P. Reinhardt, G. L. Katona, O. Hellwig, and M. Albrecht, "Double exchange bias in ferrimagnetic heterostructures", Phys. Rev. B **95**, 104410 (2017) 10.1103/PhysRevB.95.104410.

[307] J. Y. Chen, N. Thiyagarajah, H. J. Xu, and J. M. D. Coey, "Perpendicular exchange bias effect in sputter-deposited CoFe/IrMn bilayers", Applied Physics Letters **104**, 152405 (2014) 10.1063/1.4871711.

[308] B. Kocaman, "Tailoring magnetic properties by tuning the interface in a Pt/-Co/Pt/IrMn system with perpendicular and double-exchange biases", Journal of Physics D: Applied Physics **55**, 245003 (2022) 10.1088/1361-6463/ac5b45.

[309] E. Ma and J. Ding, "Compositional fluctuation and local chemical ordering in multi-principal element alloys", Journal of Materials Science & Technology (2024) https://doi.org/10.1016/j.jmst.2024.09.008.

[310] C. Liu and R. Maaß, "Elastic Fluctuations and Structural Heterogeneities in Metallic Glasses", Advanced Functional Materials **28**, 1800388 (2018) https://doi.org/10.1002/adfm.201800388.

[311] F. Zhu, A. Hirata, P. Liu, S. Song, Y. Tian, J. Han, T. Fujita, and M. Chen, "Correlation between Local Structure Order and Spatial Heterogeneity in a Metallic Glass", Phys. Rev. Lett. **119**, 215501 (2017) 10.1103/PhysRevLett.119.215501.

[312] C. Binek, "Training of the exchange-bias effect: a simple analytic approach", Phys. Rev. B **70**, 014421 (2004) 10.1103/PhysRevB.70.014421.

[313] F. Canet, S. Mangin, C. Bellouard, and M. Piecuch, "Positive exchange bias in ferromagnetic-ferrimagnetic bilayers: FeSn/FeGd", Europhysics Letters **52**, 594 (2000) 10.1209/epl/i2000-00479-1.

[314] F. Canet, C. Bellouard, S. Mangin, C. Chatelain, C. Senet, R. Siebrecht, V. Leiner, and M. Piecuch, "Exchange bias like effect induced by domain walls in FeGd/FeSn bilayers", The European Physical Journal B - Condensed Matter and Complex Systems **34**, 381–394 (2003) 10.1140/epjb/e2003-00235-y.

[315] M. J. O'Shea and A.-L. Al-Sharif, "Inverted hysteresis in magnetic systems with interface exchange", Journal of Applied Physics **75**, 6673–6675 (1994) 10.1063/1.356891.

[316] L. Opherden, T. Bilitewski, J. Hornung, T. Herrmannsdörfer, A. Samartzis, A. T. M. N. Islam, V. K. Anand, B. Lake, R. Moessner, and J. Wosnitza, "Inverted hysteresis and negative remanence in a homogeneous antiferromagnet", Phys. Rev. B **98**, 180403 (2018) 10.1103/PhysRevB.98.180403.

[317] S. Gu, W. He, M. Zhang, T. Zhuang, Y. Jin, H. ElBidweihy, Y. Mao, J. H. Dickerson, M. J. Wagner, E. D. Torre, and L. H. Bennett, "Physical Justification for Negative Remanent Magnetization in Homogeneous Nanoparticles", Scientific Reports **4**, 6267 (2014) 10.1038/srep06267.

[318] E. C. Stoner and E. P. Wohlfarth, "A mechanism of magnetic hysteresis in heterogeneous alloys", Philos. Trans. Royal Soc. A **240**, 599–642 (1948) 10.1098/rsta.1948.0007.

[319] F. Vajda and E. Della Torre, "Characteristics of magnetic media models", IEEE Transactions on Magnetics **28**, 2611–2613 (1992) 10.1109/20.179573.

[320] A. Stancu and I. Chiorescu, "Crossover condition in the coherent rotation model and the Preisach-type models", IEEE Transactions on Magnetics **33**, 2573–2579 (1997) 10.1109/20.595917.

[321] S. A. Mathews, A. C. Ehrlich, and N. A. Charipar, "Hysteresis branch crossing and the Stoner-Wohlfarth model", Scientific Reports **10**, 15141 (2020) 10.1038/s41598-020-72233-x.

[322] S. A. Mathews, J. Prestigiacomo, and P. C. Mulford, "Hysteresis branch crossing in permalloy", Journal of Magnetism and Magnetic Materials **588**, 171454 (2023) https://doi.org/10.1016/j.jmmm.2023.171454.

[323] R. Street and J. C. Woolley, "A Study of Magnetic Viscosity", Proceedings of the Physical Society. Section A **62**, 562 (1949) 10.1088/0370-1298/62/9/303.

[324] V. Neu, C. Schulze, M. Faustini, J. Lee, D. Makarov, D. Suess, S.-K. Kim, D. Grosso, L. Schultz, and M. Albrecht, "Probing the energy barriers and magnetization reversal processes of nanoperforated membrane based percolated media", Nanotechnology **24**, 145702 (2013) 10.1088/0957-4484/24/14/145702.

[325] I. S. Jacobs and J. S. Kouvel, "Exchange Anisotropy in Mixed Manganites with the Hausmannite Structure", Phys. Rev. **122**, 412–418 (1961) 10.1103/PhysRev.122.412.

[326] P. J. Ford, "Spin glasses", Contemporary Physics **23**, 141–168 (1982) 10.1080/00107518208237073.

[327] P. Nordblad, L. Lundgren, and L. Sandlund, "A link between the relaxation of the zero field cooled and the thermoremanent magnetizations in spin glasses", Journal of Magnetism and Magnetic Materials **54-57**, 185–186 (1986) https://doi.org/10.1016/0304-8853(86)90543-3.

[328] W. Zhang, M. B. Jungfleisch, W. Jiang, J. E. Pearson, A. Hoffmann, F. Freimuth, and Y. Mokrousov, "Spin Hall Effects in Metallic Antiferromagnets", Phys. Rev. Lett. **113**, 196602 (2014) 10.1103/PhysRevLett.113.196602.

[329] T. Nishio, K. Ito, H. Kura, K. Takanashi, and H. Yanagihara, "Uniaxial magnetic anisotropy of $L1_0$-FeNi films with island structures on $LaAlO_3$(110) substrates by nitrogen insertion and topotactic extraction", Journal of Alloys and Compounds **976**, 172992 (2024) https://doi.org/10.1016/j.jallcom.2023.172992.

[330] P. Wasilewski, "Magnetic characterization of the new magnetic mineral tetrataenite and its contrast with isochemical taenite", Physics of the Earth and Planetary Interiors **52**, 150–158 (1988) https://doi.org/10.1016/0031-9201(88)90063-5.

[331] V. Thiruvengadam, B. B. Singh, T. Kojima, K. Takanashi, M. Mizuguchi, and S. Bedanta, "Magnetization reversal, damping properties and magnetic anisotropy of L1-ordered FeNi thin films", Applied Physics Letters **115**, 202402 (2019) 10.1063/1.5126324.

[332] M. Saito, H. Ito, Y. Suzuki, M. Mizuguchi, T. Koganezawa, T. Miyamachi, F. Komori, K. Takanashi, and M. Kotsugi, "Fabrication of L1-FeNi by pulsed-laser deposition", Applied Physics Letters **114**, 072404 (2019) 10.1063/1.5087041.

[333] K. Takanashi, M. Mizuguchi, T. Kojima, and T. Tashiro, "Fabrication and characterization of $L1_0$-ordered FeNi thin films", Journal of Physics D: Applied Physics **50**, 483002 (2017) 10.1088/1361-6463/aa8ff6.

[334] M. Mizuguchi, S. Sekiya, and K. Takanashi, "Characterization of Cu buffer layers for growth of L1-FeNi thin films", Journal of Applied Physics **107**, 09A716 (2010) 10.1063/1.3337649.

[335] K. Ito, M. Hayashida, H. Masuda, T. Nishio, S. Goto, H. Kura, T. Koganezawa, M. Mizuguchi, Y. Shimada, T. J. Konno, H. Yanagihara, and K. Takanashi, "Epitaxial L1-FeNi films with high degree of order and large uniaxial magnetic anisotropy fabricated by denitriding FeNiN films", Applied Physics Letters **116**, 242404 (2020) 10.1063/5.0011875.

[336] K. Ito, M. Hayashida, M. Mizuguchi, T. Suemasu, H. Yanagihara, and K. Takanashi, "Fabrication of $L1_0$-FeNi films by denitriding FeNiN films", Journal of the Magnetics Society of Japan **43**, 79–83 (2019) 10.3379/msjmag.1907R002.

[337] S. Goto, H. Kura, E. Watanabe, Y. Hayashi, H. Yanagihara, Y. Shimada, M. Mizuguchi, K. Takanashi, and E. Kita, "Synthesis of single-phase $L1_0$-FeNi magnet powder by nitrogen insertion and topotactic extraction", Scientific Reports **7**, 13216 (2017) 10.1038/s41598-017-13562-2.

[338] J.-W. Yeh, S.-K. Chen, S.-J. Lin, J.-Y. Gan, T.-S. Chin, T.-T. Shun, C.-H. Tsau, and S.-Y. Chang, "Nanostructured High-Entropy Alloys with Multiple Principal Elements: Novel Alloy Design Concepts and Outcomes", Advanced Engineering Materials **6**, 299–303 (2004) https://doi.org/10.1002/adem.200300567.

[339] M.-H. Tsai and J.-W. Yeh, "High-Entropy Alloys: A Critical Review", Materials Research Letters **2**, 107–123 (2014) 10.1080/21663831.2014.912690.

[340] W. B. Beeson, D. Bista, H. Zhang, S. Krylyuk, A. V. Davydov, G. Yin, and K. Liu, "Single-Phase $L1_0$-Ordered High Entropy Thin Films with High Magnetic Anisotropy", Advanced Science **11**, 2308574 (2024) https://doi.org/10.1002/advs.202308574.

[341] J. B. J. Chapman, P.-W. Ma, and S. L. Dudarev, "Dynamics of magnetism in Fe-Cr alloys with Cr clustering", Phys. Rev. B **99**, 184413 (2019) 10.1103/PhysRevB.99.184413.

[342] A. Schneider, C.-C. Fu, and C. Barreteau, "Local environment dependence of Mn magnetism in bcc iron-manganese alloys: A first-principles study", Phys. Rev. B **98**, 094426 (2018) 10.1103/PhysRevB.98.094426.

[343] V. Tang Nguyen, F. Mazaleyrat, and N. Randrianantoandro, "Investigation of Mn-Fe magnetic interaction in mechanically alloyed Fe doped-MnAlC by ^{57}Fe Mössbauer spectrometry", Journal of Magnetism and Magnetic Materials **568**, 170437 (2023) https://doi.org/10.1016/j.jmmm.2023.170437.

[344] J. L. Tsai, Y. C. Lin, and C. J. Hsu, "$L1_0$ CrPt underlayer thickness effects on FePt film ordering", Journal of Physics D: Applied Physics **41**, 025002 (2007) 10.1088/0022-3727/41/2/025002.

[345] A. M. Miller, M. Lemon, M. A. Choffel, S. R. Rich, F. Harvel, and D. C. Johnson, "Extracting information from X-ray diffraction patterns containing Laue oscillations", Zeitschrift für Naturforschung B **77**, 313–322 (2022) doi:10.1515/znb-2022-0020.

[346] M. Maret, M. Albrecht, J. Köhler, R. Poinsot, C. Ulhaq-Bouillet, J. M. Tonnerre, J. F. Berar, and E. Bucher, "Magnetic anisotropy and chemical long-range order in epitaxial ferrimagnetic $CrPt_3$ films", Journal of Magnetism and Magnetic Materials **218**, 151–164 (2000) https://doi.org/10.1016/S0304-8853(00)00367-X.

[347] Y. Kwon, T. H. Rho, S. Lee, and S. C. Hong, "Magnetic structures of $CrPt_3$ by first-principles calculations", Journal of Applied Physics **93**, 7151–7153 (2003) 10.1063/1.1558609.

[348] S. J. Pickart and R. Nathans, "Neutron Diffraction Investigation of Pt-Based Alloys of the First Transition Series", Journal of Applied Physics **34**, 1203–1204 (1963) 10.1063/1.1729434.

[349] T. D. Leonhardt, Y. Chen, M. Rao, D. E. Laughlin, D. N. Lambeth, and M. H. Kryder, "$CrPt_3$ thin film media for perpendicular or magneto-optical recording", Journal of Applied Physics **85**, 4307–4309 (1999) 10.1063/1.370351.

[350] M. J. Besnus and A. J. P. Meyer, "Magnetic Properties of the Ordered and Disordered $CrPt_3$ and CrPt Phases", physica status solidi (b) **58**, 533–542 (1973) https://doi.org/10.1002/pssb.2220580213.

[351] T. Kato, D. Oshima, Y. Yamauchi, S. Iwata, and S. Tsunashima, "Fabrication of $L1_2$-$CrPt_3$ Alloy Films Using Rapid Thermal Annealing for Planar Bit Patterned Media", IEEE Transactions on Magnetics **46**, 1671–1674 (2010) 10.1109/TMAG.2010.2044559.

[352] E. Suharyadi, D. Oshima, T. Kato, and S. Iwata, "Nanoscale Patterning of $CrPt_3$ Magnetic Thin Films by Using Ion Beam Irradiation", Results in Physics **6** (2016) 10.1016/j.rinp.2016.03.010.

[353] Y. M. Hu, J. C. A. Huang, C. W. Chen, C. H. Lee, and M. J. Lin, "Perpendicular magnetization of epitaxial $CrPt_x$ films", Journal of Applied Physics **98**, 013901 (2005) 10.1063/1.1929862.

[354] A. Tomou, I. Panagiotopoulos, V. Tzitzios, W. Li, and G. C. Hadjipanayis, "Chemical synthesis and $L1_2$ ordering of $CrPt_3$ nanoparticles", Journal of Magnetism and Magnetic Materials **334**, 107–110 (2013) https://doi.org/10.1016/j.jmmm.2013.01.025.

[355] Y. Shiratsuchi, M. Yamashita, R. Nakatani, H. Nomura, and M. Yamamoto, "Magnetic Properties of $L1_2$-type $CrPt_3$(111) film having the different order parameters", Journal of The Magnetics Society of Japan **33**, 447–450 (2009) 10.3379/msjmag.0907MC0003.

List of publications

[**1**] J. Lisik, M. Rojas, S. Myrtle, D. H. Ryan, R. Hübner, P. Omelchenko, C. Abert, A. Ducevic, D. Suess, I. Soldatov, R. Schaefer, J. Seyd, M. Albrecht, and E. Girt, "Transition from ferromagnetic to noncollinear to paramagnetic state with increasing Ru concentration in FeRu films", Phys. Rev. B **110**, 104429 (2024) 10.1103/PhysRevB.110.104429.

[**2**] M. Stiehl, S. Wust, N. Schmidt, T. Dannegger, J. Seyd, M. Berritta, P. M. Oppeneer, M. Albrecht, U. Nowak, and M. Aeschlimann, "All-optical switching in Cr- and Mn-doped $L1_0$ FePt thin films", Phys. Rev. Appl. **21**, 054064 (2024) 10.1103/PhysRevApplied.21.054064.

[**3**] S. A. Sam, J. Seyd, A. Ullrich, F. Jung, F. Groß, M. Krupiński, M. Albrecht, and S. Thomas, "Size-dependent bistability of magnetic states in soft magnetic cap arrays", Appl. Phys. Lett. **35**, 225701 (2024) 10.1088/1361-6528/ad2c5c.

[**4**] A. Chanda, N. Schulz, C. Holzmann, J. Seyd, M. Albrecht, M.-H. Phan, and H. Srikanth, "Thermal Generation of Spin Current and Magnon Propagation Length in Compensated Ferrimagnetic $Gd_3Fe_5O_{12}$ Thin Films", IEEE Trans. Magn. **58**, 1-5 (2022) 10.1109/TMAG.2022.3144835.

[**5**] A. Chanda, C. Holzmann, N. Schulz, J. Seyd, M. Albrecht, M.-H. Phan, and H. Srikanth, "Scaling of the Thermally Induced Sign Inversion of Longitudinal Spin Seebeck Effect in a Compensated Ferrimagnet: Role of Magnetic Anisotropy", Adv. Funct. Mater. **32**, 2109170 (2022) https://doi.org/10.1002/adfm.202109170.

[**6**] C. Weiss, R. Hübner, M. Saunders, A. Semisalova, J, Ehrler, N. Schmidt, J. Seyd, M. Albrecht, S. Answar, J. Lindner, K. Potzger, and M. Kostylev, "Effects of hydrogen absorption on magnetism in $Ni_{80}Fe_{20}$/Y/Pd trilayers", Phys. Rev. B. **104**, 094429 (2021) 10.1103/PhysRevB.104.094429.

[7] J. Seyd, I. Pilottek, N. Y. Schmidt, O. Caha, M. Urbánek, and M. Albrecht, "Mn_3Ge-based tetragonal Heusler alloy thin films with addition of Ni, Pt, and Pd", J. Phys. Condens. Matter **32**, 145801 (2020) 10.1088/1361-648X/ab5e16.

[8] D. L. M. Cordova, S. S. Fender, T. M. Kam, J. Seyd, M. Albrecht, P. Lu, R. Fischer, and D. C. Johnson, "Designed Synthesis and Structure–Property Relationships of Kinetically Stable $[(PbSe)_{1+\delta}]_m(VSe_2)_1$ (m = 1, 2, 3, 4) Heterostructures", Chem. Mater. **31**, 8473-8483 (2019) 10.1021/acs.chemmater.9b02826.

Conference contributions

- "Double Exchange Bias and Ultraslow Magnetization Relaxation in TbFe-based Bilayers", oral presentation, DPG-Frühjahrstagung, Berlin, Germany (2024).

- "Double Exchange Bias and Ultraslow Magnetization Relaxation in TbFe-based Bilayers", oral presentation, Joint European Magnetism Symposia (JEMS), Madrid, Spain (2023).

- "All-optical switching of magnetically hard Co/Pt and $L1_0$-FePt in contact with a Gd-layer", poster presentation, Ultrafast Magnetism Conference (UMC), Nancy, France (2022).

- "All-optical switching of magnetically hard Co/Pt and $L1_0$-FePt in contact with a Gd-layer", poster presentation, DPG-Frühjahrstagung, Regensburg, Germany (2022).

- "Magnetic Compensation in Mn_3Ge-based Heusler Alloys with Addition of Ni, Pt, and Pd", oral presentation, DPG-Frühjahrstagung, Regensburg, Germany (2019).

Acknowledgements

As the saying goes: "We stand on the shoulders of giants." Likewise, I could not have completed this thesis all by myself. There are many people standing next to me on those shoulders, people that i was able to lean on or that in any other way helped me through these tough past years. For this I am immensely grateful. I cannot name all of them, but will try my best to include the most relevant ones.
In no particular order, I want to thank:

- Prof. Dr. Manfred Albrecht for providing a research position in his group and creating a work environment that grants the PhD students a lot of free space to develop their ideas and pursue their research in their own way. He also creates many opportunities for joining conferences or visiting collaboration partners, even in faraway places. His knowledge of magnetic thin films and enthusiasm were of immense help during the research process.
- The technicians at EP IV: Wolfgang Reiber, Birgit Knoblich, Olga Lik, and Fabian Hirschberger. Without you, none of us students would be able to pursue our research the way we do.
- Our EP IV seretaries Claudia Löflath and Bettina Schestak for taking care of and helping with any kind of bureaucracy.
- Dr. Aladin Ullrich and Birgit Knoblich for TEM measurements and sample preparation.
- My present and former colleagues in the magnetism and thermoelectrics groups: Christian Holzmann, Timo Schmidt, Stephan Glamsch, Maximilian Mihm, Joe Sunny, Tamer Karaman, Benedikt Eberts, David Stein, Dr. Aladin Ullrich, Dr. Matthias Küß, Dr. Nataliia Schmidt, Dr. Felix Timmermann, Dr. Mario Fix, Dr. Florian Jung, Dr. Michael Heigl, Dr. Marc Lindorf, Dr. Clemens Mühlenhoff, Dr. Mariam Hassan, Dr. Oana Ciubotariu, Dr. Michał Krupiński, Julian Hintermayr and Isabel Pilottek. One of the factors that made me start the PhD journey was the relaxed and friendly atmosphere that we have always had in our group, and the fact that some of us also became friends outside of university. The way we share our knowledge and experience, not always only work-related, made me happy to be part of this community.
- All other colleagues from EPIV for creating a great working environment, including the frequent bringing and sharing of cakes.
- Nataliia Schmidt for being my mentor in the earlier years and a friend today.

- Arina Nadeina and Martin Schäfer, originally from the chair of solid state chemistry, for being amazing human beings.
- Prof. Dr. Senoy Thomas, Prof. Dr. M. R. Anantharaman, and the rest of the team at CUSAT for welcoming Christian and me on our trip to Kochi.
- A variety of people I had the joy of meeting at conferences, workshops, or other trips: Maxime and Mattia from 's Hertogenbosch; Daniel, Thom, Niels, and Rose from Nijmegen; Andrea and Eleonora from Messina; Shan, Anija, Navya, Sandra, and Thoufeeq from Kochi. All of you made me feel welcome and accepted.
- My therapist Assja Metzger for accompanying me through difficult times and helping me to understand myself better.
- My D&D crew Julian, Felix, Mario, and Marc for showing up basically every week for six years(!), which allowed us to make up a world in which we collectively created a fantastic story. While it could sometimes be stressful in a way, I really enjoyed the creative process and the evenings we spent together, and I possibly even picked up some group leading skills on the way.
- All my friends from Kempten. I find it amazing that we managed to regularly keep in touch throughout the years, and I hope this will never change.
- My mother Karena, my siblings Jakob and Melanie, my nephew Fynn, my father Enrico, and my partner in life Raluca. All of you make my life better in your own ways.

Lastly, I want to express my gratitude for living in a country with free access to education, which is a supreme luxury and should not be taken for granted.